



HAL
open science

Scaling and coupling analysis of wind speed and wave height using CFOSAT and other satellites

Yang Gao

► **To cite this version:**

Yang Gao. Scaling and coupling analysis of wind speed and wave height using CFOSAT and other satellites. Ocean, Atmosphere. Université du Littoral Côte d'Opale; Xiamen university (Chine), 2023. English. NNT : 2023DUNK0652 . tel-04120013

HAL Id: tel-04120013

<https://theses.hal.science/tel-04120013>

Submitted on 7 Jun 2023

HAL is a multi-disciplinary open access archive for the deposit and dissemination of scientific research documents, whether they are published or not. The documents may come from teaching and research institutions in France or abroad, or from public or private research centers.

L'archive ouverte pluridisciplinaire **HAL**, est destinée au dépôt et à la diffusion de documents scientifiques de niveau recherche, publiés ou non, émanant des établissements d'enseignement et de recherche français ou étrangers, des laboratoires publics ou privés.



Thèse de Doctorat

Discipline: Sciences agricoles et écologiques
Spécialité: Sciences de la Mer - Océanographie Physique

présentée à *l'Ecole Doctorale en Sciences Technologie et Santé (ED 585)* de
l'Université du Littoral Côte d'Opale
et
à *l'Ecole doctorale Collège des Sciences de l'Océan et de la Terre*
de l'Université de Xiamen
par

Yang Gao

pour obtenir le grade de Docteur de l'Université du Littoral Côte d'Opale &
Xiamen University

Analyse de mise à l'échelle et de couplage de la vitesse du vent et de la hauteur des vagues, à l'aide de CFOSAT et d'autres satellites

Soutenue le 27 Février 2023, après avis des rapporteurs, devant le jury d'examen :

M. Alexei Sentchev, Professeur, ULCO

M^{me} Anne-Claire Bennis, Professeur, UNICAEN

M. Shengqi Zhou, Professeur, SCSIO

M. Jianyu Hu, Professeur, XMU

M. Lipo Wang, Professeur Associé, SJTU

M. Enrico Calzavarini, Professeur Adjoint, ULille

M. Francois Schmitt, Professeur, CNRS

M. Yongxiang Huang, Professeur Associé, XMU

Président

Rapporteur

Rapporteur

Examineur

Examineur

Examineur

Directeur de thèse

Co-encadrant





Thesis of Doctorate

*Discipline: Agricultural and Ecological Sciences
Speciality: Marine Sciences - Physical Oceanography*

Presented at *the Doctoral School in Science Technology and Health (ED 585)*
of the Université du Littoral Côte d'Opale
and
at the College of Ocean and Earth Science
Xiamen University

Yang Gao

To obtain the degree of doctor of Université du Littoral Côte d'Opale & Xiamen University

Scaling and Coupling Analysis of Wind Speed and Wave Height Using CFOSAT and Other Satellites

Defended on February 27, 2023, after the opinion of the rapporteurs, before the examination jury:

Mr. Alexei Sentchev, Professeur, ULCO
MRs. Anne-Claire Bennis, Professeur, UNICAEN
Mr. Shengqi Zhou, Professeur, SCSIO
Mr. Jianyu Hu, Professeur, XMU
Mr. Lipo Wang, Professeur Associé, SJTU
Mr. Enrico Calzavarini, Professeur Adjoint, ULille
Mr. Francois Schmitt, Professeur, CNRS
Mr. Yongxiang Huang, Professeur Associé, XMU

President
Reviewer
Reviewer
Jury Member
Jury Member
Jury Member
Supervisor
Co-supervisor





博士学位论文

专业:物理海洋学

Université du Littoral Côte d'Opale & 厦门大学

高阳

中法海洋卫星等卫星风速与波高的标度 及耦合关系分析

答辩时间: 2023年2月27日

答辩委员会成员:

Alexei Sentchev, ULCO	答辩委员会主席
Anne-Claire Bennis, UNICAEN	评阅人
周生启, SCSIO	评阅人
胡建宇, XMU	答辩委员会成员
王利坡, SJTU	答辩委员会成员
Enrico Calzavarini, ULille	答辩委员会成员
Francois Schmitt, CNRS	论文指导老师
黄永祥, XMU	论文指导老师



Abridged French Version - Version Française Abrégée

Les vagues de surface de l'océan et le vent jouent un rôle crucial dans les échanges air-mer de quantité de mouvement, de chaleur et de masse, et sont par conséquent vitaux pour le contrôle du temps et du climat. Alors que la connaissance fondamentale des interactions air-mer fait encore défaut. Par conséquent, les sorties des modèles météorologiques et climatiques comportent de grandes incertitudes. De plus, en raison de la gamme extrêmement large d'échelles impliquées dans les mouvements des champs de vent et de vagues, par exemple, des structures d'écoulement allant de millimètres à des milliers de kilomètres, il existe des dynamiques multi-échelles très importantes, et sont souvent accompagnées d'une puissance-loi de comportement des fluctuations dans les domaines spatial et temporel. Pendant ce temps, les flux d'énergie et d'entrophie d'échelle à échelle existent intrinsèquement dans les systèmes turbulents de vent et de vagues qui sont induits par des interactions non linéaires entre différentes échelles. L'image floue de la cascade augmente également les incertitudes du modèle. Pour réduire les incertitudes des modèles météorologiques et climatiques actuels, une bonne compréhension de la relation vent-vague et de la cascade est nécessaire.

L'analyse dynamique du vent et des vagues a principalement été effectuée séparément dans les études précédentes, en raison de la limitation des données disponibles. Grâce au satellite d'océanographie Chine France (CFOSAT), les données de vitesse du vent (U_{10}) et de hauteur significative des vagues (H_s) peuvent être observées simultanément depuis l'espace pour la première fois. Dans lequel U_{10} est observé par le radar à faisceau en éventail rotatif en bande Ku conçu par la China National Space Administration, les données sont fournies depuis décembre 2018, et la résolution spatiale est de 12.5 km, avec une largeur de fauchée de 1,000 km. Les précisions des données sont de 2 m/s pour la magnitude et de 20° pour la direction. Les données H_s sont collectées par le radar à ouverture réelle en bande Ku fourni par le Centre National d'Etudes Spatiales. Les données sont fournies depuis juillet 2019. Les données H_s utilisées dans ce travail sont à une résolution de 1.5 km, avec une précision de 0.25-0.3 m.

CFOSAT offre une chance unique d'analyser ensemble le vent et les vagues à l'échelle mondiale. Dans cette thèse, la dynamique multi-échelle du vent et des vagues de surface océanique est principalement étudiée avec les données longitudinales de CFOSAT, ainsi

que les données d'autres missions satellitaires. Les caractéristiques d'échelle, l'énergie d'échelle à échelle et les flux d'entrophie pour les processus de surface de l'océan sont examinés. Enfin, la relation couplée entre le vent et les vagues est obtenue.

Dans le premier travail de cette thèse, la dynamique multi-échelle des données CFOSAT est considérée comme des grandeurs atmosphériques et océaniques influencées par la turbulence, qui est due aux interactions entre différentes échelles de mouvements, et à l'absence d'échelle caractéristique. Les comportements en loi de puissance pour U_{10} et H_s sont étudiés par une analyse spectrale de puissance de Fourier améliorée via le théorème de Wiener-Khinchine qui peut traiter les données avec des lacunes. Tout d'abord, laisser les données perdre au hasard pour générer de nouveaux ensembles de données, puis mesurer la fonction d'auto-corrélation moyenne. De cette façon, le biais est réduit par des phases aléatoires de réalisations indépendantes. Après cela, avec un transfert de Fourier rapide, le spectre correspondant peut être récupéré. D'autres tests montrent que la méthode améliorée d'estimation du spectre de puissance de Fourier pourrait traiter les données avec un taux de données manquantes maximal de 85%. Avec la nouvelle méthode, les spectres pour CFOSAT observés simultanément U_{10} et H_s sont mesurés à différentes échelles pour obtenir la dynamique multi-échelle correspondante.

Au sens moyen global, on trouve des caractéristiques de loi de puissance pour U_{10} et H_s . Les plages d'échelle pour le vent vont de 100 à 3,000 km, dans lesquelles l'exposant d'échelle est égal à $5/3$ dans la plage de 100 à 500 km. Pour les plages supérieures à 500 km, les valeurs de l'exposant de mise à l'échelle sont comprises entre 2 et 3. Comme pour les données de vagues, les plages de mise à l'échelle se situent entre 3 et 3,000 km. Les valeurs de l'exposant de mise à l'échelle sont proches de $5/3$, 2 et 3 dans les plages de 3 à 50 km, 100 à 1,000 km et 1,000 à 3,000 km, respectivement.

Les spectres moyennés des composantes zonales et méridiennes de U_{10} sont également calculés pour tester provisoirement l'isotropie directionnelle horizontale du champ de vent. Les deux spectres mesurés montrent des caractéristiques d'échelle similaires, avec le spectre de la composante zonale légèrement plus grand que celui méridien. Le rapport isotrope est également estimé et trouvé proche de la valeur théoriquement prédite de $3/4$ pour la turbulence isotrope.

Pour examiner la corrélation spatiale entre le vent et les vagues, le spectre croisé et le spectre de cohérence entre le vent et les vagues sont estimés. Les caractéristiques de la loi de puissance se trouvent dans le spectre croisé aux échelles de 30 à 2500 km, dans lesquelles les exposants d'échelle sont égaux à 1.8 et 2.4 dans les plages de 30 à 250 km

et de 250 à 2500 km, respectivement. Les valeurs du spectre de cohérence sont comprises entre 0.04 et 0.13 pour toutes les échelles, et le maximum se situe vers 1200 km. Ces résultats indiquent que le vent et les vagues sont spatialement couplés.

Les caractéristiques d'échelle pour le vent et les vagues sont également prises en compte dans les échelles de bassin pour éviter l'influence du mélange d'informations d'échelle induit par différents systèmes climatiques dans différents bassins. Les spectres mesurés à partir de différents bassins océaniques ont tous la même forme et partagent les mêmes propriétés d'échelle. Les spectres de U_{10} présentent une échelle très nette avec des exposants proches de 2 dans des échelles de 25 à 2500 km pour tous les bassins, ce qui est tout à fait remarquable. Pour clarifier ce point, un test est effectué, à savoir, une région de l'océan Pacifique (dans la région latitudinale de 25°S-25°N) qui contient le signal de caractéristique d'échelle tropicale est choisie pour estimer les spectres de la vitesse du vent. Le résultat montre qu'une excellente mise à l'échelle est perdue et que des ruptures d'échelle sont trouvées autour de 500 km lorsque la région tropicale est également considérée. Concernant H_s , les exposants d'échelle sont proches de 3, et 2 pour les gammes de 500 à 3,000 km et 50 à 500 km, respectivement. Alors que pour les échelles inférieures à 50 km, les spectres de H_s montrent plus de rugosité par rapport à ceux à plus grande échelle. Cela peut indiquer que les processus complexes de sous-mésoéchelle sont dominants à ces échelles.

À l'exception de l'étude des caractéristiques d'échelle à l'échelle globale et à l'échelle du bassin, les caractéristiques à méso-échelle sont également examinées. Cela signifie que les exposants d'échelle pour U_{10} sont estimés en 1,000 km fois 1,000 km de surface carrée, et celui pour H_s est en 1,000 km le long de la section de voie. Ensuite, les distributions globales et les variations saisonnières de β sont extraites dans une vue globale. Les exposants d'échelle mesurés pour U_{10} et H_s présentent tous deux une nette dépendance latitudinale. Des limites distinctes qui séparent les exposants d'échelle dont les valeurs sont supérieures ou inférieures à 1.8 se trouvent autour des latitudes des chevaux (30 degrés au nord et au sud de l'équateur) pour U_{10} . Un β plus grand pourrait être lié au fait que des caractéristiques synoptiques plus fortement énergétiques aux latitudes moyennes augmentent le niveau d'énergie à grande échelle. De plus, une petite partie avec de grands exposants d'échelle se trouve près du Pacifique oriental équatorial (par exemple, environ 90°W à 160°W et 10°S à 10°N), qui, par coïncidence, se trouve dans la même région que le célèbre Pacifique équatorial sec zone. Pour les régions voisines, telles que la zone de convergence intertropicale (ITCZ), le bassin chaud du Pacifique équatorial (PWP) et

la zone de convergence de l'Atlantique Sud (SACZ), les exposants d'échelle pour U_{10} sont proches de $5/3$ en raison des activités convectives énergétiques. Pour H_s , les exposants d'échelle sont plus grands que ceux dérivés de U_{10} pour la plupart des régions, les variations méridiennes sont relativement faibles par rapport au cas U_{10} . Les exposants d'échelle pour H_s sont tous supérieurs à 2.1, sauf pour les zones côtières. De plus, des β relativement petits se trouvent dans les régions tropicales.

Les variations saisonnières des caractéristiques de mise à l'échelle sont obtenues en soustrayant les exposants de mise à l'échelle moyens d'hiver des exposants moyens d'été. Les résultats montrent que les variations saisonnières de β sont plus faibles aux moyennes latitudes que celles observées aux basses latitudes, aussi bien pour U_{10} que pour H_s . Les exposants d'échelle pour U_{10} sont plus grands en hiver que ceux en été pour la plupart des régions. Ceci est traditionnellement associé à l'activité barocline à son apogée pendant l'hiver. Pour H_s , les variations saisonnières de β sont relativement compliquées. Pour l'hémisphère nord, β est plus grand en été que ceux en hiver pour la plupart des régions ; dans la zone tropicale de l'hémisphère sud, β pour H_s est plus grand en hiver, alors pour les régions plus au sud que 25°S , les différences saisonnières s'avèrent vagues.

Les caractéristiques de mise à l'échelle extraites pour U_{10} à partir de CFOSAT sont confirmées par l'analyse des données QuikSCAT. Des variations spatiales et temporelles similaires pour β et $\zeta(2)$ sont trouvées, mais les résultats sont plus lisses en raison de la moyenne à long terme des données QuikSCAT. Pour les données collectées par d'autres satellites, par exemple HY-2B, MetopB et MetopC, les spectres de puissance de Fourier moyens mondiaux sont également estimés. Les caractéristiques d'échelle se retrouvent les mêmes pour les échelles de 100 à 1,000 km. Pour les échelles inférieures à 100 km, des différences sont évidentes, mais une explication manque encore. À l'exception de l'analyse d'échelle pour U_{10} collectée à partir de satellites, les données fournies par l'ECMWF sont également prises en compte dans ce travail. Les résultats montrent que les β pour U_{10} de l'ECMWF sont plus grands que ceux des données satellitaires, et les variations saisonnières correspondantes sont opposées à celles de l'analyse des données satellitaires.

En outre, une analyse de la fonction de structure est également effectuée pour confirmer les caractéristiques d'échelle dérivées de l'analyse spectrale. La fonction de structure de second ordre mesurée pour U_{10} et H_s montre des caractéristiques d'échelle aux échelles de 50 à 500 km et de 10 à 1,000 km, respectivement, avec l'exposant d'échelle $\zeta(2) \approx 1$. Cela signifie que la prédiction de turbulence isotrope de la relation entre les exposants d'échelle $\zeta(2)$ pour la fonction de structure de second ordre et β pour l'analyse spectrale

de puissance de Fourier, à savoir, $\zeta(2) = \beta - 1$, est à peu près satisfaite pour les données U_{10} et H_s dans les échelles sous 500 km, indique une caractéristique isotrope horizontale pour le champ de vent dans cette plage. De plus, la caractéristique isotrope horizontale pour U_{10} est en outre diagnostiquée en estimant les exposants d'échelle pour les deux composantes du champ de vent, où le spectre de puissance de Fourier et la fonction de structure de second ordre sont pris en compte. De plus, le spectre bidimensionnel et la structure-fonction bidimensionnelle de U_{10} sont extraits, et la caractéristique d'isotropie horizontale est trouvée pour des échelles de 100 à 1,000 km dans ces études.

L'analyse structure-fonction d'ordre élevé est également effectuée pour étudier les caractéristiques d'intermittence pour U_{10} et H_s . Pour U_{10} , les caractéristiques de loi de puissance sont trouvées de 12.5 à 1,000 km, tandis que pour H_s , deux plages sont détectées, par exemple, 2 à 30 km et 100 à 1,000 km. Les exposants d'échelle extraits $\zeta(q)$ sont comparés au modèle K41 et au modèle lognormal modifié proposé par Li et Huang (2014). Les résultats montrent que H_s est plus intermittent que U_{10} et que $\zeta(q)$ pour H_s à grande échelle peut être bien décrit par le modèle log-normal avec le nombre de Hurst $H = 0.6$ et le paramètre d'intermittence $\beta = 0.3$, ce qui coïncide avec la valeur pour les écoulements à forte turbulence de Reynolds Frisch (1995).

En résumé, pour le premier travail, les caractéristiques d'échelle pour le vent et les vagues sont extraites, alors que les résultats ne sont pas cohérents avec les théories de turbulence existantes, la raison pourrait être liée au fait que les données sont collectées au bas de la limite atmosphérique plus tard. De plus, les résultats obtenus à partir des données QuikSCAT sont proches de ceux des données CFOSAT, cependant, de grandes différences sont trouvées pour les caractéristiques d'échelle dérivées des données de réanalyse. Pour d'autres travaux, nous prévoyons de caractériser davantage l'intermittence dans ces plages d'échelle, en considérant les fonctions de structure conjointes et également l'analyse spectrale de Hilbert (HSA) d'ordres supérieurs, qui ne sont pas fortement impactées par le forçage énergétique. En outre, la raison d'obtenir différentes caractéristiques d'échelle à partir de diverses données satellitaires sera étudiée en tenant compte des différences de conception des diffusiomètres, des algorithmes utilisés pour la récupération du vent et du critère de contrôle de la qualité, pour n'en citer que quelques-uns.

Dans le deuxième travail, une technique d'espace de filtre (FST) améliorée est proposée pour extraire le flux d'énergie Π_E et le flux d'enstrophie Π_Ω entre différentes échelles pour le champ de vent de surface océanique. Le FST est d'abord utilisé dans le domaine de la turbulence pour les grands travaux de simulation de tourbillons et a été largement utilisé

pour déterminer la direction et l'intensité des cascades. Bien que l'analyse longitudinale de la fonction de structure du troisième ordre et l'approche spectrale puissent toutes deux estimer les flux, ces deux méthodes ont des limites inévitables. Par exemple, l'analyse structure-fonction du troisième ordre nécessite que le champ soit dans un état d'isotropie. L'interprétation du résultat est liée au choix de la théorie de la turbulence 2D ou 3D. Quant à l'approche spectrale, elle n'est adaptée qu'aux données de terrain régulières, et ne peut pas être appliquée aux données observées par satellite. Ainsi, FST est choisi pour faire l'analyse de flux ici. Ici, le noyau du filtre est défini comme gaussien en partie parce qu'il a de bonnes propriétés passe-bas dans l'espace de Fourier. Nous notons que l'inconvénient de la FST est évident : elle est chronophage puisque la convolution est impliquée pour chaque échelle r , mais elle est encore beaucoup plus rapide que l'approche structure-fonction puisque la convolution basée sur la FFT est effectuée.

Avant de traiter le champ de vent fourni par CFOSAT, des contrôles de qualité basés sur le filtre Hamper des données ont été effectués. De plus, une projection du vecteur vent est effectuée sur les données. À savoir, projeter le vecteur de vent d'origine à partir de la coordonnée basée sur la latitude longitudinale vers la coordonnée basée sur la trajectoire du satellite. Ensuite, les flux ont pu être estimés à différentes échelles avec les ajustements des échelles de filtre. De plus, l'information locale sur les flux peut être conservée. Dans ce travail, une matrice de masque est introduite pour que le FST gère le problème du continent ou des données manquantes afin de rendre cette approche adaptée à l'analyse globale. Les tests montrent que pour les échelles inférieures à 500 km qui sont considérées dans ce travail, les impacts des données manquantes sur le flux d'énergie moyen sont inférieurs à 20% pour le taux manquant inférieur à 40% dans la plupart des cas. Ainsi, en pratique, pour améliorer la précision de notre analyse, les données contenant plus de 40% d'écarts sont exclues de cette étude.

Les vues globales de Π_E et Π_Ω pour le champ de vent CFOSAT sont étudiées aux échelles de 12.5 à 500 km. Les résultats montrent que les valeurs des flux d'énergie et d'entropie se situent respectivement autour des décades de 10^{-5} et 10^{-7} m^2/s^3 . Les flux positifs et négatifs se retrouvent à petite et grande échelles. De plus, Π_E et Π_Ω sont presque symétriques hémisphériques, avec des variations spatiales et temporelles évidentes pour toutes les échelles. Plus précisément, des Π_E positifs et négatifs sont trouvés pour les échelles inférieures et supérieures à 60 km, respectivement. Quant à Π_Ω , l'échelle de transition est d'environ 150 km, et les cascades directes et inverses correspondent aux échelles inférieures et supérieures à cette échelle. Nous notons ici que les schémas de distribution

pour Π_{Ω} sont relativement complexes par rapport à ceux de Π_E , ce qui pourrait être induit par la qualité des données de vent. Deux fois les gradients spatiaux sont effectués pour estimer le Π_{Ω} ; tandis que pour Π_E , un seul gradient est requis.

Dans l'espace physique, des flux plus forts se produisent aux latitudes moyennes que dans les régions tropicales, à l'exception d'une région étroite autour de 10°N , qui correspond à l'ITCZ, où de forts flux sont observés. À l'échelle de 250 km, des flux d'énergie négatifs à l'échelle du bassin se trouvent aux latitudes moyennes pour les deux hémisphères en hiver. Alors que pour l'été, la direction de la cascade d'énergie tourne vers l'avant dans les latitudes moyennes de l'hémisphère nord. Ces caractéristiques sont également confirmées par les diagrammes d'évolution des flux avec les données recueillies dans trois régions sélectionnées de l'océan Pacifique. En ce qui concerne le flux d'énstrophie, les cascades avant et arrière sont mélangées aux latitudes moyennes à l'échelle de 250 km, et des schémas de distribution complexes sont illustrés. Les différences saisonnières pour l'énstrophie à cette échelle étudiée ne sont pas claires.

Ici, les flux moyens annuels d'énergie et d'énstrophie pour les échelles de 12.5 à 500 km sont estimés, puis les résultats moyens longitudinaux correspondants sont extraits. Les diagrammes de phase mesurés à l'échelle de la latitude pour les flux d'énergie et d'énstrophie montrent des schémas de distribution symétrique hémisphérique pour les flux, avec des caractéristiques de distribution méridiennes évidentes : des grandes aux latitudes moyennes et une plage étroite autour de l'ITCZ, des plus petites dans les aires de repos. Les cascades avant et arrière pour l'énergie et l'énstrophie se trouvent respectivement à petite et grande échelle.

À l'exception de l'analyse temporelle et spatiale moyennée des flux, les flux d'énergie et d'énstrophie simultanés pour le typhon Maysak (2020) ont été estimés. Des schémas spatiaux compliqués pour les flux d'énergie et d'énstrophie ont été trouvés autour du centre du typhon. Des patches de flux positifs et négatifs sont alternativement distribués autour du centre du typhon. Les structures du typhon sont bien capturées par les cartes de flux, indiquant une dynamique complexe. Les grandeurs des flux d'énergie et d'énstrophie sont de l'ordre de $10^{-5} \text{ m}^2/\text{s}^3$. Les flux moyennés spatialement à d'autres échelles sont également estimés. Pour les flux d'énergie, des cascades directes nettes sont trouvées pour toutes les échelles, indiquant que l'énergie totale est transférée des échelles supérieures à 500 km vers les échelles inférieures à 12.5 km. Pour le flux d'énstrophie, des cascades vers l'avant sont trouvées pour des échelles inférieures à 50 km et des échelles supérieures à 200 km. Dans les fourchettes entre ces deux échelles, on trouve une cascade nette vers

l'arrière.

Les caractéristiques des flux d'échelle à échelle dérivés des données CFOSAT sont confirmées avec l' U_{10} fourni par la mission QuikSCAT. En utilisant le même algorithme FST, les données de vent QuikSCAT sur 10 ans sont traitées, les mêmes variations spatiales et temporelles pour les flux aux échelles de 12.5 à 500 km sont obtenues. Les valeurs des flux d'entrophie se trouvent légèrement inférieures à celles de l'analyse des données CFOSAT, ce qui pourrait être induit par les différences de conception des diffusionmètres, les algorithmes de récupération des données ou les qualifications du contrôle qualité. De plus, l'évolution mensuelle des flux d'entrophie est légèrement différente des deux jeux de données. Des échelles de transition relativement grandes sont trouvées pour les flux d'entrophie des données QuikSCAT par rapport aux résultats CFOSAT. Des flux d'entrophie positifs sont observés tout au long de l'année à petite échelle (inférieure à l'échelle de transition) pour les données QuikSCAT, tandis que des flux d'entrophie négatifs sont visibles à petite échelle en juillet pour les données CFOSAT.

Les caractéristiques de flux énergie/entrophie à l'échelle de 250 km sont également testées avec les données du produit ECMWF au niveau de pression de 1,000 hPa. De grandes différences sont trouvées entre les résultats des observations et de la réanalyse. Bien que les flux directs et inverses puissent être reproduits dans l'analyse des données de l'ECMWF, les valeurs des flux et les variations spatiales et temporelles correspondantes sont différentes des analyses des données satellitaires. Alors que les résultats sont proches de ceux obtenus à partir de l'analyse des données brutes de vent CFOSAT (sans contrôle de qualité). Une analyse plus poussée de la fonction de densité de probabilité des données de vent brutes CFOSAT et des données de réanalyse montre que les fonctions de densité de probabilité possèdent toutes deux de longues queues dans les grandes parties de vitesse du vent. Cependant, la partie de queue de la fonction de densité de probabilité des données de vent CFOSAT à qualité contrôlée disparaît. Ainsi, les écarts dans les flux dérivés des données de réanalyse pourraient être induits par des valeurs anormalement élevées. Les valeurs extrêmement élevées de l'ensemble de données auront un effet vital sur le calcul du gradient de données, de même que sur les valeurs de flux finales. Ainsi, même avec très peu de valeurs aberrantes dans l'ensemble de données, les impacts sont difficiles à limiter avec des moyennes spatiales ou temporelles. Par conséquent, les résultats dérivés des données sans contrôle de qualité ne sont pas fiables. Ainsi, un contrôle de qualité minutieux doit être effectué pour l'analyse des flux avec FST.

Enfin, la fonction de structure longitudinale de troisième ordre a été appliquée à l' U_{10}

fourni par CFOSAT. Les résultats montrent que le taux de dissipation d'énergie ϵ est positif et négatif aux échelles inférieure et supérieure à 200 km, respectivement. Ce qui correspond à une cascade directe et inverse pour le flux d'énergie. De plus, des variations méridiennes du taux de dissipation sont également trouvées pour toutes les échelles. Des ϵ positifs sont trouvés pour la plupart des latitudes pour des échelles inférieures à 300 km, sauf pour les régions autour de 10°N, 10°S et 60°S, où des ϵ négatifs sont trouvés pour toutes les échelles étudiées. Pour les échelles supérieures à 300 km, ϵ est négatif, sauf pour deux régions étroites autour de 20°N et l'équateur. De plus, les ϵ mesurés sont tous négatifs dans les régions proches de l'ITCZ.

Dans l'ensemble, un FST amélioré est proposé pour extraire les flux d'énergie et d'entrophie d'échelle à échelle pour le mouvement atmosphérique de la surface de l'océan avec les données de champ de vent fournies par CFOSAT. Les cascades directes et inverses se trouvent à petite et à grande échelle. Des variations spatiales et temporelles des flux sont obtenues. Ces résultats sont confirmés par l'analyse des données QuikSCAT. De plus, les chiffres préliminaires d'énergie et de flux d'entrophie pour un typhon sont dérivés. Pour approfondir l'étude de la cascade de typhons ou d'autres événements extrêmes, des analyses systématiques sont encore nécessaires. Dans des travaux ultérieurs, nous envisageons d'étudier le transport spatial des flux d'énergie et d'entrophie à partir des données de missions multi diffusiomètres. Un diagnostic de chaque terme des fonctions de flux d'énergie et d'entrophie sera envisagé. De plus, des comparaisons de différentes approches pour la mesure des flux seront également faites dans des études futures.

Pour le dernier travail, la méthode d'identification de la houle et la relation vent-vague sont considérées. Dans une mer pleinement développée, H_s et U_{10} sont classiquement liés par une équation quadratique, par exemple, $H_s=0.0246U_{10}^2$. Alors que pour un véritable océan, le H_s est souvent contaminé par la houle qui se propage depuis des endroits éloignés, cette relation est donc souvent violée. Pour améliorer la relation vent-vague, une identification de la houle est nécessaire au préalable. Sur la base d'une analyse statistique des données de vent et de vagues collectées à long terme par les bouées offshore, un algorithme basé sur la probabilité est proposé pour dériver la houle sans connaître le spectre des vagues a priori.

Les données des bouées utilisées dans ce travail sont fournies par le National Data Buoy Center avec une fréquence d'échantillonnage d'une heure. La précision des données de vent est de 0.55 m/s et celle de la hauteur des vagues est de 0.2 m. Notez que les données de vent ne sont pas collectées à une hauteur de 10 m au-dessus de la surface de la mer.

Ainsi, une conversion de la vitesse du vent est effectuée sur la base d'une hypothèse de stabilité neutre avant le traitement des données.

Pour décomposer l'onde de houle, la fonction de densité de probabilité conjointe pour la vitesse du vent et la hauteur des vagues est d'abord mesurée. Ensuite, le squelette du pdf joint est extrait. En supposant que la houle domine par vent faible, la hauteur significative de la houle est estimée en faisant la moyenne de la hauteur significative de la houle correspondant à la probabilité maximale dans des conditions de vent faible (inférieur à 4 m/s).

Ensuite, les vagues de vent pourraient être extraites par deux approches différentes. La première est basée sur une décomposition linéaire, c'est-à-dire en subordonnant la hauteur significative des vagues de la houle à la hauteur significative moyenne des vagues. Une autre approche pour dériver l'onde de vent est basée sur la décomposition avec conservation de l'énergie. A savoir, la vague de vent est égale à la racine carrée des différences entre le carré de la hauteur significative de la vague et le carré de la hauteur significative de la houle. Les magnitudes des vagues de vent distinguées de la théorie de la conservation de l'énergie sont légèrement plus grandes que celles de la décomposition linéaire. De plus, les vagues de vent des deux approches différentes présentent toutes deux des propriétés d'échelle avec des vitesses de vent supérieures à 4 m/s. Le préfacteur α et l'exposant d'échelle η pourraient être mesurés par l'algorithme d'ajustement des moindres carrés. De cette manière, les vagues de houle pourraient être dérivées par l'approche basée sur la probabilité, et la relation entre le vent et les vagues pourrait être établie avec une formule de loi de puissance.

Pour examiner la décomposition de la houle basée sur la probabilité et la relation loi de puissance vent-vague, une analyse de partition d'énergie spectrale (SEP) est utilisée. SEP est considéré comme le meilleur moyen de faire la décomposition de la houle. Elle ne peut être réalisée qu'avec l'existence d'informations spectrales d'onde. Alors que pour la plupart des observations sur le terrain, les spectres d'ondes ne sont pas pris en compte. Ainsi, l'utilisation de SEP est limitée par les données et n'a pas pu être appliquée dans la plupart des cas. Les informations spectrales sur les vagues sont également collectées par la bouée qui a fourni les données sur le vent et les vagues pour l'analyse de probabilité. Par conséquent, SEP pourrait être effectué. Les résultats montrent que la hauteur de vague significative de la houle séparée avec SEP est proche de celles extraites avec une analyse basée sur les probabilités, et les vagues de vent correspondantes de l'analyse SEP se chevauchent bien avec celles de la décomposition à conservation d'énergie. Après la

décomposition, la hauteur significative des vagues est reconstruite avec la vague de vent et la vague de houle à partir de différentes approches décomposées. Les reconstructions sont proches les unes des autres sous la vitesse du vent de 20 m/s. Par conséquent, l'efficacité de la nouvelle décomposition de la houle basée sur la probabilité proposée et de la relation généralisée vent-vague puissance-loi est confirmée par l'analyse SEP et pourrait être utilisée dans d'autres ensembles de données.

Ensuite, la nouvelle méthode d'identification de la houle est appliquée à 17 ans de données JASON sur le vent et les vagues pour diagnostiquer les modèles globaux de houle. Les résultats montrent que les valeurs de la hauteur de houle moyenne saisonnière sont de 0.5 à 4 mètres, avec une valeur moyenne de 1.8 m. De plus, des variations spatiales et temporelles claires sont observées avec de fortes houles aux latitudes moyennes pendant l'hiver. Par exemple, les hauteurs moyennes des vagues significatives de la houle autour de 50°N sont égales à 2.3 m et 1.2 m en hiver et en été, respectivement. Ceci est en partie dû au fait que la houle est positivement corrélée avec la vitesse du vent aux hautes latitudes. Les schémas spatiaux de la hauteur de houle mesurée concordent bien avec ceux rapportés par Semedo et al. (2011), où une analyse SEP a été effectuée sur 45 ans de données de réanalyse ECMWF ERA-40 pour extraire des vues globales de la houle et des vagues de vent. Par exemple, de grandes houles sont observées dans les zones extratropicales de l'hémisphère nord avec de petites dans plusieurs régions en hiver, par exemple, le golfe du Mexique, la zone de mousson indienne, la mer de Chine méridionale et la côte nord et est de l'Australie, pour lister un peu. De plus, la courbe moyenne longitudinale montre une forme presque symétrique. Dans l'hémisphère sud, les valeurs élevées se trouvent principalement dans la région ACC, c'est-à-dire environ dans la plage de 48°S à 58°S, avec presque aucune influence sur le continent. En été, la houle augmente du nord vers le sud et atteint sa valeur maximale dans la région du ACC.

Après cela, les relations globales vent-onde puissance-loi sont établies. En raison de la plage limitée des valeurs de vitesse du vent, l'ajustement de la loi de puissance généralisée se fait via un algorithme de recherche automatique avec une largeur d'une demi-décade des plages de vitesse du vent supérieures à 4 m/s. Alors que l'algorithme d'ajustement échoue sur certaines géolocalisations, par exemple, des lacunes sont observées autour de l'équateur, correspondant aux régions de vent léger. Les valeurs de α_l extraites des vagues de vent décomposées linéairement sont plus petites que celles dérivées de la décomposition avec conservation de l'énergie, et les différences sont d'environ un facteur 10. Les modèles spatiaux pour α estimé à partir de deux vagues de vent définies sont similaires,

avec de petites valeurs dans l'équateur et les grands aux latitudes moyennes. De plus, des différences saisonnières sont observées et des α relativement importants se produisent dans l'hémisphère hivernal.

L'exposant d'échelle correspondant η_l est supérieur à ceux η_e ajustés à partir des ondes de vent à énergie conservée. En moyenne, l'hypothèse de la mer pleinement développée avec un exposant d'échelle égal à 2 pourrait être satisfaite dans plus d'un tiers de l'océan pour le cas de décomposition linéaire, principalement dans la région du courant circumpolaire antarctique autour de l'année, et à la haute latitude de l'hiver de l'hémisphère nord, où un vent fort est présent. L'exposant s'écarte largement de la prédiction du FDS pour la basse latitude de 20°S à 20°N, où un vent faible est observé. En partie à cause de l'influence de la mousson et de la couverture des terres dans l'hémisphère nord, il existe une forte variation saisonnière pour α et η présentés dans ce travail. Par exemple, les grandes valeurs de η se trouvent principalement de 25°S à 25°N. Le η moyen longitudinalement est presque symétrique en hiver, alors qu'il est fortement asymétrique en été. De plus, des variations méridiennes opposées pour η sont obtenues par rapport à celles de α : de grands η se produisent aux basses latitudes, correspondant à la zone des vents légers.

La relation entre α et η mesurés est également discutée. Des relations exponentielles ont été trouvées avec l'exposant d'échelle $\Gamma = 2.55$ et le préfacteur $\omega = 1.65$ pour la décomposition linéaire. En ce qui concerne la décomposition de l'énergie conservée, Γ et ω se trouvent respectivement à 2.45 et 2.55. Des différences sont trouvées entre la relation mesurée et la prédiction théorique basée sur PM64, qui pourraient être induites par l'ignorance des ondes de houle dans la théorie PM64. Un examen fin montre que Γ possède une dépendance linéaire de la latitude dans l'hémisphère sud, les valeurs de Γ décroissent linéairement de la latitude moyenne à l'équateur. Les variations méridiennes sont plus complexes dans l'hémisphère nord: des décroissances linéaires des hautes latitudes aux basses latitudes sont constatées pour l'hiver, le printemps et l'automne, tandis que celle de l'été montre une tendance à la hausse de 60°N à 10°N.

Sur la base de la méthode d'identification de la houle basée sur la probabilité et du modèle généralisé de loi de puissance des vagues de vent, la distribution globale des vagues de vent et la hauteur significative des vagues pourraient être extraites avec des vitesses de vent données. Ici, le vent moyen saisonnier fourni par les observations JASON est utilisé pour reconstruire des vues globales des vagues de vent et de la hauteur significative des vagues. Les résultats montrent que la distribution spatiale et les différences saisonnières pour les ondes de vent générées correspondant à la décomposition linéaire et celles pour

la décomposition à conservation d'énergie sont proches les unes des autres, de grandes valeurs sont toutes obtenues aux latitudes moyennes pendant l'hiver, et de plus petites sont observées autour de l'équateur pour toutes les saisons et les latitudes moyennes en été. Bien que les différences soient nettes, les valeurs de un correspondant à la décomposition linéaire sont relativement faibles, la différence moyenne est d'environ 1 m. Ces résultats sont également comparés à ceux rapportés par Semedo et al. (2011), la hauteur significative locale des vagues dérivée de l'analyse SEP est proche de celles obtenues par le modèle de relation vent-vague basé sur la conservation de l'énergie. Par exemple, des vagues de vent relativement importantes se trouvent autour de 50°N dans l'Atlantique Nord en hiver, avec une valeur proche de 3.5 m, tandis que les vagues de vent sont proches de 2 m à 50°S dans l'océan Indien. En été, les valeurs sont passées à 3.5 m dans la même zone. De plus, de grandes vagues de vent d'une valeur de 3 m sont également observées dans la région côtière somalienne contrôlée par les jets.

De plus, avec la relation vent-vague établie dans ce travail, une vue globale de H_s peut être obtenue lorsque seule la vitesse du vent est disponible. Par exemple, avec les informations U_{10} moyennes annuelles fournies par CFOSAT, les H_s correspondants peuvent être facilement reproduits. D'autres comparaisons entre la sortie du modèle et les observations montrent qu'il y a plus de 88% des correspondances avec des différences inférieures à 0.25 m, le biais est de 1.2 cm, l'erreur quadratique moyenne est de 17 cm et l'indice de dispersion est de 0.071. De plus, pour les valeurs inférieures et supérieures à 3 m, le H_s modélisé à partir du modèle de loi de puissance est légèrement sous-estimé et surestimé, respectivement. Ces résultats confirment la précision du modèle de loi de puissance vent-vague dérivé.

Sans connaître le spectre des vagues a priori, l'estimateur de houle basé sur la probabilité proposé repose sur au moins deux hypothèses étroitement liées : i) la hauteur de vague significative enregistrée est dominée par la houle pour des conditions de vent faible, et ii) la houle est soit faiblement ou indépendant du vent local. Ces deux hypothèses sont confirmées par la méthode SEP. Un avantage de la proposition actuelle est que l'influence des données anormales sera automatiquement exclue puisque le squelette des PDF joints est pris en compte. Cependant, pour estimer avec précision le squelette (c'est-à-dire la houle nominale), une taille d'échantillon importante est nécessaire. Ainsi, les données de vent et de vagues observées par CFOSAT ne sont pas utilisées dans ce travail pour dériver les schémas globaux des relations houle et vent-vagues. Pour améliorer la précision de l'analyse, 17 années de données JASON sont utilisées, et les données sont séparées en

quatre saisons pour étudier les variations saisonnières des relations houle et vent-vagues. Nous aimerions apporter un commentaire sur le mécanisme physique associé à la relation vent-vague. Alors que le mécanisme exact est encore un mystère, la loi quadratique améliorée est une relation empirique sans impliquer les premiers principes. Une considération théorique élégante de la houle et de la houle locale fait encore défaut dans la littérature scientifique.

En résumé, les caractéristiques d'échelle pour le vent et les vagues CFOSAT le long de la trajectoire sont examinées avec une analyse du spectre de puissance basée sur le théorème de Wiener-Khinchin et également une analyse de la fonction de structure. Des divergences ont été trouvées entre la prédiction théorique et les analyses de données. Les données de vent utilisées dans cette thèse sont proches du fond de la couche limite atmosphérique marine, qui est fortement influencée par les conditions du fond, par exemple, la rugosité effective et la hauteur des vagues, les profils de température et la variation de l'épaisseur de la couche limite. Ainsi, les caractéristiques d'échelle mesurées sont toujours différentes de celles prédites par les modèles de turbulence. Nous essaierons d'améliorer les théories existantes pour adapter les caractéristiques d'échelle dérivées du vent de 10 m. En ce qui concerne les caractéristiques d'échelle pour la hauteur significative des vagues, l'explication manque toujours. En considérant les données de profil de vague à haute fréquence fournies par le programme d'information sur les données côtières, une théorie possible peut être proposée. En plus des travaux théoriques, nous notons que les caractéristiques d'échelle obtenues à partir de l'analyse spectrale de puissance de Fourier et de l'analyse structure-fonction du second ordre sont légèrement différentes, ce qui peut être lié à l'effet des forçages énergétiques sur l'analyse structure-fonction du second ordre. Ici, nous avons également pris en compte les fonctions de structure conjointes, l'analyse spectrale de Hilbert, ainsi que la transformée en ondelettes synchronisée, qui ne sont pas fortement impactées par ces structures énergétiques intégrées dans l'ensemble de données. En outre, les différences d'échelle obtenues à partir de divers ensembles de données satellitaires à des échelles inférieures à 100 km seront également prises en compte dans les études futures, en se concentrant sur les points suivants : 1) les différences de conception des diffusiomètres ; 2) les algorithmes de récupération du vent ; 3) les qualifications de contrôle de qualité.

Pour le travail sur les flux d'énergie et d'énstrophie d'échelle à échelle, seules les caractéristiques de flux de base ont été obtenues dans cette thèse. Relativement peu de travaux ont été consacrés aux flux d'énergie et d'énstrophie des mouvements atmosphériques dans

une vision globale. Nous envisageons d'étendre nos travaux à l'étude du transport spatial des flux d'énergie et d'entrophie à partir des données de missions multidiffusomètres. Un diagnostic de chaque terme des fonctions de flux d'énergie et d'entrophie sera envisagé. Des comparaisons des résultats issus de différentes approches de mesure des flux seront effectuées. Les termes de forçage des flux d'énergie et d'entrophie seront discutés pour étudier le mécanisme dynamique de la direction et de l'intensité de la cascade. De plus, la relation statistique latente entre l'énergie et l'entrophie sera également considérée dans les travaux futurs. Notez qu'en raison de la limitation des résolutions spatiales des diffusiomètres, les analyses de mise à l'échelle et de flux d'énergie/entrophie dans cette thèse n'ont pas pu s'étendre aux échelles inférieures à 10 km, à savoir les sous-mésoéchelles. La dynamique sous-méso-échelle est importante pour les processus de surface de l'océan en raison du fait que de grandes quantités d'énergie sont contenues dans ces échelles, et donc importantes pour l'échange régional de propriétés et la structure des écosystèmes marins. Avec les données de vent du radar à synthèse d'ouverture (SAR, avec une résolution spatiale d'environ 50 m) à haute résolution, l'analyse de mise à l'échelle du champ de vent pourrait atteindre l'échelle de 0.1 km, à deux décennies des travaux actuels. De plus, l'analyse des flux d'énergie et d'entrophie peut également être appliquée aux données SAR, mais nous notons que les informations sur la direction du vent provenant des produits SAR ne sont pas directement observées, la direction du vent du modèle est fournie. Il faut donc être prudent dans l'interprétation des résultats. Un autre ensemble de données à haute résolution sur le vent et les vagues sera pris en compte dans les études futures à partir de radars à haute fréquence (HF) dans les régions côtières, qui peuvent fournir des données à haute résolution temporelle et spatiale sur le vent et les vagues dans une plage de plusieurs kilomètres à des centaines de kilomètres avec prélèvements horaires. Ainsi, les informations régionales sur la dynamique des vents et des vagues et les couplages pourraient être systématiquement étudiés.

Dans nos derniers travaux, nous avons proposé une décomposition de l'onde de houle basée sur la probabilité mais principalement basée sur les données fournies par JASON. Avec l'accumulation des données de CFOSAT, cette étude peut également convenir à être réalisée sur les données collectées par CFOSAT dans une vue globale, avec une haute résolution spatiale. La périodicité diurne ou semi-diurne de la relation vent-vague sera davantage prise en compte par les données recueillies par toutes les bouées NDBC. De plus, la prédiction moyenne temporelle montre un bon accord avec l'observation. La prédiction instantanée sera considérée avec l'apprentissage automatique dans les études futures.

Dans l'ensemble, les caractéristiques multi-échelles obtenues du vent et des vagues et le modèle de loi de puissance vent-vague dans cette thèse non seulement enrichissent notre connaissance fondamentale des processus de surface océanique, mais pourraient également constituer de nouvelles références pour les modèles océaniques ou atmosphériques.

Acknowledgements

The ocean has been accompanying me for more than ten years, I have learned a lot in my cosy ivory tower with the help of many kind teachers and disciples. I would like to thank all of them for their selflessly helping and guiding, especially for my three supervisors at Xiamen University and Université du Littoral Côte d’Opale, who are Dr. Yongxiang Huang, Dr. Jianyu Hu, and Dr. François G. Schmitt. My growth is inseparable from the education and supervision of these three masters, not only in academic researches, but also in normal life.

Dr. Jianyu Hu is the guide for my research in physical oceanography. He often offers me directional guidance when I encounter bottlenecks, brings me silver lining in cloud. Knowledge is infinite like the boundless ocean, which often makes me confused, but Dr. Jianyu Hu always can give me the most explicit advice based on my own characteristics and ability. In the works of studying the ocean surface current with GPS drifters, and the water mass analysis in the northern South China Sea, Dr. Jianyu Hu made and deployed the drifters with us in person. After that, he helped me to revise and polish the manuscripts over and over again, which illustrates a rigorous attitude towards scientific research.

Dr. Yongxiang Huang is my closest teacher during my master’s and doctoral periods. He is often more like an elder brother, who has witnessed the whole process of me varying from ignorance at the beginning to still ignorance at the end. The first ignorance is the innocence of the fluids field or turbulent systems. The main research direction of my study at Xiamen University is the statistical analysis of turbulent data. With the accumulation of data analysis, the ignorance state about the turbulence field slowly evolved to half-understanding. Afterward, with the further study of turbulence theories, the more ignorant I felt about turbulent systems. The corresponding degree of freedom of the systems has surpassed my ordinary understanding. Thus, I still know nothing about what turbulence is! However, influenced by Dr. Yongxiang Huang’s scientific attitude, I gradually changed my point of view on doing research. I don’t have to seek the final explanation of the turbulence problem (because turbulence has no solution at all!!!), but we need to pay more attention to other interesting problems encountered in the solution process. He taught things not only like how to deal with data, but also how to find and solve problems, e.g., “Bold assumptions and careful verification”. “Bold assumptions” asks me to

dare to question the so-called scientific authority, “careful verification” requires that the assumptions must be systematically verified with scientific evidence. These two points will benefit me for the rest of my life.

Dr. François G. Schmitt is a kind and amiable teacher who supervised me during my study in France. He is enthusiastic about the study of turbulence and creative in the field of complex systems. There were so many following scenes have happened during my Ph.D. studies: a new scientific idea came to me suddenly, then a wide investigation was made, and finally, some previously published works related to the idea were found, and these works were done by Professor Schmitt and his colleagues! This not only happened to me, but also to a Postdoc (Roy) who worked with him. He is so farsighted and has wide knowledge in the turbulence field. Thus, Roy and I privately called him “God of Turbulence”. With his heuristic help, the main work of this thesis was finished in France.

I would also like to thank other teachers who have guided and helped me, such as Dr. Rui Huang from Woods Hole Oceanographic Institution; Dr. Xiangsan Liang from Fudan University; Dr. Lipo Wang from Shanghai Jiaotong University; Dr. Peng Cheng, Dr. Hongyang Lin, Dr. Zhiyu Liu, Dr. Xiaoyi Yang, and Mrs. Jia Zhu from Xiamen University; Dr. Enrico Calvazarini and Dr. Stefano Berti from University of Lille; Dr. Alexei Sentchev from Université du Littoral Côte d’Opale, to list a few.

At the same time, I would also like to thank my classmates and friends who studied with me during the master’s or doctoral period, for letting me understand that I am not the only one suffering. For example, Bo Tong from the South China Sea Institute of Oceanography, University of Chinese Academy of Sciences; Zhou Le from Sun Yat-Sen University; Wenwei Wu from Shanghai Jiaotong University; Hui Zheng, Tian Xia, Yong Chen, Pengfei Tuoba, Wenqiang Lin, Yinxiang Ma, Qimeng Liu, Shuo Zhou, Tinghui Yan, Weian Shi, Ruhui Huang, Shuixing Peng, et al., from Xiamen University; Roy, Gabi, Lucas, Kien, Daniel, Sarah, Manh, et al., from Université du Littoral Côte d’Opale.

Thousands of words are indescribable of my gratitude, only hope that I can live up to the expectations in the future and continue to explore the mysterious ocean. I would like to thank my family at the end. Since I was studying far away from home and could not take good care of my family. It is their support that allows me to concentrate on my studies. I am very grateful to Mrs. Jiawen Zhang, who has been with me and supported me for more than 12 years since high school, as well as the gift given to me in the final stage of my doctoral studies, our lovely Yiyi Gao. Growing up is never a personal thing, thanks to all the lovely souls in my world.

The works illustrated in the thesis are supported by the National Natural Science Foundation of China, the National Basic Research Program of China, and the French space agency.

This thesis was a cotutelle between ULCO (France) and Xiamen University (China). It was cofunded by Xiamen University (when I was in China) and Région Hauts-de-France for my stay in France. I have stayed in France (Laboratoire d’Océanologie et de Géosciences) from November, 2019 to April, 2021. I have also been involved in a CNES project called MultiW2 (Spatial and temporal multi-scale analysis of interactions between turbulent wind forcing and wave height dynamics, using CFOSAT data), PI F.G. Schmitt. This project supported my PhD work, including participation to 7 international conferences where my PhD work was presented. This CNES funding is thus acknowledged here.

Yang Gao

19/09/2022



Contents

Abridged French Version	vii
Acknowledgements	xxiii
Chapter 1 Introduction to Turbulence Wind and Waves	1
1.1 Turbulence in the Atmosphere and Ocean	1
1.2 The Marine Atmospheric Boundary Layer	4
1.3 Classical Theories for the Generation of Waves by the Surface Wind	7
1.4 Dissertation Organization	10
1.4.1 Research Questions	10
1.4.2 Overview of This Work	12
Chapter 2 Data and Methods	15
2.1 Data Introduction	15
2.2 Methods	20
2.2.1 Fourier Power Spectral Analysis with Missing Data	20
2.2.2 Structure Function Analysis	33
2.2.3 Energy and Enstrophy Fluxes Analysis	34
Chapter 3 Scaling Analysis of CFOSAT Along-Track Wind and Waves	39
3.1 Theories	39
3.1.1 Theories for Atmospheric Wind	39
3.1.2 Theories for the Oceanic Waves	41
3.2 Fourier Power Spectral Analysis	42
3.2.1 Global Scale	42
3.2.2 Co-Spectral Analysis	43
3.2.3 Basin Scale	44

3.2.4	Mesoscale	45
3.3	Structure-Function Analysis	50
3.3.1	Second-order Structure-Function Analysis	51
3.3.2	High-order Structure-Function Analysis	54
3.4	Discussion	56
3.4.1	Wind Data	56
3.4.2	Wave Data	62
3.4.3	Scaling Features for Global Ocean Surface Wind via QuikSCAT	63
3.4.4	Scaling Comparisons Between Various Satellite Missions	65
3.4.5	Scaling Analysis of ECMWF Model Data	67
3.5	Conclusion	69
Chapter 4	Scale-to-Scale Energy and Enstrophy Fluxes of Wind	
	Field via CFOSAT	73
4.1	Method	73
4.1.1	Scale-to-scale Energy and Enstrophy fluxes	73
4.1.2	Wind Vector Projection	76
4.1.3	FST Estimation With Missing Data Problem	76
4.2	Spatial and Temporal Variations of the Energy and Enstrophy Fluxes	80
4.2.1	Global Views of Energy and Enstrophy Fluxes at the Scale of 250 km	81
4.2.2	Multiscale Energy and Enstrophy Fluxes	82
4.2.3	Energy and Enstrophy Fluxes During a Typhoon	84
4.3	Discussion	85
4.3.1	Energy and Enstrophy Fluxes for QuikSCAT Data	86
4.3.2	Evolution of Energy and Enstrophy Fluxes	88
4.3.3	Energy and Enstrophy Fluxes for ECMWF Reanalysis Data	90
4.3.4	Energy Flux Measurement with Third-order Longitudinal Structure Function Analysis	92
4.4	Conclusion	93
Chapter 5	Coupling Analysis of Wind and Waves	97
5.1	Introduction of PM64 Wind-Wave Relation	97
5.2	Swell Identification	99

5.2.1	Conventional Methods	100
5.2.2	Probability-based Swell Identification	101
5.3	Local Wind Wave Identification	103
5.3.1	Linearly Decomposed Wind Wave	103
5.3.2	Energy Conservation Based Wind Wave Identification	104
5.4	Validation of the Decomposition	105
5.5	Spatial and Temporal Variations for the Global Swell and the Wind- Wave Relation	109
5.5.1	Validation of JASON observations	109
5.5.2	The Global Distribution Features for Swell	110
5.5.3	Local Wind-Wave Relation	112
5.6	Discussions	117
5.6.1	Global Views of Wind Waves Based on Power-law Model	118
5.6.2	CFOSAT Wind Data Based Wave Height Hindcast Verification	120
5.7	Conclusion	124
Chapter 6	Conclusion and Future Work	127
6.1	Conclusion of the Dissertation	127
6.1.1	Scaling Analysis of Wind and Waves	127
6.1.2	Scale-to-scale Energy and Enstrophy Fluxes Analysis of Wind	128
6.1.3	Coupling Analysis of Wind and Waves	128
6.2	Highlights of the Dissertation	129
6.3	Prospects for Future Works	130
References		133
List of Publications		147
Abstract		154

Chapter 1 Introduction to Turbulence Wind and Waves

1.1 Turbulence in the Atmosphere and Ocean

In 1922, Richardson (1922) imaged a modern factory dedicated to weather prediction, in which the employees work on data observations, field experimentation, and mathematical calculations, to list a few. The ultimate goal was to figure out the weather states in the coming days. His work is the first one using numerical processes to forecast the weather and climate. The numerical part is based on a plain and important idea: the atmospheric movements are composed of eddies of various sizes, and the energy is transferred from large-scale eddies to small-scale ones. This figure was described by Richardson in a famous poem:

**big whirls have little whirls
that feed on their velocity
and little whirls have lesser whirls
and so on to viscosity in the molecule sense**

It is now widely accepted as the forward energy cascade concept (Frisch, 1995; Alexakis and Biferale, 2018), see Figure 1.1.

Richardson provided a qualitative description of the energy cascade feature in atmospheric or oceanic motions. A mathematical quantification was firstly given by Kolmogorov (1941b), and a formula for the energy spectrum of turbulent flows was proposed by Obukhov (1941). The spectrum gives the distribution of energy among turbulence vortices as a function of vortex size. His theory is based on three important hypotheses combined with dimensional arguments and experimental observations:

1. Local isotropy hypothesis: for homogeneous and isotropic turbulence, the kinetic energy is the same everywhere and the eddies behave the same in all directions; at high Reynolds number (Re), the small-scale (l) turbulent motions are statistically isotropic. We note that the term isotropy means isotropy at small scales, not for large-scale motions.
2. First similarity hypothesis: the statistical features for small-scale motions are universal, namely, they are similar in high Re turbulent flow. In addition, the statistics

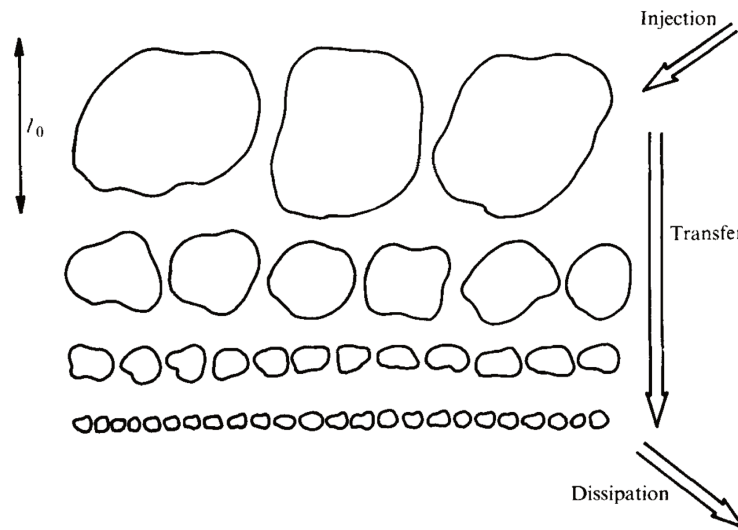


Figure 1.1 Illustration of the turbulence forward energy cascade concept, figure adapted from Frisch (1995).

of the small-scale motions are uniquely determined by the energy to receive rate ϵ and kinematic viscosity ν .

3. Second similarity hypothesis: the eddies with intermediate scales (corresponds to the so-called inertial subrange) are not affected by ν , but only determined by ϵ .

With the three hypotheses, the famous ‘Kolmogorov -5/3 spectrum’ can be extracted by dimensional analysis in the form of,

$$E(k) = C_0 \epsilon^{2/3} k^{-5/3}, \quad (1.1)$$

where C_0 is a constant, ϵ is the mean energy dissipation rate per unit mass, and k is the wavenumber. Scaling features for the spectra of turbulence flows versus k can be found in a log-log plot. The theoretical prediction of $-5/3$ scaling by Kolmogorov (1941b) has been validated by many authors in the study of atmospheric or oceanic movements. For instance, Grant et al. (1962) studied the downstream velocity data in a tidal channel with one dimensional spectra, found a $-5/3$ scaling feature for several decades in wavenumber as predicted by Kolmogorov. Nastrom et al. (1984) applied energy spectrum analysis to study the commercial aircraft flights collected wind data in the midlatitudes near the tropopause level. They found that the spectra follow a -3 power-law in the spatial range of about 1000-3000 km and a $-5/3$ power-law in the range of 3 – 400 km, see Figure 1.2. Xu et al. (2011) performed a spectral analysis of QuikSCAT winds over the global ocean and found that the scaling exponents β revealed spatial variability in the wavelength range

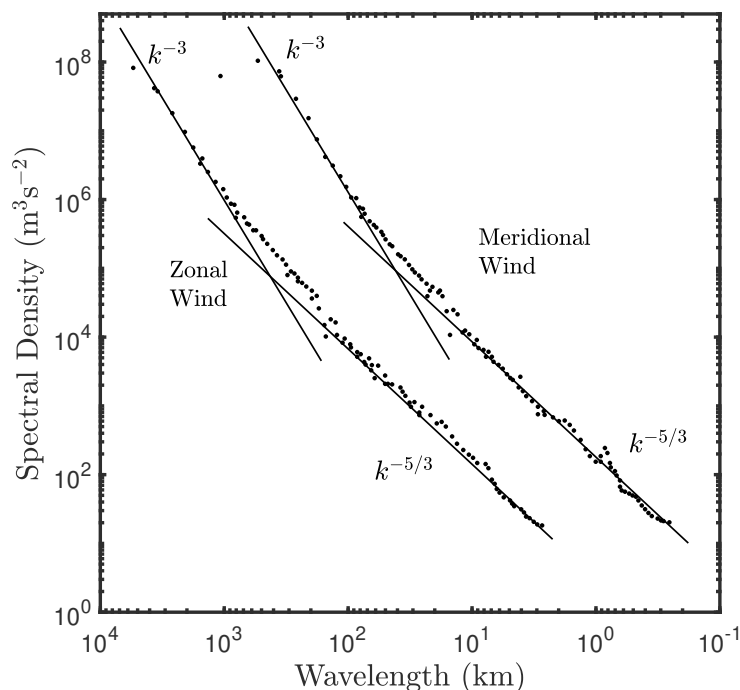


Figure 1.2 Kinetic energy spectrum near the tropopause from Global Atmospheric Sampling Program aircraft data. The spectrum for meridional winds is shifted one decade to the right. Lines with slopes -3 and $-5/3$ are entered at the same relative coordinates for each variable for comparison (Reproduced figure according to FIG 1 in Nastrom et al. (1984)).

of 1000 – 3000 km, with values varying from 1.6 to 2.9. Guo et al. (2013) studied the wind data collected on two Danish offshore wind farms with power spectrum analysis, after considering the conditional average, they confirmed the universal characteristics of the $-5/3$ power-law in the mesoscale and -3 for synoptic scale.

In the field of multiscale analysis for turbulence or turbulence-like systems, structure functions were also introduced by Kolmogorov (1941a), and have been widely used to examine the scaling features (Frisch, 1995; Schmitt and Huang, 2016; Gao et al., 2016; Huang and Wang, 2018; Jian et al., 2019). Structure functions are the multi-order statistics of the increments for passive/active scalars at two points in space/time, separated by some distances r or time lags τ . The structure-function analysis is used to retrieve the scale-invariance, the multiscale interactions, and also the intermittency features for high Reynolds turbulent flows.

According to the seminal proposal of Kolmogorov's theory in 1941 Kolmogorov (1941a), the structure functions can be written as follows (using velocity field u as an example),

$$S_q(r) = \langle \Delta u_r^q \rangle \quad (1.2)$$

where $\Delta u_r = |u_i - u_j|_{r_{ij}=r}$ is the velocity increment between two points which has the separation scale of r , q is the statistical moment, it can be an integer or float. The angle brackets $\langle \cdot \rangle$ means ensemble average.

Van Atta and Chen (1970) tested the structure-function with the wind data collected in the atmospheric boundary layer, they found that the behavior of second-order structure quantities shows substantial agreement with the predictions of Kolmogorov's original theory over a wide range of separation scales. In the study of Lindborg (1999a), he found that the structure functions to be more discerning of the turbulence energy or enstrophy cascades properties than the Fourier-space spectrum, and he developed a theory for distinguishing two- and three-dimensional flows with the structure-function analysis. Vogelzang et al. (2015) studied one-year ocean surface wind data from four different scatterometers in nine areas in the Tropical Pacific with second-order structure-function analysis, they confirmed that the second-order structure functions are well suited as a proxy for the spatial variance and the corresponding scaling exponents $\zeta(2)$ are between $2/3$ and 1 in the tropical regions.

By assuming that the system is statistically self-similar, the value of structure-function can be generated to high-order moment, $q \geq 0$ on the form:

$$S_q(r) \propto r^{\zeta(q)} \quad (1.3)$$

where $\zeta(q)$ is the moment scaling function (Frisch, 1995; Schmitt and Huang, 2016). This function characteristics the intensity of fluctuations at all scales. For K41, we have $\zeta(q) = q/3$. This scaling relation is valid between a small and a large scale. In turbulence, this corresponds to the inertial range, between the injection scale and the dissipation scale.

Intermittency was detected in turbulence by Batchelor and Townsend (1949). It was later modelled by Oboukhov (1962), and Kolmogorov (1962). Intermittency corresponds to large fluctuations having long-range correlations. It is captured by a non-linear $\zeta(q)$ curve, which is concave. The more concave the curve, the more intermittent the process (Schmitt and Huang, 2016).

The second-order moment $\zeta(2)$ is related to the Fourier power-law slope β as:

$$\beta = \zeta(2) + 1 \quad (1.4)$$

Hence in case of isotropy, $\zeta(2)$ should be directly related to β .

1.2 The Marine Atmospheric Boundary Layer

The marine atmospheric boundary layer (MABL) plays an important role in the climate system. It is the part of the atmosphere that has direct contact with the ocean and is thus directly influenced by the ocean. MABL is the place where the air-sea interactions happen, namely, where the ocean and atmosphere exchange momentum, heat, and matter. For instance, solar radiation is converted by wind energy, then to wave energy. The amount of energy per unit volume becomes more concentrated in the cascade process (Falnes, 2007). Thus, the wind and waves are two main active factors to influence the exchange processes, consequently are vital to the study of air-sea interactions (Villas B. et al., 2019).

The wind speed at 10 m (U_{10}) and significant wave height (H_s) are mainly used to study the dynamical characteristics of the MABL. Relatively accurate measurements of U_{10} were possible after the invention of the anemometer by Thomas Romney in 1846. Then, more precise U_{10} observations have been achieved by the development of hot wire anemometers, while the wind could only be measured at a fixed point, until the occurrence of Doppler radars. For estimating the wind at a global scale, a satellite onboard wind scatterometer was developed during the Seasat mission in the 1970s. After that, a series of satellites that can observe the wind field have been launched, such as Nimbus-7 (1979), Advanced Earth Observing Satellite (ADEOS, 1996), Quick Scatterometer (QuikSCAT, 1999), Meteorological Operational Satellites (METOP-A, METOP-B, and METOP-C, mission since 2006), Cyclone Global Navigation Satellite System (CYGNSS, 2017), HaiYang-2B (HY-2B, 2018), to name a few. Before 1975, significant wave height (H_s) data have been mainly collected by buoys or coastal marine observation stations. Since that year, global ocean wave heights could be retrieved by satellites equipped with radar altimeters, such as for instance, Geodetic Earth Orbiting Satellite-3 (GEOS-3, 1975), European Remote-Sensing Satellite (ERS-1, 1991), Topography Experiment/Poseidon (TOPEX, 1996), JASON-1 (2001), and followed by JASON-2 (2008), and JASON-3 (2016), HaiYang-2A (HY-2A, 2011), to list a few.

Until the year of 2018, simultaneously U_{10} and H_s data were observed from space for the first time after the launch of the China France Oceanography Satellite (CFOSAT). A rotating fan beam scatterometer (SCAT) and surface waves investigation and monitoring radar (SWIM) are boarded on China France Oceanography Satellite (CFOSAT) to collect the U_{10} and H_s , respectively. Both instruments use Ku band microwave frequencies, and SCAT uses medium incidence angles (from 26° to 46°) to retrieve the wind vectors at 10m height, whereas SWIM operates at near-nadir incidence angles (from 0° to 10°) to

retrieve sea-surface waves (Liu et al., 2020). With an orbital repetition cycle of 13 days and accounting for the instrument geometry, which can provide a 1000 km width of swath for the wind field, the system provides a global coverage within 3 days for wind fields and nearly global for waves (Hauser et al., 2016).

The wind field provided by SCAT is not directly measured; it is estimated using a geophysical model function, which gives the relation between the microwave scattered field, incidence angle, wind direction, and speed close to the sea. Using this approach, an algorithm is designed to retrieve the 10 m wind intensity, and direction, from backscattered data from the scatterometer. When the scatterometer has an inclined beam, both wind speed and direction can be retrieved. This is why rotating beam scatterometers are used since SeaWinds onboard the satellite QuikSCAT (Spencer et al., 1997).

For obtaining H_s , an “adaptive retracking” algorithm is performed (Tourain et al., 2021). The main idea of this algorithm is the following. Different pulses are received by the satellite sensor, coming from reflections at the ocean’s surface. These different backscattered echos are classically treated using a model of the ocean’s rough surface (Brown, 1977), seen as the convolution of a point source, a flat sea surface, and an assumed probability density function of sea elevation. Different improvements of this algorithm have been proposed since, and a modified version, used for CFOSAT, is described in detail in Tourain et al. (2021). This algorithm is still based on the fit of the Brown model echo (Brown, 1977) to the recorded waveform and the use of a maximum likelihood estimator. One of the improvements as compared to the conventionally used algorithms for other altimeter missions is the use of the real point target response from the SWIM sensor, instead of a theoretical one. Other improvements are linked with inversion methods using new analytical models.

Furthermore, buoy collected U_{10} and H_s are also used in the thesis. We note that the directly observed wind speed is not at 10 m for most buoys. The equipped anemometers are often with heights from 3 to 5 m. Suppose the wind is collected at $z = 4.1$ m (a typical height for offshore buoy collected wind data), a conversion from $U_{4.1}$ to U_{10} is required before further studying the relation between wind and waves. Here we assume that the MABL is in a neutral stability logarithmic state, and the surface wind profile is

$$U_z = \frac{u_*}{\kappa} \ln \frac{z}{z_0} \quad (1.5)$$

where κ is the von Kármán constant and z_0 is the roughness length, which is usually set as $\kappa = 0.4$ and $z_0 = 9.7 \times 10^{-5}$ m, respectively; z is the height above the sea surface; u_* is the friction velocity which can be experimentally derived from U_{10} and the drag coefficient

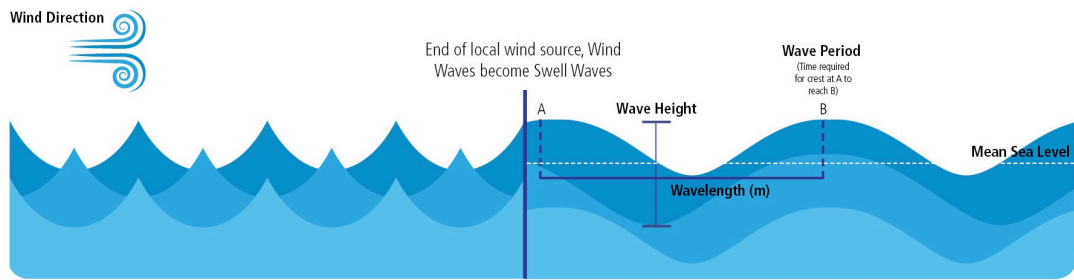


Figure 1.3 Schematic diagram of the generation of waves by the wind. Figure adapted from <https://www.stormgeo.com/> (2019).

C_d (always set as 1.2×10^{-3}) as follows,

$$u_* = \sqrt{C_d} U_{10} \quad (1.6)$$

Combining the above two equations, U_z for $z > 0$ can be re-expressed using U_{10} . By considering the measured value at a height z_1 we have (Ribal & Young, 2019),

$$U_{10} = U_{z_1} \sqrt{\frac{\kappa^2}{C_d} \frac{1}{\ln(z_1/z_0)}} \quad (1.7)$$

Finally, applying $z_1 = 4.1$ m in the above equation, the converted wind speed at 10 m can be simplified as $U_{10} = 1.084U_{4.1}$. A further test shows that the variation of the height, e.g., $3 \lesssim z \lesssim 5$ m, will have less than 2% difference in the estimation of U_{10} .

1.3 Classical Theories for the Generation of Waves by the Surface

Wind

Waves can be seen as part of the wind's energy transferred to the surface of the water. Most waves are caused by wind. To put it simply, ocean surface waves can be distinguished into wind waves and swell, the latter is the older wind waves that lost the support of wind energy, thus the waves are created by the friction between wind and surface water, see Figure 1.3. The size of wind-generated waves depends on the wind speed, the duration of winds, the length of fetch, and the depth of water, to list a few. To evaluate the size of waves, the significant wave height H_s is normally used, which has been originally defined as the average of the highest one-third of waves that occur during a given period. Nowadays it is usually defined as four times the standard deviation of the ocean surface elevation.

If we carefully consider the question about how the wind generates waves, we will find that the answer is quite fuzzy. The movements of wind and waves are both turbulent, vary in space and time randomly, and the flows nonlinearly interact over a wide range of scales (from millimeters to kilometers in space, and from seconds to days in time). To answer the question completely, one has to use the nonlinear Navier-Stokes equations with the complex air-sea boundary. But it is impossible to do this. Thus, some assumptions were proposed to simplify the question.

In the 19th century, Hermann von Helmholtz and William Thomson (later Lord Kelvin) proposed the idea that waves are generated by wind through a shear-flow instability. They argued that fluid instability occurs when there is velocity shear in a single continuous fluid or a velocity difference across the interface between two fluids. This process is also known as the Kelvin-Helmholtz instability. However, according to this idea, not until the value of wind speed reaches 6.5 m/s the waves can be generated. Thus, their interpretation is apparently not suitable for the true nature.

A great progress was made by Harald Sverdrup and Walter Munk during World War II. Scaling arguments were used to estimate the wave height from the intensity and duration of wind. An empirical model for how winds locally generate waves was established, and it is still used until now. Based on the study of some photographs taken by a B-17 bomber, Cox and Munk (1954) proposed that the waves with short wavelength are closely coupled to the wind and that the intensity of the coupling depends on the wave slope.

Based on the idea of Kelvin-Helmholtz, Miles (1957) proposed that a shear-flow instability occurs at the height where the wind speed matches the phase speed of the growing wave, energy and momentum are transferring from the wind to the waves due to the instability. The growth rate of the waves depends not on the wind speed or its gradient, but on the curvature of the wind profile at the critical height. During the same time, Phillips (1957) proposed a mechanism that the waves developed from wavelets, which sources from the resonance between pressure fluctuations in the wind (turbulent eddies) and surface water. Miles's theory works on short-wavelength waves but it ignores the effects of viscosity, and interactions between different scales of waves, while Phillips's theory is only suitable for waves with amplitudes smaller than a few millimeters. A modified mechanism was proposed by Belcher and Hunt (1993), turbulence theories are introduced to quantify the effect of pressure difference caused by sheltering in the presence of turbulent eddies, and realistic estimates of wave growth for short waves are produced by their model.

Though the mechanisms for the generation of waves by wind are still confused, the statistical relation between wind and waves can be established. For instance, by assuming

that the wind blows steadily for a long time over a large area, the waves would come into an equilibrium state, namely, the fully developed sea. Pierson Jr. and Moskowitz (1964) (hereafter PM64) calculated the wave spectra for various wind speeds with 420 selected wave measurements collected by the ship-borne wave recorders in the northern Atlantic Ocean weather ships. They found that the spectra have a form as below,

$$E(f) = C_0 g^2 (2\pi)^{-4} f^{-5} e^{-\frac{5}{4}(\frac{f_m}{f})^4}, \quad (1.8)$$

where $C_0 = 8.1 \times 10^{-3}$ is the Phillips constant; g is the acceleration of gravity (set as $10 \text{ N} \cdot \text{kg}^{-1}$ here); f is frequency; f_m is the frequency at the maximum of the spectrum, which can be deduced from U_{10} with the experimental relation of $f_m = 0.855g/(2\pi U_{10})$. Finally, the relationship between H_s and U_{10} is derived as $\overline{H}_s(U_{10}) \simeq 0.0246U_{10}^2$ (see Chapter 5 for a detailed derivation).

Since then, this relation has been widely adopted and employed by offshore engineering applications (Goda, 1997; Liu et al., 2017). Note that, PM64 is an idealized model assuming the fully developed sea without the existence of swell waves. However, in shallow waters, coastal regions, or weak wind areas, the failure of these assumptions could lead to an unreliable output of PM64 model.

An improved WAVE Model (WAM) for wind speed ranging from 0 to 30 m/s was proposed by the WAMDI Group (1988). According to this model, the wind-wave relation for fully developed seas can be expressed as (Pierson Jr, 1991),

$$H_s(U_{10}) = \begin{cases} 1.614 \times 10^{-2} U_{10}^2, & 0 \leq U_{10} \leq 7.5 \text{m/s} \\ 10^{-2} U_{10}^2 + 8.134 \times 10^{-4} U_{10}^3, & 7.5 < U_{10} \leq 30 \text{m/s} \end{cases} \quad (1.9)$$

It is also known as the third-generation wind-wave model, which solves the energy balance equation with nonlinear wave-wave interactions. However, differences between WAM model results and observations have been reported (Romeiser, 1993; Gulev et al., 1998; Heimbach et al., 1998; Johnson et al., 1999).

For predicting H_s with U_{10} more precisely, the water depth is also taken into account by Andreas and Wang (2007). In their work, the data on the northeast coast of the United States observed by buoys were fitted with a parameterization that with the form of:

$$H_s(U_{10}) = \begin{cases} C(D), & U_{10} \leq 4 \text{m/s} \\ a(D)U_{10}^2 + b(D), & U_{10} > 4 \text{m/s}, \end{cases} \quad (1.10)$$

where C is a depth D -dependent constant which is determined by averaging all the wave

heights for $U_{10} \leq 4\text{m/s}$; a , and b are decided by the water depth. For low wind speed fields, the existence of Hs is presumed due to the constantly presented swell. For high wind speed conditions, a quadratic formula is adopted to describe the relation between U_{10} and Hs , but with two coefficients related to the water depth used to adjust the fitting curves to the *in situ* collected data.

Another attempt of using a quadratic function to extract the empirical relationship of Hs and U_{10} was performed by Sugianto et al. (2017) with the data collected in the Java Sea. Slightly different from the one used by Andreas and Wang (2007), a linear term is introduced in their formula, but without considering swell waves, which is written as,

$$Hs(U_{10}) = cU_{10}^2 + dU_{10} \quad (1.11)$$

where c and d are determined by fitting the collected data.

Here we use the wind and wave data provided by NDBC (National Data Buoy Center) buoy 41001 to make comparisons between the different models, the results are shown in Figure 1.4. Due to the fact that the swell waves are not well considered by some of the models, the predicted significant wave height are all underestimated by the PM64-based wind-wave relation (black curve), WAM model based wind-wave relation (red curve), and the JAVA sea data based model (magenta curve). While the one for Andreas and Wang (2007) could be used to describe the wind-wave relation for this case.

In all the aforementioned models, either the swell waves are not well considered, or the scaling exponent is fixed as 2, where the FDS hypothesis is involved. It is worth mentioning that, in several works, the wave frequency spectrum is scaling in the form $f^{-\zeta}$, with values of ζ varying from 3 to 6 for different situations (Toba, 1972; Donelan et al., 1985; Young and Verhagen, 1996; Young, 1998). This is partially due to the influence of the water depth, length of wind fetch, and other factors. In such cases, the quadratic relation might not be valid (Resio et al., 1999). Indeed, if the f^{-5} spectrum is replaced by $f^{-\zeta}$, using $Hs = 4(\int_0^\infty E(f)df)^{1/2} \simeq 4(\int_{f_m}^\infty E(f)df)^{1/2}$ gives, i.e., $\overline{Hs}(U_{10}) = \alpha U_{10}^\beta$, with the exponent $\beta = (\zeta - 1)/2$. Using the observed $3 \leq \zeta \leq 6$, one obtains β values in the range $1 \leq \beta \leq 2.5$, which corresponds to a generalization of the quadratic law.

1.4 Dissertation Organization

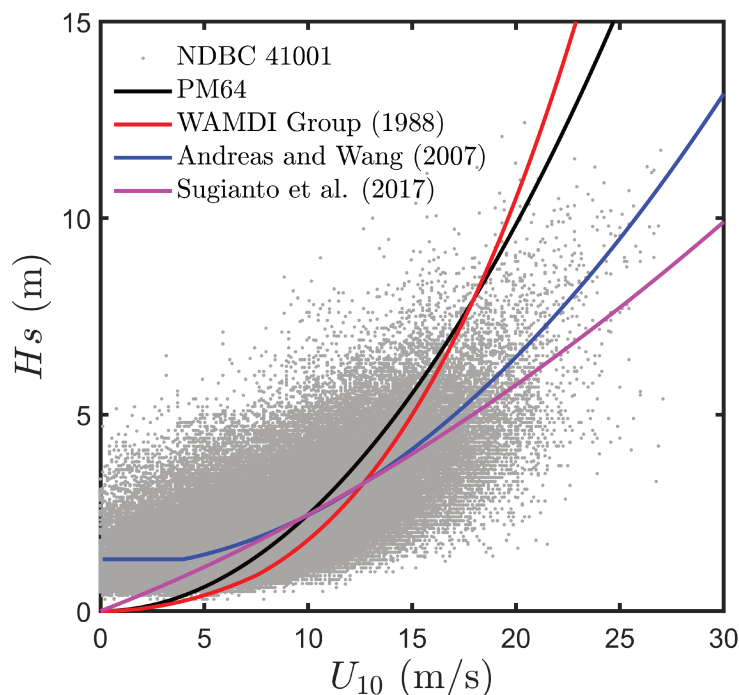


Figure 1.4 Wind and wave data collected by NDBC buoy 41001 (1976-2020). The solid curves are various models described in this section.

1.4.1 Research Questions

The air-sea interface is of complex nature, with interactions among different scales of wind and wave motions, the absence of characteristic scales, various external and internal forcing, and extremely high Reynolds numbers. We are here interested in global ocean surface wind and waves and their multiscale coupling.

In this framework, we will address in this thesis the following questions which concern wind and waves and their relations:

1. What are the scaling features of wind speed and wave height at various scales?
2. What are the spatial distribution and temporal variation characteristics of the scaling features?
3. Do the wind speed and wave height have spatially coupled dynamical links? If so, what scale-dependent features of the links?
4. Do the scaling features extracted from different satellite products possess different characteristics?

Moreover, this work will also focus on the scaling features of energy and enstrophy fluxes in the atmosphere:

1. What are the directions of the energy and enstrophy fluxes for the ocean surface wind field at various scales?
2. What are the corresponding intensities for the fluxes?
3. What are the spatial and temporal features for the energy and enstrophy fluxes?

Finally, the following questions related to swell waves are addressed:

1. How to practically distinguish the swell part from wind waves?
2. How to describe the relation between wind speed and the wave height induced by the local wind?
3. What are the global images of swell distribution and the corresponding temporal variation?
4. What is the wind-wave relation for seas that are not fully developed?

1.4.2 Overview of This Work

One of the objectives of this thesis is to consider the scaling features of ocean surface wind and waves using the methods introduced by the field of turbulence. Moreover, a practical relation between wind speed and wave height was proposed based on a swell separation algorithm. To clearly illustrate the context, the thesis is scheduled as follows.

(1) In chapter two, a brief introduction of the data used in this study will be given. Then, the methods used are presented. Among which, the Fourier-based approach to retrieve the power spectrum with missing data is a manuscript to be submitted.

(2) In chapter three, based on the Fourier power spectral analysis of the CFOSAT along-track wind and wave data, the global multiscale scaling features for the wind field and wave height are extracted. In addition, comparisons of the scaling features derived from different satellite products are performed. This chapter is based on a publication, see Gao et al. (2021), and one manuscript in preparation.

(3) In chapter four, a complementary study of the scale-to-scale energy and enstrophy flux of ocean surface wind is presented to analyze the strength and direction of the cascade for wind at various scales. This chapter corresponds to a submitted manuscript.

(4) In chapter five, a probability-based approach is proposed to classify the swell waves from wind waves without knowing the wave spectrum *a priori*. Then a power-law

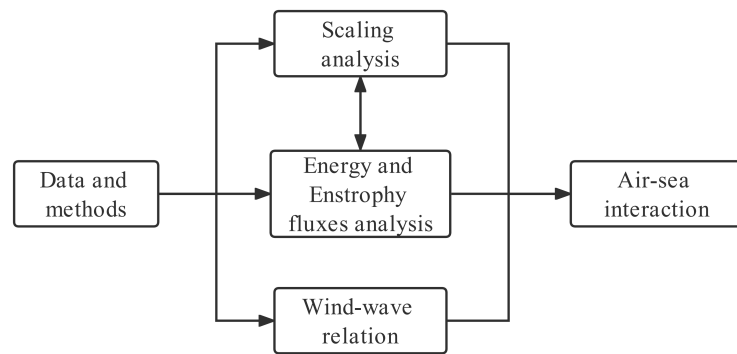


Figure 1.5 Configurations for the main contents of this work.

relation model is generated to describe the coupled relationship between wind speed and local wave height. This chapter also corresponds to a submitted manuscript.

(5) In chapter six, conclusions and highlights of the dissertation and some prospects for future works are presented.

The configurations for the main contents of this work are illustrated in Figure 1.5.

Chapter 2 Data and Methods

2.1 Data Introduction

The works introduced in this dissertation are mainly based on the simultaneously observed U_{10} and H_s data provided respectively by a rotating fan beam scatterometer (SCAT) and surface waves investigation and monitoring radar (SWIM), both boarded on the CFOSAT (China France Oceanography Satellite) launched in October 2018. An artistic illustration of the SCAT and SWIM instruments is shown in Figure 2.1.

Both instruments use Ku band microwave frequencies. SCAT uses medium incidence angles (from 26° to 46°) to retrieve the wind vectors at 10m height, whereas SWIM operates at near-nadir incidence angles (from 0° to 10°) to retrieve sea-surface waves (Liu et al., 2020). With an orbital repetition cycle of 13 days and accounting for the instrument geometry, which can provide a 1000 km width of swath for the wind field as illustrated in Figure 2.2 a, the system provides a global coverage within 3 days for wind fields and nearly global for waves (Hauser et al., 2016).

The wind field is not directly measured; it is estimated using a geophysical model function, which gives the relation between the microwave scattered field, incidence angle, wind direction, and speed close to the sea. Using this approach, an algorithm is designed to retrieve the 10 m wind intensity, and direction, from backscattered data from the SCAT instrument. When the scatterometer has an inclined beam, both wind speed and direction can



Figure 2.1 An artistic illustration of the deployed CFOSAT spacecraft in orbit. (image credit: CNES (2011))

be retrieved. This is why rotating-beam scatterometers are used since SeaWinds onboard the satellite QuikSCAT (Spencer et al., 1997). A similar design is used in CFOSAT, using two fan beams, one vertically polarized, and the other horizontally polarized (Lin and Dong, 2011; Lin et al., 2018). The processing done involves averaging several backscatter values having similar incidence and azimuth angles: the larger the number of views, the more precise results can be obtained. As compared to fixed fan beams or pencil beams scatterometers, the rotating fan beam system used by SCAT can obtain more observations of the azimuth angles within a single swath: normally 4–16, more than ten in most areas for SCAT, while for fixed fan beams or pencil beams, the maximum number is equal to 4 (Zhang et al., 2021a). Thus, the wind information retrieval accuracy is greatly increased in the CFOSAT mission (Liu et al., 2020).

For obtaining H_s , an “adaptive retracking” algorithm is performed (Tourain et al., 2021). The main idea of this algorithm is the following. Different pulses are received by the satellite sensor, coming from reflections at the ocean’s surface. These different backscattered echos are classically treated using a model of the ocean’s rough surface (Brown, 1977), seen as the convolution of a point source, a flat sea surface and an assumed probability density function of sea elevation. Different improvements of this algorithm have been proposed since, and a modified version, used for CFOSAT, is described in detail in Tourain et al. (2021). This algorithm is still based on the fit of the Brown model echo (Brown, 1977) to the recorded waveforms and the use of a maximum likelihood estimator. One of the improvements as compared to the conventionally used algorithms for other altimeter missions is the use of the real point target response from the SWIM sensor, instead of a theoretical one. Other improvements are linked with inversion methods using new analytical models.

With all of these improvements, the performance of the CFOSAT mission was found to be remarkable: the accuracy of the H_s is 25 – 30 cm or 5% of the mean value; the accuracy of the wind field is 2 m/s in magnitude and 20° in direction (Suquet et al., 2019; Liu et al., 2020; Hauser et al., 2020; Li et al., 2021). The U_{10} data used in this study are in a 12.5 km resolution covering the period from December 18, 2018, to February 28, 2022, which is nearly 17,000 orbits. For each orbit, the satellite can generate a wind field with a size of 84×3440 pixels. Conventionally, the measured U_{10} is treated as 10-meter wind above the sea surface. In other words, it is still in the marine-atmospheric boundary layer. The H_s data analyzed here were collected from July 29, 2019, to February 28, 2022, which is 1,5000 orbits with a nominal spatial resolution of 1.5 km. Figure 2.2 a shows an example of the simultaneously observed along-track wind field and H_s data collected in the Pacific Ocean on January 16, 2022. The corresponding along-track U_{10} and H_s

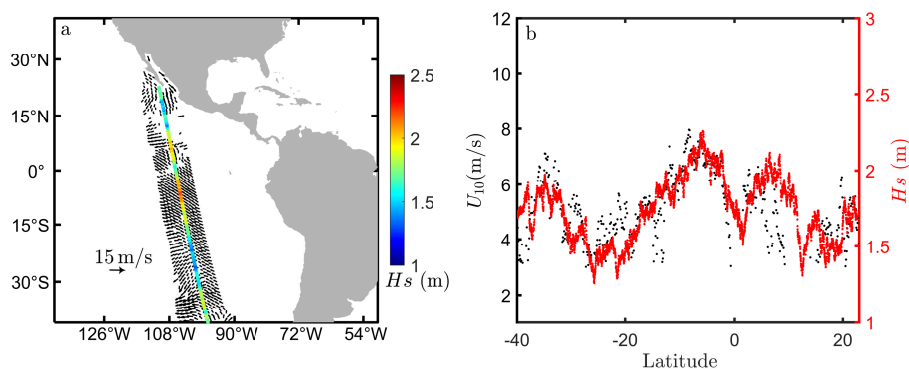


Figure 2.2 (a) Simultaneously observation of wind vectors (black arrows) and H_s (color dots) by CFOSAT in the western Pacific Ocean on January 16, 2022. (b) The corresponding along-track U_{10} observed by SCAT (black dots) and H_s observed by SWIM (red dots).

are shown as black and red dots respectively in Figure 2.2 b. Similar latitudinal variation trends in the wind speed and wave height are found. Note that the U_{10} and H_s data used in this thesis are Level-2 products, which means the data are processed without any further interpolations. Thus, the original dynamical features of the atmosphere and ocean surface can be well-preserved in these data.

Before processing the data, quality control (QC) was performed. For U_{10} , only the data collected by more than two beams are considered. As for H_s , a Hampel identifier (Davies and Gather, 1993) is chosen to detect the outliers. Hampel identifier uses the median and median absolute deviation as a robust estimate of the location and spread of the outliers. For each data series, firstly a value of W points of the window half-width is given. Then the identifier computes the median and the median absolute deviation of a window composed of the sample and its $2W$ surrounding samples, W data points per side. If a sample differs from the median by more than three times the standard deviations, it is treated as an outlier. This identifier has been proven extremely effective in practice for various fields (Pearson, 2002; Pearson et al., 2015, 2016). In this study, the window half-width is set as 150 data points and the abnormal data are set as Not-a-Number (NaN). As a result, there are roughly 15% of the U_{10} and 2% of the H_s data discarded.

Figure 2.3 shows an example of the U_{10} and H_s data before and after QC. The black dots represent the raw data provided by the CFOSAT, and the red dots are the data after QC. To minimize the estimation bias for the calculated Fourier power spectrum, a small portion of normal data successive to the abnormal ones is also excluded in the QC procedure. Figure 2.4 shows the probability density functions (pdf) of U_{10} and H_s before and after QC, computed over all the data: the pdf tails are cut off after QC.

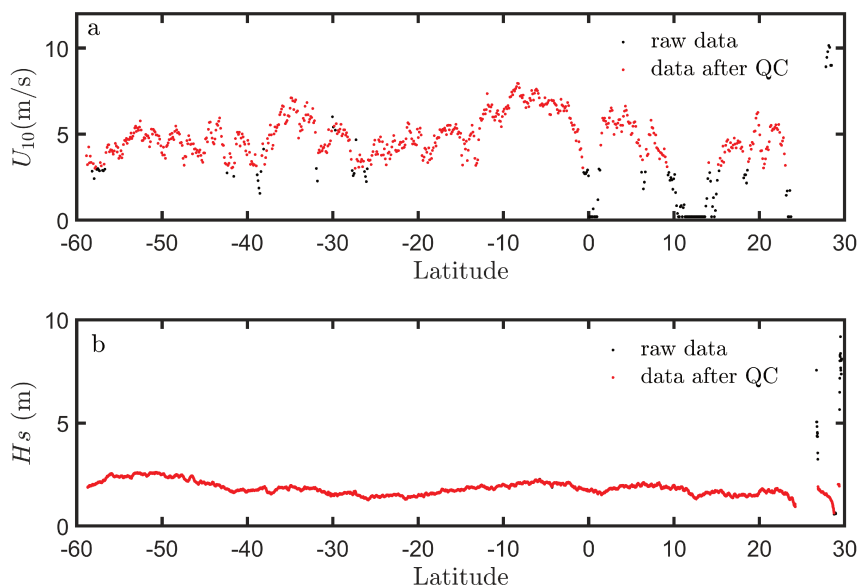


Figure 2.3 Comparisons of raw data (black dots) and the data after quality control (red dots). (a) and (b) indicate U_{10} and H_s data, respectively.

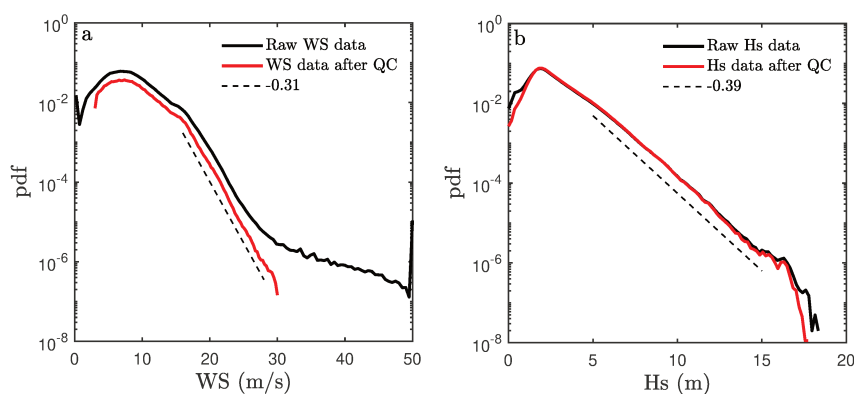


Figure 2.4 The comparisons of the pdfs of U_{10} and H_s data before (black curves) and after (red curves) QC. Dashed lines emphasize the exponential tails which are found, and the fitted slopes are indicated.

The pdf of U_{10} shows an exponential tail for values larger than 16 m/s. The tail is in the form of $\exp(-x/V_0)$ where the characteristic scale is $V_0 = 1/0.31 = 3.22$ m/s. For H_s data, there is also an exponential form in the ranges of 5 to 15 m: here the tail is in the form of $\exp(-x/L_0)$ where the characteristic scale is $L_0 = 1/0.39 = 2.56$ m.

However, for further exploring and double-checking the scaling analysis results, 10 years (October 1999 - November 2009) Quikscat, 7 years Metop-a (January 2007 - April 2014), 10 years Metop-b (October 2012 - June 2022), 3 years Meto-c (October 2019 - June 2022), and 2 years (June 2020 - June 2022) HaiYang-2B observed Level-2 U_{10} data are also used. All the data have a spatial resolution of 12.5 km, except for the one provided

by HaiYang-2B, which has a resolution of 25 km.

In the work of coupling analysis of wind and waves, a long-term buoy collected wind and wave dataset provided by the National Data Buoy Center (NDBC, www.ndbc.noaa.gov) is used to develop the swell decomposition method and to establish the new coupled relation between wind and wave. The spatial distribution of the buoys is shown in Figure 2.5 as red dots, the black triangles indicate the selected buoys for further studies.

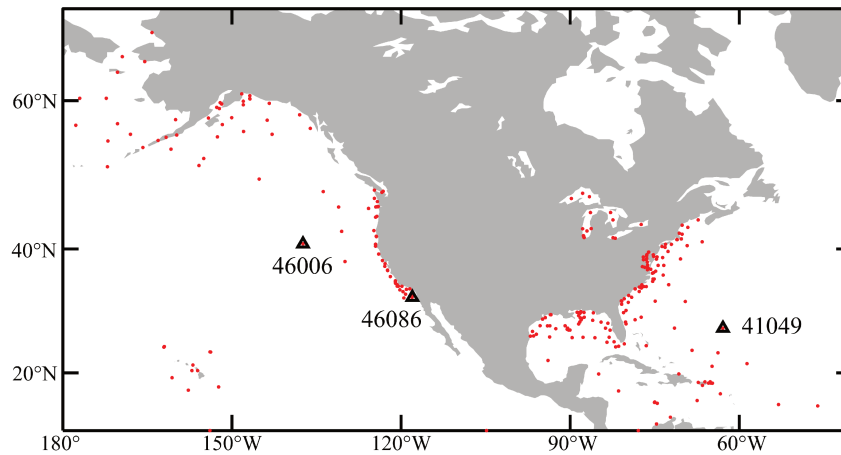


Figure 2.5 The spatial distributions of NDBC buoys (red dots), three selected off-shore buoys are indicated by black triangles.

The NDBC collected *in situ* dataset is of high quality and has been extensively used to study the wind-wave interactions, validate model results, and calibrate satellite systems (Ebuchi et al., 2002; Evans et al., 2003; Andreas and Wang, 2007; Zieger et al., 2015). As a demonstration of the new method, the hourly averaged wind speed and significant wave height collected by the offshore buoy 46086 located at $32^{\circ}29'55''$ N and $118^{\circ}3'9''$ W (see the middle black triangle in Figure 2.5) for more than ten years (i.e., from January 1, 2009, to December 31, 2021) is considered. The wind speed is measured by an anemometer located at $z = 4.1$ m above the sea surface. The typical measure accuracy is 0.55 m/s, and 0.5 m respectively for wind speed and significant wave height (Evans et al., 2003).

As aforementioned, $U_{4.1}$ should be converted to U_{10} before we process the wind data ($U_{10} = 1.084U_{4.1}$). Figure 2.6 shows the converted U_{10} and H_s data collected by buoy 46086, annual cycles for wind speed and wave height both can be observed.

Another dataset is 17 years (from 2002 to 2018) of JASON observed global U_{10} and H_s calibrated by Ribal and Young (2019). The JASON on-boarded altimeter emits pulses, and by estimating the shapes and return time of the pulse signal (“radar echo” from the sea surface), information on the mean sea level can be obtained. The backscattered return from the sea surface is always recognized as the specular reflection, which is inversely

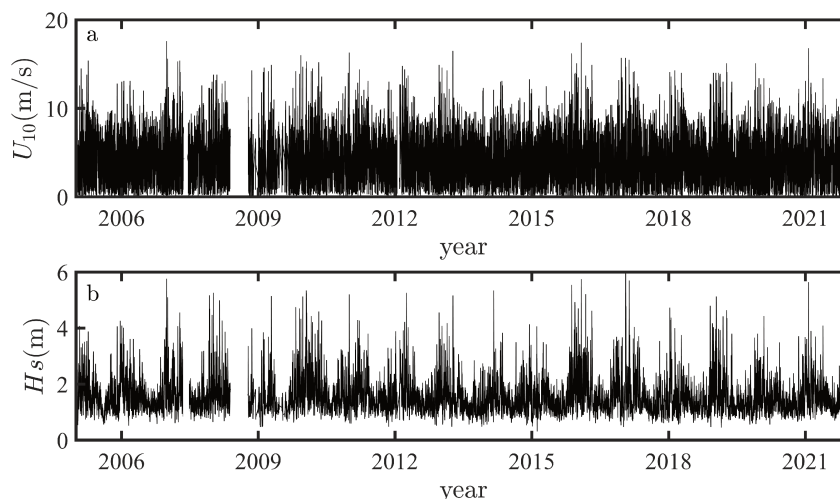


Figure 2.6 Illustration of the NDBC buoy 46086 collected (a) U_{10} and (b) H_s .

proportional to the mean square slope (MSS) of the sea surface. According to the work of Cox (1954), the MSS is closely connected to the surface wind speed, thus according to some empirical equations, the sea surface wind speed can be derived from the backscatter coefficient (Gourrion et al., 2002). As for the measurement of significant wave height, it is based on the fact that the distortion of the mean shape of the return pulse is directly related to the significant wave height, the earlier return from the wave crests, and the retarded return from the wave troughs lead to the deformation of the return pulse. Thus, for a Gaussian sea state, the relation between pulse shape and wave height can be theoretically determined.

This dataset was carefully quality controlled and calibrated to ensure long-term stability and cross-mission consistency. The wind and wave data were archived in 1° by 1° bins in this dataset. It has been shown that this data set agrees well with those provided by buoy and model reanalysis product (Young and Donelan, 2018; Takbash et al., 2019; Young and Ribal, 2019).

2.2 Methods

In this section, the methods which are used for data analysis are presented.

2.2.1 Fourier Power Spectral Analysis with Missing Data

2.2.1.1 Fourier Power Spectrum

Fourier power spectrum is often used to describe the distribution of power into frequency/wavenumber components composing the signal. The spectrum of a signal contains essential information about the nature of its physical process. For instance, the dominated scales can be identified by the frequencies/wavenumbers which correspond to the spectrum peaks. As for turbulence or turbulence-like systems, due to the absence of characteristic scales, and the interactions among different scales, power-law behaviors, namely scaling features, are often obtained in the spectra. The power-law behavior can provide useful information in the understanding of the underlying dynamics that are associated with the collected discrete dataset, such as the famous Kolmogorov five-third law in high Reynolds turbulence flows, e.g., $E(k) \propto k^{-5/3}$ (Frisch, 1995; Schmitt and Huang, 2016).

2.2.1.2 Fast Fourier Transfer and missing data

In practice, the Fast Fourier Transform (FFT) algorithm is most often implemented to digitally retrieve the power spectrum. The FFT algorithm requires regular sampling steps without gaps (e.g., missing data points or irregular sampling steps). However, the data collection in the real world often faces problems of missing data or irregular sampling steps due to many reasons, such as the presence of sea ice, lands, and bad measurements, which violates the requirement of the application of the FFT algorithm (Lomb, 1976; Percival and Walden, 1993). Missing data is a typical problem in the geosciences field, including for collected temperature data (Huang and Schmitt, 2014), the velocity provided by laser doppler velocimetry (LDV) in turbulence experiments (Adrian and Yao, 1986; Benedict et al., 2000; Huisman et al., 2013), and also the satellite data used in this study, see the wind field gaps in Figure 2.2.

Conventionally, special treatments like interpolation or resampling techniques are adopted to handle this problem: for instance, applying interpolation algorithms to the collected data set to generate a new set with even sampling steps without gaps, such as nonuniform-FFT (NUFFT)(Dutt and Rokhlin, 1993; Liu and Nguyen, 1998; Greengard and Lee, 2004). The Fourier spectrum can also be calculated via a least-square spectral analysis, also known as Lomb-Scargle Fourier transform (Lomb, 1976; Scargle, 1982). These approaches are useful to recover periodic signals, such as daily or annual cycles in geophysical data. For example, B. (2009) recognized bias sources (e.g., aliasing, truncation, etc.) by resampling the data on an equidistant grid for irregular data without considering the data loss patterns. Results concluded that when more data are used for the estimation, bias effects will not diminish since they are independent of the sample size.

Sujbert and Orosz (2016) studied the influence of the three different data loss patterns, including random independent, block-based, and Markov model-based data loss. A zero-padded technique with a maximal overlap ratio of 75% is proposed to recover the Fourier power spectrum. Zhang et al. (2018) proposed a general L_p norm ($0 < p \leq 1$) minimization approach for estimating the power spectrum with missing data and found a significant enhancement of the estimation of the spectrum using an adaptive basis re-weighting scheme even in cases of 80% missing data. Despite these findings, bias will always be introduced when the scaling property is concerned (Huang and Schmitt, 2014). This is why we propose here another approach. This work forms a manuscript that is in preparation: Gao, Y, Schmitt FG, Hu JY, and Huang YX (2022), “Fourier power spectrum of scaling processes with missing data” (to be submitted).

2.2.1.3 Wiener-Khinchin Theorem and Fourier Power Spectrum

For reducing the effect of missing data on the Fourier power spectral analysis of CFOSAT along-track wind and wave data, a bootstrap-like Wiener-Khinchin theorem-based approach is proposed in this work.

Let us consider here a discrete time series $x(t_i)$ with equal distance. Its Fourier transform is defined as, i.e.,

$$X(f_k) = \sum_0^{N-1} x(t_i) \exp(-j2\pi f_k t_i), \quad i = 0, 1, \dots, N-1 \quad (2.1)$$

where $j = \sqrt{-1}$, and $f_k = k/N$ is the frequency. The corresponding Fourier power spectrum is then defined as, i.e.,

$$E(f_k) = \frac{1}{N} |X(f_k)|^2, \quad k = 0, 1, \dots, N-1 \quad (2.2)$$

The Wiener-Khinchin theorem states that the power spectrum $E(f_k)$ and the corresponding autocorrelation function $\rho(\tau_i)$ are a Fourier-Transform pair, i.e.,

$$E(f_k) = \sum_{-\infty}^{+\infty} \rho(t_i) \exp(-j2\pi f_k t_i), \quad \rho(\tau_i) = \sum_{-\infty}^{+\infty} E(f_k) \exp(j2\pi f_k t_i) \quad (2.3)$$

The autocorrelation function is defined as, i.e.,

$$\rho(\tau_i) = \frac{1}{M(\tau_i)} \sum_{m=1}^{M(\tau_i)} \tilde{x}(t_m + i\delta t)\tilde{x}(t_m) \quad (2.4)$$

where \tilde{x} is the centered x , and $M(\tau_i)$ is the sample size at the separation scale $\tau_i = i\delta t$. Although the above defined $\rho(\tau_i)$ is valid also for the missing data case, both $\rho(\tau_i)$ and $E(f_k)$ could be biased in this case.

Equation (2.3) is widely used in the calculation of the correlation function from the power spectrum or vice versa. For example, Adrian and Yao (1986) proposed the so-called sample and hold (SH) method to interpolate the Laser Doppler Velocimetry (LDV) data into equal-distance sampling data. The correlation function is first calculated based on the new time series, then the Fourier power spectrum is estimated through the Wiener-Khinchin theorem (Benedict et al., 2000). The SH algorithm will introduce bias, which might be partially corrected via a Wiener-filter-like correction step as below, i.e.,

$$E_{\text{Exp}}(f) = \frac{1}{1 + f^2/\tilde{f}^2} \left(E_{\text{Est}}(f) + \frac{2\sigma_u^2}{\tilde{f}^3 T_\lambda^2} \right) \quad (2.5)$$

where \tilde{f} is the mean frequency of the arrived particles, σ_u is the standard deviation of the measured turbulent velocity; and T_λ is the corresponding Taylor microscale-based Reynolds number. This type of formula has also been proposed to correct the aliasing effect (Kirchner, 2005). More detail about this approach can be found in Benedict et al. (2000).

2.2.1.4 Effects of Missing Data

In this section, a toy model, namely fractional Brownian motion (fBm) with power-law statistics, is considered to show the influence on scaling exponents retrieved from the missing data in detail for the case of random independent data loss.

Fractional Brownian motion is a generalization of the classical Brownian motion, which was first introduced by Kolmogorov (1940), and then studied extensively by Mandelbrot *et al.*, in the 1960s (Mandelbrot and Van Ness, 1968). Since then, it was considered as a classical mono-scaling stochastic process in many fields, e.g., financial activity, turbulence, telecommunication networks, (Beran, 1994; Rogers, 1997; Doukhan et al., 2003; Schmitt and Huang, 2016; Fuliński, 2017), to list a few. Considering an fBm process $x_h(t)$

with $t \in [0, T]$, its autocorrelation function is written as following, i.e.,

$$\rho_h(t, s) = \frac{1}{2} (|t|^{2h} + |s|^{2h} - |t - s|^{2h}), \quad (2.6)$$

where h is the Hurst number or Hurst index in $(0, 1)$ used as a measure of long-term memory of time series, which was developed by the climatologist Hurst (Hurst, 1951). For instance, a value of $h = 1/2$ indicates a completely uncorrelated process, known as Brownian motion, $h > 1/2$ indicates a long-range correlation, while $h < 1/2$ implies an anti-correlation. One definition of the fBm is written as,

$$x_h(t) = \int_0^t W_h(t') dt' \quad (2.7)$$

where $W_h(t)$ is the so-called fractional Gaussian noise (fGn for short). The autocorrelation function of fGns is written as,

$$\rho_h(\tau) = \frac{1}{2} (|\tau - 1|^{2h} - 2|\tau|^{2h} + |\tau + 1|^{2h}), \quad (2.8)$$

where τ is the time lag. fBm is self-similar, since, in terms of the probability distribution, it satisfies the following scaling relation, i.e.,

$$x_h(at) \sim |a|^h x_h(t) \quad (2.9)$$

Fourier power spectra of fBm processes are well-known to have a power-law behavior, i.e.,

$$E_h(f) \propto f^{-\gamma(h)}, \quad (2.10)$$

where f is the frequency; $\gamma(h) = 1 + 2h$ is the scaling exponent. In this work, an FFT-based Wood-Chan algorithm was used to generate the fBm data (Wood and Chan, 1994) through the following steps:

1. Generate the autocorrelation function $\rho_h(\tau)$ of fGns via Eq. (2.8);
2. Obtain the corresponding Fourier series through the Wiener-Khinchin theorem, e.g., Eq. (2.3) with a random phase;
3. Retrieve fGns time series via the inverse FFT;
4. Obtain the final fBm time series via Eq. (2.7).

Figure 2.7(a) shows the measured autocorrelation function $\rho_L(\tau)$ of a fBm with

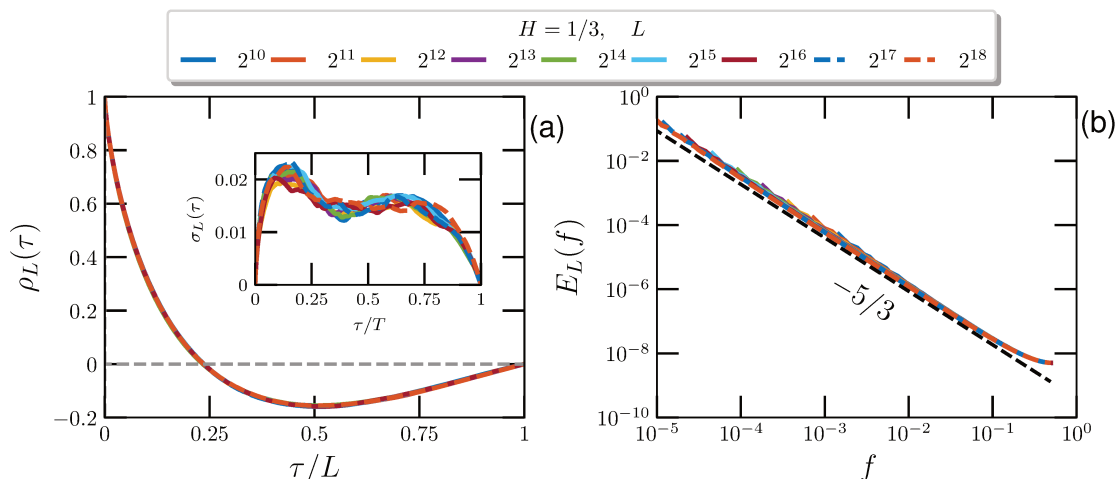


Figure 2.7 (a) Measured correlation function $\rho_L(\tau)$ for $h = 1/3$ with data length on the range $2^{10} \leq L \leq 2^{18}$ (in data points). The inset shows the standard deviation $\sigma_L(\tau)$ obtained from 100 runs with 100 realizations each. (b) The corresponding measured power spectra $E_L(f)$; the dashed line is a pure power-law $E(f) \propto f^{-5/3}$ for reference. The discrepancy at the high-frequency part is due to the aliasing effect. For comparison, the measured $E_L(f)$ have been vertically shifted.

$h = 1/3$ with a data length in the range $2^{10} \leq L \leq 2^{18}$ data points for 100 runs with 100 realizations each to show a possible finite length effect. The inset shows the standard deviation $\sigma_L(\tau)$ obtained from 100 runs. Graphically, both $\rho_L(\tau)$ and $\sigma_L(\tau)$ curves collapse with each other, suggesting that the finite length effect can be ignored with a large number of realizations. The corresponding Fourier power spectrum $E_L(f)$ is retrieved for each run by applying the Wiener-Khinchin theorem. The final spectrum is then defined as an average spectrum from 100 runs. Figure 2.7 (b) shows the experiment Fourier spectra $E_L(f)$, where the dashed line represents a pure power-law, e.g., $E(f) \propto f^{-5/3}$, for reference. For comparison, the curves $E_L(f)$ have been vertically shifted to overlap the measured spectrum. Visually, they can collapse with each other, suggesting that the scaling of measured spectra is almost independent of the data length L since fBm is expected to follow a pure power-law relation. Therefore, in the following, if there is no further clarification, a data length of $L = 2^{14}$ is used. Note that due to the aliasing effect, the deviation from the pure power-law is found for $f \geq 0.1$.

Here, we consider a Hurst number $h = 1/3$ in our following numerical experiment on the effect of missing data. For simplicity, we only assume here a random independent data loss with a missing data ratio in the range $0 \leq \mathcal{R} \leq 80\%$. The index of missing data points is generated via the Matlab function `randperm.m` (by inputting `randperm(n)`, the code returns a row vector containing a random permutation of the integers from 1

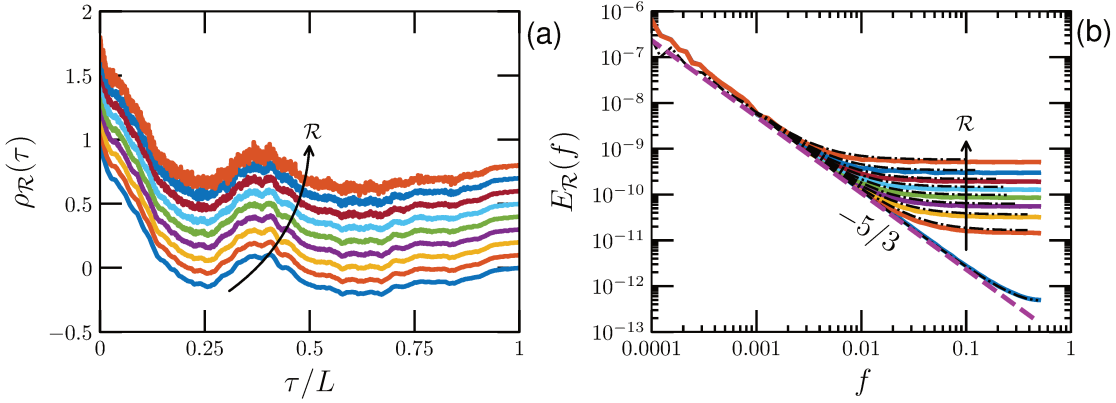


Figure 2.8 (a) Measured correlation function $\rho_{\mathcal{R}}(\tau)$ for $h = 1/3$ with a data length $L = 2^{14}$ data points and missing data ratio \mathcal{R} from 0 (resp. raw data without missing data, bottom) to 80% (resp. top), with a 10% increment in each curve. For display clarity, the curve is vertically shifted. (b) Measured Fourier power spectrum $E_{\mathcal{R}}(f)$ with 100 realizations; the thick solid line is the original Fourier power spectrum $E_0(f)$ without missing data. The dashed line is a pure power-law $E(f) \propto f^{-5/3}$ for reference. The dash-dotted lines are the spectral curves provided by the Lomb-Scargle algorithm. The discrepancy at the high-frequency part (resp. $f > 0.1$) is due to the aliasing effect.

to n without repeating elements). Figure 2.8(a) shows one realization of the measured correlation function $\rho_{\mathcal{R}}(\tau)$. For display convenience, the curves $\rho_{\mathcal{R}}(\tau)$ have been each vertically shifted by 0.1. Visually, they share the same shape but are less and less smooth with the increase of the missing data ratio \mathcal{R} . Figure 2.8 (b) shows the measured averaged spectrum $E_{\mathcal{R}}(f)$ for 100 realizations. For comparison, the spectrum curve provided by the Lomb-Scargle estimator is also shown as a dash-dotted line. The range of the flat part increases with \mathcal{R} , which suggests a white-noise-like behavior as reported in Sujbert and Orosz (2016), and also an aliasing effect (Kirchner, 2005). It can be formulated as follows, i.e.,

$$\tilde{\rho}(\tau) = \rho(\tau) + \bar{\rho}(\tau), \quad \tilde{E}(f) = E(f) + \bar{E}(f) \quad (2.11)$$

where $\tilde{\rho}(\tau)$ and $\tilde{E}(f)$ are measured correlation function and spectrum; $\bar{\rho}(\tau)$ and $\bar{E}(f)$ are the additional bias from either the missing data or the resampling procedure, respectively. This is one reason why the bias will not diminish for more data since $\bar{E}(f) > 0$ (B., 2009).

To characterize this bias effect quantitatively, we introduce here a relative error func-

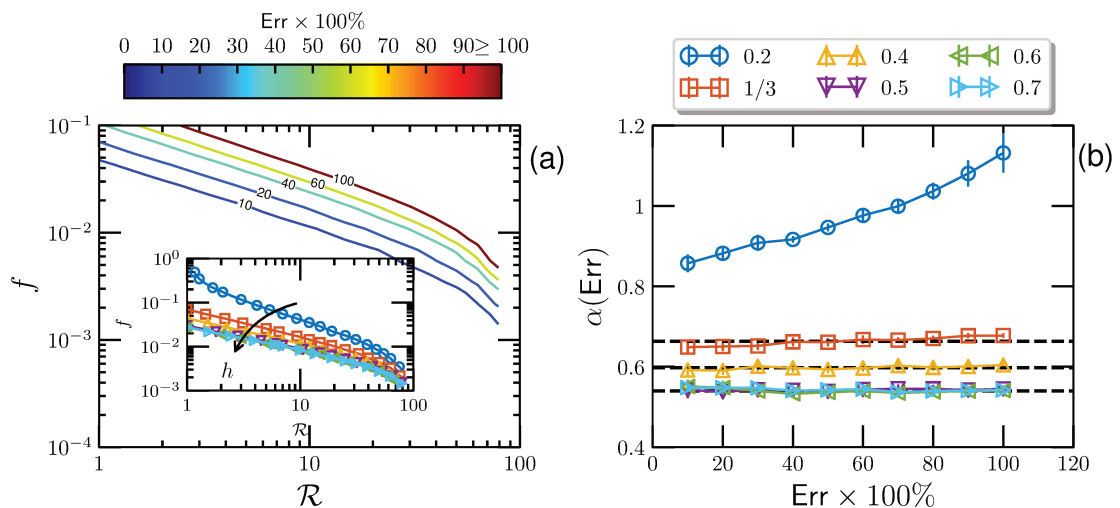


Figure 2.9 (a) Contour lines of the error function Err between the measured spectrum with and without the missing data problem for $h = 1/3$. The inset shows the contour line $\text{Err}(\mathcal{R}, f) = 10\%$ for Hurst numbers from 0.2 (top) to 0.7 (bottom), indicated also by the arrow. Power-law behavior is observed for the contour line, e.g., $f \propto \mathcal{R}^{-\alpha}$. (b) The corresponding scaling exponent $\alpha(\text{Err})$, where the dashed line indicates an average value over Err .

tion, which is written as, i.e.,

$$\text{Err}(\mathcal{R}, f) = \frac{|E_{\mathcal{R}}(f) - E_0(f)|}{E_0(f)} \times 100\% \quad (2.12)$$

where $E_0(f)$ is the Fourier power spectrum without missing data. Figure 2.9 (a) displays the contour lines of the measured $\text{Err}(\mathcal{R}, f)$ defined by Eq.(2.12) for $h = 1/3$. A power-law behavior is observed for the contour line of a given value of $\text{Err}(\mathcal{R}, f) = \text{const.}$, i.e.,

$$f \propto \mathcal{R}^{-\alpha(\text{Err})} \quad (2.13)$$

In the inset of Figure 2.9 (a), the contour line $\text{Err} = 10\%$ is shown for various Hurst numbers h , and the power-law behavior is observed for all h . Figure 2.9 (b) shows the measured α with respect to different relative errors Err and h . Except for small values of h (e.g., $h < 0.3$), α is almost independent of Err . This is partially due to the fact that this FFT-based fBm generation algorithm will fail when $h \rightarrow 0$.

2.2.1.5 A Bootstrap-like Algorithm to Reduce the Influence of Missing Data

The above observation suggests that the bias produced by the missing data is white-

noise-like with a random phase for both $\rho(\tau)$ and $E(f)$. Therefore, such bias can be canceled via more realizations for the estimation of the correlation function $\rho(\tau)$ since $\bar{\rho}(\tau)$ can be positive or negative. Considering a collected data $x(t)$ with a missing data ratio \mathcal{R} , a resampling procedure is employed to have a new data set with more missing data ratios, i.e.,

$$\mathcal{R}' = n\mathcal{R} \quad (2.14)$$

where $1 \leq n < \frac{100}{\mathcal{R}}$. The correlation function is then estimated for each new time series, e.g., $\tilde{\rho}_i(\tau)$. After repeating this resampling procedure for N times, the ensemble average correlation function is obtained by

$$\tilde{\rho}_N(\tau) = \frac{1}{N} \sum_{i=1}^N \tilde{\rho}_i(\tau) = \rho_T(\tau) + \frac{1}{N} \sum_{i=1}^N \bar{\rho}_i(\tau) \quad (2.15)$$

where $\rho_T(\tau)$ represents the true correlation function without the influence of the missing data problem. It is natural to assume the following asymptotic behavior, i.e.,

$$\lim_{N \rightarrow \infty} \tilde{\rho}_N(\tau) = \rho_T(\tau) \quad (2.16)$$

The corresponding Fourier power spectrum $\tilde{E}_N(f)$ is then calculated via the Wiener-Khinchin theorem, see Eq. (2.3). We, therefore, expect the true Fourier power spectrum to be fully recovered by the above equation, e.g., $\lim_{N \rightarrow \infty} \tilde{E}_N(f) = E_T(f)$.

Figure 2.10 (a) shows the measured Fourier power spectrum $\tilde{E}_N(f)$ for the case $h = 1/3$ with $\mathcal{R} = 50\%$, $n = 1.2$ and N up to 1,000. As expected, the measured $\tilde{E}_N(f)$ asymptotically approaches the one without missing data. Figure 2.10 (b) shows the contour line of the measured relative error $\text{Err}(N, f)$. The power-law trend convergence is observed, which is written as, i.e.,

$$f \propto N^\beta \quad (2.17)$$

where the scaling exponent β characterizes the convergence rate. To determine a more accurate scaling exponent β , we performed a numerical experiment with 1,000 independent simulations. Figure 2.11 shows (a) the measured spectrum $\tilde{E}_N(f)$, and (b) the corresponding contour line of the relative error $\text{Err}(N, f)$. The measured scaling exponent β is found to be $\beta = 0.33 \pm 0.02$. According to this scaling trend, one needs 50,000 realizations to obtain a measured spectrum $\tilde{E}_N(f)$ with a relative error less than 10% for the frequency below $f \lesssim 0.2$, see dash-dotted line in Figure 2.10 (a) and 2.11 (a). The inset in Figure 2.11 (b) shows the measured relative error $\text{Err}(N, f)$ for $N = 50,000$, confirming this empirical prediction. This algorithm is thus able to retrieve the full scaling behavior and

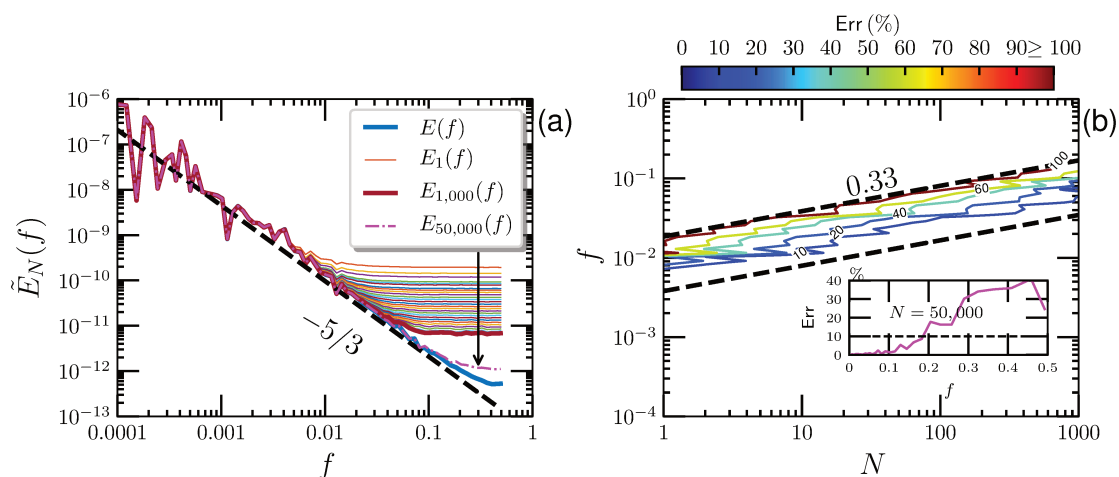


Figure 2.10 (a) Measured Fourier power spectrum $\tilde{E}_N(f)$ for one realization with $h = 1/3$ and a missing data ratio of $\mathcal{R} = 50\%$ and $n = 1.2$. The number of realizations N is up to 1,000, which is indicated by the arrow. (b) Contour line of the measured error functions Err between the measured spectrum with and without the missing data problem. A pure power-law relation $f \propto N^{0.33}$ is shown as a dashed line for reference. Inset shows the relative error function $\text{Err}(f)$ for the case of $N = 50,000$.

scaling power spectrum, even for a process with missing data. It was shown here numerically for a simple fBm process. We test it below for real-world data.

2.2.1.6 Spectra Measurement for CFOSAT Along-Track H_s Data

After the numerical validation of the proposed method, we apply it here to real-world data. A CFOSAT along-track H_s segment which is composed of 3,400 data points (5,100 km) is used to verify the performance of the introduced algorithm. The measured auto-correlation function and spectrum of the raw data are shown as the black curves in Figures 2.12 a and b, respectively. Then the Matlab function `randperm.m` is used to randomly generate gaps in the selected H_s dataset, and the missing ratio is set from 10% to 80%. The corresponding autocorrelation functions and spectra calculated with these data are shown in Figures 2.12 a and 2.12 b as colored curves. As we indicated with the black arrow, with the increase in missing ratio, the autocorrelation functions have become coarser, and the values of spectra in large wavenumber ranges ($k > 0.01 \text{ km}^{-1}$) increase, making the spectra tend to be a plateau. The results show that the effects of missing data on the estimation of spectra are the same as we found in the fBm data test, e.g., equivalent to the effects of induced white noise in the raw data.

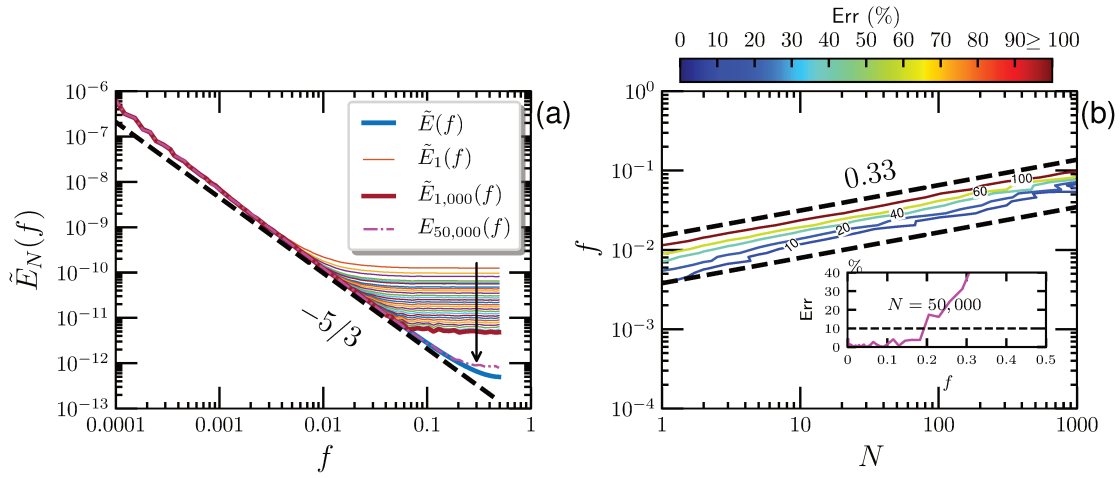


Figure 2.11 (a) Measured Fourier power spectrum $\tilde{E}_N(f)$ for $h = 1/3$ with a data missing rate of $\mathcal{R} = 50\%$ and $n = 1.2$. The number of realizations N is in the range $1 \leq N \leq 1,000$, which is indicated by the arrow. (b) Contour line of the measured error functions Err between the measured spectrum with and without the missing data problem. Power-law behavior is observed for the contour line, e.g., $f \propto N^\beta$ with an experimental value of $\beta = 0.33 \pm 0.02$ (dashed line). Inset shows the relative error for $N = 50,000$ to illustrate the power-law prediction that the measured $\text{Err}_N(f) \leq 10\%$ for $f \leq 0.2$.

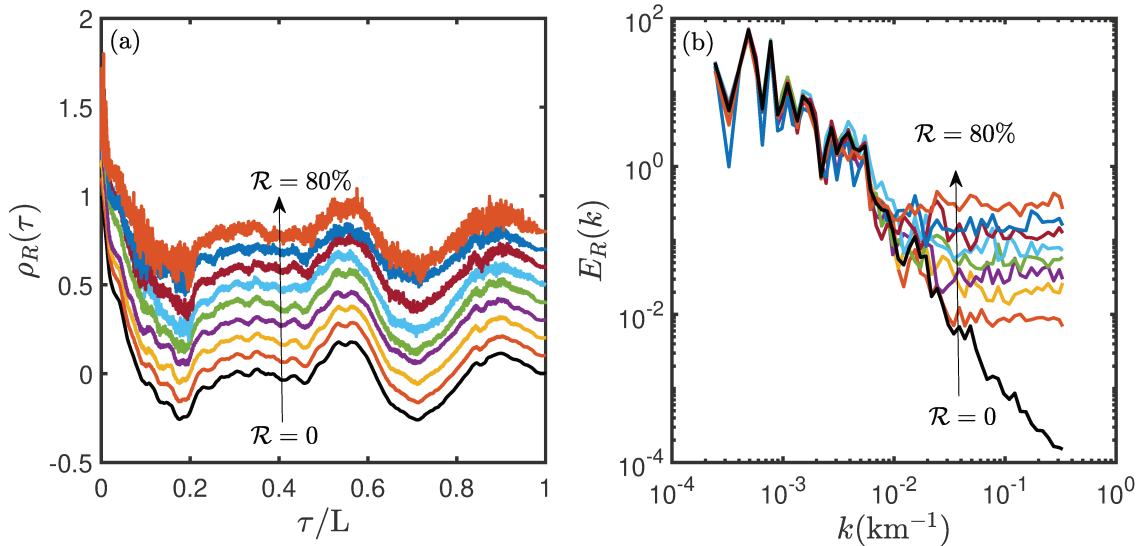


Figure 2.12 (a) Measured correlation functions for CFOSAT along-track H_s with the missing data ratio from 0 (bottom) to 80% (top). (b) The corresponding Fourier power spectra. The data length is 3,400.

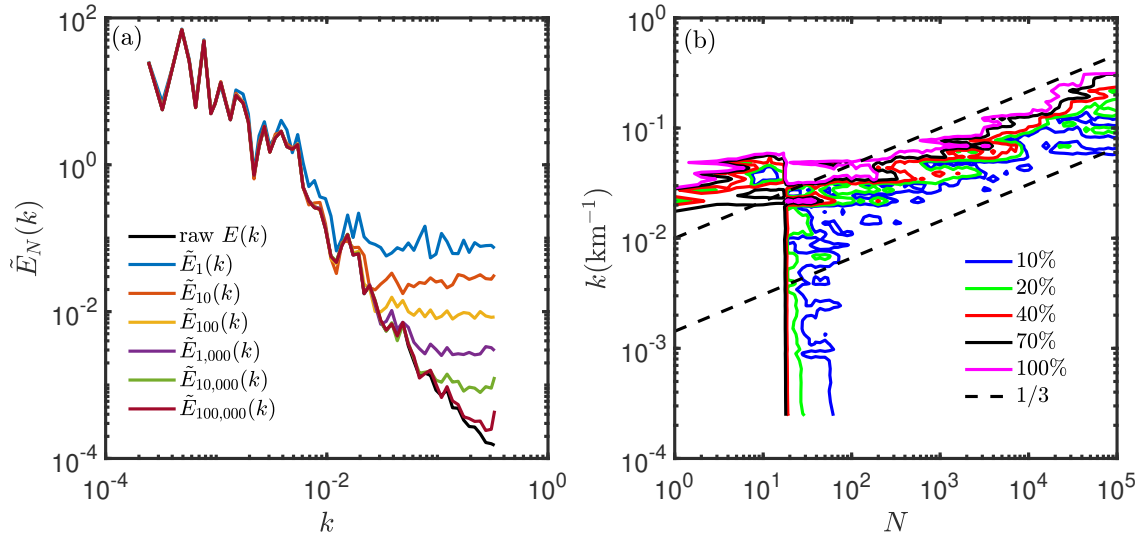


Figure 2.13 (a) Measured Fourier power spectrum for CFOSAT along-track H_s data with the data missing ratio $\mathcal{R} = 50\%$ and $n=1.2$. The number of realizations N is in the range $1 \leq N \leq 100,000$ (b) Contour line of the error function Err between the measured spectrum with and without the missing data problem. Power-law behavior is observed for the contour line, e.g., k^β with an experimental value of $\beta = 1/3$ (dashed line).

After that, the data with 50% missing ratio are used to reproduce the spectrum with the bootstrap-like algorithm. The spectra with the realization numbers from 1 to 100,000 and the corresponding error functions are measured, the results are illustrated in Figure 2.13. Figure 2.13 a shows the spectra estimated with different realizations, the black curve is the spectrum for original data: with the increasing of realizations, the measured spectra tend to be close to the original one. Figure 2.13 b is the counter plot for the error function: power-law features are found in the ranges of $k > 0.01^{-1}$ where the scaling exponent closes to $1/3$, which is the same as we found in the fBm test. Note that, a vertical distribution for the values of the error function is found with the realization times less than 100, which is due to the fact that the tested data are too short.

2.2.1.7 Applying to CFOSAT Observed 2D Wind Field Data

Another simple example is given here to show the efficiency of performing the algorithm on 2D data which contain gaps. The CFOSAT collected 2D wind fields in the latitude range of 25°S to 25°N is chosen. The pictures with the missing ratio of less than 50% are kept in the test, total 5000 snapshots are used: namely, 5000 realizations are performed in the calculation of the autocorrelation function. The result is illustrated in

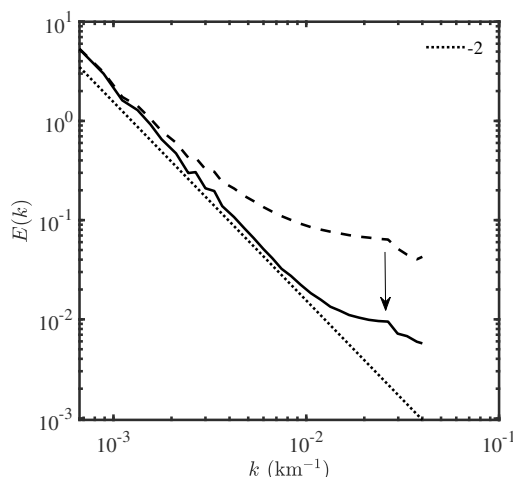


Figure 2.14 Directly (dashed curve) and after performing the bootstrap-like algorithm (solid curve) measured Fourier power spectra for CFOSAT observed wind field. The dotted line is given as a reference with the slope of -2.

Figure 2.14, the directly measured Fourier power spectrum is shown as a dashed curve, and the one extracted from the bootstrap-like algorithm is shown as a solid curve. The scaling information from these two spectra is largely different in the high wave number range. The corrected one shows a scaling exponent close to 2 in the spatial range of 100-1000 km.

2.2.1.8 Conclusion for the Algorithm

The algorithm proposed here can be extended to 2D or higher-order dimensions. Concerning the satellite remote images in 2D, quite often part of the area is covered by the cloud or occupied by the island. Hence, part of the data is unavailable. Another issue worth mentioning is the measurement noise, which is different from the white-noise-like caused by the missing data. The noise-induced affection is embedded in the collected data and cannot be canceled with each other using the bootstrap-like procedure, while the effect of missing data, as shown in this work, can be reduced due to the fact that the additional noise effect through the resampling algorithm has a random phase. They can cancel up via the use of N th-realizations. It also implies that to recover the raw Fourier spectrum, one needs a much large sample size if some data are missing.

We may note that the irregular time step sampling problem (such as LDV data in turbulence) can be converted to the missing data problem by choosing a uniform bin. Two types of bias are involved (B., 2009). One is from the missing data, where there are no values in some bins, while the other one is from the shifting position (i.e., δt), see

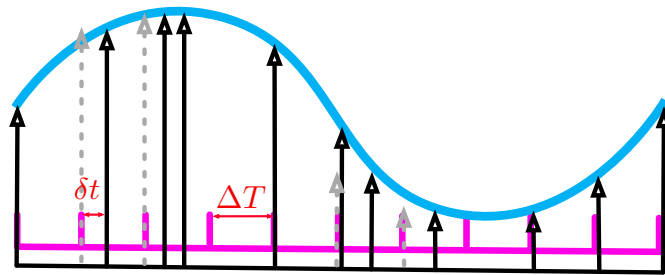


Figure 2.15 (Color online) An illustration of irregular sampling steps (solid line with arrow). It can be converted to the missing data problem (dashed line with arrow).

an illustration in Fig. 2.15. Both these biases can be reduced via the present proposed bootstrap-like algorithm (not shown here).

In summary, the Fourier spectrum was estimated via a combination of the Wiener-Khinchin theorem and a bootstrap-like algorithm to reduce the bias introduced by the missing data. It was experimentally found that the bias increased with the missing data ratio \mathcal{R} in a power-law behavior. We demonstrated that due to the missing data problem, the power-law behavior is biased. However, the spectrum can be recovered asymptotically by the proposed algorithm with a power-law convergence rate. The algorithm proposed in this work is model-free and could be applied to other collected data sets, with face problems of missing data or irregular sampling steps. This algorithm is numerically validated and would need further mathematical proof.

2.2.2 Structure-Function Analysis

In the scaling analysis of CFOSAT along-track wind and wave data, the second-order structure-function (i.e., $S_2(r)$) is considered to extract the scaling features. Moreover, the corresponding scaling exponent $\zeta(2)$ can be linked with the scaling exponent β for the Fourier power spectrum as $\zeta(2) = \beta - 1$ (Frisch, 1995) to valid the results for spectral analysis.

Unlike spectral analysis, the structure-function analysis is suitable for irregularly sampled data or data which contain gaps, thus, it is widely used. However, a drawback of this kind of analysis is the time-consuming calculation when the dataset is irregular. The structure-function analysis requires matching all the data into couples at first, which means that if the dataset contains N data points, we have to generate $\frac{N \times (N-1)}{2}$ ($\sim \mathcal{O}(N^2)$) matching pairs to calculate the corresponding increments. With the generated increments, the multi-order statistic processes then can be performed.

The data provided by satellites are always large with thousands upon thousands of data points (for CFOSAT wind observation, one trajectory can generate 84×3440 data points), it will take a long time to process three years of CFOSAT wind data if we use the original way to match the data pairs. The spatial resolution of CFOSAT observed wind data is 12.5 km, which means that the distance between two consecutive observed points is equal to 12.5 km, no matter whether these two nearby points are located in the equator or in the poles. Since the structure-function analysis is considered in log-log, the scale of separation distance bins can be set as one-tenth of the decade. Then the two subsets of U_{10} data which have the distances corresponding to one of the bins can be regarded as one pair to do the increment calculation. In this way, the calculation speed can be greatly enhanced.

Note that, as argued by Huang et al. (2010) the structure-function scaling exponent might be contaminated when the analyzed dynamical system contains large energetic scales. The movements of ocean surface waves and atmospheres are related to the climate systems, and these systems are determined by complex internal or external factors (land-sea distribution, solar radiations, air-sea interactions, and human activities, to list a few). Thus, large-scale structures inevitably exist in the ocean wave and wind data. Nevertheless, structure-function analysis has already been widely used in the ocean surface wave and wind analysis (Vogelzang et al., 2015; King et al., 2015; Scannell et al., 2017) to study the ocean surface dynamic features.

2.2.3 Energy and Enstrophy Fluxes Analysis

In the field of fluid dynamics and geophysical research, several approaches have been proposed to determine the direction of the energy/enstrophy cascade, which is associated with nonlinear interactions between different spatial scales. For example, assuming locally homogeneous isotropic turbulence in a 3D incompressible fluid, one has the negative third-order longitudinal structure-function with the famous four-fifth Kolmogorov law in the inertial range (Kolmogorov, 1941b; Nie and Tanveer, 1999), i.e.,

$$S_3(r) = \langle \Delta_r u(x)^3 \rangle = -\frac{4}{5}\epsilon r, \quad (2.18)$$

where $\Delta u_{||}(x, r)$ is the longitudinal velocity increment between two points separated by r , x is the location of a given point, ϵ is the energy flux (i.e., mean energy dissipation per unit mass, with dimensions $\text{length}^2/\text{time}^3$). Note that, as suggested by Kraichnan (1974) that ϵ is better to be interpreted as the energy flux across scales. Therefore, the sign of

$S_3(r)$ is believed to indicate the direction of the energy cascade. This has been widely used in high Reynolds number turbulent flows (Moisy et al., 1999; Antonia and Burattini, 2006; Kaneda et al., 2008; Ishihara et al., 2009; Salort et al., 2012; Antonia et al., 2019), and used to indicate the direction of the energy cascade of the turbulent flows (Xia et al., 2008, 2011; Zhang et al., 2021b). For a 2D isotropic turbulent flow, positive third-order longitudinal structure functions with the value equal to $3/2Pr$ are expected, in which the energy input power Pr is induced by a small-scale driving force (Lindborg, 1999b), a positive sign is a reflection of the fact that the energy flux is in the direction from small to large r .

Another popular approach is spectral representation. The temporal evolution of energy spectrum $E(k)$ can be derived from the Fourier space-based Navier-Stokers (NS) equation, as

$$\frac{\partial E(k)}{\partial t} = T(k) - 2\nu\Omega(k), \quad (2.19)$$

where $T(k)$ represents the rate of energy transfer at the wavenumber k (corresponding to the spatial scale of $r = 1/k$ in the physical space) owing to nonlinear interactions (Kraichnan and Montgomery, 1980); ν is the kinematic viscosity; $\Omega(k) = k^2 E(k)$ is the enstrophy spectrum. Then one can obtain the energy flux for a velocity field in the Fourier space as,

$$\Pi(k) = \int_k^\infty T(k')dk' \quad (2.20)$$

The spectral approach is suitable to extract the energy flux in a regular domain (Alexakis and Biferale, 2018), and has been widely used to diagnose the scale-to-scale energy fluxes for turbulent flows (Scott and Arbic, 2007; Bai et al., 2013; Khatri et al., 2018). The Fourier transform process in this method requires the data to be uniformly distributed without gaps, thus it may not be directly performed to analyze the field observed dataset. Some interpolations are always employed to generate the velocity data on rectangular grids before doing the Fourier transform. However, interpolations will contaminate the dynamic features of the original field. Besides, the energy fluxes extracted by the spectral approach are always associated with noise leading to unreliable high values of the flux divergence (Scott and Wang, 2005).

We note that, the spectral representation and third-order longitudinal structure function can be related by manipulating the Kármán-Howarth equation in 2D (Cerbus and Chakraborty, 2017). The relation shows that the sign of $S_3(r)$ is affected by values of both energy and enstrophy fluxes. Thus, the sign of $S_3(r)$ might not imply the true direction of the energy cascade.

An alternative approach to diagnose the direction of energy cascade is the Filter-Space-Technique (FST), which was first introduced by Leonard (1975) in the field of turbulence for Large-Eddy-Simulation (LES) works. Then it was further developed by Eyink (2005) to study the local energy cascade of turbulent flows. FST has attracted much attention in fluid dynamics or geophysical fields to quantify the energy transfer among different scales. For instance, Ni et al. (2014) used experimental data in 2D and the results of a 3D simulation for turbulent flow to verify the utility of FST. The results show that FST is useful to analyze turbulence experimental data, even with limited spatial resolution. Zhou et al. (2016) studied 2D Rayleigh-Taylor turbulence with FST: they found the inverse cascade of kinetic energy and forward cascades for thermal energy and enstrophy. Wang and Huang (2017) found an inverse energy cascade for 2D bacterial turbulence via FST. Aluie et al. (2018) implemented the filtering technique to the data from a high-resolution eddy primitive equation model of the North Atlantic Ocean: the results show that the regions where forward and backward cascades of the energy fluxes both can be identified and located.

For atmospheric movement, the energy cascade is usually related to the famous $-5/3$ scaling of the spectra for wind speed in the spatial scales from 10 to 500 km (Nastrom et al., 1984; Vinnichenko, 1970; Nastrom and Gage, 1985), while the explanation of this scaling is still in debate. For instance, Gage (1979) proposed that the $-5/3$ scaling is probably a manifestation of the reverse-cascading energy for two-dimensional turbulence (Kraichnan, 1971). The inverse cascade perspective was supported by Lilly (1983), Métais et al. (1996), and Vallgren et al. (2011) later. On the contrary, another voice is supporting the view of forward cascade which related to nonlinearly interacting gravity waves (Cho and Lindborg, 2001; Dewan, 1979, 1997; Lindborg, 2006; Waite and Bartello, 2004; Riley and DeBruynkops, 2003; Koshyk and Hamilton, 2001; Cho and Lindborg, 2001; Lindborg and Cho, 2000; Lindborg, 2002). In reality, however, the forward and inverse/backscatter cascades are always coexistent (Lumley, 1992). For example, due to several reasons, such as the geometry constrain, rotating, baroclinic instabilities, etc., to list a few, the overall energy cascade could be inverse in either three- or two-dimensional turbulent flows with the same $-5/3$ scaling (Kraichnan, 1967; Charney, 1971; Sukoriansky et al., 2007; Boffetta, 2007; Celani et al., 2010; Cencini et al., 2011; Biferale et al., 2012; Lucarini et al., 2014; Zhou et al., 2016; Young and R., 2017; Wang and Huang, 2017), see the nice reviewers by Alexakis and Biferale (2018); Zhou (2021). Another confusing point is whether the -3 scaling region is the result of the forward enstrophy cascade or not. O’Gorman and Schneider (2007) shows that the range of -3 scaling is not necessary for the existence of an enstrophy cascade with an idealized general circulation model (GCM). Lovejoy et al.

(2009) proposed that the observed -3 scaling regime is very narrow, and for large scales, it should be a -2.4 scaling. Therefore, one can not determine the direction of the energy or enstrophy cascades just based on the scaling exponents of the Fourier power spectrum or the second-order structure-function (Alexakis and Biferale, 2018; Zhou, 2021). Robust ways to extract the scale-to-scale energy and enstrophy fluxes are demanded.

Chapter 3 Scaling Analysis of CFOSAT Along-Track Wind and Waves

In this chapter, one of the main contributions of our work is presented. The multi-scale information for both wind speed (U_{10}) and significant wave height (H_s) observed by China France Oceanography SATellite (CFOSAT) are extracted by spectral analysis. Fourier power spectra for both U_{10} and H_s exhibit power-law features in the ranges of 100 km to 3000 km with a scaling exponent β varying from $5/3$ to 3. The global distributions and seasonal variation of β for both U_{10} and H_s have also been considered. The results show that due to the energetic convective activities in the low-latitude zones, the scaling exponents β in these regions are closer to the value of $5/3$. Concerning the seasonal variations, for most regions, the scaling exponents in winter are larger than those in summer for U_{10} . The seasonal variations of β in low-latitudes are stronger than those in the mid-latitudes. Our preliminary results contribute to the fundamental knowledge of ocean surface processes. This chapter is based on the published manuscript: Gao, Y, Schmitt FG, Hu JY, and Huang YX (2021), “Scaling analysis of the China France Oceanography Satellite along-track wind and wave data” , *Journal of Geophysical Research : Oceans*, 126, e2020JC017119, <https://doi.org/10.1029/2020JC017119>.

3.1 Theories

3.1.1 Theories for Atmospheric Wind

Assuming that there are no characteristic length scales, over given scale ranges, several scaling laws have been proposed for the wind field in the atmosphere. Here these theoretical proposals are recalled briefly. They will be used as comparisons and potential explanations when considering the CFOSAT data analysis in the following sections.

The most classical scaling is Kolmogorov’s 1941 assumption of universal fluctuations of the turbulent wind velocity in the inertial range, using locally isotropic and homogeneous hypotheses. For very large Reynolds numbers, as is the case in the atmosphere, one obtains Kolmogorov (1941b); Obukhov (1941):

$$E_u(k) = C_0 \epsilon^{-2/3} k^{-5/3}, \quad (3.1)$$

where $E_u(k)$ is the Fourier power spectrum of the wind velocity, ϵ is the mean energy dissipation rate per unit mass, k is one component of the wavenumber vector $\mathbf{k} = (k_x, k_y, k_z)$, and C_0 is a constant. In case of intermittency, there may be some small corrections to the value of the spectral slope $-5/3$, with slopes that may be slightly steeper, e.g., an experimental value of -1.70 has been reported (Monin and Yaglom, 1971; Frisch, 1995). This framework corresponds to a cascade of energy as proposed by Richardson in the 1920s Richardson (1922): the energy is injected at large scales, is cascading in the inertial range, and is dissipated at small scales, smaller than the Kolmogorov scale, which is of the order of millimeters. The Reynolds number in the atmosphere is in the order of 10^7 to 10^9 , and the $-5/3$ slope has been found from atmospheric observations by many authors (Sreenivasan and Antonia, 1997; Calif and Schmitt, 2012; Schmitt and Huang, 2016; Schmitt et al., 1993).

The atmosphere is stratified and at very large scales the atmospheric motions seem to be quasi-two-dimensional (Danilov and Gurarie, 2000). This motivated the application of 2D turbulence phenomenology, as developed by Kraichnan. The phenomenology of 2D turbulence is very different from 3D turbulence. There is no vortex-stretching term, and the enstrophy (square of vorticity) can be introduced to propose an enstrophy cascade picture (Wyngaard, 2010): enstrophy is produced at large scales through mean vorticity gradient, and is destructed at small scales by viscosity. The enstrophy spectrum has dimensionally a -1 slope, and since this is k^2 times the energy spectrum, in this range of scales the energy spectrum follows (Kraichnan, 1967):

$$E_u(k) = C_1 \zeta^{2/3} k^{-3}, \quad k > k_f \quad (3.2)$$

where C_1 is a constant, ζ represents the dissipation rate of enstrophy, and k_f is the wavenumber corresponding to the forcing. At this forcing scale, the enstrophy goes down to small scales, and the energy has an inverse cascade, going to large scales, with a scaling range as (Kraichnan, 1967; Vallis, 2017):

$$E_u(k) = C_2 \epsilon^{2/3} k^{-5/3}, \quad k < k_f \quad (3.3)$$

At very large scales, the energy is assumed to be dissipated by friction through Ekman layers. For the application of this approach to the atmosphere, a quasigeostrophic theory has been proposed (Charney, 1971), where the enstrophy is replaced by a pseudo potential enstrophy. In such a framework, contrary to Kraichnan's 1967 model, there is a -3 slope at large scales and a $-5/3$ slope at small scales, for the power spectrum of the velocity

field.

Finally, let us also mention the 23/9D model proposed by Schertzer and Lovejoy in the 1980s (Schertzer and Lovejoy, 1985, 1987; Lovejoy et al., 2009). Anisotropic features are suggested at all scales with different scaling exponents in the horizontal and vertical directions, where the former is dominated by the energy flux with a slope of $-5/3$ and the latter by the buoyancy variance flux with a slope $-11/5$ (Bolgiano, 1959; Obukhov, 1959). Later, the horizontal anisotropy has been taken into account in the 23/9D model and verified by using the European Centre for Medium-Range Weather Forecasts (ECMWF) reanalyses data (Lovejoy and Schertzer, 2011). This model is also discussed and checked in more recent works (Lovejoy and Schertzer, 2013; Pinel and Lovejoy, 2014). The results show that this model is capable to explain numerous claims of transition phenomena, for instance, the spurious -2.4 slope for aircraft collected data can be interpreted by the anisotropic 23/9D turbulence model, rather than the isotropic 3D or 2D turbulence models.

3.1.2 Theories for the Oceanic Waves

Under a turbulent wind forcing over the sea, a part of the wind energy is transferred to the water masses through the surface wind shear. Since the wind forcing, in the inertial range, has no characteristic scale, and since the related processes involve no obvious characteristic scales, scaling laws for the sea surface height (SSH) have been proposed since the 1950s. They write as:

$$E_{\Psi}(k) \sim k^{-B} \quad (3.4)$$

where $E_{\Psi}(k)$ is the Fourier power spectrum of the spatial 2D SSH field, and B is the scaling exponent. This is valid in a range found over high wavenumbers corresponding to a so-called equilibrium range involving gravity waves. Such range describes breaking waves that have large curvatures, and even nearly discontinuous slopes, with sharp and random crests. By considering dimensional analysis, one early proposal was $B = 4$ by Phillips (1985a). This value was also advanced later by Belcher and Vassilicos (1997) using different dynamical and geometrical arguments: $B = 5 - D$ was proposed. Considering the balance arguments, a value of the dimension $D = 1$ was found. On the other hand, Phillips (1985b) revoked the $B = 4$ result and proposed $B = 7/2$, for taking into account wave breaking and wave-wave interactions, and assuming that the nonlinear energy flux, wind forcing, and dissipation are in balance, proportional, and of comparable magnitude.

These results concern the SSH variable, at small scales, in part smaller than the scale range spanned by satellites. What is recorded by the CFOSAT satellite is H_s , a local

indicator, at the pixel size, of the intensity of the waves. As the value of Hs is estimated locally, it may have also spatial variations. However, its relation with SSH is not direct and there are no theoretical predictions in the literature concerning a scaling behavior of Hs , either directly or in relation to theoretical proposals for SSH.

3.2 Fourier Power Spectral Analysis

3.2.1 Global Scale

The global averaged spectra of U_{10} (blue curves) and Hs (red curves) are shown in Figure 3.1. The dotted and solid curves indicate the raw and alias-filtered spectra, respectively. The straight lines are given as references with different slopes. In the high wavenumber range, due to the existence of spectral aliasing, the raw spectra exhibit upward trend, mainly visible for U_{10} . After applying the alias-filtered processes, the tails are downward recovered. In the wavenumber ranging from 1×10^{-3} to $1 \times 10^{-2} \text{ km}^{-1}$, corresponding to the spatial scales (r) from 100 to 1000 km, the scaling exponent β for Hs is close to 2, as shown in Figure 3.1. For wavenumbers smaller than $1 \times 10^{-3} \text{ km}^{-1}$ ($r \geq 1000 \text{ km}$), β for Hs approaches 3. As for the wavenumbers higher than $1 \times 10^{-2} \text{ km}^{-1}$ ($r \leq 100 \text{ km}$), the spectrum of Hs illustrates a conspicuous decreasing trend in the spatial scales from 30 to 100 km, then small fluctuations occur along the spectrum. The spectrum of U_{10} also exhibits power-law features in the range from 100 to 3000 km, and the values of β are between $5/3$ and 3 with small variations. A finer inspection shows that in the range from 100 km to 250 km, the slopes of U_{10} spectra are close to $-5/3$. These multiscale features for U_{10} and Hs are also emphasized in the compensated spectra as insets.

The averaged spectra of zonal and meridional components of U_{10} are also calculated to tentatively test the horizontal directional isotropy of the wind field. The comparison of these two spectra is illustrated in Figure 3.2 a. The blue and red curves represent the zonal and meridional component along track spectra, respectively. These two spectra show similar scaling features, with the zonal component spectrum slightly larger than the meridional one, which has been previously reported by Freilich and Chelton (1986). In order to better compare these two spectra, we introduce their ratio as:

$$I(k_y) = \frac{E_v(k_y)}{E_u(k_y)}, \quad (3.5)$$

where k_y is the wavenumber parallel to the velocity component v . This ratio is displayed

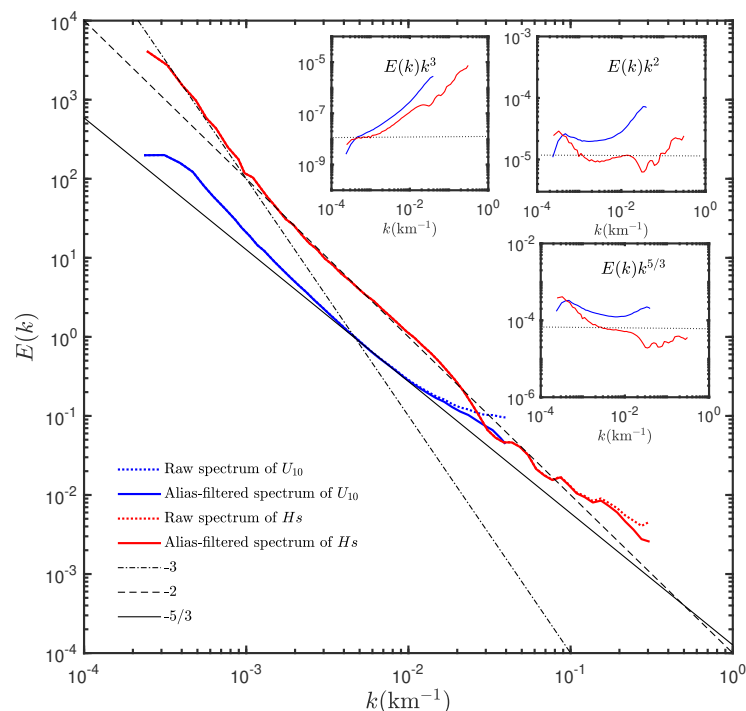


Figure 3.1 The global averaged Fourier power spectra of U_{10} (blue curves) and H_s (red curves), the dotted and solid line styles mean the raw spectra and the spectra after alias-filtered. The black dash-dotted, dashed, and thin lines are given as references with the slopes of -3 , -2 , and $-5/3$. The insets show the corresponding compensated spectra.

in Figure 3.2 b. The inset in log-log plot shows a horizontal line, confirming that zonal and meridional spectra have the same scaling exponent, from 100 to 3000 km. In turbulence, such ratio is called the isotropy ratio and for $5/3$ spectra, in the case of isotropy, the value $I(k_x) = 3/4$ is derived, using symmetry arguments, from the continuity equation (Kolmogorov, 1941b; Monin and Yaglom, 1971).

3.2.2 Co-Spectral Analysis

To identify the relation between U_{10} and H_s , the co-spectrum is normalized with the 1D spectra for U_{10} and H_s to get the coherency spectrum (Bendat and Piersol, 2011),

$$H_{U_{10}-H_s}(\mathbf{k}) = \frac{|E_{U_{10},H_s}(\mathbf{k})|^2}{E_{U_{10}}(\mathbf{k})E_{H_s}(\mathbf{k})}, \quad (3.6)$$

where $0 \leq H_{U_{10}-H_s}(\mathbf{k}) \leq 1$. When the value of coherence function value is equal to 1, there is a perfect linear relationship between the two signals. When the value is 0, then

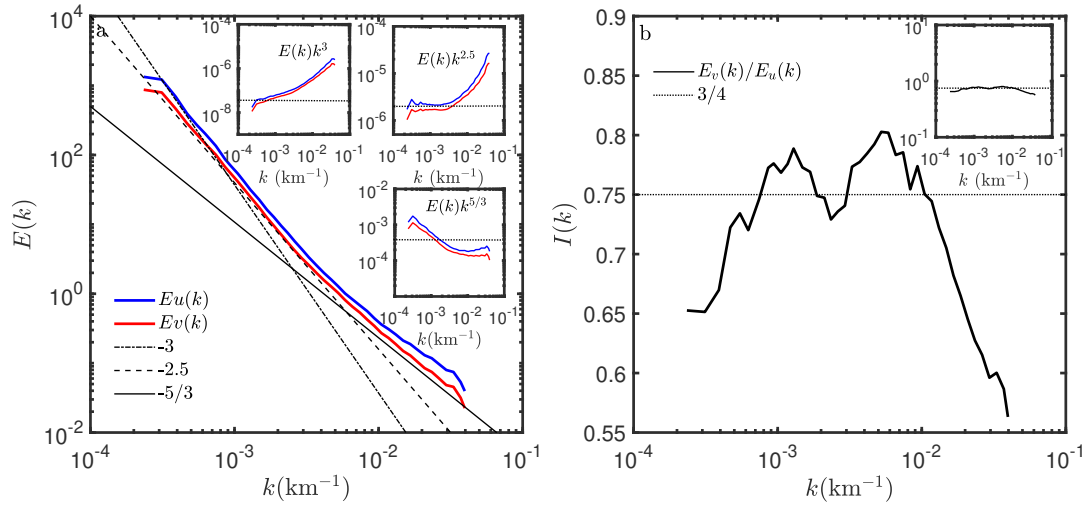


Figure 3.2 (a) The global averaged Fourier power spectra of zonal (blue curve) and meridional (red curve) components of U_{10} ; the black lines are references. The insets show the corresponding compensated spectra. (b) The corresponding isotropy ratio function; the dashed black line indicates the theoretical value $3/4$ expected in the case of isotropy (Kolmogorov, 1941b); the inset is in log-log plot.

there is no relationship between the two signals (Formenti, 1999).

The co-spectrum $E_{co}(k) = E_{U_{10}, Hs}(k)$ for U_{10} and Hs is estimated and illustrated in Figure 3.3 a. Power-law features can be found in the corresponding spatial ranges from 30-250 km and 250-2000 km with the scaling exponents equal to 1.8 and 2.4, respectively. The compensated spectra as inset confirm the scaling features. The coherence function $H_{U_{10}-Hs}(k)$ between U_{10} and Hs is also estimated and shown in Figure 3.3 b, where a log-log plot is shown as inset. The values of the coherence function lie between 0.04 and 0.13 in the whole wavenumber domain, with a peak value occurring in the separation scale around 1200 km.

3.2.3 Basin Scale

In order to perform more analyses on smaller portions of the globe, the world ocean is separated into five regions: the Indian Ocean, the North Atlantic Ocean, the South Atlantic Ocean, the North Pacific Ocean, and the South Pacific Ocean (see Figure 3.4). This provides scaling characteristics of U_{10} and Hs spectra in different oceanic areas. The measured ensemble averaged Fourier power spectra are shown in Figure 3.5 a (U_{10}) and Figure 3.5 b (Hs). The spectra measured from different ocean basins have all the same shape and share the same scaling properties.

The spectra of U_{10} display a very clear scaling with exponents close to 2, for scales

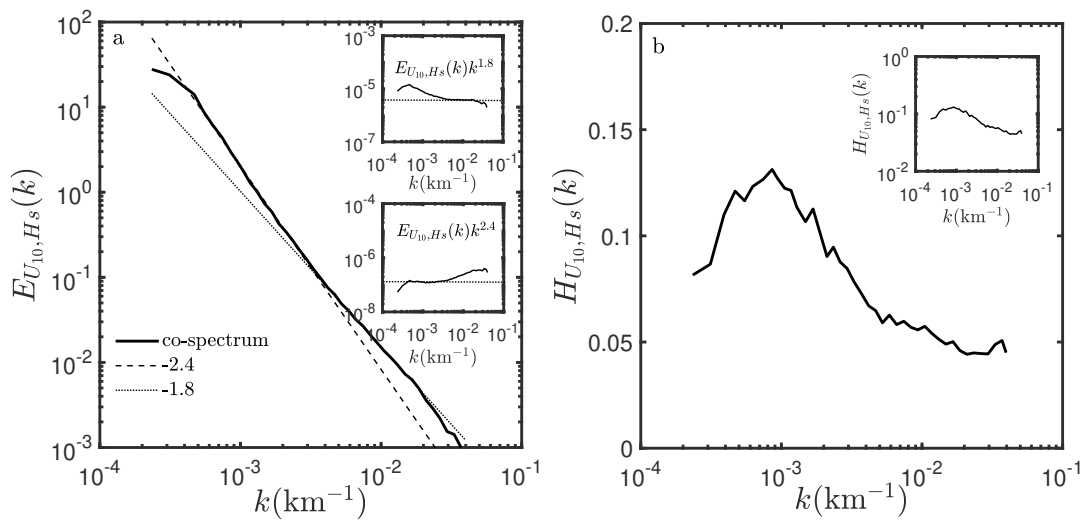


Figure 3.3 (a) Global averaged cross-spectrum of U_{10} and H_s . The insets show the corresponding compensated spectra. (b) The coherence function between U_{10} and H_s in the semi-log coordinate; the inset is in log-log plot.

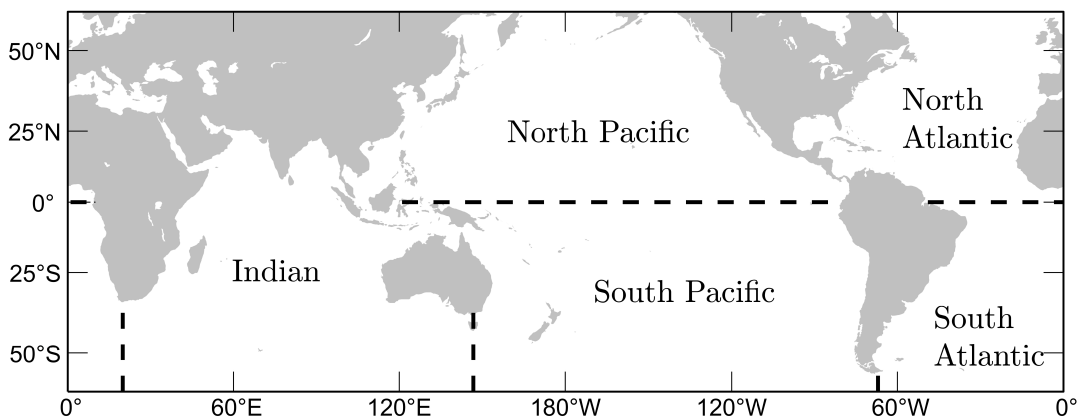


Figure 3.4 Roughly separation of the global ocean into five basins, the dashed lines are the boundaries.

from 25 to 2500 km, for all basins. Concerning H_s , the scaling exponents β are close to 3, and 2 for the ranges from 500 to 3000 km and 50 to 500 km, respectively. The compensated spectra are also given in Figure 3.5 to emphasize the scaling feature.

3.2.4 Mesoscale

In the above analysis, the whole basin as a unit was considered to calculate the spectra of U_{10} and H_s . The results were nearly identical for different ocean basins. In order to better characterize the dynamical features of U_{10} and H_s in different oceanic regions,

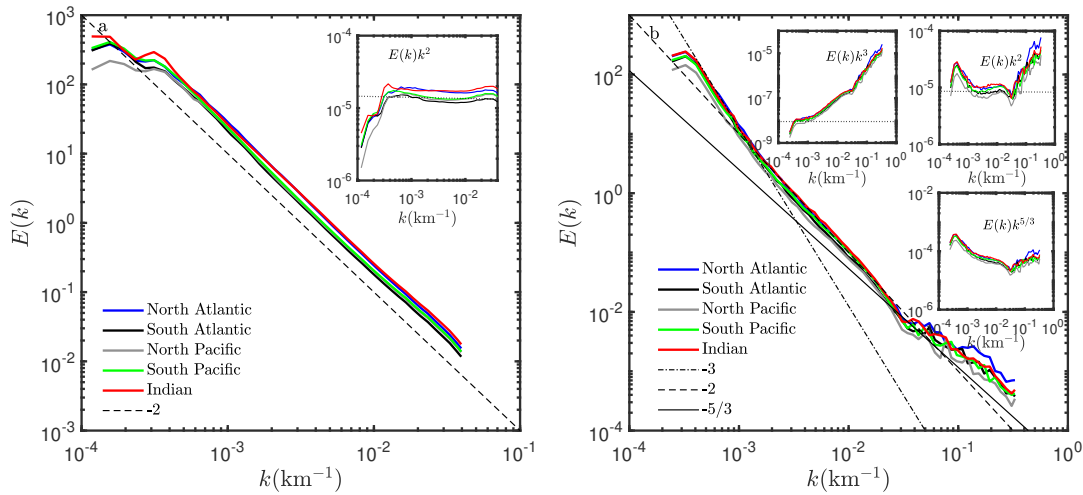


Figure 3.5 The ensemble-averaged Fourier power spectra of the U_{10} (a) and H_s (b) in different oceanic basins; the black dash-dotted, dashed, and thin lines are given as references. The insets show the corresponding compensated spectra.

datasets of finer scale are used to measure the power spectra.

For U_{10} , the data were separated into 84×84 boxes for each orbit, each one being approximately a square area with a spatial scale of about $1000 \text{ km} \times 1000 \text{ km}$. Figure 3.6 gives an example of a 2D domain, in which the selected subset is shown as gray dots. The radially averaged Fourier power spectrum is then estimated by the aforementioned algorithm for the U_{10} magnitude. For comparison, another approach to derive the scaling features for U_{10} with the scales below 1000 km is to consider the 1D U_{10} data along the satellite track (red dots in Figure 3.6 a). The global averaged Fourier power spectra for the subsets of U_{10} in 1D (along the track) and 2D (spatial zone) are illustrated in Figure 3.6 b. Scaling features are found for both spectra on the scale range of $100\text{-}1000 \text{ km}$ with a scaling exponent close to a value of 2, see the compensated curves in the insets.

Concerning H_s , 700 along-track data points (which form a total of nearly 1000 km) are selected as a whole to calculate the spectrum at smaller scales. In this way, the lowest wavenumber of spectra is around $1 \times 10^{-3} \text{ km}^{-1}$. In order to increase the number of measurements to cover the global ocean, the selected data are overlapped 75% along the satellite track. Figure 3.7 illustrates the global averaged Fourier power spectrum for the H_s case. A scaling feature is distinguished in the range of $10\text{-}1000 \text{ km}$, again with a scaling exponent close to a value of 2.

The global distributions of scaling exponents for U_{10} and H_s are derived by averaging the scaling exponents which are located on the same $2^\circ \times 2^\circ$ grid. This is done for the scale ranges chosen for each field (e.g., $100\text{-}1000 \text{ km}$ for U_{10} , and $10\text{-}1000 \text{ km}$ for H_s).

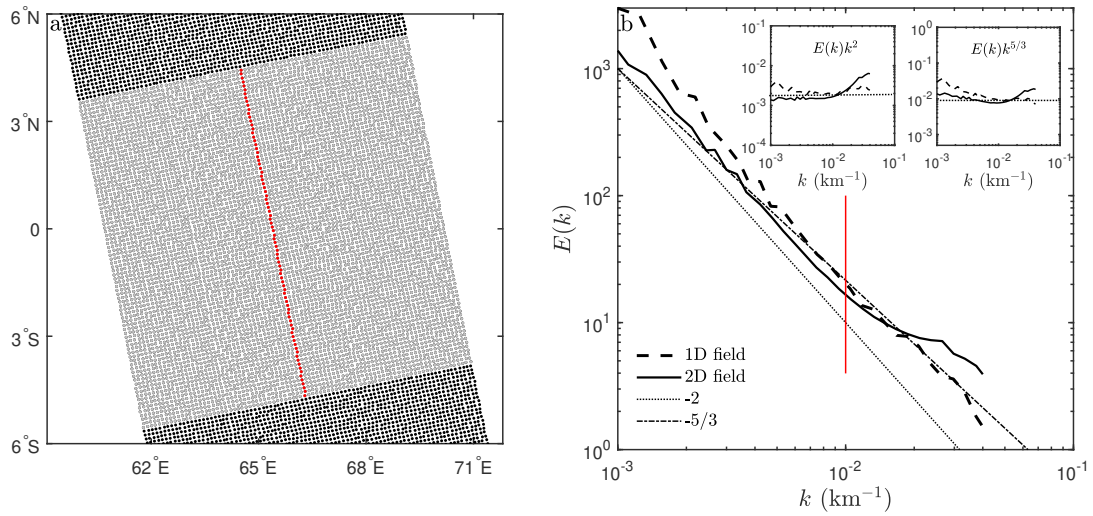


Figure 3.6 (a) An example of the selected 84×84 2D domain of U_{10} (gray dots); the line formed by red dots indicates the 1D field along the track of the satellite. (b) The global averaged Fourier power spectra were measured from the 1D (dashed curve) and 2D (solid curve) U_{10} subsets. The dotted line and dash-dot line are given as references with slopes equal to -2 and $-5/3$, respectively. The insets are the corresponding compensated spectra. The red line in (b) indicates the separation scale of the spectra, to emphasize the chosen scale, 100-1000 km.

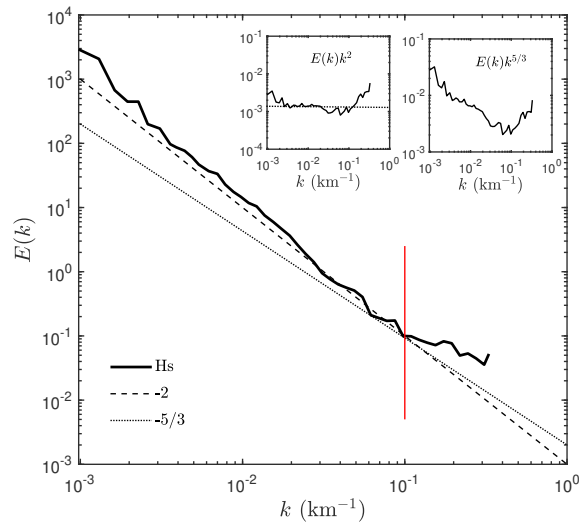


Figure 3.7 The global averaged Fourier power spectrum measured from the subsets of H_s ; the dashed and dotted lines are given as references with slopes of -2 and $-5/3$. The insets are the corresponding compensated spectra. The red line indicates the separation scale of the spectrum to emphasize the chosen range, 10-1000 km.

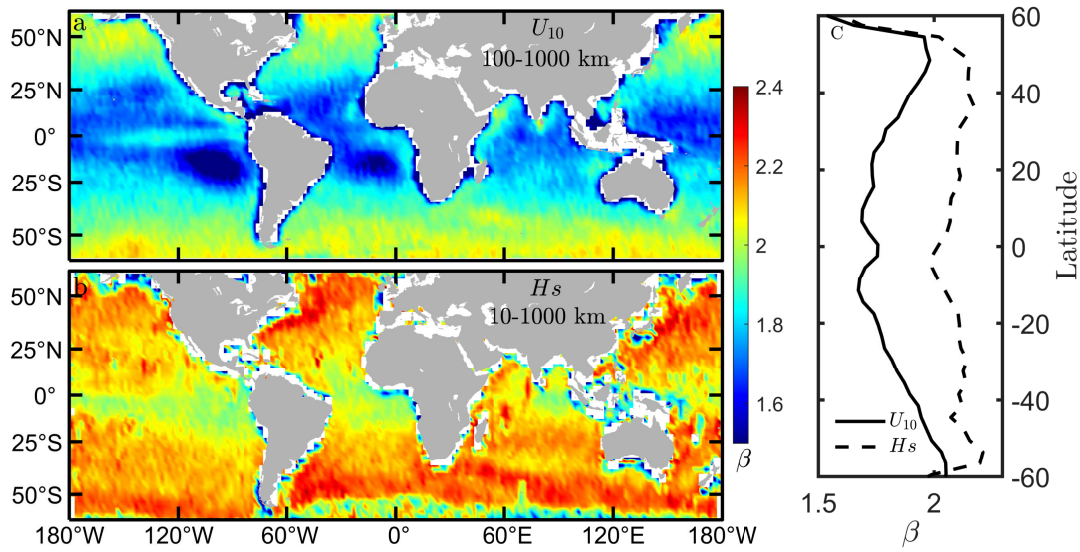


Figure 3.8 The global distribution of the scaling exponents β measured from (a) U_{10} (100-1000 km) and (b) H_s data (10-1000 km). (c) The meridional variations of β inside the Pacific Ocean. The solid and dashed curves indicate β measured from U_{10} and H_s , respectively.

The results are illustrated in Figure 3.8 respectively (a) for U_{10} and (b) for H_s . The scaling exponents for U_{10} and H_s both exhibit clear latitudinal dependence. Distinct boundaries which separate the scaling exponents whose values are larger or smaller than 1.8 are found around the horse latitudes (30 degrees north and south of the equator) for U_{10} . Moreover, a small portion with large scaling exponents is found near the equatorial eastern Pacific (e.g., roughly 90°W to 160°W and 10°S to 10°N), which coincidentally is in the same region as the famous Pacific equatorial dry zone (Hastenrath, 1999). For the nearby regions, such as the Intertropical Convergence Zone (ITCZ), equatorial Pacific Warm Pool (PWP), and South Atlantic Convergence Zone (SACZ), the scaling exponents for U_{10} are close to 5/3. For H_s , the scaling exponents are larger than the ones derived from U_{10} for most regions, the meridional variations are relatively weak as compared to the U_{10} case. Overall the global ocean, β for H_s is larger than 2.1 except for the coastal areas. Again, relatively small β is found in tropical regions.

To quantify the meridional variation of β , a region inside the Pacific Ocean is chosen (150°E to 100°W, 60°S to 60°N) to perform a meridional average of β . Figure 3.8 c illustrates the measured meridional variations of β for U_{10} (solid curve) and H_s (dashed curve). The variation trends of β for U_{10} and H_s are similar, the maximums occur in mid-latitudes, with small values in tropical regions. Averaged β derived from U_{10} and H_s are mainly in between 1.6 – 2.2 and 1.8 – 2.3, respectively. A crest value can be found near

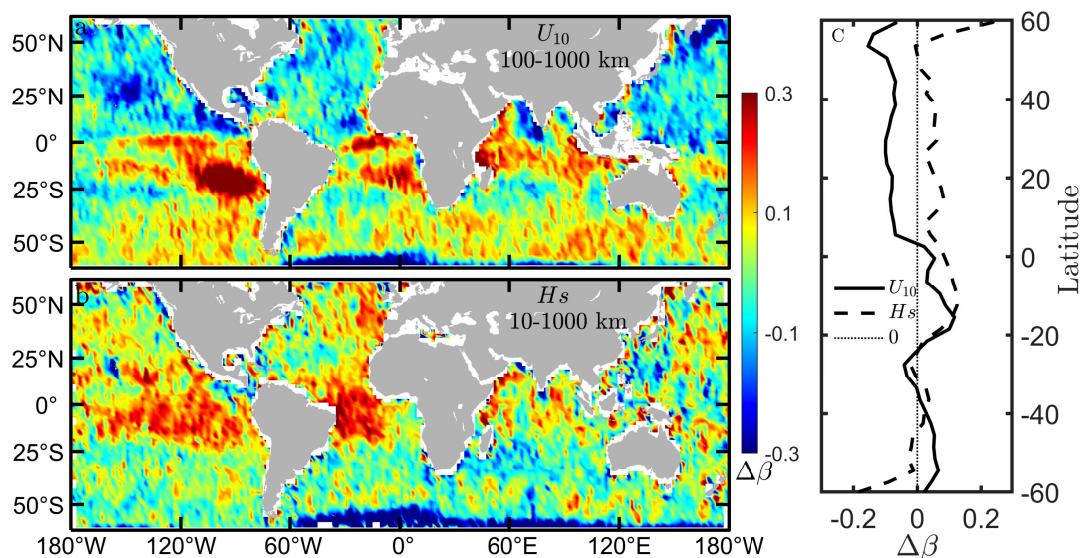


Figure 3.9 The global distribution of $\Delta\beta = \beta_s - \beta_w$, where β_s is the summer (June, July, and August) scaling exponent and β_w is the winter (December, January, and February) scaling exponent, for (a) U_{10} in the wavelength band of 100-1000 km, and (b) H_s in the wavelength band of 10-1000 km. (c) The meridional variations of $\Delta\beta$ inside the Pacific Ocean. The solid and dashed curves indicate $\Delta\beta$ measured from U_{10} and H_s , respectively.

the equator for U_{10} case, which corresponds to the Pacific equatorial dry zone mentioned above.

Finally, we focus on the seasonal changes of these scaling parameters. For this, the difference $\Delta\beta = \beta_s - \beta_w$ is considered, where β_s is the boreal summer scaling exponent, and β_w the boreal winter one. The boreal summer is composed of the months of June, July, and August, and the boreal winter of the months of December, January, and February. The results are given in Figure 3.9. The seasonal variations of β are weaker in mid-latitudes than those observed in low-latitudes, for both U_{10} and H_s . The scaling exponents for U_{10} are larger in winter than those in summer for most areas. For H_s , the seasonal variations of β are relatively complicated. For Northern Hemisphere, β is larger in summer than those in winter for most regions; in the tropical area of the Southern Hemisphere, β for H_s is larger in winter, then for the regions further south than 25°S , the seasonal differences are found to be vague.

The above results show the global distribution of scaling exponents for 2D U_{10} subsets, while as we illustrated in Figure 3.6, the spectra of wind data also can be estimated along the one-dimensional direction, namely along-track (red dots) or cross-track (orthogonal to the track) direction. These two directions are close to the north-south (NS) and west-east (WE) directions for most areas, except for the high-latitudes, which are not con-

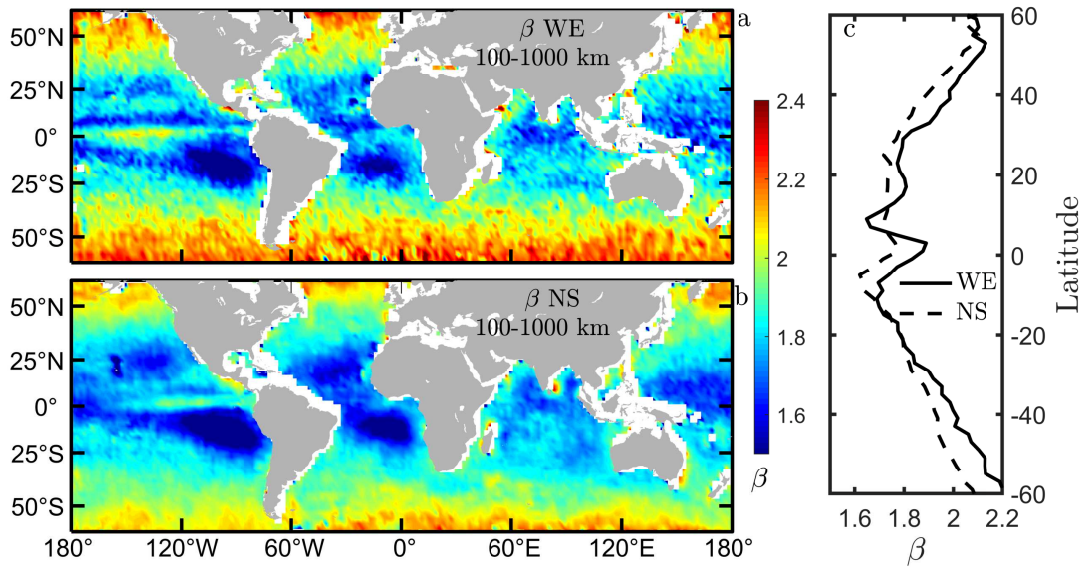


Figure 3.10 The global distribution of the scaling exponents β measured from U_{10} (100-1000 km) with (a) cross-track direction and (b) along-track direction. (c) The meridional variations of β inside the Pacific Ocean. The solid and dashed curves indicate β measured from U_{10} along cross-track and along-track directions, respectively.

sidered in our work. The averaged discrepancy between the along-track and NS direction is around 11° , and the same for the difference between the cross-track and WE directions. Thus, the along-track and cross-track measured spectra can be treated as a long NS and WE direction estimations. The global distribution of extracted scaling exponents for 1D U_{10} subsets (84 data points for each realization, and fitted in the ranges 100-1000 km for the spectra) along these two directions are shown in Figure 3.10. In which, Figure 3.10 a and b indicate the scaling exponents measured with cross-track and along-track directions, respectively. The meridional variations are shown in Figure 3.10 c with longitudinal averages. Similar patterns are found for these two different estimations. However, the result got from the cross-track measurements are more varied than the one from the along-track one. This may imply that the multiscale interactions of ocean surface wind field are nearly isotropic in the scales from 100-1000 km.

3.3 Structure-Function Analysis

This part of this chapter was not published in Gao et al. (2021); these results are presented in a manuscript in preparation: Gao, Y, Schmitt FG, Hu JY, and Huang YX (2022), “Structure-Function Analysis of CFOSAT Observed Wind and Waves” (in prep.).

As a supplementary to the spectral analysis, here the structure-function analysis is chosen for comparison with the above-illustrated results. The 84×84 2D U_{10} domain, and Hs subsets which contains 700 data points for each are used in this section.

3.3.1 Second-order Structure-Function Analysis

The ensemble-averaged second-order structure-function for U_{10} and Hs are shown in Figure 3.11. The experimental functions are close to the reference line with the scaling exponent of 1, which means that the corresponding Hurst number $H=1/2$. In this sense, the ocean surface atmospheric movement and the surface waves can be treated as Brownian motions. Note that, this concept has been accepted and used to construct climate models to describe the atmospheric multiscale nonlinear dynamics. For example, Hasselmann (1976) introduced the general idea of stochastic climate models based on the Brownian motion analog, the red spectra of oceanic fluctuations are hence a consequence of the amplification of low-frequency weather fluctuations.

The power-law ranges for U_{10} and Hs are found in 50-500 km and 10-1000 km, respectively. Thus, the detected scaling ranges for Hs with structure-function analysis are the same as the ones found using spectral analysis (see Figure 3.7), while the power-law ranges for U_{10} are relatively narrower in the structure-function plots than the ones shown in the spectral analysis (see Figure 3.6). A finer check for the averaged spectral and second-order structure functions for U_{10} and Hs shows that the isotropic turbulence prediction of the scaling exponents $\zeta(2) = \beta - 1$ is roughly satisfied in our study.

The global distribution and seasonal differences for $\zeta(2)$ measured from U_{10} are shown in Figure 3.12. The distribution pattern is similar to the one for β extracted from U_{10} , see Figure 3.13. In the comparisons, meridional variations are found with larger $\zeta(2)$ in mid-latitudes and smaller ones near tropical regions. The seasonal differences for $\zeta(2)$ are clear, measured $\zeta(2)$ are larger in the winter time than the ones in summer, keeping the same variation features as we found for β . The relation between β and $\zeta(2)$ is further studied in the joint probability density functions, see the colored map in Figure 3.14. A linear distribution trend is found, with a slight discrepancy with the theoretical prediction $\zeta(2) = \beta - 1$ (red dashed line).

Here the second-order structure-function for U_{10} also can be measured in along-track and cross-track directions as we performed the spectral analysis for 1D U_{10} subsets. The results for the global distribution of $\zeta(2)$ corresponding to cross-track and along-track directions are shown in Figure 3.15 a and b, respectively. The meridional variations are given in the right panel with solid and dashed curves in Figure 3.15 c. The fitting range for

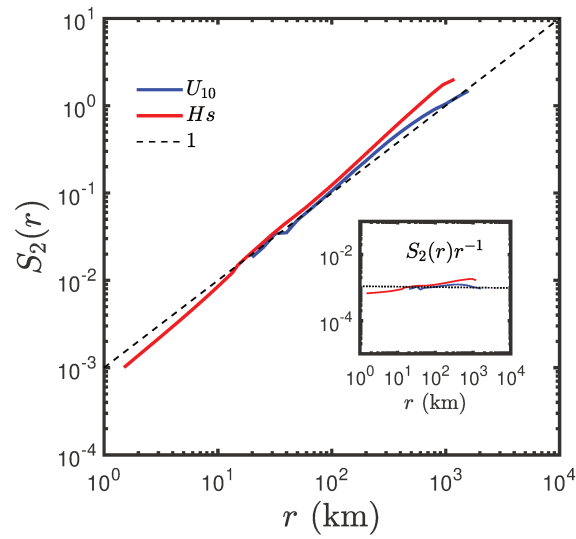


Figure 3.11 (a) The ensemble-averaged second-order structures for U_{10} (red curve) in 84×84 2D domains and H_s subsets (blue curve). The inset shows the corresponding compensated function values.

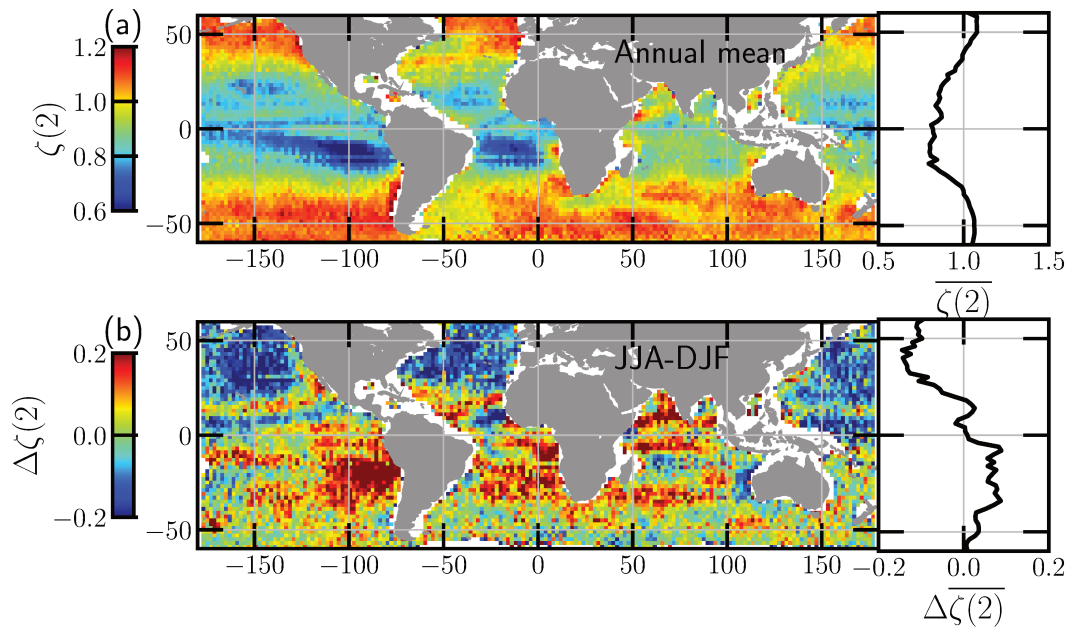


Figure 3.12 The global distribution of the (a) annually averaged scaling exponents $\zeta(2)$, and (b) the seasonal differences for U_{10} . The meridional variations are given in the right panels.

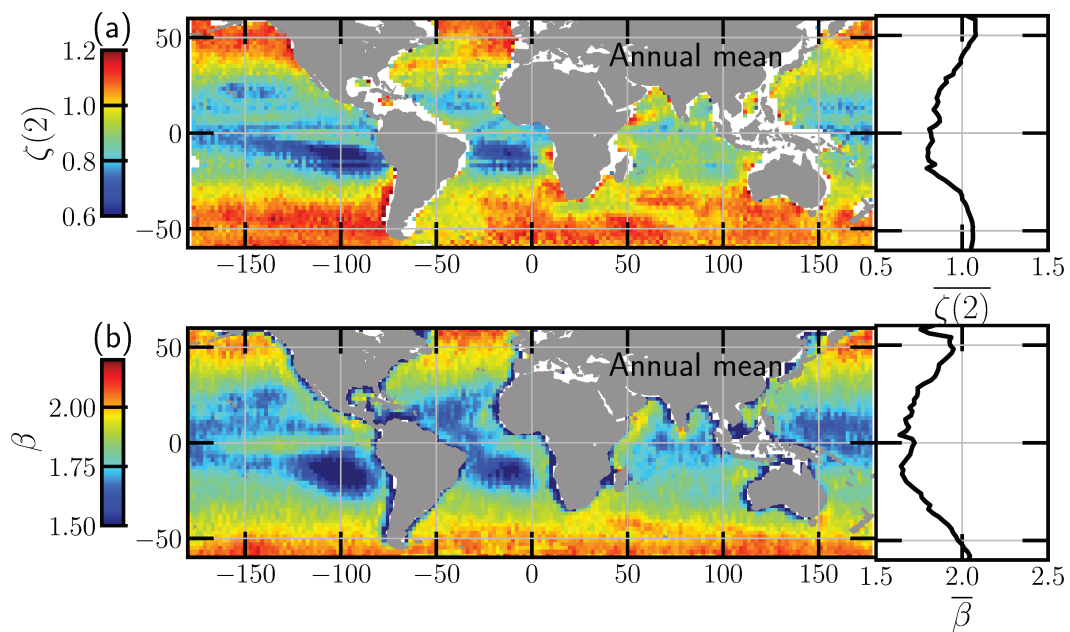


Figure 3.13 The global distribution of the annually averaged scaling exponents (a) $\zeta(2)$ measured from U_{10} (50-500 km) in the structure-function analysis, and (b) β from U_{10} (100-1000 km) in the spectral analysis. The meridional variations are given in the right panels.

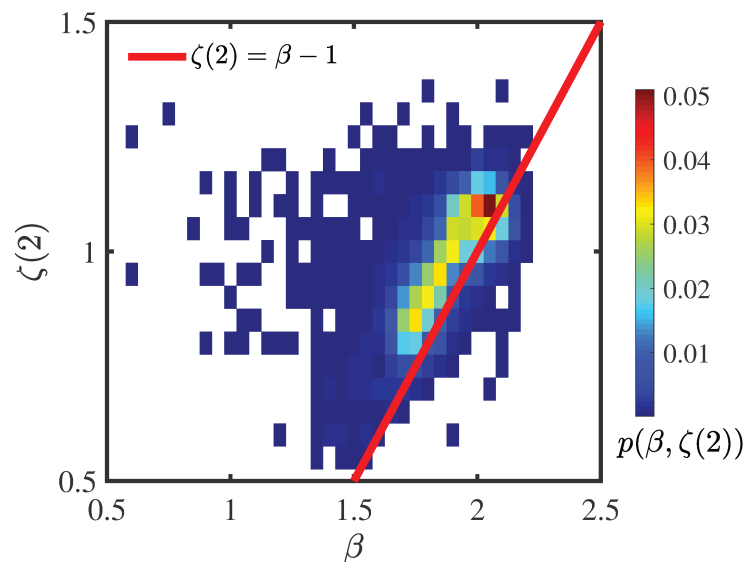


Figure 3.14 Measured joint probability density functions for β and $\zeta(2)$, the red dashed line is the theoretical prediction of the relation between β and $\zeta(2)$.

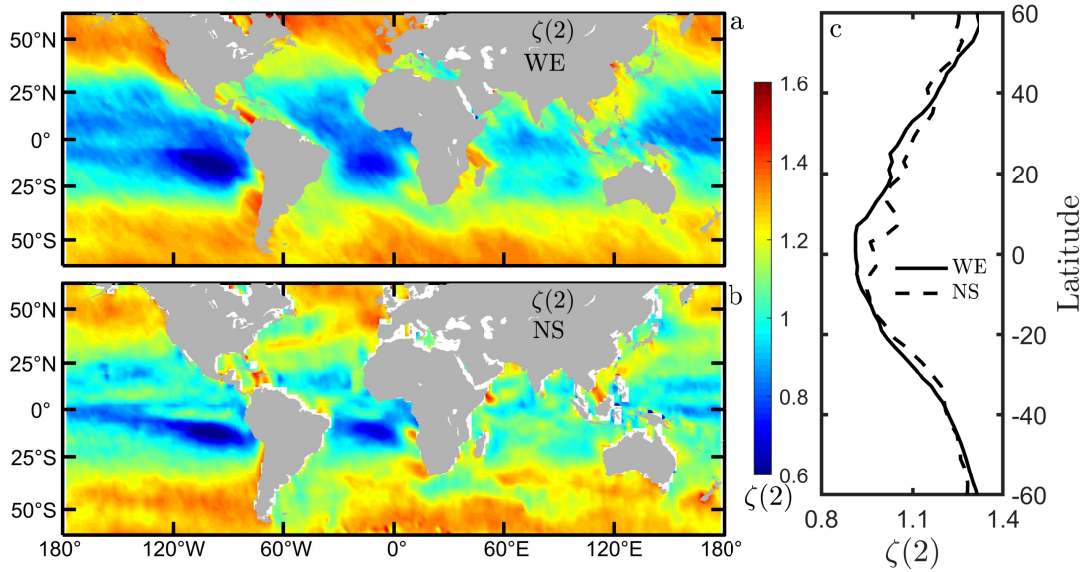


Figure 3.15 The global distribution of the scaling exponents $\zeta(2)$ measured from U_{10} (50-500 km) with (a) cross-track direction and (b) along-track direction. (c) The meridional variations of $\zeta(2)$ inside the Pacific Ocean. The solid and dashed curves indicate $\zeta(2)$ measured from U_{10} along cross-track and along-track directions, respectively.

the second-order structure-function is fixed at 50-500 km. The distribution patterns and the meridional variations are all similar.

Combining with the results in Figure 3.10, the joint PDFs for β and $\zeta(2)$ estimated in cross-track and along-track directions are shown in Figure 3.16 a, and b, respectively. The distribution of maximums for the PDF are all close to the theoretical prediction as shown with the red dashed line.

After we show the structure-function analysis for U_{10} , the global distribution and seasonal differences of $\zeta(2)$ estimated from Hs subsets are shown in Figure 3.17a and c. The longitudinal average of $\zeta(2)$ and $\Delta\zeta(2)$ are illustrated in the right panels. The meridional variation of $\zeta(2)$ is found, with large values in mid-latitudes and small ones in low-latitudes. For most regions, $\zeta(2)$ is larger in winter than in summer. The spatial and temporal variations of $\zeta(2)$ for Hs are close to the ones for β .

3.3.2 High-order Structure-Function Analysis

The high-order structure-function analysis is also performed to study the intermittency features for U_{10} and Hs . The ensemble-averaged structure-function for CFOSAT along-track U_{10} and Hs with the orders from 0 to 4 are shown in Figure 3.18 a and b, re-

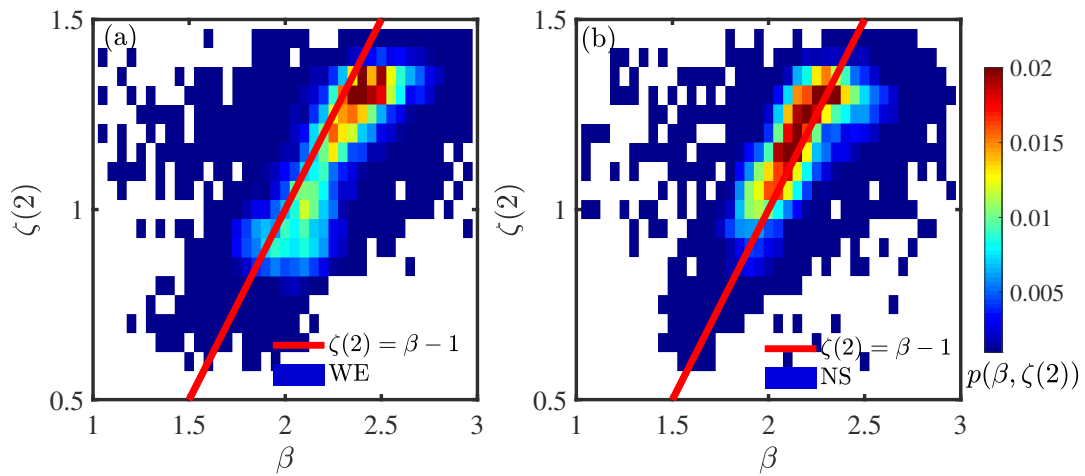


Figure 3.16 Measured joint PDFs for β and $\zeta(2)$ for 1D U_{10} subsets in (a) cross-track and (b) along-track directions. The red dashed line is the theoretical prediction of the relation between β and $\zeta(2)$.

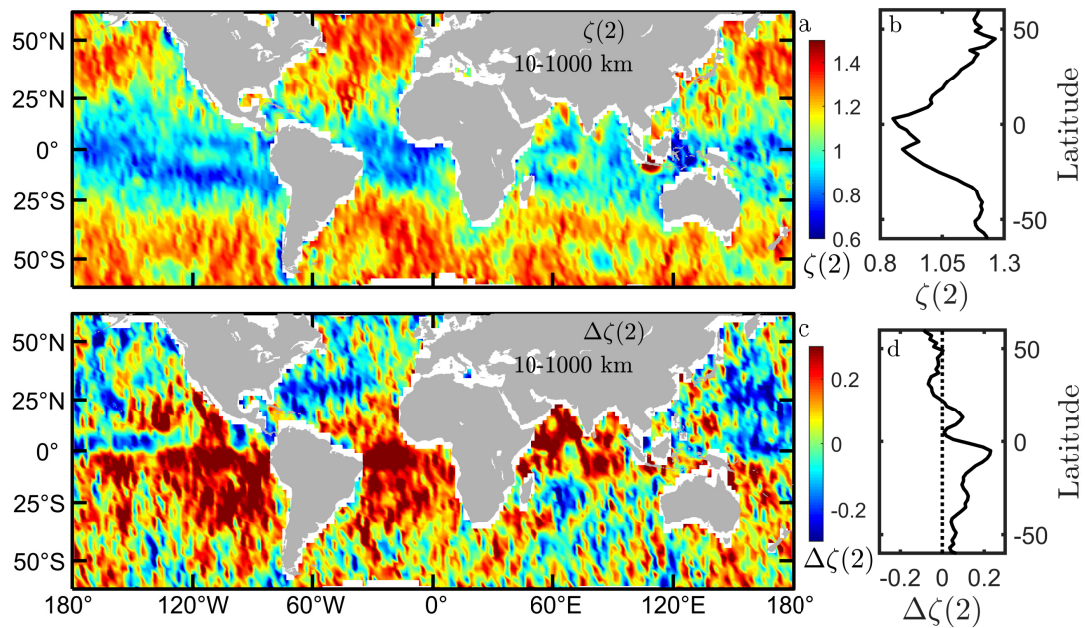


Figure 3.17 The global distribution of the (a) annually averaged scaling exponents $\zeta(2)$, and (c) the seasonal differences of the scaling exponents $\zeta(2)$ for H_s . The meridional variations are given in the right panels.

spectively. Neat power-law features are found from 12.5 km to 1000 km for U_{10} , while for H_s , two power-law ranges are found, e.g., 2-30 km and 100-1000 km.

The extracted scaling exponents are illustrated in the right two panels. For U_{10} case, a linear distribution feature for $\zeta(q)$ is found, see Figure 3.18 b, but different from Kolmogorov's prediction, namely $\zeta(q) = q/3$. The best fitting of the scaling exponents for U_{10} is $\zeta(q) = 0.55q$ here. Measured $\zeta(q)$ is also normalized $\zeta(q)$ with $\zeta(3)$, as shown in the inset, the result is overlapped with $q/3$. The linear trends of $\zeta(q)$ and $\zeta(q)/\zeta(3)$ (known as Extended-Self-Similarity, ESS) indicate that the ocean surface wind can be treated as non-intermittent in the ranges of 100-1000 km. While for H_s , $\zeta(q)$ and the ESS curves both are convex, which means that H_s are intermittent in the ranges from 2-30 km and 100-1000 km. The scaling exponents for H_s extracted from these two ranges are close to each other below the second order. Discrepancies are found in the ranges of $q > 2$. Here a modified lognormal model proposed by Li and Huang (2014) is used to fit the scaling exponents for H_s in the larger ranges. This model is defined as below,

$$\zeta(q) = qH - \frac{\mu}{2}(q^2H^2 - qH), \quad (3.7)$$

where H is the Hurst number, and μ is the intermittency parameter, which can be used to characterize the deviation from the linear relation of qH . In other words, the larger μ , the more intermittent the system (Kolmogorov, 1962; Frisch, 1995; Schmitt and Huang, 2016). Here the measured $H = 0.6$, and $\mu = 0.3$. The scaling exponents for H_s in the large scales show good agreement with this model for all the orders, while for $\zeta(q)$ in the small scales, the model can only cover orders below 2.

3.4 Discussion

3.4.1 Wind Data

In this work, different scaling laws have been found for the wind velocity data set. First, the global averaged Fourier power spectrum for CFOSAT observed U_{10} shows power-law features from 100 to 3000 km where β varies from 5/3 to 2.5. Figure 3.2 a displaying the global averaged Fourier spectra of zonal and meridional components of the wind field, shows that horizontally the wind field is roughly directionally isotropic since the two curves follow the same laws as indicated by the insets. The scaling exponents are close to -2.5 for scales from 300 to 3000 km, and close to $-5/3$ for smaller scales, from

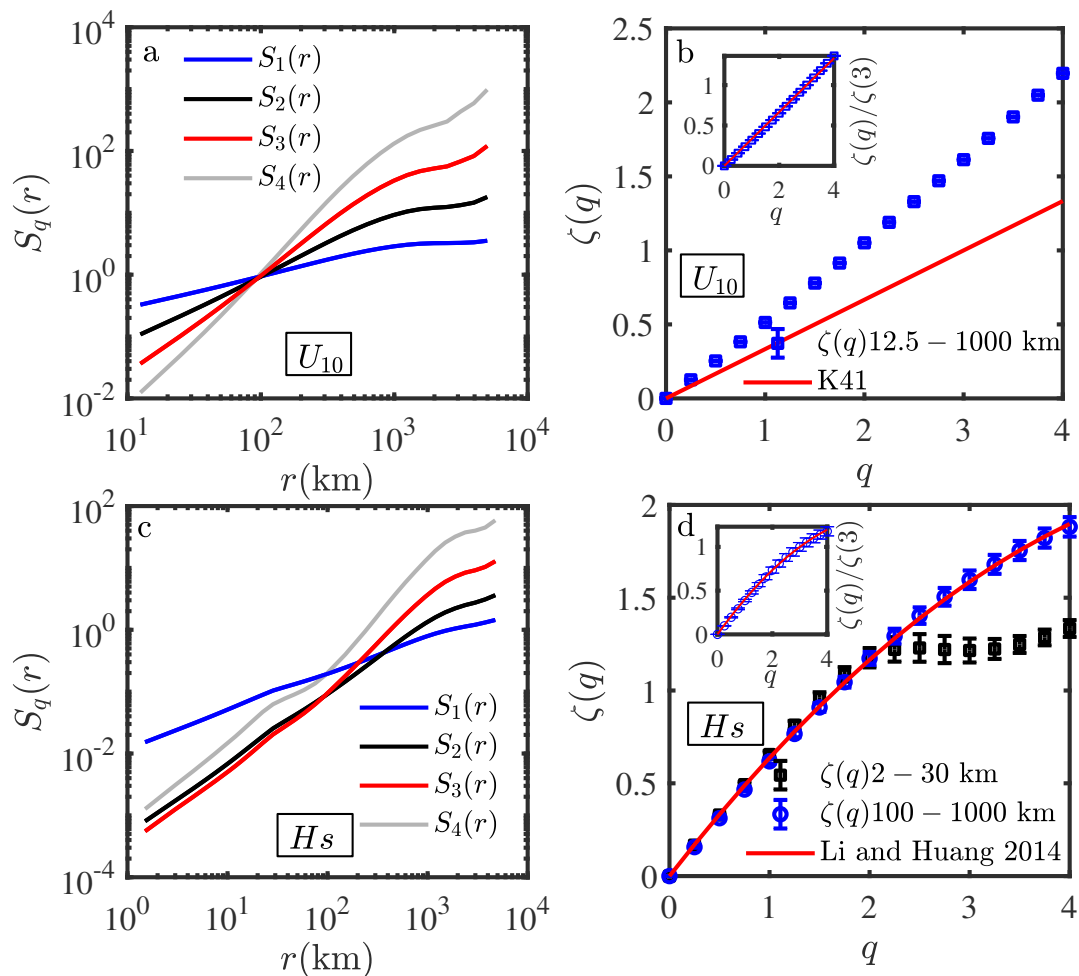


Figure 3.18 The global averaged structure-function for (a) U_{10} and (c) H_s , the blue, black, red, and gray curves are the first-, second-, third-, and fourth-order structure-functions, respectively. (b) and (d) are the corresponding exponents $\zeta(q)$ at various statistical moments q . The red line in (b) is Kolmogorov's prediction of $\zeta(q) = q/3$; the red curve in (d) is the fitting by the modified lognormal model proposed by Li and Huang (2014). The insets are the normalized $\zeta(q)$.

30 to 300 km, corresponding roughly to the mesoscale.

The fact that the meridional spectrum is slightly below the zonal spectrum is due to symmetry reasons. Indeed, this ratio is $3/4$ for $5/3$ isotropic turbulence, and it is a constant of the form $I(k) = 2/(1 + \beta)$ for isotropic turbulence with spectral slope β Monin and Yaglom (1971). This ratio is displayed in Figure 3.2 b: it is close to $3/4$ for some range of scales for which there is no $5/3$ spectrum. Hence, the value found here is not proof of horizontal symmetry, since, for the scales for which an approximate $5/3$ slope is found (the larger wave numbers), the ratio is decreasing. This may be due to the fact that these spectra are not perfectly scaling. However, this ratio in log-log plot (inset of Figure 3.2 b)

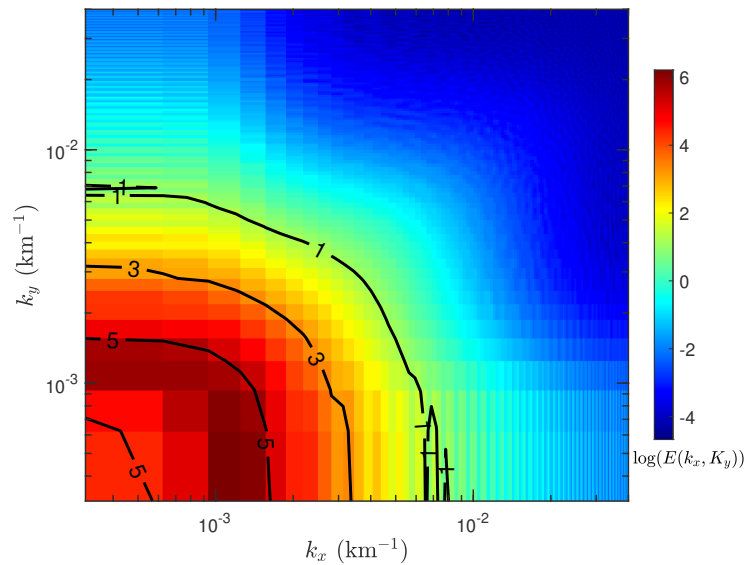


Figure 3.19 Two-dimensional spectrum of wind speed versus the longitudinal wavenumber k_x and latitudinal one k_y . The solid lines are the contour levels.

still shows that there is no clear scaling difference between both spectra: the wind field data appear to be nearly directionally isotropic on the horizontal plane.

For further testing the horizontal isotropy, the global averaged 2D Fourier power spectrum for U_{10} is estimated and shown in Figure 3.19. In the range of 100-1500 km, the value of 2D spectrum is approximately directionally isotropic on the horizontal plane as shown by the circular contour levels. Thus, the radial average can be safely performed.

Note that previous studies have shown that the atmospheric movements could be anisotropic with different scaling exponents estimated along meridional, zonal, and vertical directions (Lovejoy et al., 2007, 2009; Pinel et al., 2014). For example, using the ECMWF reanalyses data, Lovejoy and Schertzer (2011) found horizontal anisotropy at 700 mbar, corresponding to the top of clouds. As aforementioned, the 10-meter wind field is in the marine-atmosphere boundary layer, where the horizontal directional isotropy might be restored due to the interaction with the sea surface.

Another indication of horizontal directional isotropy is found in the 2D structure-function analysis for U_{10} . Here we show the estimated 2D second-order structure functions for wind speeds in 5 selected directions: see Figure 3.20 (0° and 90° indicate latitudinal and longitudinal directions, respectively). The power-law features are identical below 1000 km for all the directions, which may yield a horizontal scaling isotropy feature for the CFOSAT observed wind field.

At the global scale, different regimes, climates, and boundary conditions are mixed. The basin-scale analysis is a way to avoid mixing signals from different zones, especially

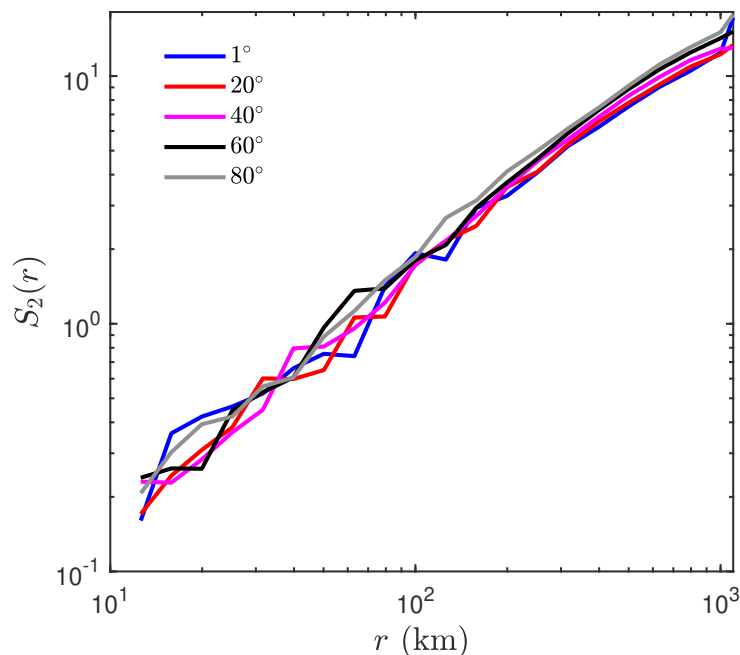


Figure 3.20 Second-order structure-functions of wind speed estimated along various directions.

tropical zone, which provides specific scaling properties. This is why the basin scale analyses show different results from the global analysis (Figure 3.1 versus Figure 3.5). Indeed at the basin scale, there is a very neat power law, from 25 to 2500 km, with a scale ratio of 2 decades, and there is no scale breaks found here. Each basin shows the same universal property, which is quite remarkable. To clarify this point, a test is performed here. A region in the Pacific Ocean (within the latitudinal region of 25°S-25°N) which contains the signal of tropical scaling feature is chosen to estimate the spectra for U_{10} . The result is shown in Figure 3.21 below. The excellent scaling is lost and breaks are found when the tropical region is also considered.

To have results at finer scales, the analysis has been performed over shorter segments, over the range from 100 to 1000 km. Globally the estimated β displays patterns emphasizing the tropical regions, and latitude dependence. This latitude dependence could best be considered in the Pacific Ocean (Figure 3.8 c), the differences in the value of β are more marked at high latitudes. Such patterns show the climatic influences on wind scaling regimes.

Globally, no scaling range with k^{-3} has been found here. It does not seem to sustain the enstrophy cascades corresponding to the quasigeostrophic theoretical framework. We find a $k^{-5/3}$ range, at mesoscales from 25 to 300 km (Figure 3.2 a), followed by an empirical fit close to the slope of -2.5 for larger scales, from 300 to 3000 km, having

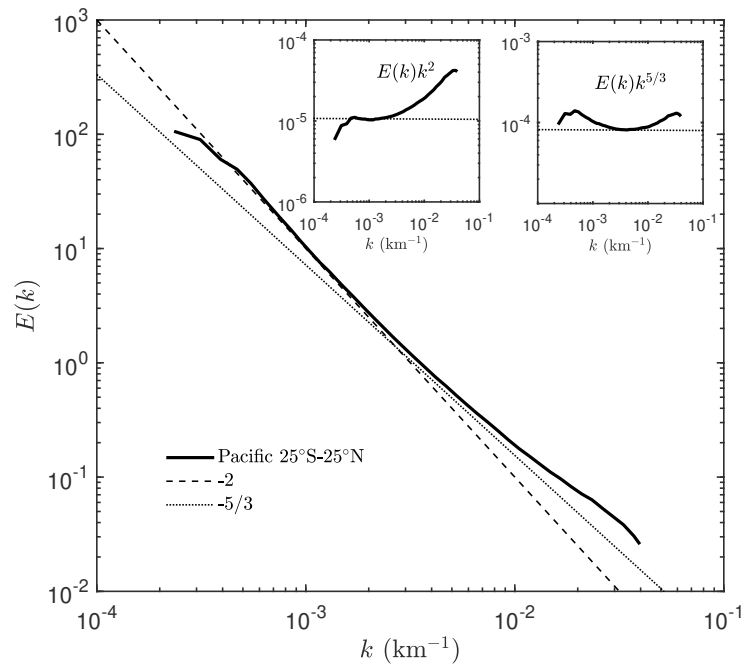


Figure 3.21 The ensemble-averaged Fourier power spectrum of U_{10} in Pacific within the latitudinal region of 25°S - 25°N , the dashed and dotted lines are given as references. The insets show the corresponding compensated spectra.

no theoretical explanation. The more detailed analyses (Figure 3.8) show that the scaling exponents are not so universal and depend on the location. Strong patterns in this figure illustrate spatial variations of scaling features associated with different types of climate. Quite often in tropical regions, the exponents are close to $5/3$, whereas they are between 1.8 and 2.2 for the other areas (see also Figure 3.8 c).

The -2 slopes that are found in the oceanic basins are in agreement with none of the theories discussed above. It was in fact already found in previous studies using satellite data. For instance, Freilich and Chelton (1986) examined the Seasat-A satellite scatterometer observed wind vector data over the Pacific Ocean, and found an energy spectrum proportional to k^{-2} in the range of 200 to 2200 km. Pinardi and Milliff (2004) found also a k^{-2} slope for the spectrum of the Mediterranean surface winds from QuikSCAT for spatial scales between 200 km and 1000 km. Chelton et al. (2006) studied the wavenumber spectra of the QuikSCAT zonal and meridional wind components and the wind speed in the North Pacific. The results show that the dependence on wavenumber k for these three variables are all approximately k^{-2} for scales below 1000 km.

We may compare our results with other previous studies. Wikle et al. (1999) considered wind data from three different sources (e.g., reanalysis of wind data from National Centers for Environmental Prediction, satellite-based ERS-1 scatterometer observed wind,

and wind from high-resolution aircraft observations). They found that the combined spectra from these data demonstrate a power-law relation over the range 1-1000 km, with a best-fit slope close to the value of $-5/3$, and the energy spectra for subsets of the data support spectral slopes of $-5/3$ and -2 . Patoux and Brown (2001) investigated the spectra of QuikSCAT observed wind vectors. They fitted the spectra on the range of 100-1000 km to derive the scaling exponents. The values of measured β were roughly between $5/3$ and 3 , with wide variations from 1.8 to 2.6. Then the spatial and seasonal variations of the spectra slopes were examined. They found that the energy spectra were steeper in midlatitudes, and all the more so in winter, also with steeper slopes in the tropics in the presence of convection. They concluded that when convection is enhanced, the energy level is raised at all scales. Consequently, the energy spectrum is steeper. The seasonal variations correspond to enhanced baroclinic activities in winter in the midlatitudes. According to our results, in the strong convection regions, e.g., ITCZ, PWP, and SACZ, the measured β in 100-1000 km scales is close to $5/3$. The corresponding spectra are flatter than the ones in nearby regions, i.e., equatorial dry zone with relatively steady atmospheric movements. Xu et al. (2011) performed a spectral analysis of QuikSCAT winds over the global ocean, and found that β possesses spatial variability in the scale range of 1000-3000 km, with values varying from 1.6 to 2.9. The slopes of spectra were observed to become steeper toward high-latitudes in the Pacific and in the South Atlantic. Besides, the spectra are steeper in winter than those in summer for most regions of the Northern Hemisphere midlatitude. This was also explained by the baroclinic argument. Furthermore, the seasonal differences which are observed in our analysis might also be related to the temporal variations of the baroclinic instability strength.

Globally, the analysis for U_{10} subsets found in the present study is relatively consistent with the results reported by Patoux and Brown (2001) and Xu et al. (2011). With the same fitting range set as Patoux and Brown (2001), we found β for U_{10} subsets varies from 1.6 to 2.2 for most regions, and β are larger in midlatitudes than those in tropics. The regions in the same latitudes but with strong convection show β close to $5/3$.

The results of second-order structure-function analysis for U_{10} confirm the scaling features obtained via Fourier power spectral analysis in the scales below 500 km. The scaling exponents $\zeta(2)$ and β show good agreement in the U_{10} analysis, except for the scaling ranges which are different. This might be induced by some large-scale structures which contaminate the structure-function.

Let us mention some limitations or specific properties of CFOSAT data used in this study. The wind speed retrieved by the SCAT sensor is typically treated as 10 meters above the sea surface. This height is close to the bottom of the marine atmospheric boundary

layer, which is often in the order of $\mathcal{O}(1)$ km (Lang et al., 2018). The 10-meter wind is thus strongly influenced by the bottom conditions, e.g., the effective roughness/wave height, temperature profiles, and the variation of the boundary layer, to name a few. Hence, it is not purely large-scale turbulence and boundary conditions may have an influence on the statistics. For the same reason, one cannot fully compare the results from this sensor to one of the altitude measurements using the commercial aircraft, such as the one obtained by Nastrom and Gage (1985) or other similar measurements done at the height $\mathcal{O}(10)$ km.

3.4.2 Wave Data

From global analysis, features for H_s are found in the ranges of 10 to 1000 km and 1000 to 3000 km with β close to 2 and 3, respectively. Some heave and roll features that occur in the spectrum range below 50 km may be the signature of energy injections induced by some energetic submesoscale processes, such as eddies and fronts or other interactions between surface currents, closely related to the upper ocean dynamics, thermodynamics, and biogeochemistry. At the basin scale, spectra for H_s in different oceanic basins are identical in the spatial ranges of 50 to 2000 km (Figure 3.5). As indicated above, there is no theory to explain such results. We may only compare these findings with previously published works. Similar studies estimating the spectra for satellite collected H_s were performed by Monaldo (1988, 1990), where 100 Geosat radar altimeter sampled H_s trajectories around the world were used to calculate the energy spectra. The scaling exponents were found to be around 1.4 in the spatial scale from several kilometers to about 50 km. Similar scaling features are observed in our study at small scales (Figure 3.1 and Figure 3.5 b) where both global and basin scale averaged spectra are shown. For the scales, less than 50 km, the scaling exponents are slightly smaller than $3/5$. Tournadre (1993) estimated the energy spectra with 583 and 689 Geosat observed H_s trajectories. The corresponding scaling exponents were derived in the range 14 to 1400 km with values equal to 1.39 and 1.21, in the North Sea and equatorial Atlantic respectively. Spatial differences are found, and values of β are larger in midlatitudes than those in tropics, which is similar to what we found in the spatial distribution of β in the scale of 10-1000 km, while in our results the slopes are steeper.

The parameter H_s is a measure of the local roughness, proportional to the small-scale variance of the wave field. This quantity shows a scale-dependent variability, with long-range correlations as revealed by the scaling regimes which have been found. Such properties of H_s are certainly inherited from the surface wave height field, for which several scaling theories have been proposed in the literature, as was discussed in a previous

section.

3.4.3 Scaling Features for Global Ocean Surface Wind via QuikSCAT

The CFOSAT mission has accumulated 3 years of global ocean surface wind data with a spatial resolution of 12.5 km. Scaling features for the CFOSAT provided wind data are illustrated in the Fourier power spectral and structure-function analyses. A global view of scaling behaviors for U_{10} was obtained with the CFOSAT observations. Then what are the scaling features for U_{10} provided by other satellite missions? Here we mainly used 10 years (from October 27, 1999, to November 21, 2009) QuikSCAT collected U_{10} to perform the same methods in the CFOSAT data analysis.

The U_{10} data collected by QuikSCAT are also with a spatial resolution of 12.5 km, while the swath of the QuikSCAT trajectory is about 1900 km (152×3248 pixels for each observation). Figure 3.22 a shows a part of the QuikSCAT land points of the trajectory. The red and black squares indicate the 2D U_{10} field composed of 152×152 ($1900 \text{ km} \times 1900 \text{ km}$) and 84×84 ($1000 \text{ km} \times 1000 \text{ km}$) observational pixels. Here the Fourier power spectra for these two domains are both estimated, the global averaged results are illustrated in Figure 3.22 b. The black and red curves are the spectra corresponding to the 84×84 and 152×152 fields, respectively. Scaling features both can be found above 100 km, with the scaling exponents close to 2 indicated by the black dashed line and also seen in the insets. The scaling features extracted from these two different sized 2D U_{10} fields are close to each other in the spatial ranges from 100 km to 1000 km, thus the 84×84 domains are still kept to do further analysis for QuikSCAT data.

The global distribution of β and the seasonal difference $\Delta\beta$ measured from QuikSCAT U_{10} are shown in Figures 3.23 a and c, respectively. The longitudinal averages, namely, the meridional variations are given in Figures 3.23 b and d. The large scaling exponents β are found in midlatitudes and in winter. These results are close to the ones we found for CFOSAT U_{10} analysis, see Figure 3.8 a and Figure 3.9 a. Since the QuikSCAT mission collected more data as compared to the CFOSAT mission, the results extracted from QuikSCAT data analysis are more smooth as compared to the ones we got from the CFOSAT data analysis.

The second-order structure-function for the 2D subsets of QuikSCAT U_{10} are also considered here: scaling features are found in the ranges from 50 to 500 km, the same as the CFOSAT case. The spatial distribution and seasonal differences for scaling exponents $\zeta(2)$ and $\Delta\zeta(2)$ are shown in Figure 3.24 a and c, respectively. These results are similar to the ones for $\zeta(2)$ and $\Delta\zeta(2)$ extracted from CFOSAT U_{10} analysis, see Figure 3.12. Again,

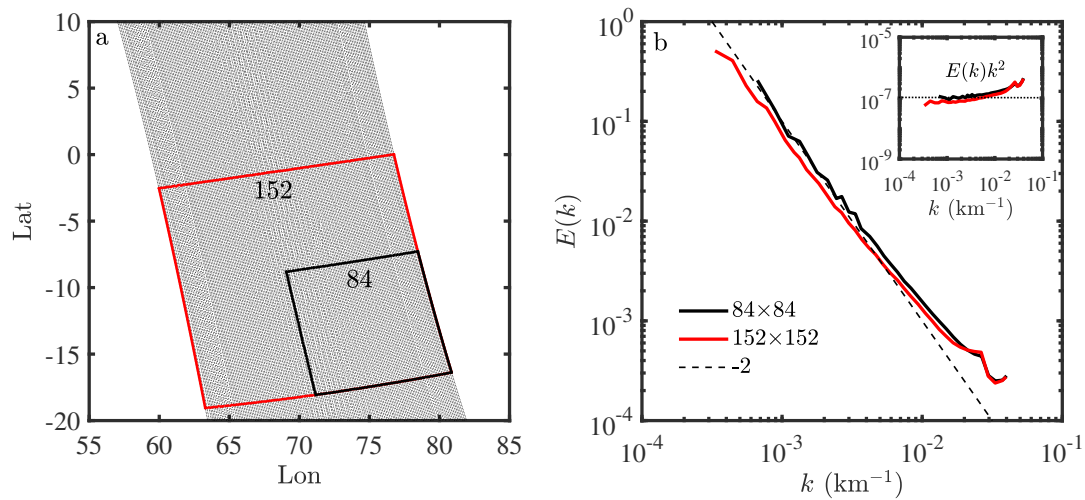


Figure 3.22 (a) An example of the selected 84×84 (black square) and 152×152 (red square) 2D domains of U_{10} ; (b) The global averaged Fourier power spectra measured from the 84×84 (black curve) and 152×152 (red curve) U_{10} subsets. The dashed line is given as references with slopes equal to -2. The inset shows the corresponding compensated spectra.

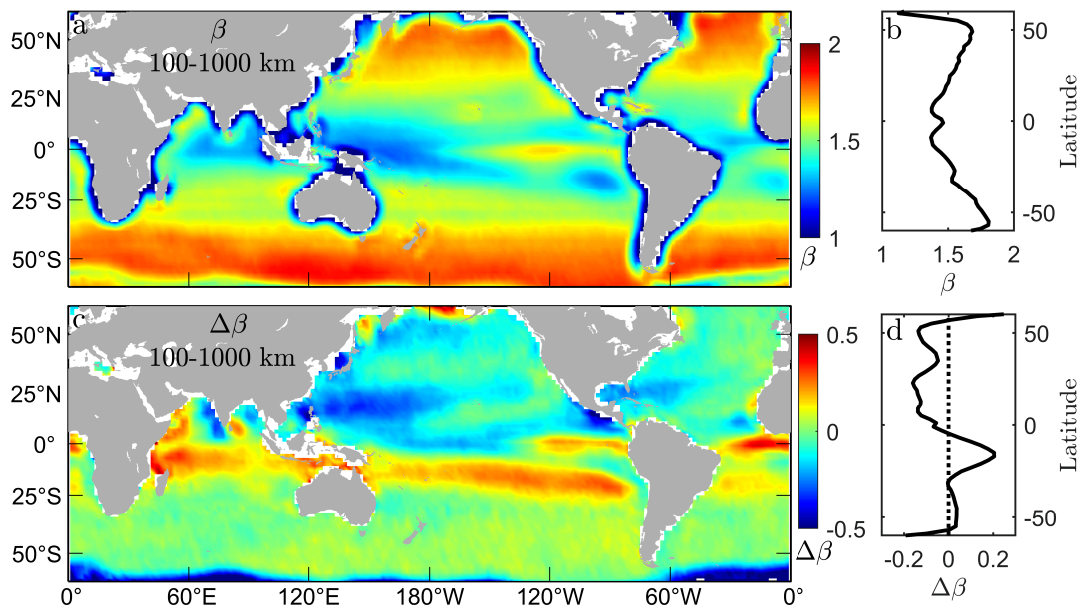


Figure 3.23 (a) The global distribution of β measured from ten-year QuikSCAT collected U_{10} (100-1000 km). (b) The meridional variations of β inside the Pacific Ocean. (c) The global distribution of $\Delta\beta = \beta_s - \beta_w$, where β_s is the summer (June, July, and August) scaling exponent and β_w is the winter (December, January, and February) scaling exponent. (d) The meridional variations of $\Delta\beta$ inside the Pacific Ocean. The dashed line indicates a reference with the value of 0.

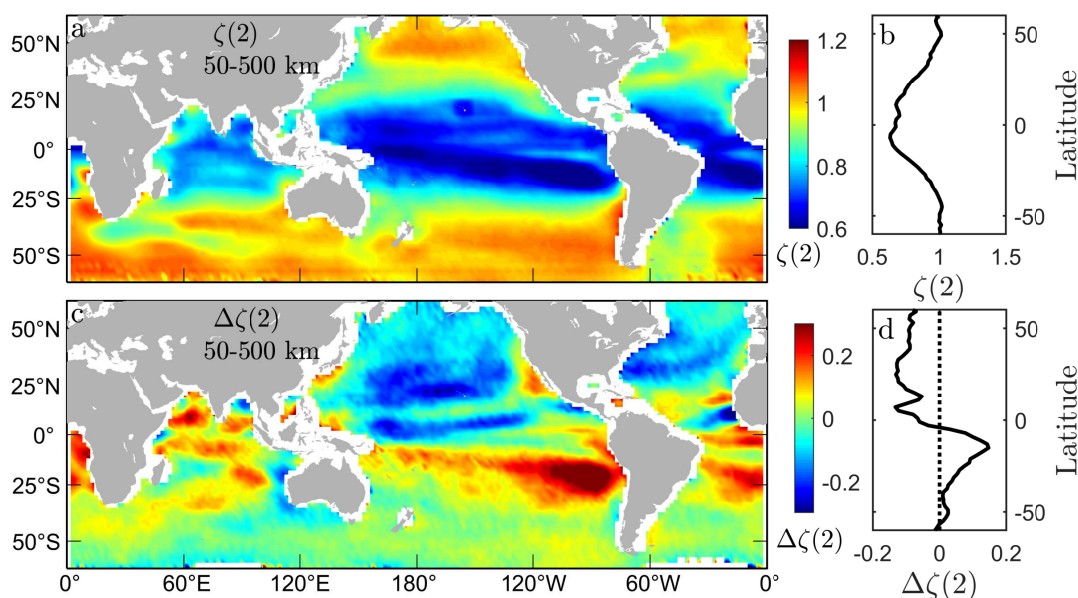


Figure 3.24 (a) The global distribution of $\zeta(2)$ measured from ten-year QuikSCAT collected U_{10} (100-500 km). (b) The meridional variations of $\zeta(2)$ inside the Pacific Ocean. (c) The global distribution of $\Delta\zeta(2) = \zeta(2)_s - \zeta(2)_w$, where $\zeta(2)_s$ is the summer (June, July, and August) scaling exponent and $\zeta(2)_w$ is the winter (December, January, and February) scaling exponent. (d) The meridional variations of $\Delta\zeta(2)$ inside the Pacific Ocean. The dashed line indicates a reference with the value of 0.

the scaling exponents in mid-latitudes and wintertime are larger than the ones in tropical regions and summertime. Here we note that $\zeta(2)$ is found around $2/3$ in the latitudinal ranges from 20°S to 20°N , close to Kolmogorov's prediction for isotropic turbulence in the inertial range. Furthermore, the spatial and seasonal differences of $\zeta(2)$ for QuikSCAT U_{10} are more smooth than the ones for CFOSAT U_{10} , the smoothed results are also related to the large data amount.

3.4.4 Scaling Comparisons Between Various Satellite Missions

The scaling analyses for U_{10} collected by QuikSCAT and CFOSAT missions show similar results, though these two missions do not compatible to the same time period. Besides the ongoing CFOSAT mission, there are also many other scatterometer missions in orbit, for instance, HaiYang-2A (HY-2A), HaiYang-2B (HY-2B), Meteorological operational satellite-A (Metop-A), Meteorological operational satellite-B (Metop-B), Meteorological operational satellite-C (Metop-C), to list a few. Both of HY-2A and HY-2B are using rotating pencil-beam scatterometers designed by China National Space Administration (CNSA) to obtain the wind fields, while the Metop-A, Metop-B, and Metop-C are

using the Advanced Scatterometer (ASCAT) provided by European Space Agency (ESA).

The scatterometer measures backscattering strengths from the ocean's surface, then based on the empirical relationship between backscattering strength and the wind field, the geophysical model functions (GMFs) can be developed to retrieve the wind speeds and directions. Due to the detailed designs for scatterometers, the retrieved wind fields from different missions always show discrepancies. To evaluate the performance of scatterometers, one may compare the satellite observations with buoy collected data or with modelling results. Normally, some basic statistics like average bias, root mean square errors (RMSEs), and standard deviations are always considered. Note that, the buoy observations are fixed at one geographical location, only one can sense the wind field at that point in time. On the other hand, the wind fields were obtained by scatterometers with a spatial resolution of 12.5 km or 25 km. Thus, the comparisons made between buoy and scatterometer data can be totally different in some cases. As for the wind data generated from models, their reliability is still in doubt, because they rely on the validity of the model. Since the perfect references for scatterometer data can never be found, the buoy observations and modelling data are the only choices. While these evaluations are all based on the value of the data, nothing is related to the dynamical information of the wind field itself.

Based on the above scaling analysis for U_{10} provided by CFOSAT and QuikSCAT missions, a global view of scaling features for ocean surface U_{10} has been obtained. Therefore, some simple comparisons can be also made to study the scaling differences for U_{10} retrieved from various satellite missions. Note that, the comparisons are made with the data collected in the same period, from December 2018 to February 2022. Figure 3.25 shows the global averaged Fourier power spectra for U_{10} collected by CFOSAT (magenta curve), HY-2B (blue curve), Metop-B (red curve), Metop-C (black dashed curve), the spectrum for Metop-A U_{10} is covered by the spectra for Metop-B and Metop-C data. Since the spatial resolution of HY-2B is 25 km, larger than the other missions, the largest wavenumber of the spectrum for HY-2B U_{10} is about 0.02 km^{-1} . In the spatial range of 100 km to 2000 km, the scaling features for the spectra estimated from HY-2B, Metop-B, and Metop-C U_{10} are nearly identical, with scaling exponents close to 2. The one extracted from CFOSAT U_{10} illustrates a scale break around 500 km, above which the scaling feature is close to the other spectra. As for the scales from 100 km to 500 km, the scaling exponent is close to $-5/3$, then for the scales less than 100 km, the spectrum shows a slope close to -1 . The spectra for Metop-B and Metop-C U_{10} show a decreasing trend for the scales less than 100 km, with scaling exponents close to 3. The differences between the spectra are mainly found below the scales of 500 km, especially for the scales less than

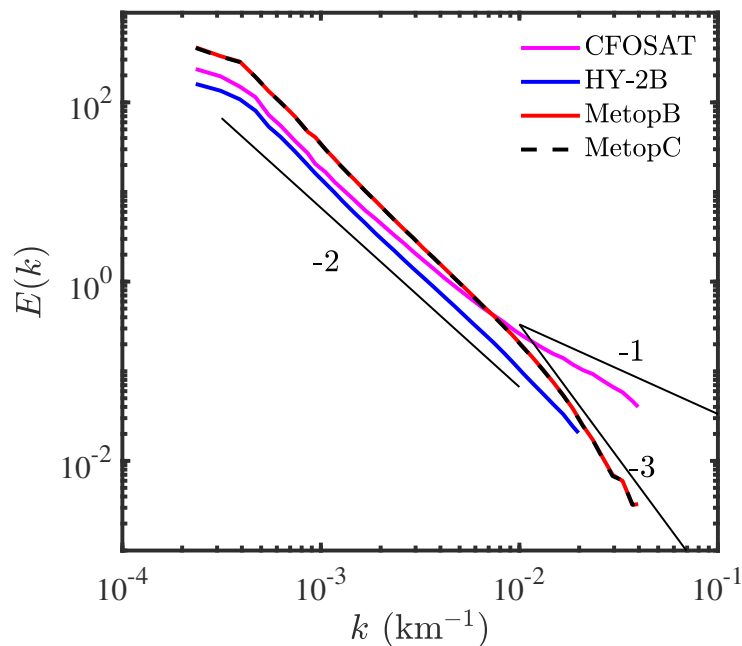


Figure 3.25 The global averaged Fourier power spectra for U_{10} collected by CFOSAT (magenta curve), HY-2B (blue curve), Metop-B (red curve), Metop-C (black dashed curve), the black lines are given as references with the slopes of -1, -2, and -3.

100 km.

To further diagnose the scaling differences for U_{10} obtained by various scatterometer missions, the global distributions of β for U_{10} collected by Metop missions are extracted. Note that, the scaling exponents shown here are estimated from 1D U_{10} subsets (about 1000 km for each subset) in the along-track direction, not the 2D subsets, since the length of swath provided by ASCAT is only 500 km. As aforementioned, the scaling features extracted from the 1D subsets are similar to the 2D dataset, see Figure 3.8 a and Figure 3.10 b. Thus, 1D Fourier power spectral analysis is used here. Figure 3.26 shows the global distributions of the scaling exponents β measured from U_{10} (100-1000 km) collected by CFOSAT (Figure 3.26 a), and Metop (Figure 3.26 c) missions. The same spatial patterns for β are found, but with a slight differences between the magnitudes. Relatively large values of β are found in the Metop data, especially in the subtropical regions.

We cannot propose here a clear explanation for these differences. This issue will need to be explained in future studies.

3.4.5 Scaling Analysis of ECMWF Model Data

The global scaling features for ocean surface wind at various scales are obtained

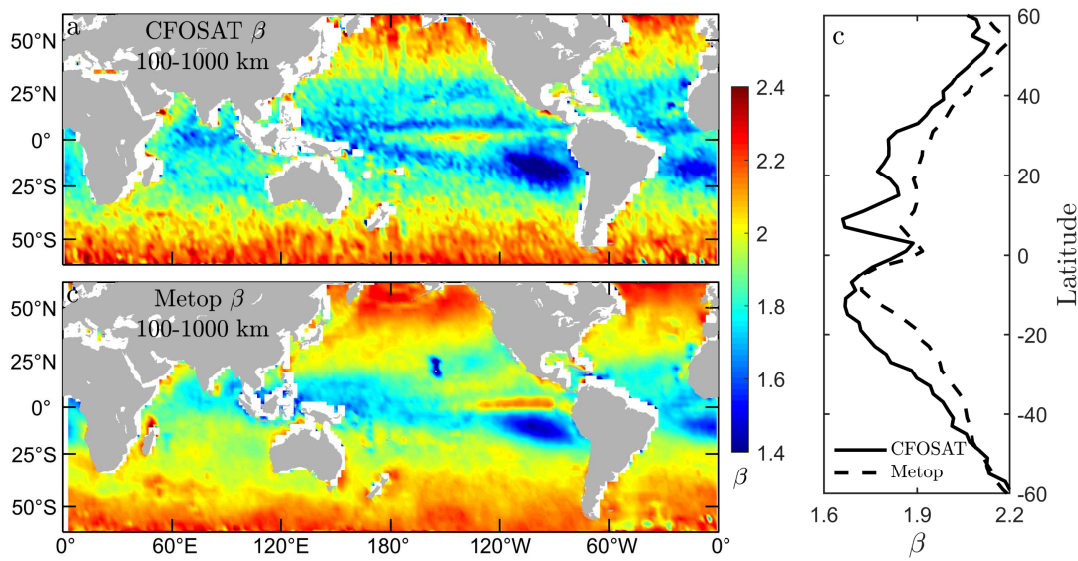


Figure 3.26 The global distributions of the scaling exponents β measured from U_{10} (100-1000 km) which collected by (a) CFOSAT, and (c) Metop missions. (b) The meridional variations of β inside the Pacific Ocean.

by Fourier power spectral analysis and structure-function analysis for the CFOSAT, QuikSCAT, and Metop satellite observed U_{10} . Consistencies are found between these two methods and the different data sources, which confirm the reasonable scaling features for U_{10} we illustrated. Thus, the results can be used as benchmarks for models or for reanalysis outputs.

Here we used three years of reanalysis data (from December 2018 to June 2022) which are provided by the latest global climate reanalysis produced by the European Centre for Medium-Range Weather Forecasts (ECMWF, <https://climate.copernicus.eu/climate-reanalysis?q=products/climate-reanalysis>) to extracted the scaling features for U_{10} . The ECMWF data has been regridded to a regular latitude-longitude grid of 0.25 degrees (25 km spatial resolution) at the height of 10 m. This dataset has been proved to be of high quality and widely used by many authors to verify satellite observations and also study the atmospheric dynamical features (Hersbach et al., 2020; Olauson, 2018; Tarek et al., 2020; Urraca et al., 2018).

The Fourier power spectral analysis is performed on 80 data points of subset for the ECMWF U_{10} data to study the global scaling features for U_{10} for the scales below 1000 km. The global averaged Fourier power spectrum for U_{10} over the sea surface from ECMWF also shows evident scaling features in the scales from 100 to 1000 km as shown in Figure 3.27. The corresponding scaling exponent is equal to 2.4 here, larger than the one derived from satellite observations.

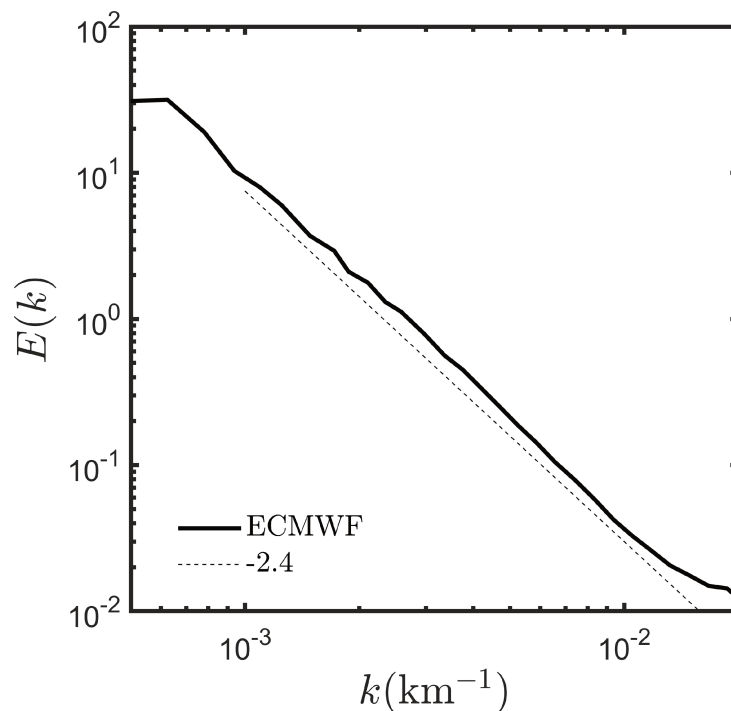


Figure 3.27 The global averaged Fourier power spectrum for U_{10} provided by ECMWF (black solid curve), the dashed line is given as a reference with a slope of -2.4.

The global distribution of the annually averaged scaling exponents for U_{10} from ECMWF is also derived and shown here, see Figure 3.28 a. Meridional variation for β is found with large ones around mid-latitude and relatively small ones in the equator. This distribution pattern is close to the ones from CFOSAT and QuikSCAT observed results, see Figures 3.23 a and 3.8 a. In addition, the value of β from reanalysis data is larger than the ones from field observations. Seasonal differences are shown in Figure 3.28 b, opposite variation trend is found as compared to the satellite data analysis, larger β are found in summer time in the Northern Hemisphere for ECMWF data.

3.5 Conclusion

Simultaneously observed wind and wave data by CFOSAT have been used to determine the multiscale features of U_{10} and H_s . Before processing the data, quality controls have been carefully performed and outliers were removed, as shown by the pdfs of the two main variables considered here. The spatial and temporal variations of the corresponding scaling exponents have been examined. Power-law features were found in the global averaged Fourier power spectra of U_{10} and H_s . The scaling exponents β for H_s are close to

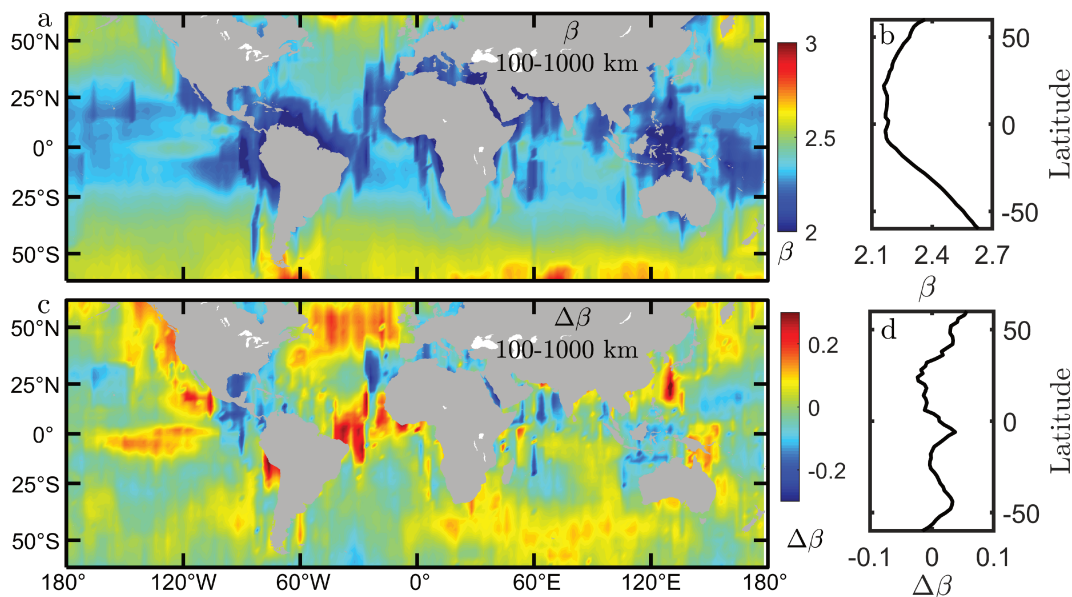


Figure 3.28 The global distributions of β measured from ECMWF U_{10} (100-1000 km) provided by ECMWF. (b) The meridional variations of β inside the Pacific Ocean. (c) The global distribution of $\Delta\beta = \beta_s - \beta_w$. (d) The meridional variations of $\Delta\beta$ inside the Pacific Ocean.

3, and 2 in the range of 1000-3000 km and 10-1000 km, respectively. For U_{10} , power-law features are found from 100 to 1000 km with β between $5/3$ and 2, with little evidence of β close to 3 for larger scales. The global averaged co-spectrum for U_{10} and Hs also showed power-law features from 30 km to 250 km and 250 km to 2000 km with scaling exponents equal to 1.8 and 2.4, respectively. The values of the coherence function lay between 0.04 and 0.13 in the whole spatial ranges, and the maximum occurs around 1200 km.

Our results showed that within each oceanic basin, the averaged Fourier power spectra for U_{10} and Hs have nearly identical shapes and scaling features from 50 km to 3000 km, while for the scales below 50 km, the spectra for Hs show more roughness as compared to those at larger scales. This may indicate that complex submesoscale processes are dominant at these scales.

A finer examination of the global distribution of β showed that the scaling exponents for U_{10} and Hs are both meridional dependent with large values occurring in middle and high latitudes and small values in the tropics. For U_{10} , the scaling exponents are smaller inside the convergence zones than those in the relatively steady equatorial dry zone. The scaling exponents in convective regions are close to $5/3$. We also considered the temporal evolution of scaling exponents. Their seasonal variations derived from U_{10} data showed small scaling exponents in summer and large ones in winter for most regions. This result

is likely related to the strength of baroclinic disturbances in different seasons. While for Hs case, β are found larger in summer than those in winter in the Northern Hemisphere; in the tropical area of the Southern Hemisphere, large β is found in winter. As for the regions further south than 25°S , the seasonal variations are unclear.

Globally these results show that some scaling properties may be obtained when considering all the data together; some universal properties are found when considering the averages in some subsamples, such as the basin scale study, especially for the wind field when a very clear k^{-2} range was found over 2 decades in scale. The variability of the field considered, and hence their spectral properties, vary in time and in space, and some adequate spatial or temporal domain must be chosen to find evolution, universality, patterns, and identify hidden processes. This is what has been done in this work, either by looking at the basin scale, the local spatial patterns, the latitude averages in one ocean, or the seasonal changes in some spatial patterns.

In this work, scaling features of U_{10} and Hs collected by CFOSAT have been derived by spectral analysis. As a complementary study, the structure-function analysis was also performed. The measured second-order structure-function for U_{10} and Hs show scaling features in the scales from 50 to 500 km and 10 to 1000 km, respectively, with the scaling exponent $\zeta(2) \approx 1$. This means that the isotropic turbulence prediction of the scaling exponents $\zeta(2) = \beta - 1$ is roughly satisfied in this work. Then the horizontal isotropic feature for U_{10} is further diagnosed by estimating the scaling exponents for the two components of the wind field, where both Fourier power spectrum and second-order structure-function are considered. Moreover, the two-dimensional spectrum and two-dimensional structure-function of U_{10} are extracted, and the horizontal isotropy feature is found for scales from 100 to 1000 km in these studies.

The high-order structure-function analysis is also performed to study the intermittency features for U_{10} and Hs . For U_{10} , power-law features are found from 12.5 to 1000 km, while for Hs , two ranges are detected, e.g., 2 to 30 km, and 100 to 1000 km. The extracted scaling exponents $\zeta(q)$ are compared to the K41 model, and the modified lognormal model proposed by Li and Huang (2014). The results show that Hs is more intermittent than U_{10} , and that $\zeta(q)$ for Hs for large scales can be well described by the lognormal model with the Hurst number $H = 0.6$, and the intermittency parameter $\mu = 0.3$, which coincidentally agrees with the value for high Reynolds turbulence flows Frisch (1995).

The extracted scaling features for U_{10} from CFOSAT are confirmed with QuikSCAT data analysis. Similar spatial and temporal variations for β and $\zeta(2)$ are found, but the results are more smooth due to the long-term average in QuikSCAT data. For the data col-

lected by other satellites, e.g., HY-2B, MetopB, and MetopC, the global averaged Fourier power spectra are also estimated. The scaling features are found the same for scales from 100 to 1000 km. For the scales less than 100 km, differences are evident, but an explanation is still lacking. Except for the scaling analysis for U_{10} collected from satellites, the data provided by ECMWF is also considered in this work. The results show that β for U_{10} from ECMWF are larger than the ones from satellite data, and the corresponding meridional variations are opposite to the ones from satellite data analysis.

For further works, we plan to further characterize the intermittency in these scaling ranges, by considering joint structure functions and also Hilbert spectral analysis (HSA) of higher orders, which are shown not to be strongly impacted by energetic forcing (Huang et al., 2008, 2011; Schmitt and Huang, 2016). Also, the reason for getting different scaling features from various satellite data will be studied by considering the differences in scatterometer designs, the algorithms used for wind retrieval, and the criterion for QC, to list a few.

Chapter 4 Scale-to-Scale Energy and Enstrophy Fluxes of Wind Field via CFOSAT

In the previous chapter, the scaling features for ocean surface wind have been systematically studied with Fourier power spectrum analysis and structure-function analysis. The spatial and temporal variations of the scaling features have been obtained. These features are related to the energy and enstrophy fluxes induced by nonlinear interactions between different scales. The energy and enstrophy fluxes are vital to the whole turbulent flow systems since the direction and intensity of the flux determine the system's dynamic features. However, the characteristics of the flux could not be provided with the scaling analysis method.

In this chapter, the energy and enstrophy fluxes of the ocean surface wind field observed by CFOSAT are obtained with an improved Filter-Space-Technique (FST). The filtered scales are set from 12.5 to 500 km due to the width of the swath for SCAT. The spatial and temporal variations for the energy and enstrophy fluxes at the aforementioned scales are extracted in a global view. As a comparison, the fluxes derived from QuikSCAT collected wind data and reanalysis data are also calculated. In addition, as a special case of atmospheric movement, a typhoon event is selected to study the corresponding energy and enstrophy fluxes. The content of this chapter is based on a manuscript submitted to *Journal of Geophysical Research : Atmospheres*: Gao, Y, Schmitt FG, Hu JY, and Huang YX (2022), "Scale-to-Scale Energy and Enstrophy Fluxes of Atmospheric Motions via CFOSAT" .

4.1 Method

Though the longitudinal third-order structure-function analysis and spectral approach both can estimate the fluxes, these two methods have some inevitable limitations. For instance, the third-order structure-function analysis requires the field to be in a state of isotropy. The interpretation of the result is related to the choice of 2D or 3D turbulence theory. Concerning the spectral approach, it is only suited for regular field data, and cannot be applied to satellite observed data. Thus, the FST is used in this study, a method borrowed from the field of turbulence.

4.1.1 Scale-to-scale Energy and Enstrophy fluxes

The derivation of FST is introduced in this section. Considering a wind field in a horizontal plane, e.g., \mathbf{u} , a low-pass (coarse-grained) filter is defined as (Aluie et al., 2018),

$$\mathbf{u}^{[r]}(\mathbf{x}, t) = \mathbf{u}(\mathbf{x}, t) * G^{[r]}(\mathbf{x}) = \int_{|\mathbf{x}'| \leq r} \mathbf{u}(\mathbf{x} + \mathbf{x}', t) G^{[r]}(\mathbf{x}') d\mathbf{x}' \quad (4.1)$$

where $*$ is a convolution, and $G^{[r]}(\mathbf{x})$ is a filter kernel that is often taken as a Gaussian one, i.e., $G^{[r]}(\mathbf{x}) \propto \exp(-|\mathbf{x}|^2/2r^2)$ (Boffetta and Ecke, 2012). This is partially due to the fact that it has good low-pass property in the Fourier space.

On the contrary, a complementary high-pass filter that retains only modes at scales less than r can be defined as

$$\mathbf{u}'^{[r]}(\mathbf{x}, t) = \mathbf{u} - \mathbf{u}^{[r]}(\mathbf{x}, t). \quad (4.2)$$

The filter can also be applied to the incompressible Navier-Stokes equation,

$$\frac{\partial \mathbf{u}}{\partial t} + (\mathbf{u} \cdot \nabla) \mathbf{u} = -\nabla p + \nu \Delta \mathbf{u}. \quad (4.3)$$

First, we recall the following property, for any function f (obtained by integration by parts):

$$\frac{\partial f}{\partial x} * G^{[r]} = \frac{\partial (f * G^{[r]})}{\partial x}. \quad (4.4)$$

Thus, filtering Eq. (4.3) gives

$$\frac{\partial u_i^{[r]}}{\partial t} + \frac{\partial}{\partial x_j} \left((u_i u_j)^{[r]} \right) = -\frac{\partial p^{[r]}}{\partial x_i} + \nu \Delta u_i^{[r]}. \quad (4.5)$$

where u_i ($i=1, 2, 3$) are the velocity components. This equation can be further expressed as

$$\frac{\partial u_i^{[r]}}{\partial t} + \frac{\partial}{\partial x_j} \left(u_i^{[r]} u_j^{[r]} \right) = -\frac{\partial p^{[r]}}{\partial x_i} - \frac{\partial}{\partial x_j} \left((u_i u_j)^{[r]} - u_i^{[r]} u_j^{[r]} \right) + \nu \Delta u_i^{[r]}. \quad (4.6)$$

Finally, one can obtain the governed equation for $\mathbf{u}^{[r]}$ as

$$\frac{\partial \mathbf{u}^{[r]}}{\partial t} + (\mathbf{u}^{[r]} \cdot \nabla) \mathbf{u}^{[r]} = -\nabla p^{[r]} - \nabla \cdot \tau^{[r]}(\mathbf{u}) + \nu \Delta \mathbf{u}^{[r]}, \quad (4.7)$$

where p is pressure, ν is the kinematic viscosity. Equation 4.7 is identical to the original

unfiltered Equation 4.3, but with an additional term from the subfilter stress (it is called subgrid stress in the LES field (Pope, 2000)), which can be expressed as:

$$\tau^{[r]}(\mathbf{u}) = (u_i u_j)^{[r]} - (u_i^{[r]} u_j^{[r]}). \quad (4.8)$$

$\tau^{[r]}(\mathbf{u})$ is a tensor that indicates the source of the force from the scales smaller than r , and injects to the larger scale processes (Pope, 2000).

From the large-scale momentum Eq. (4.3), one can derive a kinetic energy (KE) budget for scales larger than r (Germano, 1992):

$$\frac{\partial |\mathbf{u}^{[r]}|^2}{2\partial t} + \nabla \cdot \mathbf{J}_{\text{trans}}^{[r]} = -\Pi_E^{[r]} - \nu |\nabla \mathbf{u}^{[r]}|^2, \quad (4.9)$$

in which, $\mathbf{J}_{\text{trans}}^{[r]}$ is the spatial transport of large-scale KE, which can be represented as:

$$\mathbf{J}_{\text{trans}}^{[r]}(\mathbf{x}, t) = \frac{|\mathbf{u}^{[r]}|^2 \mathbf{u}^{[r]}}{2} + p^{[r]} \mathbf{u}^{[r]} - \nu \nabla \frac{|\mathbf{u}^{[r]}|^2}{2} + \mathbf{u}^{[r]} \cdot \tau^{[r]}(\mathbf{u}). \quad (4.10)$$

In this equation, the first term is the KE which is transported by the advection of $\mathbf{u}^{[r]}$, the second term is transport related to pressure, the third term is the KE diffusion caused by viscosity, the last term is the KE cascade induced by the motions with the scales below r , namely, the direct KE injection caused by small scale fluxes.

The first term on the right-hand side (RHS) of Eq. (4.9) is the so-called scale-to-scale energy flux or ‘‘cascade’’ term, which is used to estimate the energy flux from smaller to larger scales caused by nonlinear interactions. The flux is defined as:

$$\Pi_E^{[r]}(\mathbf{x}, t) = -\mathbf{S}_{ij}^{[r]} : \tau^{[r]}(\mathbf{u}), \quad (4.11)$$

where $\mathbf{S}_{ij}^{[r]}$ is the large-scale strain-rate tensor $\mathbf{S}_{ij}^{[r]} = (\frac{\partial u_i^{[r]}}{\partial x_j} + \frac{\partial u_j^{[r]}}{\partial x_i})/2$. The colon: is a tensor inner product that produces a scalar, and the sign for $\Pi^{[r]}$ indicates the KE cascade directions. Finally, one can estimate the energy flux at a given point \mathbf{x} , and a given time t as,

$$\Pi_E^{[r]}(\mathbf{x}, t) = - \sum_{i,j=1,2} \left[(u_i u_j)^{[r]} - (u_i^{[r]} u_j^{[r]}) \right] \frac{\partial u_i^{[r]}}{\partial x_j}, \quad (4.12)$$

It is the scale-to-scale energy fluxes across the filter scale r . Here we note that the analyses performed in this chapter are restricted to the horizontal plane, i.e., with 2 horizontal components of the velocity. In the turbulence inertial range where direct viscous effects can be neglected, the energy fluxes $\Pi_E^{[r]}$ between different scales are induced by internal

multiscale interactions which correspond to the nonlinear convective term (aka, advective term) in the NS equation.

The same derivations can also be applied to the NS equation for scalar vorticity to extract the enstrophy flux, which can be written as,

$$\Pi_{\Omega}^{[r]}(\mathbf{x}, t) = - \sum_{i=1,2} \left[(u_i \omega)^{[r]} - (u_i^{[r]} \omega^{[r]}) \right] \frac{\partial \omega^{[r]}}{\partial x_i}, \quad (4.13)$$

where $\omega = \nabla \times \mathbf{u}$ is the vorticity of the velocity field. With the above definition, a positive $\Pi^{[r]}$ means a forward cascade where the energy/enstrophy transfers from scales $\ell \geq r$ to $\ell \leq r$.

4.1.2 Wind Vector Projection

In the process of flux estimation, the velocity field should be projected to the coordinate composed with the directions of along- and cross-satellite track. The original U_{10} field data are given in the geographic coordinate system which is based on latitude and longitude. Thus, a velocity projection is required before estimating the fluxes. The detailed process for projection is described as follows.

Firstly, suppose there is a CFOSAT observed wind vector \mathbf{U} with the direction of θ , as represented as a magenta arrow in Figure 4.1 in the raw longitude-latitude based coordinate (x_1 - y_1 , shown as black arrows). The wind velocity components at this coordinates are shown as u_1 and v_1 . Then, a new coordinate composed of the directions of along- and cross-track (x_2 - y_2 , as shown with red arrows) is established. The angle between these two coordinates is noted as α here. In this way, the projected components u_2 , and v_2 in the satellite track coordinate can be calculated as,

$$\begin{aligned} u_2 &= \|\mathbf{U}\| \times \sin(\theta + \alpha), \\ v_2 &= \|\mathbf{U}\| \times \cos(\theta + \alpha). \end{aligned} \quad (4.14)$$

The projected components of \mathbf{U} in the satellite track coordinate are shown as blue arrows in Figure 4.1. In this way, the observed wind fields are transferred into the new coordinate and could be further used for energy and enstrophy fluxes analyses.

4.1.3 FST Estimation With Missing Data Problem

The above equations (Eqs. (4.12) and (4.13)) can be directly used to calculate the energy or enstrophy fluxes for regular 2D wind field data without gaps. However, due

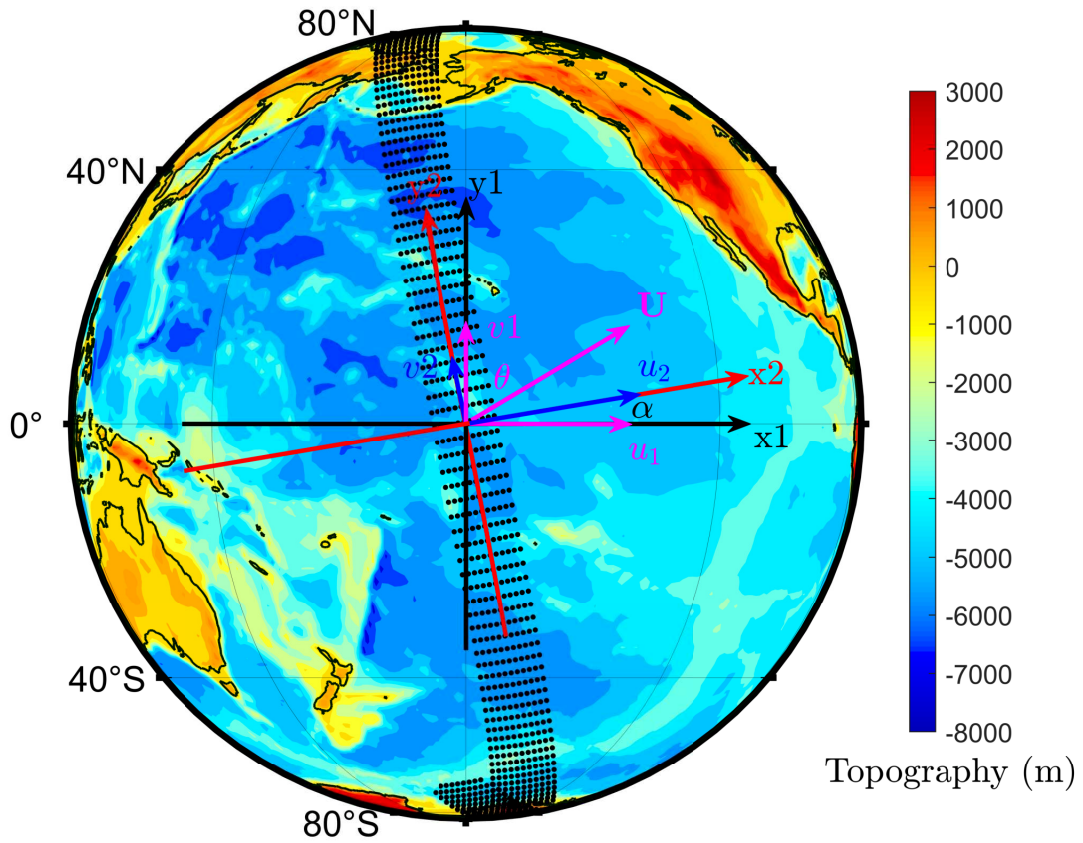


Figure 4.1 Illustration of CFOSAT footprint (black dots). The orthogonal black arrows and red arrows are the longitude-latitude based coordinate and satellite trajectory-based coordinate, respectively. A wind vector example \mathbf{U} and the corresponding two components u_1 and v_1 in the original coordinate are shown as magenta arrows. The two blue arrows are the two components u_2 and v_2 for the vector \mathbf{U} which is projected to the satellite trajectory-based coordinate.

to several inevitable reasons, such as the presence of lands, islands, sea ice, and also bad measurements, the collected U_{10} data by scatterometers are often produced with missing data problems. To process the wind field \mathbf{u}_R which contains gaps with FST (the subscript R means the ratio of data missing), the following steps are proposed to mitigate the impacts of missing data to the energy/enstrophy flux analysis in this work:

- a) suppose we have an idealized regular velocity field \mathbf{u} (Figure 4.2 a), the corresponding energy flux field is shown in Figure 4.2 e; a objective filed \mathbf{u}_R which contain gaps (Figure 4.2 b);
- b) generating a new field \mathbf{u}_z (Figure 4.2 c) via filling the gaps in \mathbf{u}_R with zeros;
- c) creating a mask field \mathbf{u}_m based on \mathbf{u}_R , in which the gaps are replaced by zeros, and the meaningful values are changed to ones (Figure 4.2 d);

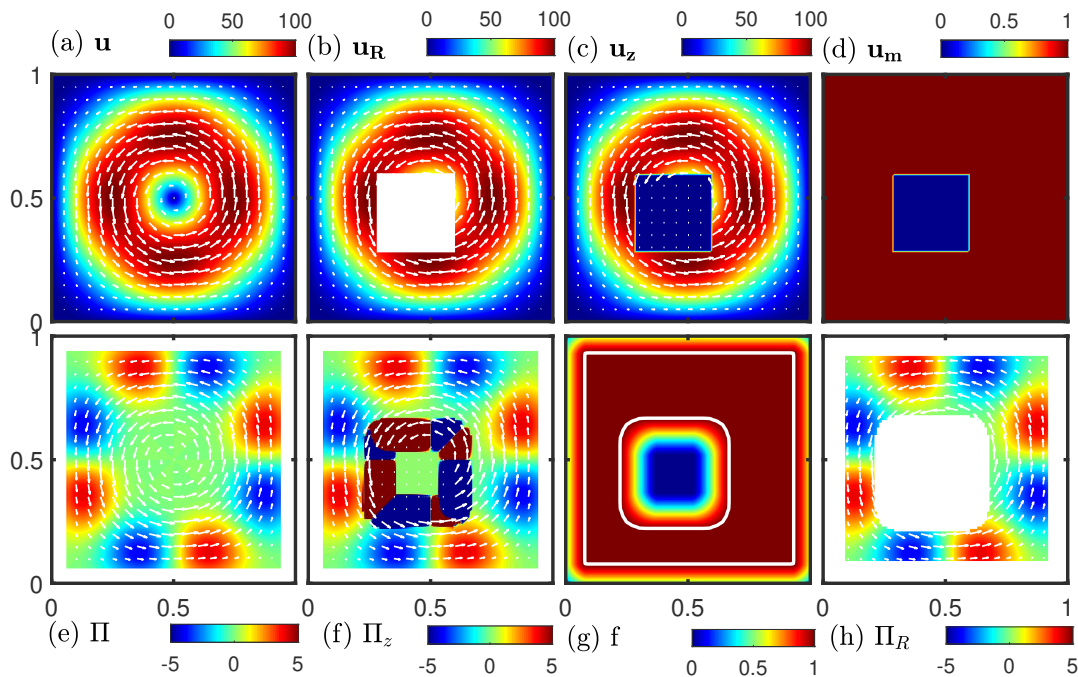


Figure 4.2 (a) An idealized velocity field without missing data. (b) The field \mathbf{u}_R contains gaps. (c) The filed \mathbf{u}_z where gaps are introduced. (d) A mask field where the meaningful values are replaced with ones. (e) The energy flux for the raw field. (f) The energy flux for the field \mathbf{u}_z . (g) Filtered field f , the white curves are the contour lines with the value of 0.99. (h) The energy flux for the filed \mathbf{u}_R .

- d) estimating the fluxes for \mathbf{u}_z via FST, the result is indicated as Π_z (Figure 4.2 f);
- e) convolving the mask \mathbf{u}_m with the Gaussian kernel to generate a flag field f (Figure 4.2 g);
- f) setting the values in f which are less than or equal to 0.99 as NaN, and the ones larger than 0.99 as ones. Finally, getting the flux field for \mathbf{u}_R by convolving Π_z with this mask field.

Normally, the gaps in the field could bias the gradient calculation in FST, and also the convolving measurement. Note that, the set of critical threshold 0.99 is based on strict pretesting, other values (less than 0.99) can also be chosen, but will show relatively larger discrepancies to the original fluxes as compared to the flag value of 0.99. In this way, the flux for the data which contain gaps like \mathbf{u}_z can be measured, the differences between the flux for \mathbf{u} and \mathbf{u}_z are visually small, see the comparison of Figures 4.2 e and 4.2 h.

To study the effects of flag value and missing data on the averaged energy flux estimation, ECMWF reanalysis data in the open Pacific Ocean with the latitudes from 67.25°S to

57.5°N, and the longitudes from 180°W to 159.25°W, corresponding to an 80×500 wind field is selected. Then more than 90,000 CFOSAT trajectory segments with the shape of 80×500 (with various missing data ratios) are used to cover the selected reanalysis dataset to mimic the naturally generated gaps in these data in an artificial way.

Here we first consider the value of the flag used in the calculation. The measured energy fluxes at the scale of 200 km for the original wind field without gaps are shown in Figure 4.3 a, both positive and negative fluxes are found in the map, with the averaged energy flux equals to $-1.546 \times 10^{-3} \text{ m}^2/\text{s}^3$. Then the missing data points contained in CFOSAT trajectory segments are used to generate gaps in the reanalysis data. Finally, three different flag values, e.g., 0.5, 0.85, and 0.99 are chosen to calculate the energy fluxes for the reanalysis data which has gaps. The differences between the measured energy fluxes for the raw data and the data containing gaps with these flag values are shown in Figure 4.3 b, c, and d, respectively. With the increase in flag values, the differences are suppressed. The averaged energy fluxes for the flags of 0.5, 0.85, and 0.99 are equal to $-1.326 \times 10^{-3} \text{ m}^2/\text{s}^3$, $-1.481 \times 10^{-3} \text{ m}^2/\text{s}^3$, and $-1.543 \times 10^{-3} \text{ m}^2/\text{s}^3$, respectively. The differences are highly withheld when the flag value is set as 0.99. Thus, in this work, 0.99 is used in the estimation of the energy fluxes for satellite observed wind fields.

To further consider the effects of missing data, an error function is defined as follows:

$$\text{Err}(r, R) = \frac{|\bar{\Pi}_0^{[r]} - \bar{\Pi}_R^{[r]}|}{\bar{\Pi}_0^{[r]}} \times D(R)^{[r]} \times 100\%, \quad (4.15)$$

where $\bar{\Pi}_0^{[r]}$ and $\bar{\Pi}_R^{[r]}$ are the averaged energy flux from raw reanalysis data and the one containing gaps with the missing ratio of R at the scale of r , respectively. $D(R)^{[r]}$ is the sign function used to indicate the change of sign for the results derived from the data with gaps as compared to the raw data, which is defined as:

$$D(R)^{[r]} = \begin{cases} 1, & \bar{\Pi}_0^{[r]} \times \bar{\Pi}_R^{[r]} > 0 \\ -1, & \bar{\Pi}_0^{[r]} \times \bar{\Pi}_R^{[r]} < 0. \end{cases} \quad (4.16)$$

The results are shown in Figure 4.4. The white curve is the contour line with the value of 0. for scales less than 250 km, the effects of missing data are limited at the level of 20% with the missing ratio up to about 42% for scales less than 75 km, and 60% for scales from 100 to 250 km. Some light patches with the values of error function between 30% and 50% occur for scales larger than 250 km under the missing ratio of 40%. Thus, for scales below 500 km which are considered in this work, the impacts of missing data on the averaged energy flux are less than 20% for the missing ratio under 40% for most cases.

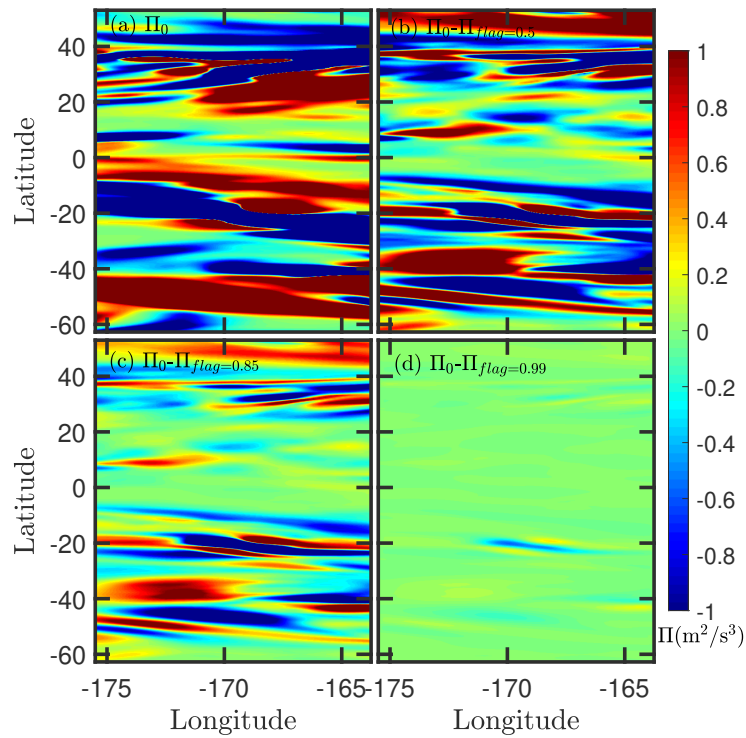


Figure 4.3 (a) The measured energy fluxes for the originally selected reanalysis wind field at the scale of 200 km. (b), (c), and (d) are the differences in the energy fluxes between the raw data and the data containing gaps with the flag values of 0.5, 0.85, and 0.99, respectively.

Furthermore, as indicated by the white curve of the boundary between the regions with values of 1 and -1, the sign of averaged energy flux is found not to change for all the scales with the missing ratio less than 63%.

Therefore, this improved FST can be used to handle the data containing gaps as shown in the above tests. In practice, to enhance the accuracy of our analysis, the data containing more than 40% gaps are excluded in this study.

The main advantage of this improved approach over the third-order longitudinal structure-function and spectral representation is that this estimator can provide local information on energy/enstrophy fluxes, which cannot be obtained from the spectral approach. In addition, FST is mathematically exact and thus can be generally used without the assumption of homogeneity or isotropy (these assumptions are required for the spectral approach and the third-order structure-function analysis). Finally, the disadvantage is obvious: it is time-consuming since the convolution is involved for each scale r , but it is still much faster than the structure-function approach since the FFT-based convolution is performed.

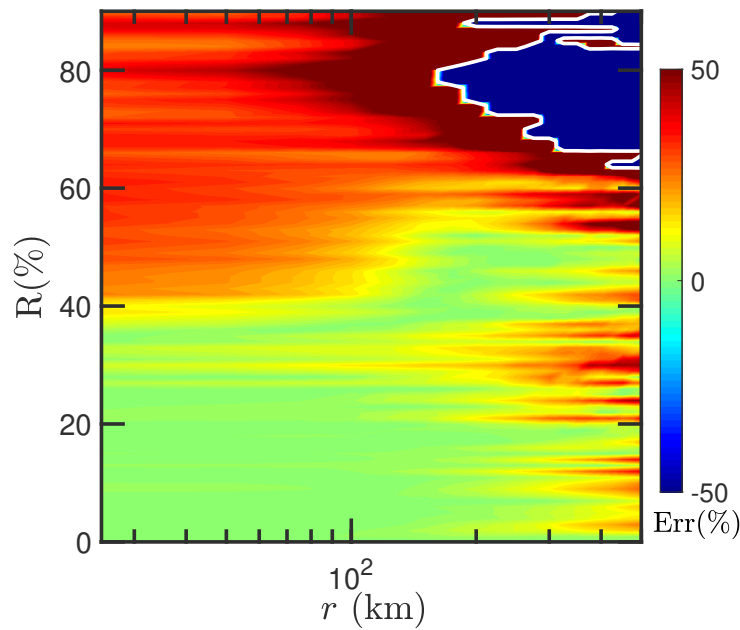


Figure 4.4 The values of the measured error function with the scale r and missing ratio R , the white curve is the contour line with the value of 0.

4.2 Spatial and Temporal Variations of the Energy and Enstrophy Fluxes

With the improved FST, CFOSAT observed U_{10} can be directly used to estimate the energy and enstrophy fluxes for the atmospheric movement above the sea surface. In this section, a given filter scale is set to show the global view of the fluxes, including the spatial distribution, and seasonal variations. Then a detailed study of the fluxes from the scales of 12.5 to 500 km is performed. Finally, a special case of atmospheric movement, e.g., a typhoon case is selected to show the complex features of energy and enstrophy fluxes around the center of the typhoon.

4.2.1 Global Views of Energy and Enstrophy Fluxes at the Scale of 250 km

In the famous works measuring the energy spectra for wind and temperature observed by commercial aircraft from the upper troposphere and lower stratosphere, a clear $-5/3$ law was found for the length scales from 10 to 500 km (Nastrom and Gage, 1985; Nastrom et al., 1984). Two opposite hypotheses have been put forward to explain this scaling feature, which corresponds to the forward and backward energy fluxes, respectively. Here a scale between 10 and 500 km, e.g., 250 km is chosen to examine the direction of energy

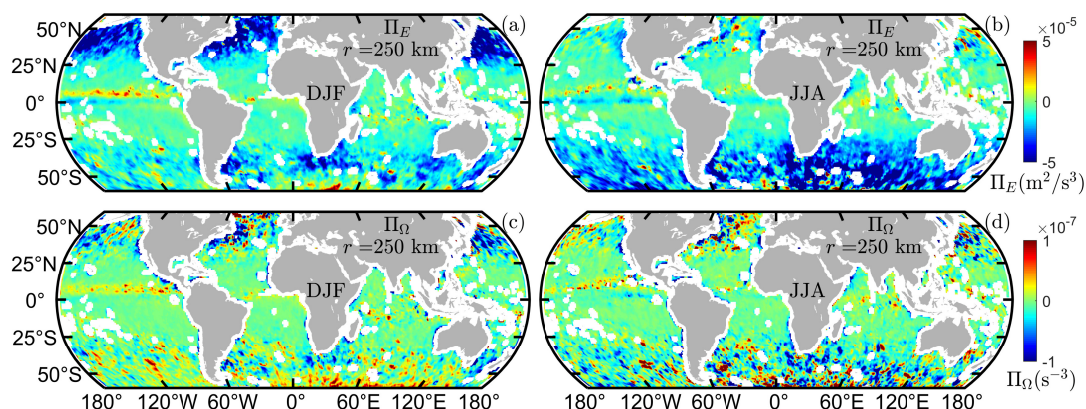


Figure 4.5 The global distributions of the seasonally averaged energy fluxes Π_E for CFOSAT U_{10} in (a) winter (DJF), and (b) summer (JJA). (c) and (d) are the same but for enstrophy fluxes Π_Ω . The filter scale is set as 250 km.

and enstrophy fluxes with FST.

The global views of energy and enstrophy fluxes at the scale of 250 km are extracted in different seasons to study the spatial and temporal variance fluctuations for the fluxes. Two seasons, winter and summer are selected to show the seasonal differences here. Note that, winter time is defined as the months of December, January, and February (DJF); summer time represents June, July, and August (JJA) in this study. Figures 4.5 a and b are the global distributions of the seasonally averaged energy fluxes in winter and summer, respectively. Figures 4.5 c and d are the ones for enstrophy fluxes. It is clear that the fluxes show meridional variations, with larger values in mid-latitudes and relatively small ones in the tropical areas, except for a narrow region around 10°N , which corresponds to the Intertropical Convergence Zone (ITCZ). At the scale of 250 km, basin-wide negative energy fluxes are found in mid-latitudes for both Hemispheres in winter. While for summer, the direction of the energy cascade turns to forward in the Northern Hemisphere mid-latitudes. As for enstrophy flux, the forward and backward cascades are mixed in the mid-latitudes at 250 km scale, and complex distribution patterns are illustrated. The seasonal differences for enstrophy at this studied scale are not clear. One interesting point is that large positive energy and enstrophy fluxes are found in the ITCZ for both winter and summer.

4.2.2 Multiscale Energy and Enstrophy Fluxes

In the above analysis, we have found that the energy and enstrophy fluxes are mainly varying along latitude, with less dependency on the change of longitude. The longitudinal

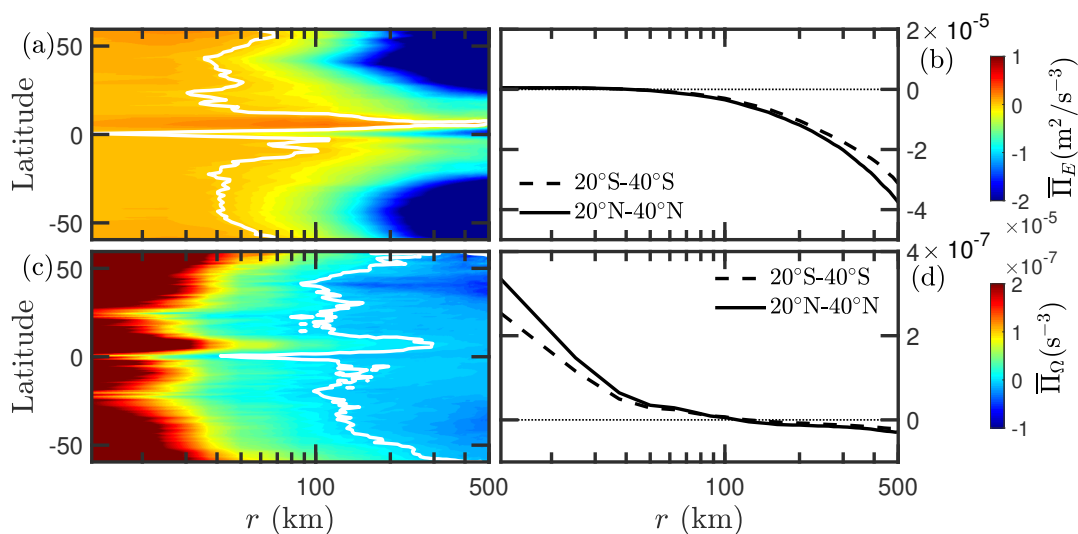


Figure 4.6 Longitudinal averaged of (a) energy fluxes Π_E and (c) enstrophy fluxes Π_Ω for CFOSAT U_{10} at various scales. The white curves are the contour lines with the value of 0. (b) and (d) are the ensemble-averaged energy flux Π_E and enstrophy flux Π_Ω curves in two latitudinal ranges, the dotted line is given as a reference with the value of 0.

average can be performed on the global fluxes to have a better understanding of the meridional variations of the fluxes. Here the annually averaged fluxes for energy and enstrophy for scales from 12.5 to 500 km are estimated, then the corresponding longitudinal average results are extracted and shown in Figure 4.6. Figures 4.6a and 4.6c are the latitude-scale phase diagrams for the energy and enstrophy fluxes, respectively. Symmetric distribution patterns for the fluxes are found between the two Hemispheres, with evident meridional distribution features: large ones in mid-latitudes and a narrow range around the ITCZ, smaller ones in the rest areas. Positive and negative fluxes are bounded with white curves as shown in the phase diagrams. Forward and backward cascades for energy and enstrophy are found on small and large scales, respectively. The transition scale also shows latitudinal variations. For instance, for the ranges from 20°S to 40°S, and 20°N to 40°N, the averaged transition scales for energy and enstrophy fluxes are around the scales of 40 km, and 100 km respectively, see Figures 4.6 b, and d. While for the latitudes close to 10°N, the transition scale is much larger than that in other regions.

Here we also consider the temporal variations of the fluxes in the latitudinal ranges of 20°S to 20°S, and 20°N to 20°N. The monthly averaged fluxes at various scales are estimated and shown in Figures 4.7. The white curves are given as references with the value of 0, to indicate the transition of flux direction. For scales smaller than the transition scale, relatively large positive energy fluxes are found in March, April, and May (MAM),

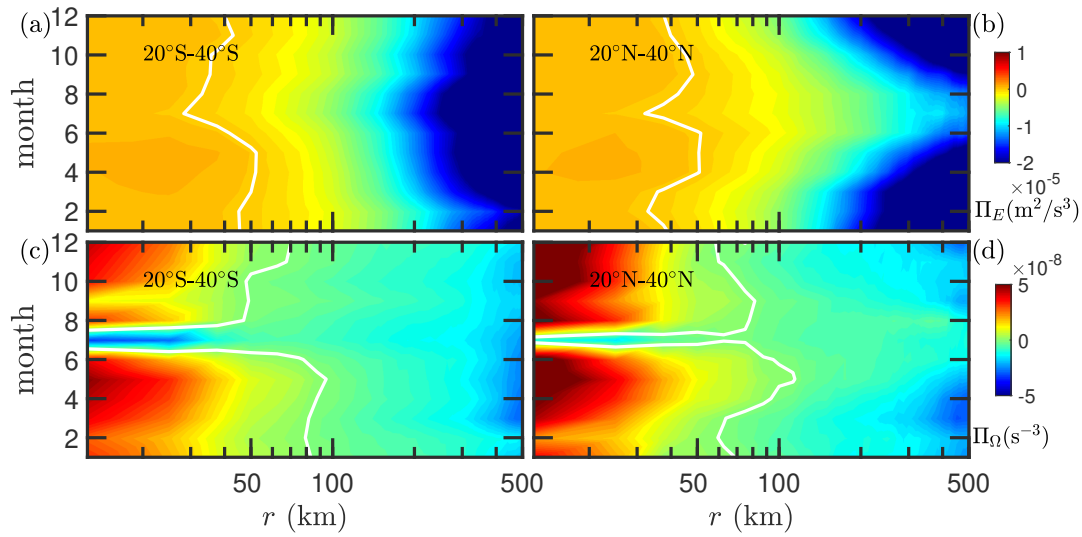


Figure 4.7 Monthly evolution for multiscale energy fluxes Π_E for CFOSAT U_{10} in the latitudinal ranges of (a) 20°S - 40°S , and (b) 20°N - 40°N . The white curves are the contour lines with the value of 0. (c) and (d) are the same, but for enstrophy fluxes Π_Ω .

and September, October, and November (SON), and smaller ones are in JJA. The above features are the same for both Hemispheres. For scales larger than the transition scale, negative energy fluxes are found with large magnitudes in JJA for the Southern Hemisphere, and in DJF for the Northern Hemisphere, namely, the larger backward energy fluxes are occurring in the winter hemisphere. For the enstrophy flux, positive values are found for scales below 100 km around the year, except for July, negative fluxes are obtained for all the scales. For scales larger than 100 km, the backward enstrophy fluxes are found larger in the winter hemisphere too.

4.2.3 Energy and Enstrophy Fluxes During Typhoon

After extracting the energy and enstrophy for U_{10} in a global view with temporal and spatial averages, instantaneous energy and enstrophy flux fields for a special atmospheric movement case, e.g., Typhoon Maysak (2020), are obtained here. The wind field of Maysak is shown in Figure 4.8 a, in which the colored map is the wind speed, and the black arrows are the velocity vectors.

By applying FST to Maysak, the energy and enstrophy fluxes at the scale from 12.5 to 500 km are obtained. For instance, at the scale of 50 km, the corresponding energy, and enstrophy fluxes are shown in Figures 4.8 b and d, respectively. The velocity fields are shown with white arrows, and the energy and enstrophy fluxes are indicated by col-

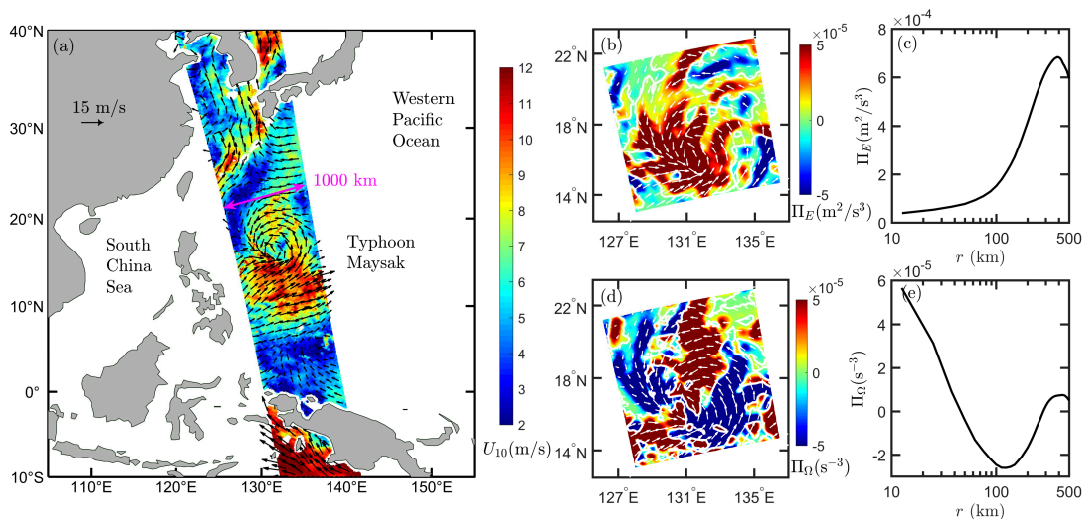


Figure 4.8 (a) CFOSAT observed wind vectors (black arrows) in the western Pacific Ocean on August 27, 2020 during Typhoon Maysak. (b) Measured instantaneous energy flux for the typhoon center at the scale of 50 km. (c) The averaged energy fluxes at various scales r . (d) and (e) are for the enstrophy flux.

ored maps. The local information for the fluxes is clearly obtained by FST, negative and positive flux patches are found alternatively distributed around the typhoon center, and the boundaries between them are illustrated with white curves. The magnitudes of energy and enstrophy fluxes are in the order of $10^{-5} \text{ m}^2/\text{s}^3$. The structures of the typhoon are well captured by the two flux maps, indicating complex dynamics. The spatially averaged fluxes at other scales are also estimated and illustrated in Figures 4.8 c and e. For energy fluxes, net forward cascades are found for all the scales, indicating that the total energy is transferred from the scales above 500 km to the scales of less than 12.5 km. For the enstrophy flux, forward cascades are found for scales below 50 km and scale larger than 200 km. In the ranges between these two scales, a net backward cascade is found.

4.3 Discussion

By applying the improved FST to CFOSAT observed wind velocity field, the energy flux and enstrophy fluxes of atmospheric motions can be extracted in physical space. The spatial and seasonal variations of energy and enstrophy fluxes for atmospheric motions above the sea surface at the scales from 12.5 to 500 km are obtained in a global view. A case study of measured energy and enstrophy fluxes for Typhoon Maysak reveals complicated dynamical structures around the typhoon center, with positive and negative flux patches which are alternatively occurring.

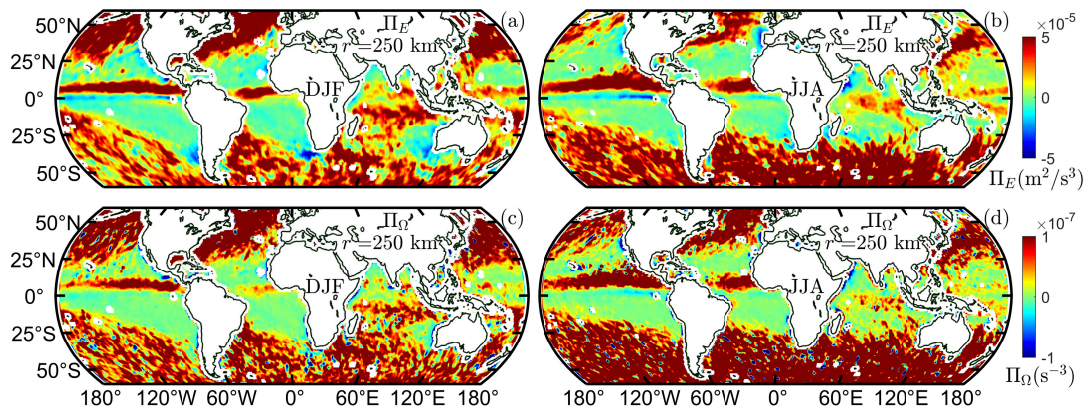


Figure 4.9 The global distributions of the seasonally averaged energy fluxes Π_E for CFOSAT wind data before QC in (a) winter (DJF), and (b) summer (JJA). (c) and (d) are the same but for enstrophy fluxes Π_Ω . The filter scale is set as 250 km.

With a temporal average of the measured flux, forward and backward fluxes are observed on small and large scales, respectively. The transition scales of flux direction and the strength of those fluxes show meridional variations. Large transition scales are found in high-latitudes and a narrow region close to 10°N , which also corresponds to strong fluxes. For the seasonal variations, strong backward energy and enstrophy fluxes are found in the midlatitudes of the winter hemisphere at large scales, as shown in Figure 4.5 and Figure 4.7. This agrees with our understanding that the atmospheric activity is more intense in winter in those regions, where baroclinic instability is enhanced, thus the potential energy is converted to kinetic energy.

Note that, the U_{10} data used in this study are strictly quality controlled, with the same criterion used in the scaling analysis of CFOSAT along-track wind data: namely, only the data collected by more than two beams by the scatterometer are kept for further process. Due to the FST containing gradient calculation, the results are sensitive to abnormal values, thus the outliers have to be removed.

A test of estimating the energy and enstrophy fluxes with original U_{10} (without QC) provided by CFOSAT is performed, and the measured fluxes at the scales of 250 km are shown in Figure 4.9. In which Figures 4.9 a, and b are the energy fluxes for raw data in DJF, and JJA, respectively. Figures 4.9 c, and d are the results for enstrophy fluxes. As compared to the results shown in Figure 4.5, evident differences are found. For the data before QC, positive energy and enstrophy fluxes are dominant in the mid-latitude at the filter scale of 250 km, while negative energy and enstrophy fluxes are found in the mid-latitudes for the data after QC. Thus, the data quality is vital in the energy and enstrophy fluxes analysis with FST.

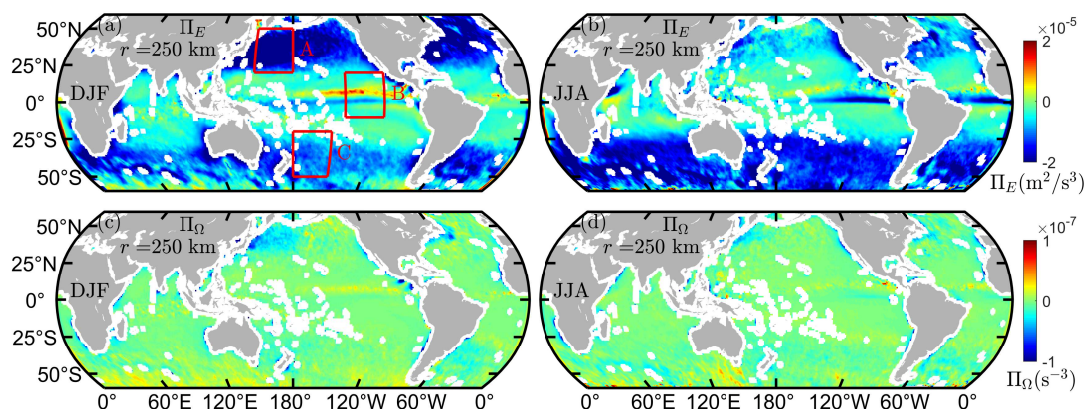


Figure 4.10 The global distributions of the seasonally averaged energy fluxes Π_E for QuikSCAT U_{10} in (a) winter (DJF), and (b) summer (JJA). (c) and (d) are the same but for enstrophy fluxes Π_Ω . The filter scale is set as 250 km. The rectangles in (a) are the selected regions for studying the evolution of fluxes.

4.3.1 Energy and Enstrophy Fluxes for QuikSCAT Data

Based on the CFOSAT U_{10} data analysis, the energy and enstrophy fluxes for the atmospheric movements above the ocean surface are obtained in a global view, and the spatial and temporal variations for the fluxes are examined. These results are derived for the first time to the best of our knowledge. A double check is performed with the U_{10} data collected by QuikSCAT again. Using 10 years of QuikSCAT data, the spatial distribution and seasonal variations for energy and enstrophy fluxes are estimated with FST. Similar results to the CFOSAT data analysis are found, with little difference in the magnitude of enstrophy fluxes.

Figure 4.10 shows the global distribution of the seasonally averaged energy and enstrophy fluxes for QuikSCAT U_{10} in DJF and JJA with the scale of 250 km. The distribution patterns for energy fluxes are close to the ones derived from CFOSAT data, both illustrate negative energy fluxes in mid-latitudes. As for the seasonal differences, strong backward energy fluxes are both found in the winter hemisphere. For enstrophy fluxes, the results from QuikSCAT U_{10} data are more close to zeros at the filter scale of 250 km as compared to the ones from CFOSAT data analysis.

The latitudinal average for the energy and enstrophy fluxes derived from QuikSCAT data for scales from 12.5 to 750 km are also performed. The results are shown in Figures 4.11a, and 4.11c. The regions of 20°S-40°S, and 20°N-40°N are also chosen to do the spatial average. The scale-dependence of the energy and enstrophy fluxes are illustrated in Figures 4.11b, and 4.11d, respectively. These results are close to the ones for CFOSAT data analysis. The transition scales of the fluxes for QuikSCAT and CFOSAT

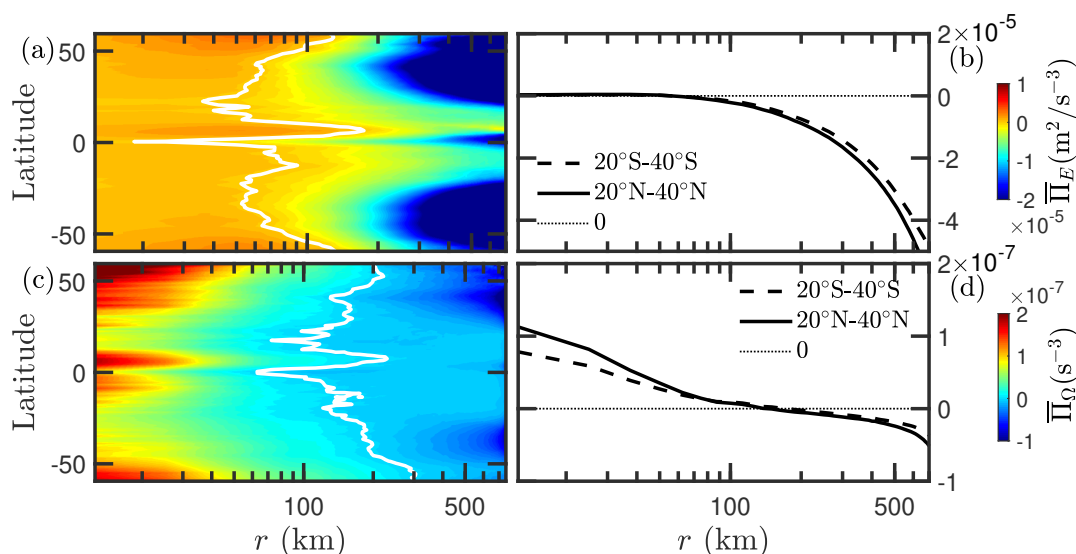


Figure 4.11 Longitudinal averaged (a) energy fluxes Π_E and (c) enstrophy fluxes Π_Ω for QuikSCAT U_{10} at various scales. The white curves are the contour lines with the value of 0. (b) and (d) are the ensemble-averaged energy flux Π_E and enstrophy flux Π_Ω curves in two latitudinal ranges, the dotted line is given as a reference with the value of 0. The inset in (d) is a part of enlargement.

data are also close to each other. On the other hand, the magnitude of enstrophy fluxes estimated from QuikSCAT data is smaller than the ones from CFOSAT U_{10} data.

The seasonal variations of energy and enstrophy fluxes extracted from QuikSCAT U_{10} data are close to the ones from CFOSAT data: both show strong fluxes in the wintertime. In addition, the transition scales for the flux direction are close to each other for both datasets. The detailed results are illustrated in Figure 4.12.

Here the seasonal variations for the fluxes for QuikSCAT wind data in the latitudinal ranges of 20°S to 40°S and 20°N to 40°N are also extracted. The results are shown in Figure 4.12. Strong fluxes are found in wintertime, as obtained in the CFOSAT data analysis. The monthly evolution of the enstrophy fluxes is slightly different from the two datasets. Relatively large transition scales are found for the enstrophy fluxes of QuikSCAT data as compared to the CFOSAT results. Moreover, positive enstrophy fluxes are found throughout the whole year in small scales (smaller than the transition scale) for QuikSCAT data, while negative enstrophy fluxes are visible in small scales in July for CFOSAT data.

4.3.2 Evolution of Energy and Enstrophy Fluxes

In the above section, similar scale-to-scale energy and enstrophy fluxes are extracted from QuikSCAT wind data and compared to the ones from CFOSAT wind data. Merid-

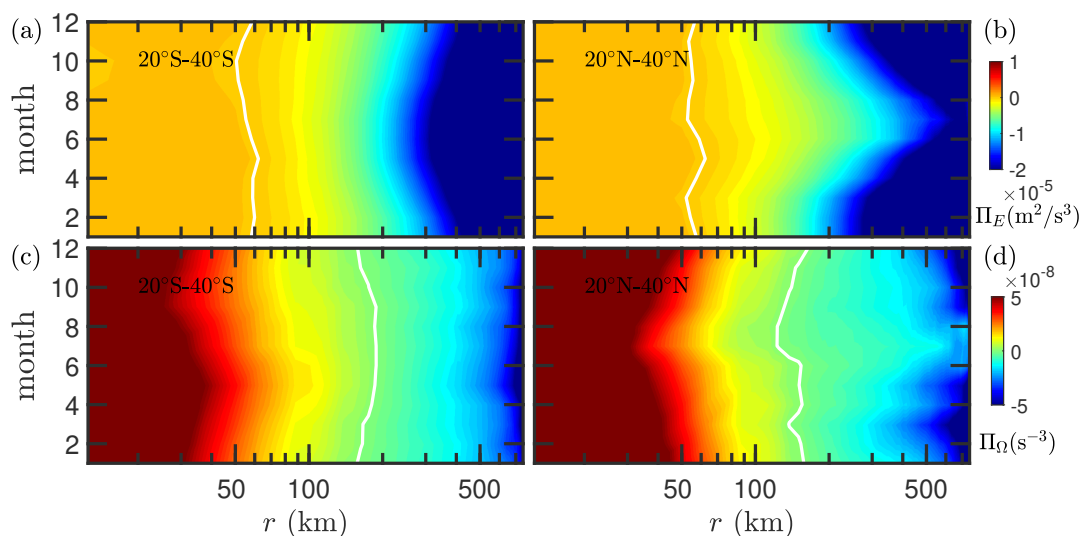


Figure 4.12 Monthly evolution for multiscale energy fluxes Π_E for QuikSCAT U_{10} in the latitudinal ranges of (a) 20°S - 40°S , and (b) 20°N - 40°N . The white curves are the contour lines with the value of 0. (c) and (d) are the same, but for enstrophy fluxes Π_Ω .

ional variation and monthly evolution for the energy and enstrophy fluxes are based on longitudinal averages with the assumption that the variance for fluxes is longitudinal independent. For different oceanic regions in the same latitudes, the intrinsic dynamical features should be different due to various topographical conditions. To study the temporal variation of the flux in a specific ocean, the signal from other oceans or from the same ocean but with different latitude regions that correspond to distinct climate systems should be excluded. Here three regions inside the Pacific Ocean are selected to show the detailed energy and enstrophy flux features. The regions are indicated with red rectangles in Figure 4.10a, in which, region A is in the longitude ranges of 150°E to 180°E , with the latitudes of 20°N to 50°N ; region B is 140°W to 110°W , and 10°S to 20°N ; region C is 180°W to 150°W , and 20°S to 50°S . The temporal variations of energy and enstrophy fluxes at the scales from 12.5 km to 750 km in these regions are extracted and shown in Figure 4.13, in which the white curves are the contour lines with the value of 0. Figures 4.13 a, b, and c are the evolution of energy flux in regions A, B, and C, respectively. Figures 4.13 d, e, and f are the same, but for the enstrophy fluxes. It is clear that strong fluxes are found in regions A, and C, e.g., relatively high latitudes, and weak fluxes are observed in region B, corresponding to tropical areas. Seasonal variations for the energy flux are clearly obtained in all regions, with opposite trends obtained in regions A and C due to the hemispheric differences. The measured energy fluxes are larger in JJA for region A, while smaller ones are found in DJF. The evolution trend is reversed in region C,

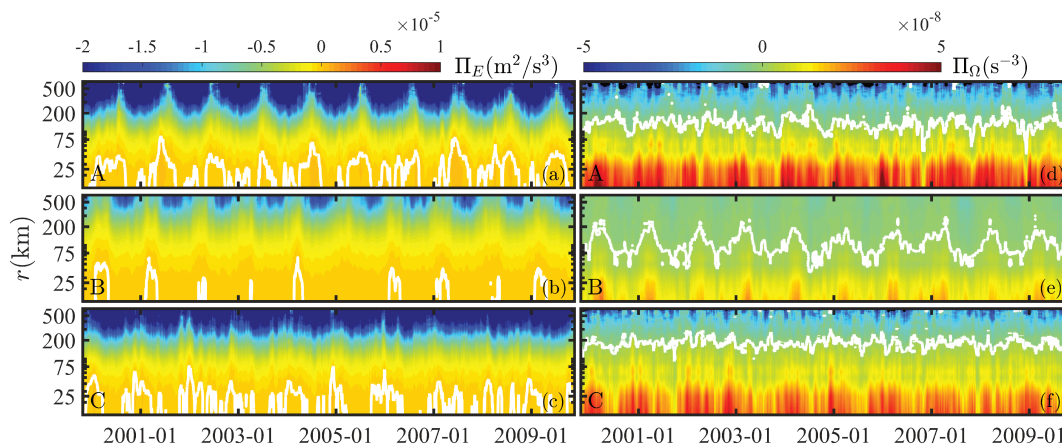


Figure 4.13 (a), (b), and (c) are the temporal evolution of energy flux Π_E in three selected regions as indicated in Figure 4.10 a. (d), (e), (f) are the cases of enstrophy fluxes Π_Ω .

with larger fluxes in DJF, and smaller ones in JJA. Relatively small seasonal differences for enstrophy fluxes are found in A and C. Moreover, relatively strong inverse energy and enstrophy fluxes are found in August in B.

The probability density functions (PDF) for the flux at the scales of 25 km, 50 km, 100 km, 200 km, and 400 km in the selected regions are also estimated. The results are shown in Figure 4.14, in which the top and bottom panels are PDFs for the energy and enstrophy fluxes, respectively. It is clear that the fluxes tend to be dominantly forward and backward for scales below and above 200 km, respectively, which correspond to the right and left-skewed features for the PDF curves at these scales.

4.3.3 Energy and Enstrophy Fluxes for ECMWF Reanalysis Data

In the above compensatory analysis of QuikSCAT data, the same energy flux feature for the wind field is found, and similar enstrophy flux characteristics are obtained. This confirms the scientific results of energy and enstrophy fluxes we got from CFOSAT data analysis. Another attempt is proposed to estimate the energy and enstrophy fluxes for ECMWF provided reanalysis U_{10} data. We show here an example of the fluxes for wind field derived from ECMWF data in the same period of CFOSAT observations with a filter scale of 250 km. The results are illustrated in Figure 4.15. The spatial distributions of measured energy and enstrophy fluxes are close to the ones estimated from the original CFOSAT U_{10} before QC, evident positive fluxes are occupied the mid-latitudes and the areas close to 10°N . For the temporal differences, the energy and enstrophy fluxes are both found more energetic in wintertime, keeping the same feature as we found in the real data

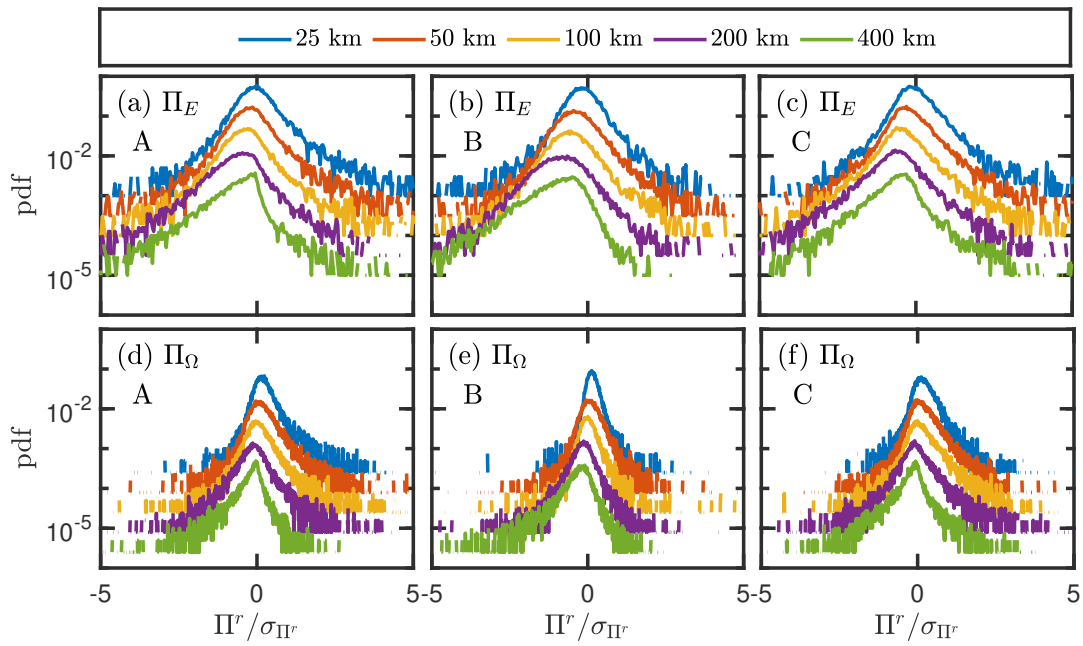


Figure 4.14 Measured PDFs of energy fluxes Π_E for scales from $25 \leq r \leq 400$ km with the wind data in three selected regions (a) A, (b) B, and (c) C. (d), (e), and (f) are the same, but for enstrophy fluxes Π_Ω .

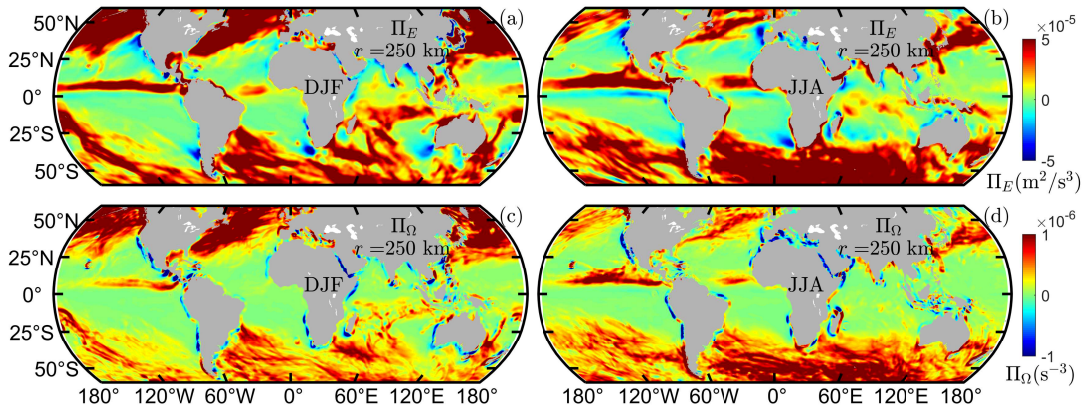


Figure 4.15 The global distributions of the seasonally averaged energy fluxes Π_E for ECMWF U_{10} in (a) winter (DJF), and (b) summer (JJA). (c) and (d) are the same but for enstrophy fluxes Π_Ω . The filter scale is set as 250 km.

analysis.

The energy and enstrophy fluxes extracted from ECMWF data show similar characteristics as we found in the raw CFOSAT data analysis. Thus, these results might relate to the quality of the reanalysis data. Figure 4.16 illustrates the measured pdfs for wind data from ECMWF reanalysis and CFOSAT observations. The pdf for ECMWF wind is close to the one for raw CFOSAT wind data, especially in the ranges of wind speed smaller than

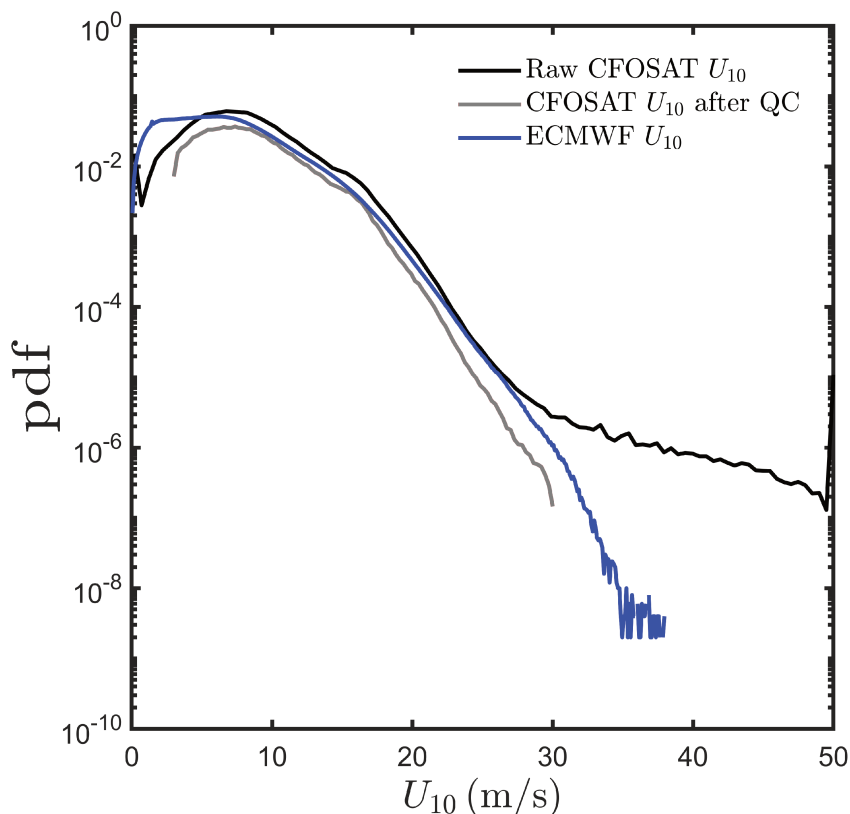


Figure 4.16 The comparisons of the pdfs for CFOSAT observed raw wind data (black curve), the data after QC (gray curve), and the wind data provided by ECMWF.

25 m/s. The extremely large values in the dataset will have a vital effect on the calculation of the data gradient, so as to the final flux values. Thus, even with very few outliers in the dataset, the impacts are hard to be restrained with spatial or temporal averages. Consequently, the results derived from the data without quality control are not reliable. As for the well-quality controlled CFOSAT wind data, the extracted fluxes are credible.

4.3.4 Energy Flux Measurement with Third-order Longitudinal Structure-Function Analysis

As we mentioned before, the scale-to-scale energy flux can be also estimated with a third-order longitudinal structure-function analysis and spectral approach. The latter method cannot process the data containing gaps, thus it is inappropriate to catch the energy flux features for CFOSAT observed data with the spectral approach. Here the third-order longitudinal structure-function is used to study the energy flux for CFOSAT. The calcu-

lation is done within the 84×84 (1000×1000 km) subsets of the U_{10} data after QC. The absolute values of global averaged third-order longitudinal structure-function are shown in Figure 4.17 a. Note that, the blue and red cycles are the structure-function with negative and positive values. For scales smaller and larger than 200 km, negative and positive third-order longitudinal structure-function are found, respectively. This indicates that forward and backward energy fluxes are dominant in the small and large scales, respectively. According to Eq. (2.18), the derived mean energy dissipation ϵ are also given in the inset. Meridional variation of ϵ at various scales is shown in Figure 4.17 b, the black curves are the contour lines with the value of 0. Positive ϵ is found for most latitudes for scales less than 300 km, except for the regions around 10°N , 10°S , and 60°S , where negative ϵ are found for all the studied scales. For scales above 300 km, ϵ are found negative, except for two narrow regions around 20°N , and the equator.

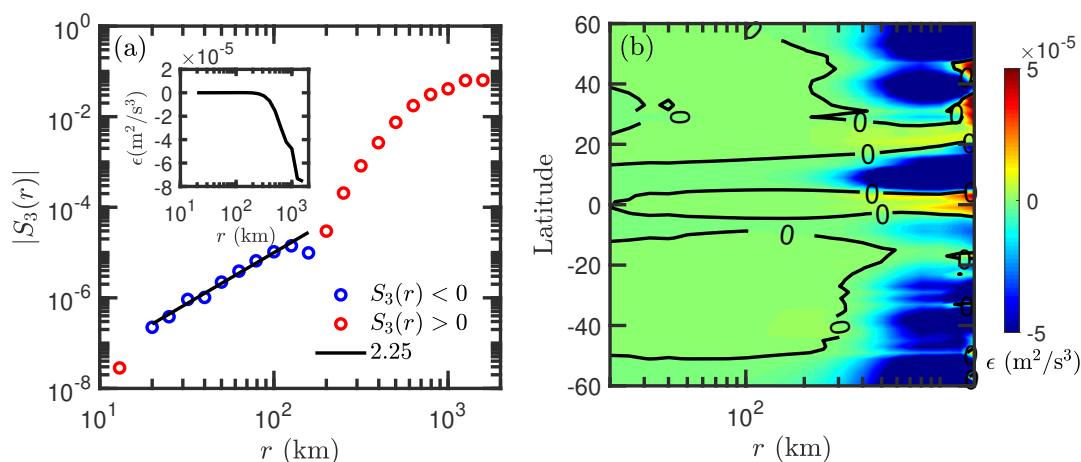


Figure 4.17 (a) Absolute values of the global averaged third-order longitudinal structure-function for CFOSAT, the blue and red cycles are the structure-function with negative and positive values. The inset is the derived global averaged energy dissipation at various scales. (b) Longitudinal averaged energy dissipation at various scales, the black curves are the contour lines with the value of 0.

The spatial distribution of ϵ at four scales, e.g., 50 km, 100 km, 200 km, and 500 km are shown in Figure 4.18. Meridional variations for ϵ are clearly found. For scales of less than 200 km, large positive ϵ are found in midlatitudes, except for the regions more south than 50°S . Relatively small ones occur in low-latitudes. For scales larger than 200 km, negative dissipation is found in mid-latitudes. In addition, measured ϵ are all negative in the regions close to ITCZ.

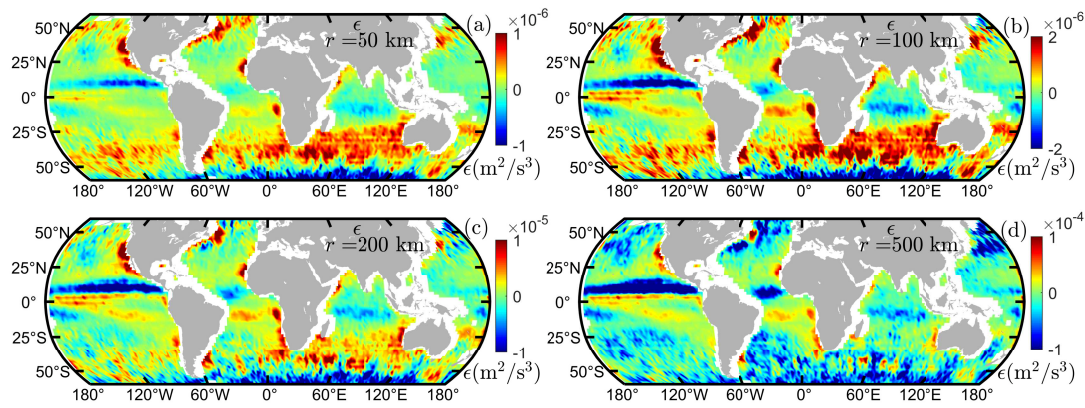


Figure 4.18 The global distribution for ϵ measured from CFOSAT U_{10} at the scales of (a) 50 km (b) 100 km (c) 200 km, and (d) 500 km.

4.4 Conclusion

The scale-to-scale energy and enstrophy fluxes for ocean surface atmospheric movement are obtained from CFOSAT observed wind data with the improved FST. Quality controls for the data have been performed before the calculation. The spatial and temporal variations of the corresponding scale-to-scale energy and enstrophy fluxes at the scales from 12.5 to 500 km have been examined. Positive and negative fluxes are found on small and large scales, respectively. The strength of the fluxes and the corresponding transition scales both show spatial variations and temporal evolutions. Among these, the values of energy and enstrophy fluxes are around the decades of 10^{-5} and 10^{-7} m^2/s^3 , respectively. The transition scales for energy flux are mainly varying from 40 to 100 km, for enstrophy flux are varying from 100 to 200 km. Strong fluxes are observed in midlatitudes and in a narrow region close to ITCZ. For temporal variations, the fluxes are stronger in winter than those in summer, which has been confirmed by the fluxes evolution diagrams with the data derived from three selected regions in the Pacific Ocean. Except for the temporal and spatial averaged analysis of the fluxes, simultaneous energy and enstrophy fluxes for Typhoon Maysak have been estimated. Complicate spatial patterns for the energy and enstrophy fluxes have been found around the center of the typhoon. Positive and negative fluxes patches are alternatively distributed. The spatial average for the fluxes around typhoons shows net forward energy fluxes from the scales from 12.5 to 500 km, while net backward enstrophy fluxes are found for scales from 50 to 200 km.

The features of scale-to-scale fluxes derived from CFOSAT data have been confirmed with the U_{10} provided by the QuikSCAT mission. Using the same FST algorithm, 10 years of QuikSCAT data are processed, and the same spatial and temporal variations

for the fluxes for scales from 12.5 to 500 km have been obtained. The values of enstrophy fluxes are found larger than the ones from CFOSAT data analysis, which might be induced by the differences in scatterometer designs, the data retrieval algorithms, or the quality control qualifications. Similar flux features have been also obtained from HY-2B, Metop-A, -B, -C observed U_{10} data, the results are not shown here.

With FST, ECMWF provided wind fields at the pressure level of 1000 hPa are also processed to extract the global view of energy and enstrophy fluxes. However, the results are largely different from satellite data analysis. The measured energy flux at the scale of 250 km is close to the one derived from the raw CFOSAT, which has not been quality controlled. As for the enstrophy flux, positive and negative fluxes are found in the Northern and Southern Hemispheres, still different from the one estimated from satellite collected data. This may be due to the influence of the model used in generating the reanalysis products. Thus, the reanalysis data are not suggested in the study of energy and enstrophy fluxes, though the dataset is regular in time and space.

Finally, the third-order longitudinal structure function was applied to the U_{10} provided by CFOSAT. The results show that the energy dissipation rate ϵ is positive and negative for scales smaller and larger than 200 km, respectively, which corresponds to forward and inverse cascade for the energy flux. In addition, meridional variations of the dissipation rate are also found for all the scales, with strong dissipation in the mid-latitudes and the region of ITCZ.

Overall, an improved FST is proposed for extracting the scale-to-scale energy and enstrophy fluxes for ocean surface atmospheric movement with the wind field data provided by CFOSAT. Both forward and inverse cascades are found on small and large scales. Spatial and temporal variations of the fluxes are obtained. These results are confirmed with QuikSCAT data analysis. In addition, the preliminary energy and enstrophy flux figures for a typhoon are derived. For further studying the cascade of typhoons or other extreme events, systematic analyses are still required. In further works, we plan to study the spatial transportation of the energy and enstrophy fluxes based on the data from multi-scatterometer missions. A diagnosis of each term in the energy and enstrophy fluxes functions will be considered. Furthermore, comparisons of different approaches for fluxes measurement will also be made in future studies.

Chapter 5 Coupling Analysis of Wind and Waves

In the Introduction chapter, some previous wind-wave relation models have been presented. As indicated in this chapter, either the swell waves are not well-considered, or the scaling exponent is fixed as 2, which is based on the fully developed sea assumption. In this chapter, based on NDBC buoy collected long-term wind and wave data, a swell decomposition method and a generalized power-law relation between local wave height and wind speed are proposed. Then 17-year of JASON observed wind and wave data are used to obtain the spatial and temporal variations of global swells and the wind-wave relation. Finally, other altimeters (GEOSAT, ERS1, TOPEX, ERS2, GFO, ENVISAT, CRYOSAT-2, HY-2A, SARAL, SENTINEL-3A, and CFOSAT) observed wind and wave data are selected to validate the swell decomposition method and also the wind-wave power-law model. This chapter is based on a manuscript published in *Frontiers of Marine Sciences*: Gao, Y, Schmitt FG, Hu JY, and Huang YX (2023), “Probability-based wind-wave relation”.

5.1 Introduction of PM64 Wind-Wave Relation

The most famous wind-wave relation model, namely $H_s = 0.0246U_{10}^2$ is recalled with a detailed derivation here. Some considerations should be noted in this widely-used classical relation, which are discussed below.

By assuming that the wind blows steadily for a long time over a large area, the waves would come into an equilibrium state, called the fully developed sea. The Pierson-Moskowitz spectrum (PM64) was proposed based on 420 selected wave measurements in the northern Atlantic Ocean with the form as (Pierson Jr. and Moskowitz, 1964),

$$E(f) = C_0 g^2 (2\pi)^{-4} f^{-5} e^{-\frac{5}{4}(\frac{f_m}{f})^4}, \quad (5.1)$$

where $C_0 = 8.1 \times 10^{-3}$ is the Phillips constant; g is the acceleration of gravity (set as $10 \text{ N} \cdot \text{kg}^{-1}$ here); f is frequency and f_m is the frequency at the maximum of the spectrum. Since the variance of the wave height σ_h^2 can be estimated from the wave spectrum as

$\sigma_h^2 = \int_0^\infty E(f)df$, one can write

$$H_s = 4\sqrt{\int_0^\infty E(f)df}. \quad (5.2)$$

Here we note that f_m is also a cutoff frequency, since for $f \leq f_m$, $E(f)$ is almost vanishing, see the wave spectrum example measured from high-frequency (1.28 Hz) buoy sampled wave profile data provided by Coastal Data Information Program (CDIP, archived at <https://cdip.ucsd.edu/>) in Figure 5.1, in which the solid curve is the wave spectrum for the wave height. The peak frequency f_m is found around 0.05 Hz here, corresponding to the time period of 20 s. In the frequency bands smaller than f_m , a collapse of the wave energy happened, the trough is located around the frequency of 0.008 Hz. Then, the spectrum for the wave height slightly enhanced to a stable low value. Thus, the value of H_s can be approximated as follows,

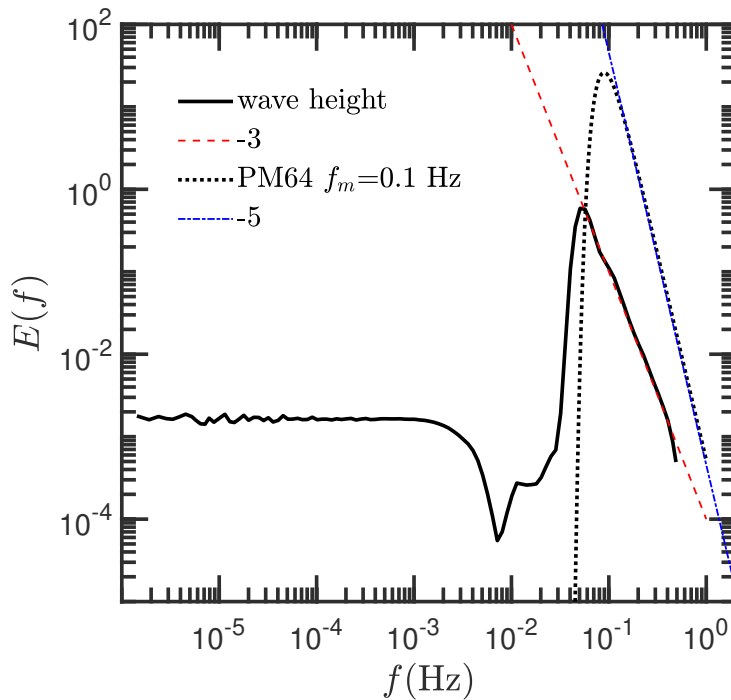


Figure 5.1 Measured Fourier power spectrum for high-frequency wave height data (solid curve) collected by CDIP buoy. The red dashed and blue dash-dotted lines are given as references with slopes of -3 and -5, respectively.

$$H_s \simeq 4\sqrt{\int_{f_m}^\infty E(f)df} = \frac{\sqrt{C_0 g}}{2\pi^2} f_m^{-2}. \quad (5.3)$$

The value of f_m is experimentally related to U_{10} as (Pierson Jr & Moskowitz, 1964),

$$f_m = 0.855g/(2\pi U_{10}). \quad (5.4)$$

Finally, the relationship between H_s and U_{10} is derived within the framework of PM64 as,

$$H_s(U_{10}) \simeq 0.0246U_{10}^2. \quad (5.5)$$

Note that the integral range is set from f_m to infinity in the above derivation, the actual energy contained in that range is only 45.6% of the total energy according to the PM64 spectrum (suppose $f_m=0.1$ Hz). If we set the lower limit as $f_m/2$ (the corresponding energy ratio is close to 1), then the prefactor of the wind-wave relation will be increased to 0.0985.

Another point is that in the above integral calculation, the correction term of $e^{-\frac{5}{4}(\frac{f_m}{4})^4}$ in Eq. (5.1) is simplified as 1, since the integral range is from f_m to infinity, for $f \gg f_m$, this term equals to 1. If we kept this term in the integral estimation, Eq. (5.3) will be in the form as follows,

$$H_s = \frac{g}{\pi^2} \sqrt{\frac{C_0(1 - e^{-5/4})}{5}} f_m^{-2}, \quad (5.6)$$

then the relation between H_s and U_{10} is changed to

$$H_s(U_{10}) \simeq 0.0186U_{10}^2. \quad (5.7)$$

Again, if the lower limit in the integral is changed to $f_m/2$, then the prefactor will be increased to 0.22 here. The effects of the lower limit on the prefactor α is tested with the lower limit kf_m (k is from 0.01 to 1) for both Eq. (5.1) and the one without the correction term. The results are shown in Figure 5.2, in which the red and black curves are respectively the spectrum with and without the correction term. According to this figure, the effects of an integral lower limit to the derived α is relatively trivial in the original PM64 spectrum form with the correlation term.

5.2 Swell Identification

The ocean surface gravity waves are mixed products of swell waves and wind waves. Swell waves are waves generated from distant climate systems, which propagate away from the support of wind. This kind of wave often has a relatively long wave period, normally larger than 10 s (Kinsman, 1984; Toffoli and Bitner-Gregersen, 2017), and wave-

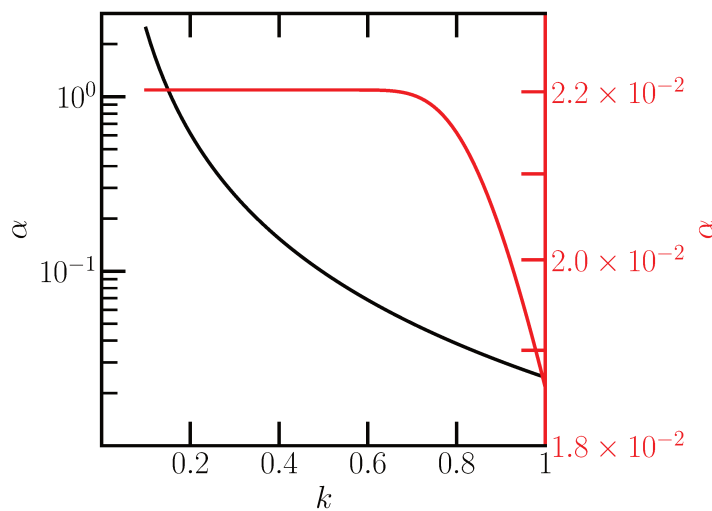


Figure 5.2 Measured prefactor α in the wind-wave relation derived from the PM64 spectrum with (red) and without (black) the correction term for various lower limits in the integral calculation.

length (greater than 260 m to a maximum of approximately 900 m), and could travel thousands of kilometers. In the previous state of swells, the wind waves are more complicated with relatively short wave periods and wavelengths. The wind waves are directly derived from the local wind, thus highly related to the wind speed and directions. To better describe the coupled relation between local winds and waves, a decomposition of the swell and wind waves should be considered.

5.2.1 Conventional Methods

There are a few choices to make this partition if additional information is available. For instance, the swell can be distinguished by the observer's visual subjective criteria (Gulev et al., 1998; Gulev and Grigorieva, 2006), but the consistency and accuracy of such visual judgment results highly depend on the experience of the observer. Two objective approaches are also briefly discussed here. The first one is proposed in the framework of the wind-wave relation from the WAM model: Chen et al. (2002) defined the sea state of swell as the situation where the measured H_s is larger than the value predicted by this relation, while the wind waves correspond to the cases where the local measured H_s is smaller than the predicted value. However, as argued by Zheng et al. (2016), the "swell" defined by Chen et al. (2002) is still a sea state of mixed seas, thus the defined "swell" may be overestimated.

Another method that is supposed to be the best way to isolate wind waves and swell

is spectral partitioning (or Spectra Energy Partition, SEP) (Gerling, 1992; Hanson and Jensen, 2004; Hanson and Phillips, 2001; Hwang et al., 2012; Portilla et al., 2009; Wang and Hwang, 2001). However, SEP analysis has strict requirements for the data observations to generate the high-frequency directional wave energy spectrum $E(f, \theta)$, which is used to describe the distribution of sea surface elevation variance as a function of wave frequency and wave propagation direction (θ). Besides, the wind direction (φ) and the wave phase speed c_p are also needed for the decomposition process. Based on the fact that the wave ages for wind waves and swell are different, the two different wave components can be distinguished in the wave energy spectrum by identifying the separation frequency f_s . For WAM model data, this critical frequency is defined as the frequency corresponding to the wave phase speed $c = 1.2 \times 28 \times u_* \cos(\theta - \varphi)$. Where the constant 1.2 is an empirical tuning parameter, 28 corresponds to the peak phase speed $c_p = 28u_*$, and u_* is the friction velocity. Finally, the wind wave and swell parts can be estimated by integrating over the high and low-frequency parts of the spectrum, respectively. The 2D wave spectrum is not easily available, normally it can be estimated by High-Frequency radar and buoy equipped with a digital directional wave module. Thus, it is difficult to apply SEP to large-scale field observations due to the lack of wave spectrum information. Nevertheless, SEP is popularly used in wave model data analysis. For the sake of its simplicity, 1D frequency wave spectrum was developed and can also be used to do the swell identification. There are different ways to define the separation frequency in a 1D wave spectrum (Portilla et al., 2009). For instance, f_s can be derived from the peak frequency f_m of the PM64 spectrum as, $f_s = 0.8f_m$ (Earle, 1984; Quentin, 2002). Additionally, Wang and Gilhousen (1998) proposed the wave steepness algorithm to extract f_s with a 1D wave spectrum-based wave steepness function. It was further developed by Gilhousen and Hervey (2002) with the consideration of U_{10} . The SEP method has been used by many authors to study the regional or global view of swell and wind wave features (Portilla, 2018; Semedo et al., 2015; Zheng et al., 2016). Portilla et al. (2009) investigated various spectral partitioning techniques and methods on the performance of identifying wind waves and swells: significant differences have been found with different partitioning methods, and the existing spectral partitioning methods may deliver inconsistent output for wave systems.

5.2.2 Probability-based Swell Identification

To take into account the swell wave and to relax the FDS assumption, we propose a generalized power-law relation between wind and waves in the present work. It is first

verified by using long-term buoy collected data to show the efficiency of decomposing swell from wind waves and of recovering the power-law relation between wind and waves. The global patterns of the swell wave and wind-wave relation are then extracted by using 17 years of JASON altimeter calibrated wind and wave data.

Here, we first consider the empirical joint probability density function (PDF) $p(H_s, U_{10})$ for the wind and wave data collected by NDBC buoy 46086 as an example. The joint PDF is shown in Figure 5.3 a as a color plot. The conditional PDF of H_s for a given U_{10} value possesses a well-defined maximum; several of these are shown in Figure 5.3 b. For a given U_{10} value, we note H_{s0} the value of H_s corresponding to this maximum. This defines a new continuous curve, in which we denote $H_{s_{sw}}$ with the following formulation:

$$H_{s_{sw}}(U_{10}) = H_{s0}; p(H_{s0}, U_{10}) = \max_{H_s} \{p(H_s, U_{10})\} \quad (5.8)$$

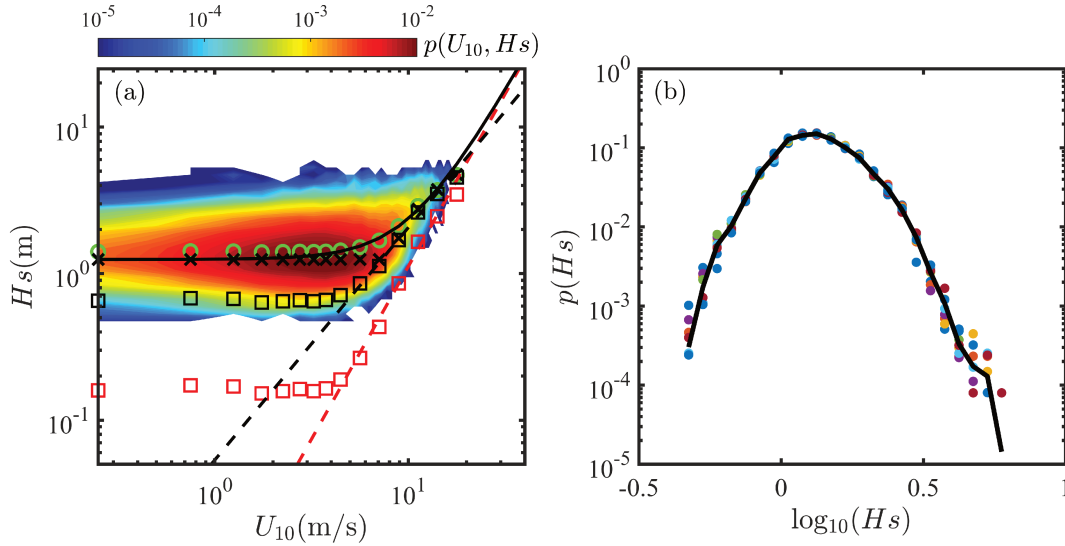


Figure 5.3 (a) Measured joint PDF of U_{10} and H_s collected by NDBC buoy 46086, where the green circles are the conditional mean $\overline{H_s}(U_{10})$; black crosses are the skeleton $H_{s0}(U_{10})$ of the joint PDF; the red squares and black squares are the local significant wave height $\overline{H_{sLi}}(U_{10})$ and $\overline{H_{sLe}}(U_{10})$ derived via the linear decomposition and energy conservation approach, respectively. The dashed lines are the best fittings of the relation between $\overline{H_{sLi}}(U_{10})$ and U_{10} . The black solid curve is a reconstruction of the significant wave height based on Equation (5.12). (b) The conditional PDFs for H_s at light wind speeds, e.g., $U_{10} \lesssim 4$ m/s. The solid curve is the average PDF.

This corresponds to a so-called skeleton of the joint PDF, illustrated as black crosses in the figure. It is visible that $H_{s_{sw}}(U_{10})$ is constant for light winds (e.g., $U_{10} \lesssim 4$ m/s), while increasing rapidly for strong winds (e.g., $U_{10} \gtrsim 4$ m/s). Thus, it is reasonable to assume that in light wind conditions, the wave height is independent or weakly de-

pendent on the local wind and that the local wave is surpassed by regular swell waves that have been generated from distant weather systems. Therefore, we propose here that the value corresponding to the maximum probability of H_s at light wind speeds, $H_{s_{sw}}(U_{10})$ is the significant swell wave height. In the same figure, the conditional mean $\overline{H}_s(U_{10}) = \int p(h, U_{10})h dh$ is also represented and illustrated as blue circles in the figure. It is visible that $\overline{H}_s(U_{10}) > H_{s_{sw}}(U_{10})$. As aforementioned, the swell wave is either a constant or weakly dependent on the local wind, one thus can further determine the overall significant swell wave height $\overline{H}_{s_{sw}}$ by averaging the almost constant swell values for low wind velocities:

$$\overline{H}_{s_{sw}} = \langle H_{s_{sw}}(U_{10}) \rangle_{U_{10} \leq U_{cr}} \quad (5.9)$$

where $\langle \cdot \rangle$ means average, U_{cr} is a critical wind speed (e.g., 4 m/s here), above which the local wave is then dominated. This way, a constant swell value $\overline{H}_{s_{sw}}$ is extracted from the data. For this case, $\overline{H}_{s_{sw}}$ is numerically found to be 1.25 m.

5.3 Local Wind Wave Identification

Ideally, the recorded significant wave height $H_s(U_{10})$ at a certain local wind speed U_{10} can be decomposed into two parts: i) the swell significant wave height $\overline{H}_{s_{sw}}$ that propagate from distant seas; ii) the local significant wave height $\overline{H}_{s_L}(U_{10})$ generated by the local wind. In the last section, the swell part is extracted by a probability-based approach, then two different wind wave estimators are introduced here.

5.3.1 Linearly Decomposed Wind Wave

The first method to do the wind wave identification is based on the idea of linear decomposition, assuming that the collected waves are linearly composed of swell and wind waves. This assumption has been taken and used by many authors to construct the relation between wind and waves (Chen et al., 2002; Andreas and Wang, 2007; Pandey et al., 1986). In this way, the local significant wave height can be obtained by removing the swell value from the conditional mean as follows,

$$\overline{H}_{s_{Ll}}(U_{10}) = \overline{H}_s(U_{10}) - \overline{H}_{s_{sw}} \quad (5.10)$$

the subscript l is used to indicate the linearly decomposed local wind waves. This quantity is plotted in Figure 5.3 a as red squares: it is shown to follow a power-law relation with

the wind speed above U_{cr} ,

$$\overline{H}_{sLl}(U_{10}) = \alpha_l U_{10}^{\eta_l}; \quad U_{10} > U_{cr} \quad (5.11)$$

where α_l is the prefactor, and η_l is the scaling exponent for the relation, the subscript l is used to emphasize the prefactor, and the scaling exponent is extracted from the linear decomposed wind waves. Note that, as aforementioned, η_l can be different from the value of 2 for the FDS. Here the measured scaling exponent is $\eta_l = 2.26$ on the wind speed range $4 \lesssim U_{10} \lesssim 15$ m/s, see the red dashed line in Figure 5.3 a.

In this way, the \overline{H}_s can be decomposed into $\overline{H}_{s_{sw}}$ and \overline{H}_{sLl} , the later one is related to U_{10} through a power-law relation. Consequently, \overline{H}_s can be expressed as,

$$\overline{H}_s(U_{10}) = \overline{H}_{s_{sw}} + \alpha_l U_{10}^{\eta_l} \quad (5.12)$$

The composited curve, i.e., $\overline{H}_{s_{sw}} + \alpha_l U_{10}^{\eta_l}$ is shown as a black solid line in Figure 5.3 a. Visually, the composited curve agrees well with the measured \overline{H}_s when $U_{10} \lesssim 20$ m/s, with a relative error $\lesssim 5.1\%$. A more careful check shows an average relative error of 0.2% when $4 \lesssim U_{10} \lesssim 20$ m/s. For $U_{10} \lesssim 4$ m/s, the reconstructed \overline{H}_s is overlapped with \overline{H}_{s_0} . Moreover, it is interesting to see a sharp transition of the skeleton $\overline{H}_{s_0}(U_{10})$ roughly at $U_{10} \simeq 8$ m/s, which confirms the above assumption that the swell wave dominates during light winds. To emphasize this point, we show the conditional PDFs for H_s at light winds ($U_{10} \leq 4$ m/s) in Figure 5.3 b. The dots in uniform color mean the measured PDF for H_s in the same wind speed bin, the black solid curve is the averaged PDF. A good collapse of these PDFs is found, indicating that in light wind conditions, the collected H_s are nearly independent of the local wind.

5.3.2 Energy Conservation Based Wind Wave Identification

In the framework of the above method, the local wave is simplified as the residual part which equals the total waves minus the swell wave. According to the ocean wave theory, the waves mainly transfer energy from one place to another without transferring matter, e.g., the total wave energy is equal to the sum of swell energy and the local wind wave energy, thus a strict analytical expression of the local significant wave height should be written as,

$$\overline{H}_{sLe}(U_{10}) = \sqrt{\overline{H}_s(U_{10})^2 - \overline{H}_{s_{sw}}^2} \quad (5.13)$$

The subscript e is adopted here to indicate the wind waves which are identified by the

energy conservation theory. Based on Eq. (5.13), $\overline{H}_{s_{Le}}$ is estimated after obtaining $\overline{H}_{s_{sw}}$ from the probability analysis, the result is shown as black squares in Figure 5.3 a. A power-law behavior is observed in high winds as indicated by the black dashed line, which can be expressed as,

$$\overline{H}_{s_{Le}}(U_{10}) = \alpha_e U_{10}^{\eta_e}; U_{10} > U_{cr} \quad (5.14)$$

The subscript e attached after α and η are used to stress the energy conservation-based results. For this case, the fitted value is $\eta_e=1.59$, smaller than the previous one. The values of $\overline{H}_{s_{Le}}$ are larger than the ones extracted by the linear decomposition method. In this way, \overline{H}_s is related with U_{10} as,

$$\overline{H}_s(U_{10}) = \sqrt{\overline{H}_{s_{sw}}^2 + (\alpha_e U_{10}^{\eta_e})^2} \quad (5.15)$$

The energy conservation based reconstruction of \overline{H}_s is shown as a red dashed curve in Figure 5.6 b, it is coincidence with the one the produced by Equation (5.12) (see the black curve) in $U_{10} \lesssim 15$ m/s.

The identified \overline{H}_{s_L} from the two introduced methods both show power-law features with \overline{U}_{10} , but with different scaling exponents due to the inconsistency of the values of \overline{H}_{s_L} . \overline{H}_{s_L} shows an asymptotic feature to \overline{H}_{s_0} in high wind speeds, the asymptotic speed for $\overline{H}_{s_{Le}}$ measured from the energy conservation-based approach is faster than the one from the linear decomposition. Consequently, the values of linearly decomposed $\overline{H}_{s_{Ll}}$ are smaller than the ones from the energy conserved decomposition, but with a relatively large scaling exponent η_l . Though differences for \overline{H}_{s_L} between the two identifiers are found, the composited curves for significant wave height are the same for $U_{10} \lesssim 15$ m/s, and close to the measured \overline{H}_s and \overline{H}_{s_0} in high and light wind speeds, respectively, indicating that the two reconstruction equations both can be used to describe the relation between wind and waves.

5.4 Validation of the Decomposition

With the introduced probability analysis, swell waves can be identified, then the wind waves are decomposed by two different methods. The proposed method is based on the data themselves, not related to the assumption of FDS, and also without the requirement of wave spectra information. As aforementioned, the best way to isolate swell from wind waves is SEP, but with the precondition of observed wave spectra data. Since most offshore buoys are not equipped with Digital Directional Wave Module (DDWM), one can-

not obtain the wave spectra according to the propagation direction of waves. Some buoys which are located in bays or in nearshore locations are equipped with DDWM, which can provide one-dimensional wave spectra data. For instance, NDBC buoy 46086 has collected the wave spectra information for several years, thus, SEP analysis could be performed to do the wave partitioning and to verify the swell and wind waves identified by probability-based method. The data we used to do the test was collected from 2015 to 2021, see Figure 5.4, a portion of the collected wave spectra by NDBC buoy 46086 during 27-31 December 2021.

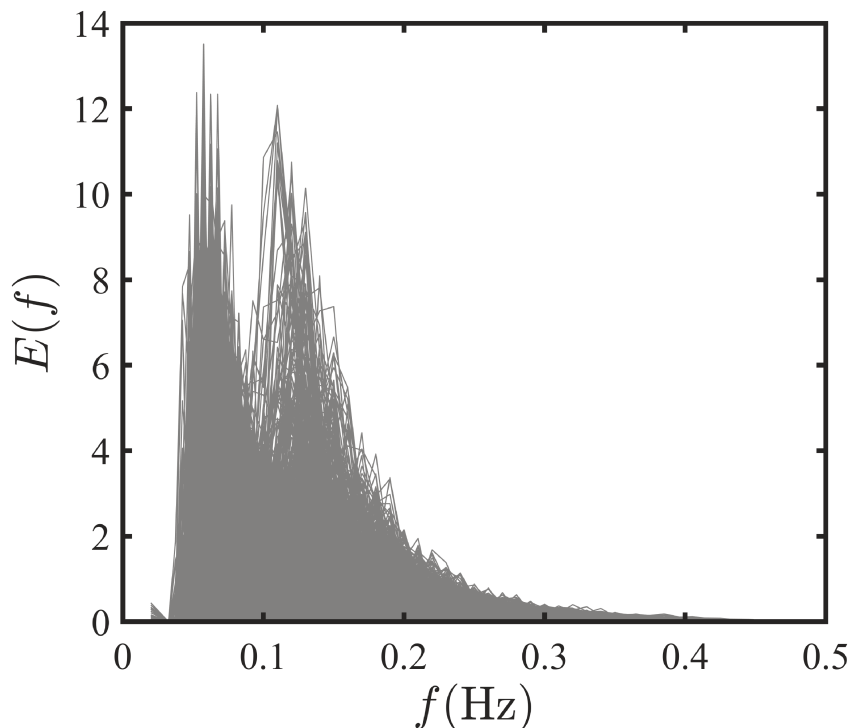


Figure 5.4 Examples of wave frequency spectra collected by NDBC buoy 46086.

Here two normally used f_s estimation methods are selected in the SEP analysis, the first one is the PM64-based algorithm (e.g., $f_s = 0.8f_m$), and another one is the steepness algorithm (Gilhousen and Hervey, 2002). The extracted average $H_{s_{sw}}$ are equal to 1.35 m, and 1.31 m, respectively: both are close to the one derived from the probability-based approach. The measured joint PDF of U_{10} and $H_{s_{sw}}$ derived by SEP with PM64-based f_s is illustrated in Figure 5.5 a, in which the red curve is the conditional average $\overline{H}_{s_{sw}}$. The mean values of $\overline{H}_{s_{sw}}$ are independent of local wind speed when $U_{10} \lesssim 13$ m/s. A decrease of $\overline{H}_{s_{sw}}$ is found when $U_{10} \gtrsim 13$ m/s, it might be caused by statistical errors in high wind speed conditions due to the data amount is not enough. Figure 5.5 b shows the joint PDF of U_{10} and H_{s_L} , as indicated by the red average curve, \overline{H}_{s_L} increase rapidly

above the wind speed of 2.5 m/s. The inset in Figure 5.5 b illustrates the ratio between $\overline{H}_{s_{sw}}$ and \overline{H}_{s_L} at various wind speeds. Under the wind speed of 4 m/s, the ratio is close to 30, meaning that the swell is dominant in light winds. The ratio dramatically drops when $U_{10} \gtrsim 4$ m/s, and reaches 1 when U_{10} is around 8 m/s. After that, with the increase of U_{10} , the ratio approaches 0, indicating that the H_s is governed by H_{s_L} . These results support the assumption we made in the probability analysis, namely, that the collected H_s is dominated by swell waves for light wind conditions.

The $\overline{H}_{s_{sw}}$ and \overline{H}_{s_L} separated by SEP are also shown in Figure 5.6 a as blue and red curves, respectively. Measured $\overline{H}_{s_{sw}}$ from SEP are close to the skeleton \overline{H}_{s_0} of the joint PDF in light winds, slightly larger than $\overline{H}_{s_{sw}}$ extracted by the probability-based method. Power-law behavior of \overline{H}_{s_L} measured via SEP is also clear when U_{10} exceeds 4 m/s, the corresponding scaling exponent is equal to 1.83. Moreover, the values of \overline{H}_{s_L} estimated by SEP are close to \overline{H}_{s_0} and $\overline{H}_{s_{Le}}$ in high winds, but larger than $\overline{H}_{s_{LL}}$.

The reconstruction of \overline{H}_s from $\overline{H}_{s_{sw}}$ and \overline{H}_{s_L} separated by SEP is shown as a blue curve in Figure 5.6 b. It is well superimposed to the measured \overline{H}_s as shown by the green circles, indicating the successful separation made by SEP. The differences between the reconstructions by SEP and the two proposed methods are found for $U_{10} \lesssim 4$ m/s, where the latter two coincidence with \overline{H}_{s_0} , slightly smaller than the one reconstructed by the SEP analysis.

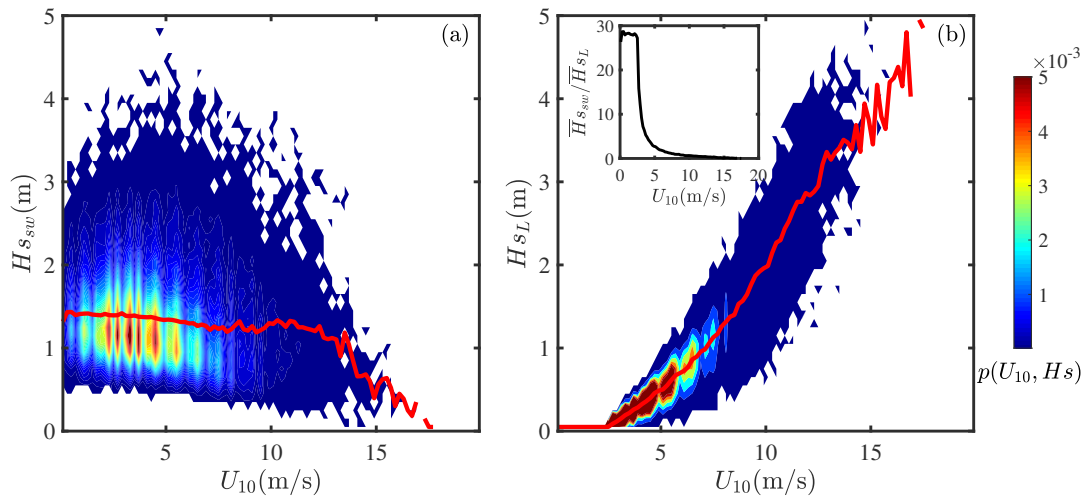


Figure 5.5 (a) Measured joint PDFs of (a) U_{10} and $H_{s_{sw}}$, and (b) U_{10} and H_{s_L} extracted from the data provided by NDBC buoy 46086 with SEP analysis. The solid curves are the conditional average H_s . The inset in (b) shows the ratio between $\overline{H}_{s_{sw}}$ and \overline{H}_{s_L} at various wind speeds.

With the proposed probability-based approach, the swell waves can be identified from the collected H_s without the wave spectrum information. Consequently, the local

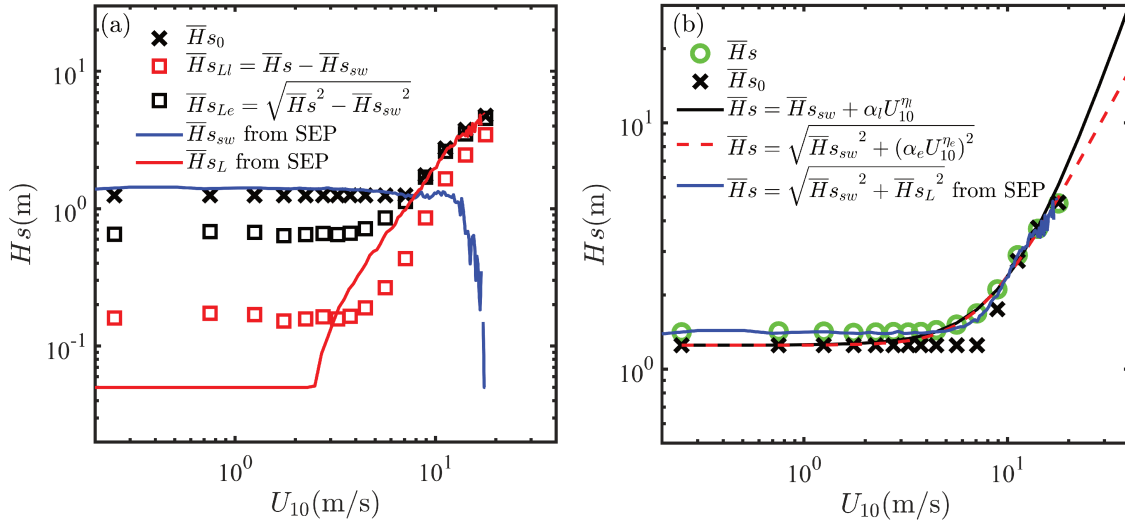


Figure 5.6 (a) Measured skeleton \bar{H}_{s_0} (black crosses) for the joint PDF of U_{10} and H_s data collected by NDBC buoy 46086. The red and blue squares are the extracted local significant wave heights $\bar{H}_{s_{Ll}}$ and $\bar{H}_{s_{Le}}$, respectively. The blue and red curves are the swell significant wave height $\bar{H}_{s_{sw}}$ and local significant wave height \bar{H}_{s_L} extracted by the SEP approach. (b) The green circles and black crosses are \bar{H}_s and \bar{H}_{s_0} , respectively. The black and red dashed curves are the reconstructions of \bar{H}_s based on Equation (5.12) and Equation (5.15), respectively. The blue curve is the reconstruction of \bar{H}_s based on the results from SEP analysis.

wind waves are obtained by a linear decomposition or an energy-conserved decomposition. After that, a power-law relation between wind speed and the local wave is established. We note that the probability-based swell identification could be put into practice only with an accumulated large number of data since the processes are based on joint PDF analysis. The corresponding results are valid in an average sense. The main advantages of the current method are as follows: i) only the overall significant wave height is needed when estimating the swell; ii) the influence of the anomalous values will be automatically excluded since they are in the tail of the PDFs; iii) the power-law relation between the local wind and waves is recovered for the high wind speeds for which the influence of the swell is nearly excluded. Similar results obtained from SEP analysis verify the efficiency of the proposed swell identification method and confirm that the relation between local wind speed and waves could be further described with a power-law equation. Moreover, the identified wind wave from the energy conservation approach is close to the one obtained by SEP; the wind wave measured by the linear decomposition is smaller than the one from SEP. The reconstructions of \bar{H}_s are all close to each other, indicating the practicality of the proposed swell identification method and the local wind-wave power-law

relations.

5.5 Spatial and Temporal Variations for the Global Swell and the Wind-Wave Relation

The buoy observations are often close to the coastal area as shown in Figure 2.5, thus at a fixed location, and only very few points are covered over the global ocean (see Figure 2.5). To access global views of the swells and wind-wave relations, satellite data are also used in this study. Here we combine the data collected by JASON-1 (from January 2002 to June 2013), JASON-2 (from July 2008 to July 2018), JASON-3 (from February 2016 to July 2018) together (hereinafter referred to as JASON) to study the global distribution and seasonal variations of the significant swell wave height \overline{H}_{sw} , and the relation between wind speed U_{10} and local significant wave height H_{sL} . The calibrated data provided by Ribal and Young (2019) were archived in $1^\circ \times 1^\circ$ bins. For enhancing the accuracy of the swell-local wave decomposition, the data are reassigned in the $2^\circ \times 2^\circ$ boxes. The data in the latitude coverage of 60°S to 60°N are considered for further analysis in this work.

5.5.1 Validation of JASON observations

Before processing the JASON data, the wind and wave data collected by offshore NDBC buoys 41049 (located at 27.49°N , 62.94°W , with the water depth of 5,459 m) and 46006 (located at 40.77°N , 137.38°W , with the water depth of 4,323 m) are selected to make comparisons with JASON observations to examine the data quality. The joint PDFs of U_{10} and H_s data observed by JASON in the areas close to the buoys are estimated, then the skeletons of the joint PDF for the data provided by buoy and JASON are extracted, see Figure 5.7. The skeletons are overlapping for $U_{10} \lesssim 6$ m/s in both cases, except for a deviation found at $U_{10} \simeq 0.75$ m/s for the second case. It might be induced by the uncertainty of satellite observations in extremely low wind conditions. According to the joint PDFs, the \overline{H}_{sw} for NDBC buoy 41049, 46006 both equal to 1.25 m, the \overline{H}_{sw} extracted from JASON data close to buoy 41049 is also 1.25 m, the one near the buoy 46006 is equal to 1.18 m.

After that, the wind waves can be identified to estimate the scaling exponents η for the local wind-wave relation. Two decomposition methods are both used here, the results are illustrated in the insets in Figure 5.7. In this figure, the squares and crosses are the wind

waves derived from the linear decomposition method and the energy conservation-based approach, respectively. The colors of green and black are used to indicate the results from buoy and satellite data. Visually, the derived wind waves are in good agreement between the buoy and satellite observed data, and similar scaling features are found. For the linear decomposition, measured η_l from the data collected by buoy 41049 and nearby JASON data are 2.03 and 2.11, respectively; the results from buoy 46006 and JASON data are 1.71 and 1.53, respectively. For the energy conservation-based approach, η_e from buoy 41049 and JASON data are 1.37 and 1.49, respectively; η_e from buoy 46006 and JASON data are 1.25 and 1.22, respectively. The differences are all less than 0.2. The results of the test show that the JASON data have remarkable performance in the swell identification and the construction of local wind-wave relations. Thus, these data could be used to study global views of swell and the local wind-wave relation with the newly proposed methods.

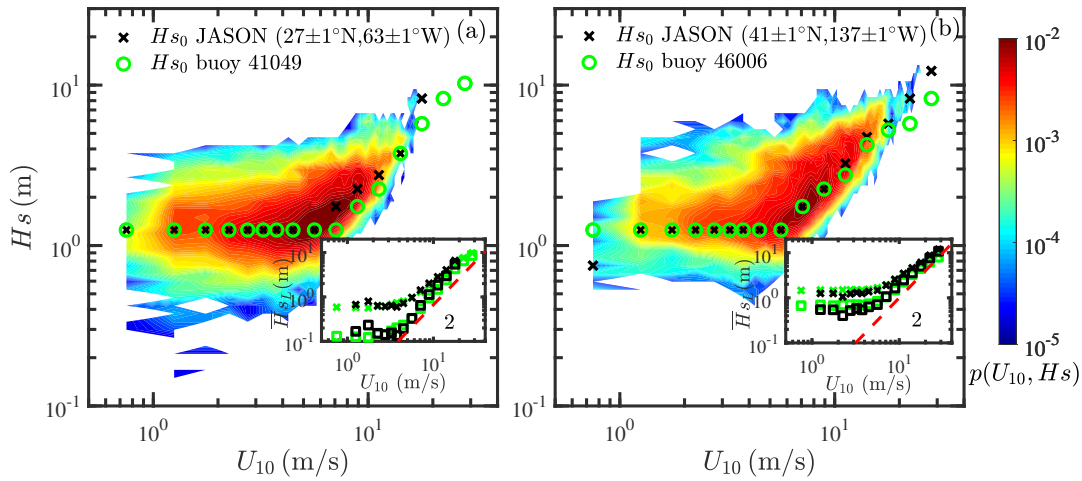


Figure 5.7 (a) Measured joint PDFs of U_{10} and H_s collected by JASON in the areas close to NDBC buoys (a) 41049 and (b) 46006. The black crosses and green circles are the skeletons of the joint PDFs for JASON and buoy data. The insets show the measured \bar{H}_{sL} , in which the squares and crosses indicate the \bar{H}_{sLl} from the linear decomposition and the \bar{H}_{sLe} from the energy conserved decomposition, respectively. The colors green and black are used to indicate the results from buoy and satellite data. The dashed line is given as a reference with the slope of 2.

5.5.2 The Global Distribution Features for Swell

The probability-based swell decomposition procedure is performed at each geographic grid to derive $\bar{H}_{s_{sw}}$ and \bar{H}_{sL} . To have a reasonable sample size for each wind bin, the data are grouped into four seasons: winter (DJF), spring (MAM), summer (JJA), and autumn (SON), respectively. The derived swell is found on the range $0.5 \sim 4$ m, with a

mean value around 1.8 m and a strong seasonal variation, see Figures 5.8. More precisely, the retrieved swell is stronger in the winter hemisphere than the ones in the summer hemisphere for most areas. For instance, the average $\overline{H}_{s_{sw}}$ around 50°N are equal to 2.3 m and 1.2 m in DJF and JJA, respectively. This is partially due to the fact that the swell is positively correlated with the wind speed at high latitudes, see the seasonal averaged \overline{U}_{10} in Figure 5.9. Large winds are observed in mid-latitudes in winter, and in the ACC region all the year. Figure 5.10 shows the comparisons between the meridional variations of \overline{U}_{10} and $\overline{H}_{s_{sw}}$ in different seasons, in which the black and red curves are the longitudinally averaged swell height and wind speed, respectively. The latitudinal variations of $\overline{H}_{s_{sw}}$ and \overline{U}_{10} are measured in each season, and positive connections between swell and local winds are found, especially in high latitudes.

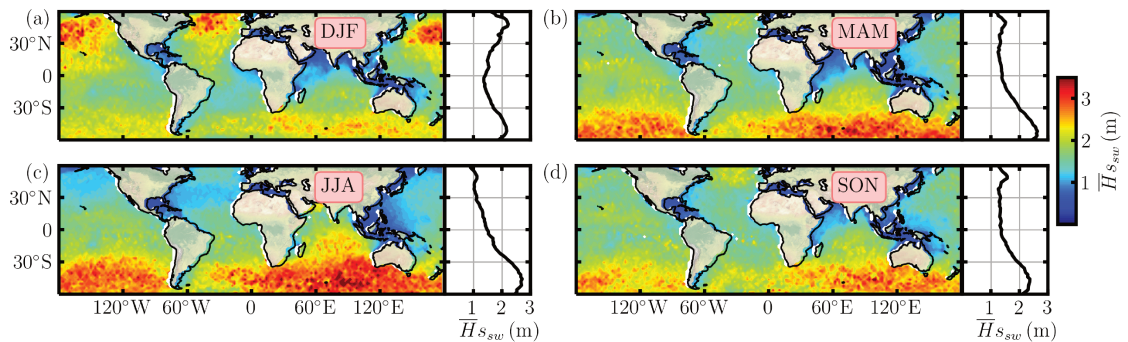


Figure 5.8 Global distributions of seasonal averaged $\overline{H}_{s_{sw}}$ in (a) DJF, (b) MAM, (c) JJA, and (d) SON. The meridional variations are shown in the right panels.

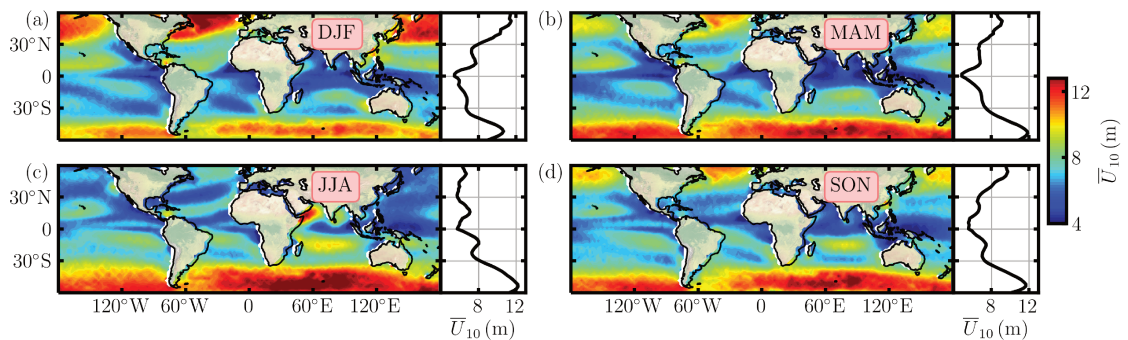


Figure 5.9 Spatial distributions for \overline{U}_{10} in (a) Winter, (b) Spring, (c) Summer, and (d) Autumn.

The spatial patterns of measured swell height agree well with the ones reported by Semedo et al. (2011), where SEP analysis was performed on 45 years ECMWF reanalysis ERA-40 data to extract global views of swell and wind waves. The obtained swell signif-

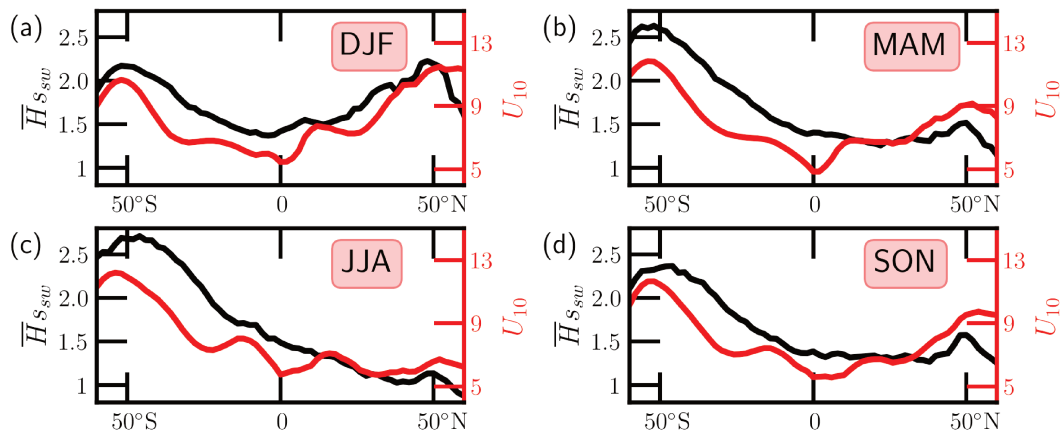


Figure 5.10 Latitudinal variations of $\overline{H}_{s_{sw}}$ (black curve) and U_{10} (red curve) estimated in (a) Winter, (b) Spring, (c) Summer, and (d) Autumn.

icant wave height by Semedo et al. (2011) in DJF and JJA are shown in Figures 5.11 a and 5.11 b, respectively. The results are very close to the ones derived from probability based analysis. For example, large swells are seen in the extratropical areas of the Northern Hemisphere with small ones in several regions in DJF, e.g., the Gulf of Mexico, Indian monsoon area, South China Sea, and north and east coast of Australia, to list a few. Additionally, the longitudinal-averaged curve shows a nearly symmetric shape, see Figure 5.8 a. In the Southern Hemisphere, high values are mainly found in the Antarctic Circumpolar Current (ACC) region, i.e., roughly on the range from 48°S to 58°S , with almost no influence on the continent. In JJA, the swell is increasing from the north to the south and reaches its maximum value in the ACC region.

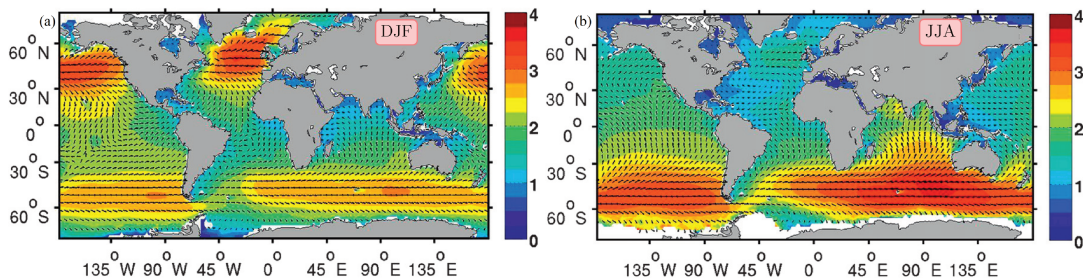


Figure 5.11 Swell significant wave height in (a) DJF and (b) JJA derived by SEP analysis of ECMWF ERA-40 wave reanalysis data (Semedo et al 2011).

5.5.3 Local Wind-Wave Relation

The local wind-wave relation is described by a power-law formula in this study, e.g.,

$\overline{H}_{sL} = \alpha U_{10}^\eta$, while different definitions of \overline{H}_{sL} correspond to distinct power-law features. In this section, the linear decomposition (Eq. 5.10) and energy conserved decomposition (Eq. 5.13) are both used to generate \overline{H}_{sL} with JASON data, then to estimate the prefactor α and the scaling exponent η in the power-law relation.

The fitting of the generalized power-law relation is done via an automatic search algorithm with a width of half decade of the wind speed ranges above 4 m/s. The choice of a half-decade is due to the limited range of wind speed values. The global distribution of measured α in DJF and JJA are shown in Figure 5.12, in which Figures 5.12 a and 5.12 b are the ones fitted with linearly decomposed \overline{H}_{sLl} ; 5.12 c and 5.12 d are the results from the \overline{H}_{sLe} estimated with the energy conservation theory. The fitting algorithm fails on some geolocations, for example, gaps are seen around the equator, corresponding to light wind regions. The values of α_l extracted from \overline{H}_{sLl} are smaller than the ones derived from \overline{H}_{sLe} , and the differences are around a factor of 10. The spatial patterns for α estimated from two defined \overline{H}_{sL} are similar, with small values in the equator and large ones in mid-latitudes. Moreover, seasonal differences are observed, and relatively large α are occurring in the winter hemisphere.

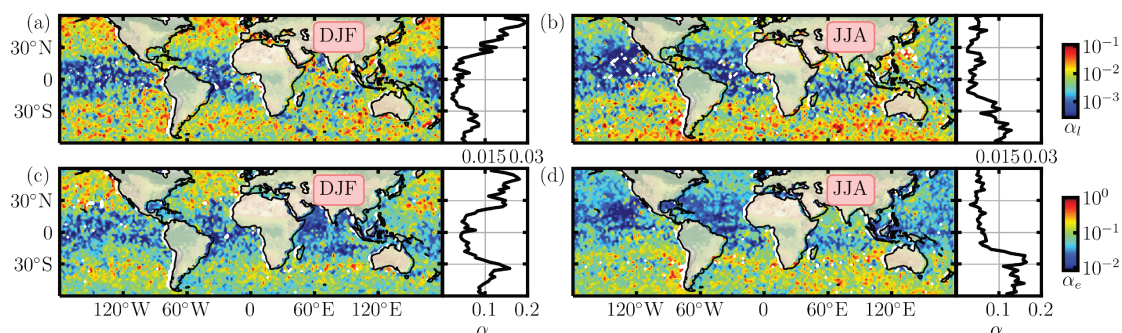


Figure 5.12 Global distributions of α_l measured with the linearly decomposed \overline{H}_{sLl} in (a) DJF and (b) JJA. (c) and (d) are the α_e derived from the \overline{H}_{sLe} decomposed by the energy conservation theory. The meridional variations are shown in the right panels.

The corresponding measured η are shown in Figure 5.13. It is clear that the values of η_l derived from \overline{H}_{sLl} (Figures 5.13 a and 5.13 b) are larger than the ones fitted with \overline{H}_{sLe} (Figure 5.13 c and 5.13 d). Linear decomposition based η_l are found close to the PM64 predicted value, e.g., 2 in winter, where large winds are present. The values of η_e are close to 1.5 in winter. Moreover, a seasonal variation and clear spatial patterns for η are also found: large values of η are found mainly from 25°S to 25°N. The longitudinally averaged η is nearly symmetric in DJF, while it is strongly asymmetric in summer. Furthermore,

opposite meridional variations for η are obtained as compared with the ones for α : large η occur in low latitudes, corresponding to the area of light winds.

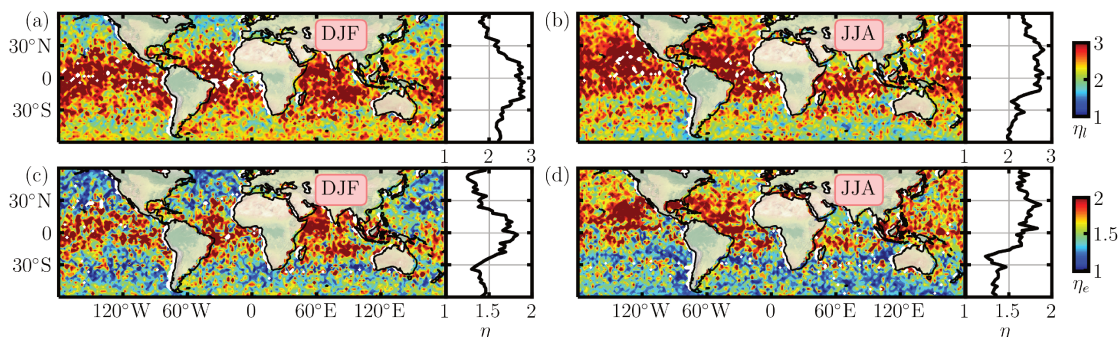


Figure 5.13 Global distributions of η_l measured with the linearly decomposed \overline{H}_{SLl} in (a) DJF and (b) JJA. (c) and (d) are the η_e derived from the \overline{H}_{SLe} decomposed by the energy conservation theory. The meridional variations are shown in the right panels.

The empirical PDFs of α and η are shown in Figure 5.14, in which Figures 5.14 (a) and (c) are the PDFs for α_l and η_l , and (b) and (d) are the ones for α_e and η_e , respectively. For the linear decomposed results, the most probable values (corresponding to the maximum of the PDFs) are $\alpha_l \simeq 0.0065$ and $\eta_l \simeq 2.11$. The latter one agrees well with the FDS's prediction by Pierson Jr. and Moskowitz (1964), while the former value is found to be roughly one-fourth of their prediction. Globally, nearly one-third of the global ocean has values of η_l in the range of [1.8, 2.2]. A longitudinal-averaged plot of which ratio of η_l values belonging to the range of [1.8, 2.2] is shown in the inset of Figure 5.14 (c). Except for summer, this ratio is nearly symmetric with large values in the high latitudes and small values (e.g., less than 0.2) around the equator from 20°S to 20°N. A special case is observed for the Northern Hemisphere in JJA, for example, a mean value of 0.18 is found from 20°N to 60°N, implying a strong influence of the monsoon. For the energy conserved decomposition, the most probable values for α_e and η_e are around 0.077 and 1.45, respectively, both significantly deviating from FDS's prediction. Which ratio of η_e in the range of [1.8, 2.2] is also measured and shown in the inset in Figure 5.14 (d). The maximums are found close to the equator, with a value of 0.2. Due to the effect of the monsoon, the JJA case shows relatively large ratios in the Northern Hemisphere.

To relate the derived α and η , phase diagrams of α versus η are shown in Figures 5.15 in a semilog view, in which the PM64-based curve (see detail in discussion) is also shown as a solid curve for comparison. It is interesting to see a nearly perfect exponential behav-

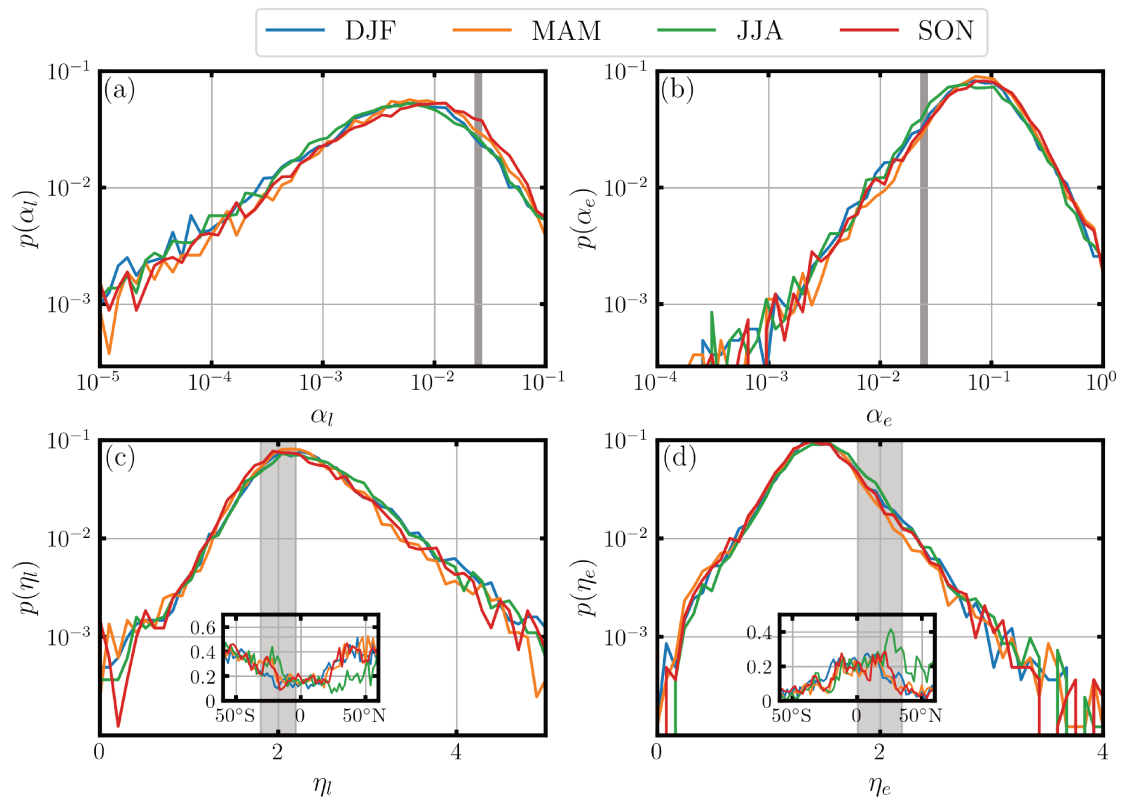


Figure 5.14 Measured PDFs for (a) α_l , (b) α_e , (c) η_l , and (d) η_e in four seasons. The insets in (c) and (d) are the ratio of η values in the range of [1.8, 2.2] for various latitudes. The curves in different colors indicate different seasons.

ior, which is written as,

$$\alpha(\eta) = \omega e^{-\gamma\eta} \quad (5.16)$$

With the least square fitting algorithm, the exponential exponents are found to be $\omega_l = 1.65$ and $\gamma_l = 2.55$. A further examination shows that the values of γ_l are latitude-dependent, e.g., a roughly linear decay is observed in the Southern Hemisphere from their maximum value of 3.0 to a minimum value of 2.25. It is then increasing linearly in the Northern Hemisphere. However, possibly due to the influence of the monsoon in the Northern Hemisphere, a strong seasonal variation is visible, e.g., a significant difference between the DJF and JJA cases is observed, and a decreasing trend is found from 10°N to 60°N for measured γ_l in JJA. As for the energy conservation case, the fitted ω_e and γ_e are found with the values of 2.44 and 2.45, respectively. Hemispherical symmetric variations for γ_e are also found, with a linear decay from mid-latitudes to the equator, except for the one in the Northern Hemisphere in JJA.

If one ignores the existence of the swell waves, a relation between α and η could be

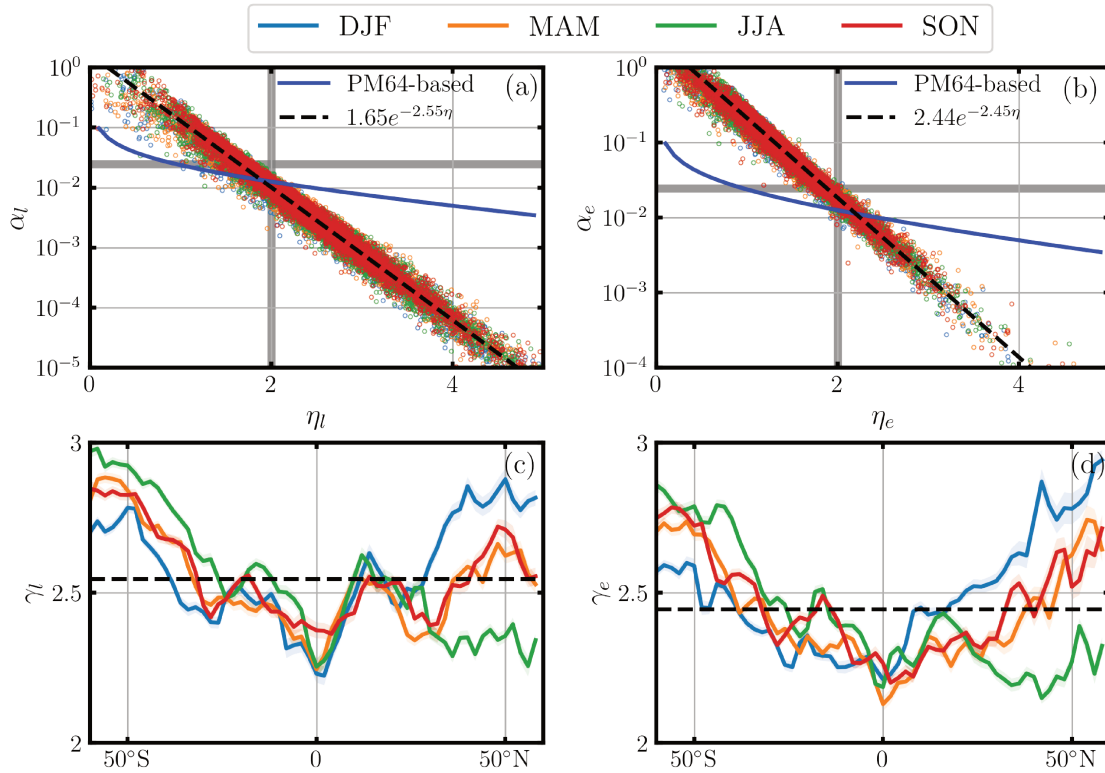


Figure 5.15 Relations between (a) α_l and η_l , (b) α_e and η_e . The dashed lines are the best fittings for the relation, the blue curve is the theoretical relation between α and η based on PM64 assumption. (c) and (d) are the meridional variations of the scaling exponents γ_l and γ_e , respectively, in which the dashed line is the average value.

derived from PM64-like theory. By introducing a variable scaling exponent ζ in the PM64 spectrum, one obtains,

$$E(f) = C_0 g^2 (2\pi)^{-4} f^{-\zeta} e^{-\frac{5}{4} \left(\frac{f_m}{f}\right)^4}, \quad (5.17)$$

Then using the same deducing procedure as we introduced before (set the lower limit of integral as f_m , and ignore the correction term), Equation (5.3) could be rewritten as,

$$Hs \simeq 4 \sqrt{\int_{f_m}^{\infty} E(f) df} = \sqrt{\frac{C_0}{\zeta - 1} \frac{g}{\pi^2} f_m^{-\frac{\zeta-1}{2}}} \quad (5.18)$$

Finally, considering the relation between f_m and U_{10} ($f_m = 0.855g/(2\pi U_{10})$), one

obtains the wind-wave relation as follows,

$$Hs(U_{10}) \simeq \sqrt{\frac{C_0}{\zeta - 1} \frac{g}{\pi^2}} \left(\frac{0.855g}{2\pi} \right)^{-\frac{\zeta-1}{2}} U_{10}^{\frac{\zeta-1}{2}} \quad (5.19)$$

Thus, the scaling exponent η in the PM64-based wind-wave relation e.g., $Hs(U_{10}) = \alpha U_{10}^\eta$, can be related to ζ as $\eta = (\zeta - 1)/2$. Consequently, α and η can be related as,

$$\alpha(\eta) = \sqrt{\frac{C_0}{2\eta} \frac{g}{\pi^2}} \left(\frac{0.855g}{2\pi} \right)^{-\eta} \quad (5.20)$$

The corresponding PM64-like prediction of the relation between α and η is illustrated as solid curves in Figure 5.15, where an exponential behavior is found when $\eta \gtrsim 1$ ($\zeta \gtrsim 3$). With the least square fit algorithm, the scaling exponent γ in the range $1 \lesssim \eta \lesssim 5$ can be obtained with the value of 0.46, largely different from the measured ones. One possible reason is that the swell wave is excluded in this theoretical prediction. A more realistic model to take the swell into account is required in the future to predict this observed exponential relation.

5.6 Discussions

Without knowing the wave spectrum *a priori*, the proposed probability-based swell estimator relies on at least two closely related hypotheses: i) the recorded significant wave height $Hs(U_{10})$ is dominated by the swell for light wind conditions, and ii) the swell wave $\overline{H}_{sw}(U_{10})$ is either weakly or independent of the local wind. These two hypotheses are confirmed by the SEP method, see Figure 5.5. One advantage of the current proposal is that the influence of the anomalous data will be automatically excluded since the skeleton of the joint PDFs is considered. However, to accurately estimate the skeleton (i.e., the nominal swell), important sample size is required. Thus, CFOSAT observed wind and wave data are not used in this work to derive the global patterns of swell and wind-wave relations. To enhance the accuracy of the analysis, 17 years JASON data are used, and the data are separated into four seasons to study the seasonal variations of the swell and wind-wave relations. Here we note that both the atmospheric and oceanic movements are driven either directly or indirectly by solar radiations. Therefore, daily and annual cycles due to earth rotation and revolution are expected. The former one is hard to be detected using the current satellite database since it requires a much larger dataset to capture the daily variations, while the latter one is confirmed. With long-term NDBC observational

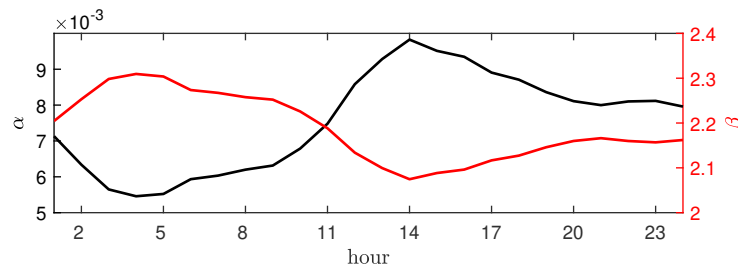


Figure 5.16 Hourly averaged α (black curve) and η (red curve) extracted from the data collected by buoy 41049.

data, daily circles can be derived, see Figure 5.16. In which the black and red curves are respective to the evolution of hourly averaged α and η estimated from the data collected by buoy 41049. Daily circles for α and η are clear, but with anti-phases of the evolution trends.

As illustrated for NDBC buoy data, the generalized power-law formula given by Eq. (5.11) is valid for the large values of the wind speed. Thus, the observed power-law relation is often found for a range of less than one order of magnitude. By removing the swell from the overall significant wave height, this power-law relation is recovered for the local wind waves, see Figure 5.3 a. To observe at least a half-decade of the power-law behavior, there should be enough data samples for the wind speed in the range $4 \lesssim U_{10} \lesssim 25$ m/s. This condition might be not satisfied in the light wind speed regions, e.g., the area around the equator, see Figure 5.12 or Figure 5.13. One possible solution is to use all the available data without dividing it into different seasons. Hopefully, with the accumulation of the observed products from the CFOSAT data, where the wind and waves are simultaneously collected, this difficulty will be overcome in the near future.

5.6.1 Global Views of Wind Waves Based on Power-law Model

Based on the probability-based swell identification method and the generalized wind-wave power-law model, the global distribution of \overline{H}_{sL} and \overline{H}_s could be extracted with given wind speeds. Here the seasonal average wind provided by JASON observations is used to reconstruct global views of \overline{H}_{sL} and \overline{H}_s .

The wind wave height could be measured with linear decomposition or energy conserved decomposition, thus two different wind-wave power-law models were obtained in the previous study. In this section, the two wind-wave relation models are both selected to generate the local wind wave height and the overall wave height with the JASON wind. The measured \overline{H}_{sL} in DJF and JJA are shown in Figures 5.17 a and 5.17 b, respectively.

Figures 5.17 c and d are the results for \overline{H}_{sLe} . The spatial distribution and seasonal differences for \overline{H}_{sLl} and \overline{H}_{sLe} are close to each other, large values are all obtained in mid-latitudes during winter, and smaller ones are observed around the equator for all seasons and the midlatitudes in summer. While the differences between \overline{H}_{sLl} and \overline{H}_{sLe} are clear, \overline{H}_{sLl} is smaller than \overline{H}_{sLe} , the mean difference is around 1 m.

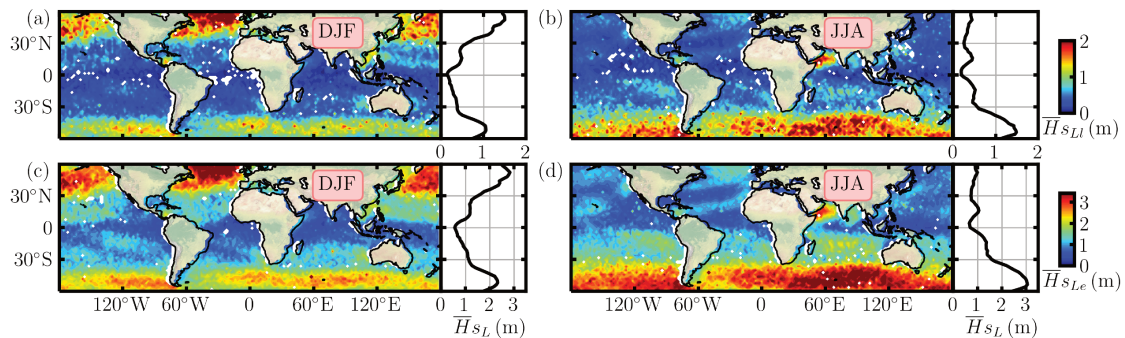


Figure 5.17 Global distributions of estimated \overline{H}_{sLl} in (a) DJF and (b) JJA. (c) and (d) are the results for \overline{H}_{sLe} .

These results are also compared with the ones reported by Semedo et al. (2011), see Figure 5.18. In which Figures 5.18 a and 5.18 b correspond to the months DJF and JJA. The local significant wave height derived from SEP analysis are close to the ones we obtained by the energy conservation-based wind-wave relation model. For instance, relatively large wind waves are found around 50°N in North Atlantic in DJF, with the value close to 3.5 m, while the wind waves are close to 2 m in 50°S in the Indian Ocean. In JJA, the values are turned to 3.5 m in the same area. In addition, large wind waves with the value of 3 m are also observed in the Somali coastal jet-controlled region.

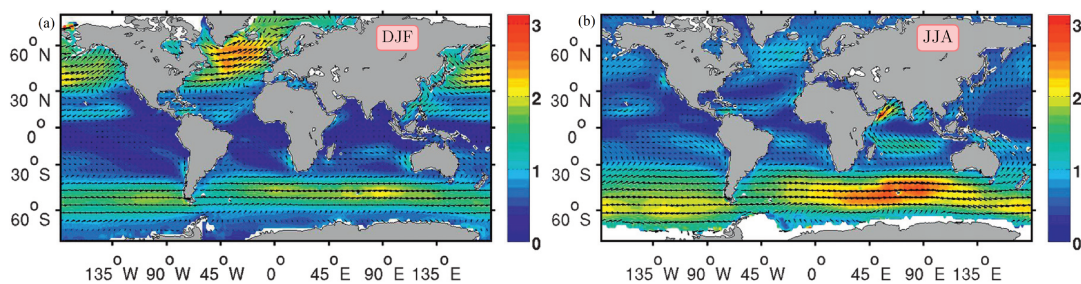


Figure 5.18 Local significant wave height in (a) DJF and (b) JJA derived by SEP analysis of ECMWF ERA-40 wave reanalysis data (Semedo et al 2011).

As shown with the buoy data analysis in Figure 5.6, the significant wave height can be recovered with the derived power-law relation and the swell wave height, the reconstructed \overline{H}_s with the two different approaches (Eq. (5.12) and Eq. (5.12)) are close to each other.

Here the linear and energy conserved reconstructions are both used to reproduce the $\overline{H_s}$ with seasonal averaged U_{10} . The generated $\overline{H_s}$ in DJF and JJA are shown in Figure 5.19, in which Figures 5.19 a and 5.19 b are the $\overline{H_s}$ estimated with the linear reconstruction, Figures 5.19 c and 5.19 d are the ones for energy conservation based reconstruction. The results derived between the two reconstructions are the same, and also close to the seasonal mean $\overline{H_s}$ from JASON observations.

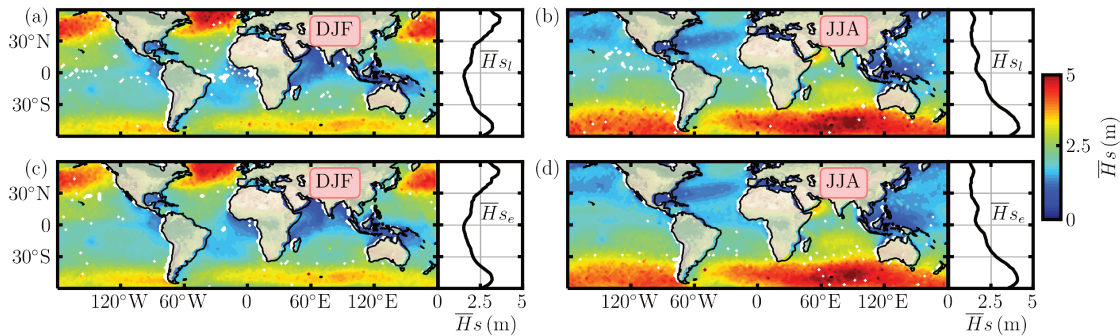


Figure 5.19 Global distributions of reconstructed $\overline{H_s}$ based on Equation 5.12 in (a) DJF and (b) JJA. (c) and (d) are the ones reconstructed by Equation 5.15 in DJF, and JJA, respectively. The meridional variations are shown in the right panels.

5.6.2 CFOSAT Wind Data Based Wave Height Hindcast Verification

Based on 17 years JASON observed wind and wave data, global views of swell and wind-wave power-law relations are obtained, then a generalized wind-wave relation was established. However, due to the short mission periods of CFOSAT or other satellite platforms, the accumulated data are relatively small, and thus cannot be used to study the global views of the swell and wind-wave power-law model. Figure 5.20 shows the joint PDFs of the wind and wave data collected by CFOSAT in the regions around NDBC buoys 41049 and 46006. The black crosses and green circles are the skeletons of the joint PDF for CFOSAT data and buoy data, respectively. It is clear that the skeletons for CFOSAT data are relatively disordered in low and high wind conditions as compared to the ones for buoy data. Thus the CFOSAT data are not recommended to derive the wind-wave relation in this work. The black curve in the figure is the generated wind-wave relation based on the buoy data, which is close to the skeleton of CFOSAT data.

Though the CFOSAT collected wind and wave data are not capable to do global identification of swell waves and establishing the wind-wave power-law relation, the wind and wave data are suitable to validate the JASON data derived wind-wave relation here.

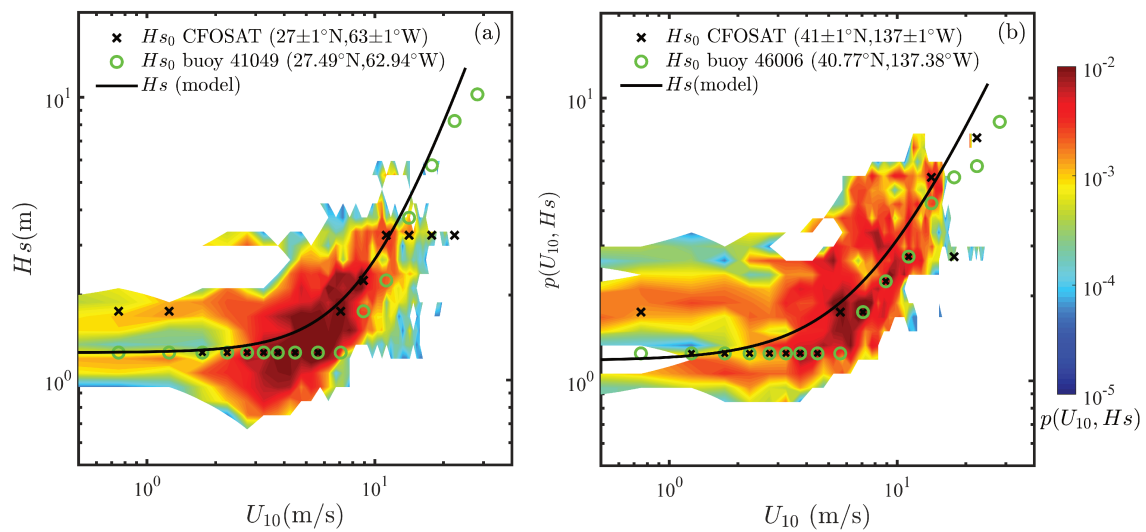


Figure 5.20 (a) Measured Joint PDF of U_{10} and H_s collected by CFOSAT in the areas close to the NDBC buoys (a) 41049 and (b) 46006. The black crosses and green circles are the skeletons of the joint PDF for CFOSAT data and buoy data, respectively.

Figure 5.21 shows the CFOSAT observed wind field, significant wave height, the model produced wave height, and the differences between model and observation.

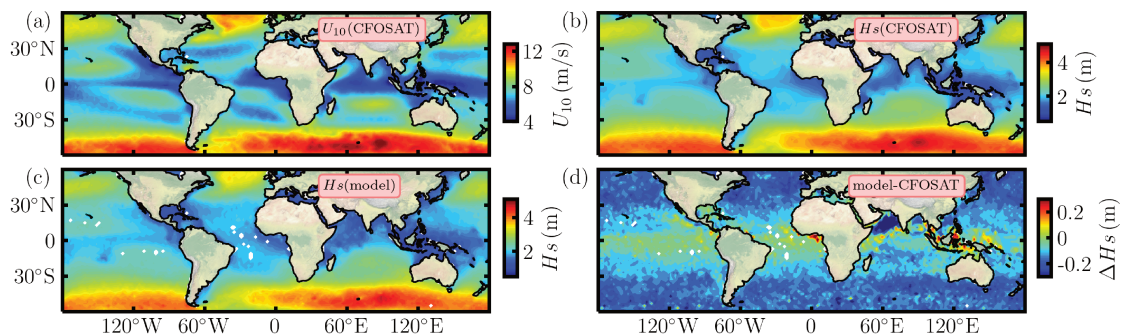


Figure 5.21 Global distribution of (a) U_{10} , and (b) H_s observed by CFOSAT. (c) Wind-wave power-law model generated H_s based on the CFOSAT wind data. (d) The differences between model results and observations.

We note that the wind-wave power-law models derived from linearly decomposed and energy conservation decomposed local significant wave heights are different, while the reconstructed wave height is the same. Thus, the linearly decomposed wind-wave relation is used in the test. As shown in Figure 5.21, the significant wave height generated by the wind-wave relation model is highly consistent with the satellite observations. The differences between model and observation are negligible in low-latitudes, whereas for the

small wave height, relatively large discrepancies are found in middle-latitudes. Generally speaking, the differences are less than 0.3 m, which means that the wave height could be retrieved by the proposed wind-wave power-law model in this work.

In order to further evaluate the performance of the above-mentioned relations between U_{10} and H_s , four different statistical parameters, namely the quality function (Q), bias ($Bias$), root-mean-square error (RMSE), and scatter index (SI) are chosen and applied to the wind and wave data provided by 11 other different altimeter missions. These parameters are estimated based on the following relations in which M and O mean the model and observation results, respectively.

$$Q = \frac{Nq}{N} \times 100\% \quad (5.21)$$

$$Bias = \frac{1}{N} \sum_{i=1}^N (M_i - O_i) \quad (5.22)$$

$$RMSE = \sqrt{\frac{1}{N} \sum_{i=1}^N (M_i - O_i)^2} \quad (5.23)$$

$$SI = \frac{\sqrt{\frac{1}{N} \sum_{i=1}^N (M_i - O_i - Bias)^2}}{\frac{1}{N} \sum_{i=1}^N O_i} \quad (5.24)$$

In which, N stands for the number of compared model-observation pairs, Nq is the number of pairs of which the difference between model and observation is less than 0.25m. Note that the model results M are the H_s calculated by performing the power-law model to the other altimeters collected time-averaged global U_{10} ; the observation ones O are the time-averaged collected H_s by altimeters.

Here we show one test with the data collected by CFOSAT, the time-averaged U_{10} is used to derive H_s with the power-law model based on JASON data analysis, then comparisons are made between the model results and observations as shown in Figures 5.21, and 5.22. For the CFOSAT case, there are 8770 model and observational pairs, in which 7726 valid pairs are corresponding to differences of less than 0.25 m, thus the Q index is equal to 88.1%. From the count plot, one can also find that the value of H_s with the largest probability is around 2 m. In addition, for the values smaller and larger than 3 m, the modeled H_s from the power-law model are relatively underestimated and overestimated. The measured $Bias$, $RMSE$, and SI are equal to 0.012 m, 0.17 m, and 0.071, respectively, indicating the good performance of the power-law model.

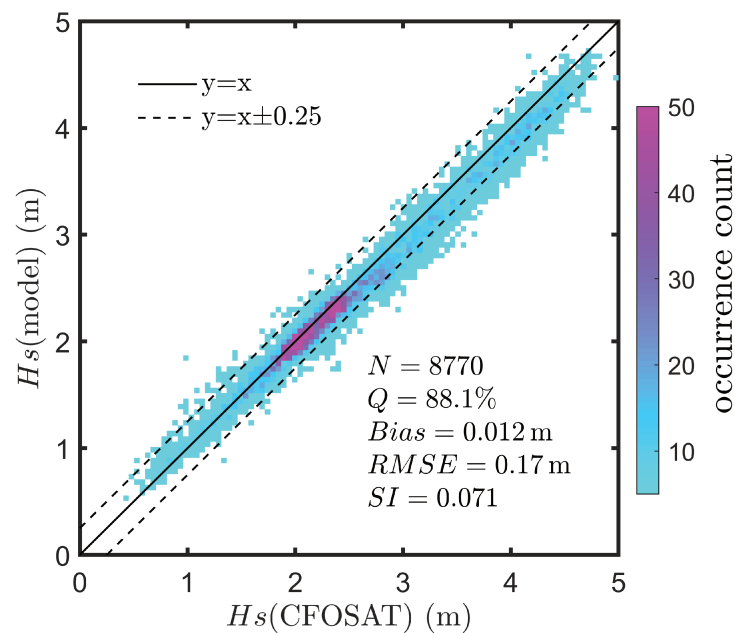


Figure 5.22 Count plot of CFOSAT observed H_s and modeled H_s reported by the wind-wave power-law model based on the SARAL wind data. The solid and dashed lines are given as references defined as $y=x$, and $y=x \pm 0.25$.

Except for testing the power-law model with CFOSAT data, 10 other satellite collected datasets are also used. The time period of the data covers from 1985 to the present, with the altimeter missions of GEOSAT, ERS1, TOPEX, ERS2, GFO, ENVISAT, CRYOSAT-2, HY-2A, SARAL, and SENTINEL-3A. The statistical errors between observations and the model outputs based on the power-law model are summarized in Table 5.1. Relatively poor performances are found with the data collected in the early stage of using altimeters to observe the wind and waves. With the developments of altimeters and data processing algorithms, the accuracy of wind and wave measurements is improved. Here we note that the best measurement is performed by SARAL, which shows the highest value of the quality function, the lowest values of Bias , RMSE , and SI as compared to the other altimeter missions. For conventional altimeters, Ku-band (13.5 GHz) is used, while for the SARAL mission, a unique Ka-band (35.75 GHz) is chosen. The selection of Ka-band for the altimeter avoids the need for a second frequency (which is necessary when using Ku-band) to correct the ionospheric delay. In addition, the use of a larger bandwidth (480 MHz for SARAL, 320 MHz for Ku-band instruments) and a better pulse-to-pulse echo decorrelation also improve the range measurement accuracy of SARAL in a ratio approach to 2 (0.3 m for SARAL, 0.5 m for Ku-band instruments) (Steunou et al., 2015; Verron et al., 2015).

Table 5.1 Statistical Errors for the Model-Observation Comparisons

Altimeters	Q (%)	$Bias$ (m)	$RMSE$ (m)	SI	time periods
GEOSAT	35.4	-0.31	0.36	0.065	03/1985–12/1989
ERS1	57.5	-0.19	0.28	0.066	08/1991–06/1996
TOPEX	62.6	-0.18	0.24	0.041	09/1992–10/2005
ERS2	84.7	-0.11	0.18	0.043	04/1995–05/2009
GFO	32.7	-0.34	0.38	0.064	06/2000–09/2008
ENVISAT	75.5	-0.15	0.21	0.041	05/2000–04/2012
CRYOSAT-2	94.0	-0.098	0.14	0.041	07/2010–07/2018
HY-2A	85.2	-0.096	0.17	0.049	10/2011–06/2018
SARAL	97.3	-0.079	0.13	0.038	03/2016–07/2018
SENTINEL-3A	94.0	-0.062	0.13	0.044	03/2016–07/2018
CFOSAT	88.1	0.012	0.17	0.071	07/2019–12/2021

With the statistical error analysis, the accuracy of the derived global power-law relation between U_{10} and H_s is verified. In addition, the performance of altimeter observations can be also performed with this relation.

5.7 Conclusion

In this chapter, a probability-based swell wave and local wave decomposition was proposed without additional wave spectrum information. It is firstly introduced by using buoy observed wind and wave data, and then verified by SEP analysis of the wave spectra, finally, it is applied to the 17-year-long JASON data. The spatial and seasonal patterns of the retrieved swell are successfully captured, and the results agree well with previous studies (Semedo et al., 2011). After the identification of swell, the local wind waves can be extracted by a linear decomposition or energy conservation-based decomposition. The separated wind waves from the two different methods both show power-law relations with the local wind. In this way, a generalized power-law formula of the wind speed and local significant wave height was advocated by generalizing the FDS hypothesis, e.g., the scaling exponent η was treated as a free parameter. Global patterns of the derived η were presented for the first time. Due to the fact that the linearly decomposed wind waves are lower than the ones from energy conserved decomposition, the corresponding scaling exponent η_l is larger than the ones (η_e) fitted from the energy conserved wind waves. On average, the FDS hypothesis with a scaling exponent equal to 2 might be satisfied in more than one-third of the ocean for the linear decomposition case, mainly in the ACC region around the year, and in the high latitude of the Northern Hemisphere wintertime, where

a strong wind is present. The exponent is largely deviating from the FDS's prediction for the low latitude from 20°S to 20°N, where a weak wind is observed. Partially due to the influence of the monsoon and coverage of the land in the Northern Hemisphere, there is a strong seasonal variation for all parameters presented in this work. For instance, in the Northern Hemisphere, the derived swell in JJA is much weaker than that in DJF (see Figures 5.8 a and 5.8 c); the estimated η in JJA are larger than the ones in DJF (see Figure 5.13); the prefactor α are larger in DJF than those in JJA (see Figure 5.12). The scaling exponents for the wind waves from the energy conservation-based decomposition are closer to 1.5, smaller than the PM64 prediction. Meanwhile, the prefactor α_e is larger than η_l and 0.0246 from the PM64 theory. Though the values of measured local wind waves and the corresponding parameters in the power-law models are different from the two decompositions, the reconstructed \overline{Hs} are the same.

The relation between measured α and η was discussed. Exponential relations have been found with the scaling exponent $\gamma = 2.55$ and the prefactor $\omega = 1.65$ for the linear decomposition. As for the energy conserved decomposition, γ and ω are found as 2.45 and 2.55, respectively. A fine examination shows that γ possesses a linear dependence on the latitude in the Southern Hemisphere, the values of γ are linearly decaying from the mid-latitude to the equator. It is a little more complex in the Northern Hemisphere: linear decreases from high-latitudes to low-latitudes are found for DJF, MAM, and SON, while the one for JJA shows an increasing trend from 60°N to 10°N, see Figures 5.15 c and 5.15. Furthermore, with the established wind-wave relation in this work, a global view of Hs can be obtained when only the wind speed is available. For example, with the seasonally averaged U_{10} information provided by CFOSAT, the corresponding Hs features can be easily reproduced, see Figure 5.21. The 17 years JASON data-based wind-wave power-law relation was further confirmed by the test of 10 more wind-wave datasets collected by altimeter missions.

In summary, this work provides an efficient approach to identifying the swell and also improves the relationship between wind and waves in the global ocean. With the accumulation of satellite data, the spatial and temporal features for swell will be more precise and the wind-wave relation will be further improved in the future. We would like to provide a comment on the physical mechanism associated with the wind-wave relation. While the exact mechanism is still a mystery (Pizzo et al., 2021), the improved quadratic law is an empirical relation without involving first principles. An elegant theoretical consideration of the swell and local wave is still lacking in the scientific literature.

Chapter 6 Conclusion and Future Work

In this chapter, the main results and conclusions of this thesis are summarized. Comments on these results are given. Finally, the prospects for future work are also mentioned.

6.1 Conclusion of the Dissertation

In this thesis, based on the topic of scaling and coupling analysis of turbulent wind and wave data, three works have been performed: 1) extracting the multiscale scaling features for wind and wave; 2) studying the scale-to-scale energy and enstrophy fluxes for ocean surface atmospheric movements; 3) establishing the coupled relation between wind and waves. The data used in this work were mainly provided by the CFOSAT project. In addition, as compensated studies for this thesis, data observed from other satellites, QuikSCAT, MetopB, MetopC, HY-2B, and JASON were also used. The corresponding results derived from these studies are summarized in the following subsections.

6.1.1 Scaling Analysis of Wind and Waves

For the first work, Fourier power spectrum analysis and structure-function analysis were used. The estimation of Fourier power spectra in this work is based on the Wiener-Khinchin theorem, namely, estimating the auto-correlation functions at first, then the spectra could be derived via Fourier transform of the auto-correlation function. In this way, the spectra for the data which contain gaps or with irregular sampling steps can be estimated. The detailed description of this method is given in Chapter 2.

In the spectral analysis, power-law features for both U_{10} and H_s were found in the scales from 100-3000 km, with the scaling exponents β varying from 5/3 to 3. The variations were found with spatial and temporal features. The scaling exponents β for U_{10} and H_s are both meridionally dependent with large values occurring in middle and high latitudes and small values in the tropics. For WS, β is smaller inside the convergence zones than those in the relatively steady equatorial dry zone. Due to the existence of energetic convective activities in the low-latitude zones, the scaling exponents β in these regions are closer to the value of 5/3. Concerning the seasonal variations, for most regions, β in winter is larger than those in summer for WS. On the other hand, for the H_s case, β are found larger in summer than those in winter in the Northern Hemisphere; in the tropical

area of the Southern Hemisphere, large β values are found in winter; as for the regions further south than 25°S , the seasonal variations are unclear. Similar results were confirmed using the structure-function analysis, but with a little difference in the power-law ranges. For WS, the power-law features were found from 12.5 to 1000 km, while for H_s , two ranges were detected, e.g., 2 to 30 km, and 100 to 1000 km. The corresponding scaling exponents for the second-order structure function $\zeta(2)$ were found close to 1 in the scales from 50 to 500 km, and 10 to 1000 km for U_{10} and H_s , respectively. The isotropic turbulence prediction of the scaling exponents $\zeta(2) = \beta - 1$ is roughly satisfied in this work. A horizontal isotropy feature for ocean surface wind field in the scales from 100 to 1000 km was confirmed by two-dimensional spectrum and two-dimensional structure-function analyses. Similar scaling features extracted from CFOSAT U_{10} data were also found with the data provided by QuikSCAT, MetopB, MetopC, and HY-2B. Finally, the scaling exponents derived from ECMWF data are relatively large compared to the ones from satellite data analysis. Furthermore, the meridional variations of β from ECMWF data show an opposite trend to the satellite results.

6.1.2 Scale-to-scale Energy and Enstrophy Fluxes Analysis of Wind

In the second work, an improved FST was proposed to process the CFOSAT along-track wind data. The scale-to-scale energy and enstrophy fluxes for oceanic wind fields caused by nonlinear interactions between different scales were obtained. Forward and backward fluxes are found for small and large scales, respectively. The variation for the fluxes and the corresponding transition scales both show spatial variations and temporal evolution. Strong fluxes are observed in midlatitudes and a narrow region close to ITCZ, weak ones are obtained around the equator. For temporal variations, the fluxes are stronger in winter than those in summer. The transition scales for the energy flux are mainly varying from 40 to 100 km, and the ones for the enstrophy flux are varying from 50 to 200 km. Similar energy and enstrophy fluxes have been derived from U_{10} data provided by QuikSCAT mission. The ECMWF reanalysis U_{10} data were also used in this study: large differences were found between the results from model data analyses and the ones from satellite data studies. Thus, we argue that the reanalysis data are not recommended in the energy and enstrophy fluxes analyses. Finally, the third-order longitudinal structure function was applied to the CFOSAT U_{10} data, The results show that the energy dissipation rate ϵ is positive and negative in the scales smaller and larger than 200 km, respectively. In addition, meridional variation of the dissipation rate is also found for all the scales, with strong dissipation in the mid-latitudes and the region of ITCZ.

6.1.3 Coupling Analysis of Wind and Waves

In the last work, a probability-based swell wave and local wave decomposition are proposed without additional wave spectrum information. Due to the fact that databases from CFOSAT are still too small for a global analysis of coupled wind and wave relation, long-term NDBC offshore buoy and JASON collected wind and wave data were used. The results show that the swell wave possesses clear spatial and temporal variations. Large $H_{s_{sw}}$ were found in midlatitudes during wintertime. The longitudinal averaged $H_{s_{sw}}$ are in between 0.5 to 2.5 m, larger $H_{s_{sw}}$ were observed in the Southern Hemisphere due to the lack of continents. Then the local wind waves are extracted by a linear decomposition or an energy conservation-based decomposition: both the derived wind waves show power-law relations with the wind speed but with a variable scaling exponent η . In this way, the relation between wind and local wave height is described with a power-law relation by relaxing the FDS assumption. The scaling exponent η and the prefactor α in the wind-wave relation both show meridional and seasonal variations. On average, for the linear decomposition case, the FDS hypothesis with a scaling exponent $\eta_l = 2$ is satisfied in more than one-third of the ocean, mainly in the ACC region around the year, and in the high latitude of the Northern Hemisphere wintertime, where a strong wind is present. The exponent is largely deviating from the FDS's prediction ($\eta_l \neq 2$) for the low latitudes from 20°S to 20°N, where a weak wind is observed. Rather large differences between the power-law relation derived from energy conservation-based decomposition and PM64 prediction are found, the peak of the probability of η_e is around 1.5. Partially due to the influence of the monsoon and coverage of the land in the Northern Hemisphere, there is a strong seasonal variation for η and α , e.g., the estimated η in JJA is larger than that in DJF; the prefactor α is larger in DJF than the one in JJA.

With the established wind-wave power-law relation in this work, a global view of H_s can be obtained when only the wind speed is available. Tests were performed with the data provided by other satellites, and relatively small differences between observations and power-law model outputs were found, showing that the new wind-wave relation has a very good performance.

6.2 Highlights of the Dissertation

In this dissertation, we mainly focused on the simultaneously observed wind and wave data provided by the CFOSAT project. Using several statistical methods from the fluid dynamic field, the dynamical information about ocean surface processes was sys-

tematically extracted. The highlights and scientific contributions of this thesis are simply summarized as follows:

- a) An improved Fourier power spectrum estimation approach was proposed to measure the Fourier power spectrum for the data which contain gaps or irregular sampling steps, without any interpolation. The bias induced by missing data was reduced by a bootstrap-like algorithm;
- b) The scaling and intermittency features for global ocean surface wind and waves were obtained;
- c) The scale-to-scale energy and enstrophy fluxes for ocean surface wind were extracted with the improved FST;
- d) A probability-based algorithm was proposed to derive the swell waves without knowing the wave spectrum *a priori*;
- e) An improved wind-wave relation was established without the contamination of swell, then the global views of swell waves and the corresponding wind-wave relation were obtained.

The multiscale features of wind and waves and the wind-wave power-law model shown in this thesis not only enrich our fundamental knowledge of ocean surface processes but also could be new benchmarks for oceanic or atmospheric models. For instance, the accuracy of ocean surface modelled wind and waves could be tested with spectral analysis or the wind-wave relation proposed in this work.

6.3 Prospects for Future Works

The complex nature of wind and wave relations is still largely unclear. The works introduced in this thesis are mainly constructed on the descriptions of phenomena; the corresponding background dynamical mechanisms are still not clear and lack suitable theoretical models. However, these mechanisms should be discussed in future studies. Here we proposed some topics as perspectives of this thesis.

In the first work of scaling analysis for wind and wave data, the scaling features were derived, then the results were compared with previously proposed wind and wave theories. Discrepancies were found between theoretical prediction and data analyses. The wind data used in this thesis are close to the bottom of the marine atmospheric boundary layer, which is strongly influenced by the bottom conditions, for instance, the effective

roughness and wave height, temperature profiles, and the variation of the thickness of the boundary layer. Thus, the measured scaling features are always different from the ones predicted by turbulence models. Here we tried to improve the existing theories to adapt the scaling features derived from 10 m wind. As for the scaling features for the significant wave height, the explanation is still lacking. By considering the high-frequency CDIP wave profile data, a possible theory may be proposed. In addition to the theoretical works, we note that the scaling features obtained from Fourier power spectral analysis and second-order structure-function analysis are slightly different, which may be related to the effect of energetic forcings on the second-order structure-function analysis. Here we also considered joint structure functions, Hilbert spectral analysis, and also synchrosqueezed Wavelet transform, which are shown not to be strongly impacted by these energetic structures embedded in the dataset. Furthermore, the scaling differences obtained from various satellite datasets in the scales less than 100 km will be also considered in future studies, focusing on the following points, 1) the differences in scatterometer designs; 2) the wind retrieval algorithms; 3) the quality control qualifications.

For the work of scale-to-scale energy and enstrophy fluxes, only basic flux features were obtained in this thesis. Relatively few works have been devoted to the energy and enstrophy fluxes of atmospheric movements in a global view. We plan to extend our work to study the spatial transportation of the energy and enstrophy fluxes based on the data from multi scatterometer missions. A diagnosis of each term in the energy and enstrophy fluxes functions will be considered. Comparisons of the results derived from different approaches to fluxes measurement will be performed. The forcing terms of the energy and enstrophy fluxes will be discussed to study the dynamical mechanism of the cascade direction and intensity. Furthermore, the latent statistical relation between energy and enstrophy will be also considered in future works.

Note that, due to the limitation of spatial resolutions of scatterometers, the scaling and energy/enstrophy fluxes analyses in this thesis could not extend to the scales below 10 km, namely the submesoscales. The submesoscale dynamics are important to the ocean surface processes due to the fact that large energy amounts are contained in these scales, and thus important to the regional exchange of properties, and structure of marine ecosystems. With high-resolution Synthetic Aperture Radar (SAR, with a spatial resolution of about 50 m) wind data, the scaling analysis for the wind field could reach the scale of 0.1 km, two decades far from the current works. In addition, the energy and enstrophy fluxes analysis may also be applied to SAR data, but we note that the wind direction information from SAR products is not directly observed, model wind direction is provided. Thus, one has to be cautious to interpret the results. Another high-resolution wind and wave dataset will

be considered in future studies from High Frequency (HF) radars in near-shore regions, which can provide high temporal and spatial resolution wind and wave data in a range from several kilometers to hundreds of kilometers with hourly samplings. Thus, regional wind and wave dynamical information and the couplings could be systematically studied.

In our last work, we proposed a probability-based swell wave decomposition but mainly based on the data provided by JASON. With the accumulation of data from CFOSAT, this study may also suit be performed on CFOSAT collected data in a global view, with a high spatial resolution. The diurnal or semi-diurnal periodicity for the wind-wave relation will be further considered by the data collected by all the NDBC buoys, explanations will be given in future studies.

Bibliography

- Adrian, R.J. and C.S. Yao (1986), "Power spectra of fluid velocities measured by laser Doppler velocimetry." *Experiments in Fluids*, 5, 17–28.
- Alexakis, A. and L. Biferale (2018), "Cascades and transitions in turbulent flows." *Physics Reports*, 767, 1–101.
- Aluie, H., M. Hecht, and G. K. Vallis (2018), "Mapping the energy cascade in the North Atlantic Ocean: The coarse-graining approach." *Journal of Physical Oceanography*, 48, 225–244.
- Andreas, E. L. and S. Wang (2007), "Predicting significant wave height off the northeast coast of the United States." *Ocean Engineering*, 34, 1328–1335.
- Antonia, R. A. and P. Burattini (2006), "Approach to the 4/5 law in homogeneous isotropic turbulence." *Journal of Fluid Mechanics*, 550, 175–184.
- Antonia, R. A., S. L. Tang, L. Djenidi, and Y. Zhou (2019), "Finite Reynolds number effect and the 4/5 law." *Physical Review Fluids*, 4, 084602.
- B., Piet M. T. (2009), "Five separate bias contributions in time series models for equidistantly resampled irregular data." *IEEE Transactions on Instrumentation and Measurement*, 58, 1370–1379.
- Bai, K., C. Meneveau, and J. Katz (2013), "Experimental study of spectral energy fluxes in turbulence generated by a fractal, tree-like object." *Physics of Fluids*, 25, 110810.
- Batchelor, G. K. and A. A. Townsend (1949), "The nature of turbulent motion at large wavenumbers." *Proceedings of the Royal Society of London. Series A. Mathematical and Physical Sciences*, 199, 238–255.
- Belcher, S. and J. Vassilicos (1997), "Breaking waves and the equilibrium range of wind-wave." *Journal of Fluid Mechanics*, 342, 377–401.
- Belcher, SE and JCR Hunt (1993), "Turbulent shear flow over slowly moving waves." *Journal of Fluid Mechanics*, 251, 109–148.
- Bendat, J. S. and A. G. Piersol (2011), *Random data: analysis and measurement procedures*. John Wiley & Sons.
- Benedict, L.H., H. Nobach, and C. Tropea (2000), "Estimation of turbulent velocity spectra from laser Doppler data." *Measurement Science and Technology*, 11, 1089.
- Beran, J. (1994), *Statistics for long-memory processes*. CRC Press.
- Biferale, L., S. Musacchio, and F. Toschi (2012), "Inverse energy cascade in three-dimensional isotropic turbulence." *Physical Review Letters*, 108, 164501.
- Boffetta, G. (2007), "Energy and enstrophy fluxes in the double cascade of two-dimensional turbulence." *Journal of Fluid Mechanics*, 589, 253–260.

- Boffetta, G. and R.E. Ecke (2012), "Two-dimensional turbulence." *Annual Review of Fluid Mechanics*, 44, 427–51.
- Bolgiano, R. (1959), "Turbulent spectra in a stably stratified atmosphere." *Journal of Geoscience Research*, 64, 2226–29.
- Brown, G (1977), "The average impulse response of a rough surface and its applications." *IEEE Transactions on Antennas and Propagation*, 25, 67–74.
- Calif, R. and F. G. Schmitt (2012), "Modeling of atmospheric wind speed sequence using a lognormal continuous stochastic equation." *Journal of Wind Engineering and Industrial Aerodynamics*, 109, 1–8.
- Celani, A., S. Musacchio, and D. Vincenzi (2010), "Turbulence in more than two and less than three dimensions." *Physical Review Letters*, 104, 184506.
- Cencini, M., P. Muratore-Ginanneschi, and A. Vulpiani (2011), "Nonlinear superposition of direct and inverse cascades in two-dimensional turbulence forced at large and small scales." *Physical Review Letters*, 107, 174502.
- Cerbus, R. T. and P. Chakraborty (2017), "The third-order structure function in two dimensions: The rashomon effect." *Physics of Fluids*, 29, 111110.
- Charney, J. G. (1971), "Geostrophic turbulence." *Journal of the Atmospheric Sciences*, 28, 1087–1095.
- Chelton, D. B., M. H. Freilich, J. M. Sienkiewicz, and Joan M Von Ahn (2006), "On the use of QuikSCAT scatterometer measurements of surface winds for marine weather prediction." *Monthly Weather Review*, 134, 2055–2071.
- Chen, G., B. Chapron, R. Ezraty, and D. Vandemark (2002), "A global view of swell and wind sea climate in the ocean by satellite altimeter and scatterometer." *Journal of Atmospheric and Oceanic Technology*, 19, 1849–1859.
- Cho, J. YN. and E. Lindborg (2001), "Horizontal velocity structure functions in the upper troposphere and lower stratosphere: 1. observations." *Journal of Geophysical Research: Atmospheres*, 106, 10223–10232.
- CNES (2011), "CFOSAT to gain new insights into sea state." *Observation*, URL <http://www.cnes.fr/web/CNES-en/9334-gp-cfosat-to-gain-new-insights-into-sea-state.php>.
- Cox, C. (1954), "Statistics of the sea surface derived from sun glitter." *Journal of Marine Research*, 13, 198–227.
- Cox, C. and W. Munk (1954), "Measurement of the roughness of the sea surface from photographs of the sun's glitter." *Josa*, 44, 838–850.
- Danilov, S. D. and D. Gurarie (2000), "Quasi-two-dimensional turbulence." *Physics-Uspekhi*, 43, 863.
- Davies, L. and U. Gather (1993), "The identification of multiple outliers." *Journal of the American Statistical Association*, 88, 782–792.

- Dewan, E. (1997), "Saturated-cascade similitude theory of gravity wave spectra." *Journal of Geophysical Research: Atmospheres*, 102, 29799–29817.
- Dewan, E. M. (1979), "Stratospheric wave spectra resembling turbulence." *Science*, 204, 832–835.
- Donelan, M. A., J. Hamilton, and W. Hui (1985), "Directional spectra of wind-generated ocean waves." *Philosophical Transactions of the Royal Society of London. Series A, Mathematical and Physical Sciences*, 315, 509–562.
- Doukhan, P., M.S. Taqqu, and G. Oppenheim (2003), *Theory and applications of long-range dependence*. Birkhauser, Berlin.
- Dutt, A. and V. Rokhlin (1993), "Fast Fourier transforms for nonequispaced data." *Journal of Scientific Computing*, 14, 1368–1393.
- Earle, M.D. (1984), "Development of algorithms for separation of sea and swell." *National Data Buoy Center Technical Report MEC-87-1, Hancock County*, 53, 1–53.
- Ebuchi, N., H. C. Graber, and M. J. Caruso (2002), "Evaluation of wind vectors observed by QuikSCAT/SeaWinds using ocean buoy data." *Journal of Atmospheric and Oceanic Technology*, 19, 2049–2062.
- Evans, D., C.L. Conrad, and F.M. Paul (2003), "Handbook of automated data quality control checks and procedures of the national data buoy center." *NOAA National Data Buoy Center Technical Document*, 03–02.
- Eyink, G. L. (2005), "Locality of turbulent cascades." *Physica D: Nonlinear Phenomena*, 207, 91–116.
- Falnes, J. (2007), "A review of wave-energy extraction." *Marine Structures*, 20, 185–201.
- Formenti, D. (1999), "What is the coherence function and how can it be used to find measurement and test setup problems?" *Sound and Vibration*, 33, 2–3.
- Freilich, M.H. and D.B. Chelton (1986), "Wavenumber spectra of Pacific winds measured by the Seasat scatterometer." *Journal of Physical Oceanography*, 16, 741–757.
- Frisch, U. (1995), *Turbulence: the legacy of AN Kolmogorov*. Cambridge University Press.
- Fuliński, A (2017), "Fractional Brownian motions: memory, diffusion velocity, and correlation functions." *Journal of Physics A: Mathematical and Theoretical*, 50, 054002.
- Gage, K.S. (1979), "Evidence for a $k^{-5/3}$ law inertial range in mesoscale two-dimensional turbulence." *Journal of Atmospheric Sciences*, 36, 1950–1954.
- Gao, SH, YJ Wang, YX Huang, Q Zhou, ZM Lu, X Shi, and YL Liu (2016), "Spatial statistics of atmospheric particulate matter in China." *Atmospheric Environment*, 134, 162–167.
- Gao, Y., Schmitt F.G., Hu J.Y., and Huang Y.X. (2021), "Scaling analysis of the China France Oceanography Satellite along-track wind and wave data." *Journal of Geophysical Research: Oceans*, 126, e2020JC017119.
- Gerling, T. W. (1992), "Partitioning sequences and arrays of directional ocean wave spectra into component wave systems." *Journal of Atmospheric and Oceanic Technology*, 9, 444–458.

- Germano, M. (1992), "Turbulence: the filtering approach." *Journal of Fluid Mechanics*, 238, 325–336.
- Gilhousen, D. B. and R. Hervey (2002), "Improved estimates of swell from moored buoys." In *Ocean Wave Measurement and Analysis (2001)*, 387–393.
- Goda, Y (1997), "Directional wave spectrum and its engineering applications." *Advances in Coastal and Ocean Engineering*, 3, 67–102.
- Gourrion, J., D. Vandemark, S. Bailey, B. Chapron, G.P. Gommenginger, P.G. Challenor, and M.A. Srokosz (2002), "A two-parameter wind speed algorithm for Ku-band altimeters." *Journal of Atmospheric and Oceanic technology*, 19, 2030–2048.
- Grant, H.L., R.W. Stewart, and A. Moilliet (1962), "Turbulence spectra from a tidal channel." *Journal of Fluid Mechanics*, 12, 241–268.
- Greengard, L. and J. Y. Lee (2004), "Accelerating the nonuniform Fast Fourier Transform." *SIAM Review*, 46, 443–454.
- Gulev, S. K., D. Cotton, and A. Sterl (1998), "Intercomparison of the North Atlantic wave climatology from voluntary observing ships, satellite data and modelling." *Physics and Chemistry of the Earth*, 23, 587–592.
- Gulev, S. K. and V. Grigorieva (2006), "Variability of the winter wind waves and swell in the North Atlantic and North Pacific as revealed by the voluntary observing ship data." *Journal of Climate*, 19, 5667–5685.
- Guo, L. X., V. Claire, and S. Larsen (2013), "Spectral structure of mesoscale winds over the water." *Quarterly Journal of the Royal Meteorological Society*, 139, 685–700.
- Hanson, J. L. and R. E. Jensen (2004), "Wave system diagnostics for numerical wave models." In *8th International Workshop on Wave Hindcasting and Forecasting, Oahu, Hawaii*, 231–238, Citeseer.
- Hanson, J. L. and O. M. Phillips (2001), "Automated analysis of ocean surface directional wave spectra." *Journal of Atmospheric and Oceanic Technology*, 18, 277–293.
- Hasselmann, K. (1976), "Stochastic climate models part I. theory." *Tellus*, 28, 473–485.
- Hastenrath, S (1999), "Dynamics of the Pacific equatorial dry zone." *Meteorology and Atmospheric Physics*, 71, 243–254.
- Hauser, D., C. Tison, T. Amiot, L. Delaye, A. Mouche, G. Guitton, L. Aouf, and P. Castellan (2016), "CFOSAT: A new Chinese-French satellite for joint observations of ocean wind vector and directional spectra of ocean waves." In *Remote Sensing of the Oceans and Inland Waters: Techniques, Applications, and Challenges* (Robert J. Frouin, Satheesh C. Shenoi, and K. H. Rao, eds.), volume 9878, 117–136, International Society for Optics and Photonics, SPIE.
- Hauser, D., C. Tourain, L. Hermozo, D. Alraddawi, L. Aouf, B. Chapron, A. Dalphinnet, L. Delaye, M. Dalila, E. Dormy, et al. (2020), "New observations from the SWIM radar on-board CFOSAT: instrument validation and ocean wave measurement assessment." *IEEE Transactions on Geoscience and Remote Sensing*, 59, 5–26.

- Heimbach, P., S. Hasselmann, and K. Hasselmann (1998), “Statistical analysis and intercomparison of WAM model data with global ERS-1 SAR wave mode spectral retrievals over 3 years.” *Journal of Geophysical Research: Oceans*, 103, 7931–7977.
- Hersbach, H., B. Bell, P. Berrisford, S. Hirahara, A. Horányi, J. Muñoz-Sabater, J. Nicolas, C. Peubey, R. Radu, D. Schepers, et al. (2020), “The ERA5 global reanalysis.” *Quarterly Journal of the Royal Meteorological Society*, 146, 1999–2049.
- Huang, Y.X. and F. G. Schmitt (2014), “Time dependent intrinsic correlation analysis of temperature and dissolved oxygen time series using empirical mode decompositions.” *Journal of Marine Systems*, 130, 90–100.
- Huang, Y.X., F. G. Schmitt, J.P. Hermand, Y. Gagne, Z.M. Lu, and Y.L. Liu (2011), “Arbitrary-order Hilbert spectral analysis for time series possessing scaling statistics: Comparison study with detrended fluctuation analysis and wavelet leaders.” *Physical Review E*, 84, 016208.
- Huang, Y.X., F. G. Schmitt, Z.M. Lu, P. Fougairolles, Y. Gagne, Y.L. Liu, et al. (2010), “Second-order structure function in fully developed turbulence.” *Physical Review E*, 82, 026319.
- Huang, Y.X., F. G. Schmitt, Z.M. Lu, and Y.L. Liu (2008), “An amplitude-frequency study of turbulent scaling intermittency using empirical mode decomposition and Hilbert spectral analysis.” *Europhysics Letters*, 84, 40010.
- Huang, Y.X. and L.P. Wang (2018), “Cascade and intermittency of the sea surface temperature in the oceanic system.” *Physica Scripta*, 94, 014009.
- Huisman, S. G., D. Lohse, and C. Sun (2013), “Statistics of turbulent fluctuations in counter-rotating Taylor-Couette flows.” *Physical Review E*, 88, 063001.
- Hurst, H. E. (1951), “Long-term storage capacity of reservoirs.” *Transactions of the American Society of Civil Engineers*, 116, 770–808.
- Hwang, P. A., F. J. Ocampo-Torres, and H. García-Nava (2012), “Wind sea and swell separation of 1D wave spectrum by a spectrum integration method.” *Journal of Atmospheric and Oceanic Technology*, 29, 116–128.
- Ishihara, T., T. Gotoh, and Y. Kaneda (2009), “Study of high-Reynolds number isotropic turbulence by Direct Numerical Simulation.” *Annual Review of Fluid Mechanics*, 41, 165–180.
- Jian, X., W. Zhang, Q. Deng, and Y.X. Huang (2019), “Turbulent lithosphere deformation in the Tibetan Plateau.” *Physical Review E*, 99, 062122.
- Johnson, H.K., H.J. Vested, H. Hersbach, J. Højstrup, and S.E. Larsen (1999), “The coupling between wind and waves in the WAM model.” *Journal of Atmospheric and Oceanic Technology*, 16, 1780–1790.
- Kaneda, Y., J. Yoshino, and T. Ishihara (2008), “Examination of Kolmogorov’s 4/5 law by high-resolution direct numerical simulation data of turbulence.” *Journal of the Physical Society of Japan*, 77, 064401.
- Khatri, H., J. Sukhatme, A. Kumar, and M. K. Verma (2018), “Surface ocean enstrophy, kinetic energy fluxes, and spectra from satellite altimetry.” *Journal of Geophysical Research: Oceans*, 123, 3875–3892.

- King, G. P., J. Vogelzang, and A. Stoffelen (2015), "Second-order structure function analysis of scatterometer winds over the Tropical Pacific." *Journal of Geophysical Research: Oceans*, 120, 362–383.
- Kinsman, B. (1984), *Wind waves: their generation and propagation on the ocean surface*. Courier Corporation.
- Kirchner, J.W. (2005), "Aliasing in $1/f^\alpha$ noise spectra: Origins, consequences, and remedies." *Physical Review E*, 71, 066110.
- Kolmogorov, A. N. (1940), "The Wiener spiral and some other interesting curves in Hilbert space." *Doklady Akademii Nauk SSSR*, 26, 115–118.
- Kolmogorov, A. N. (1941a), "The local structure of turbulence in incompressible viscous fluid for very large Reynolds numbers." *Doklady Akademii Nauk SSSR*, 30, 301–305.
- Kolmogorov, A. N. (1962), "A refinement of previous hypotheses concerning the local structure of turbulence in a viscous incompressible fluid at high Reynolds number." *Journal of Fluid Mechanics*, 13, 82–85.
- Kolmogorov, A.N. (1941b), "Energy dissipation in locally isotropic turbulence." *Doklady Akademii Nauk SSSR*, 32, 19–21.
- Koshyk, J. N. and K. Hamilton (2001), "The horizontal kinetic energy spectrum and spectral budget simulated by a high-resolution troposphere–stratosphere–mesosphere GCM." *Journal of the Atmospheric Sciences*, 58, 329–348.
- Kraichnan, R. H. (1967), "Inertial ranges in two-dimensional turbulence." *Physics of Fluids*, 10, 1417–1423.
- Kraichnan, R. H. (1971), "Inertial-range transfer in two-and three-dimensional turbulence." *Journal of Fluid Mechanics*, 47, 525–535.
- Kraichnan, R.H. (1974), "On Kolmogorov's inertial-range theories." *Journal of Fluid Mechanics*, 62, 305–330.
- Kraichnan, R.H. and D. Montgomery (1980), "Two-dimensional turbulence." *Reports on Progress in Physics*, 43, 547.
- Lang, F., Y. Huang, S.T. Siems, and M.J. Manton (2018), "Characteristics of the marine atmospheric boundary layer over the Southern Ocean in response to the synoptic forcing." *Journal of Geophysical Research: Atmospheres*, 123, 7799–7820.
- Leonard, A. (1975), "Energy cascade in large-eddy simulations of turbulent fluid flows." In *Advances in Geophysics*, volume 18, 237–248, Elsevier.
- Li, M. Y. and Y. X. Huang (2014), "Hilbert–Huang Transform based multifractal analysis of China stock market." *Physica A: Statistical Mechanics and its Applications*, 406, 222–229.
- Li, X. Z., Y. Xu, B. C. Liu, W. M. Lin, Y. J. He, and J. Q. Liu (2021), "Validation and calibration of Nadir SWH products from CFOSAT and HY-2B with satellites and in situ observations." *Journal of Geophysical Research: Oceans*, 126, e2020JC016689.

- Lilly, D. K. (1983), "Stratified turbulence and the mesoscale variability of the atmosphere." *Journal of Atmospheric Sciences*, 40, 749–761.
- Lin, W. M. and X. L. Dong (2011), "Design and optimization of a Ku-band rotating, range-gated fanbeam scatterometer." *International Journal of Remote Sensing*, 32, 2151–2171.
- Lin, W. M., X. L. Dong, M. Portabella, S. Y. Lang, Y. J. He, R. S. Yun, Z. X. Wang, X. G. Xu, D. Zhu, and J. Q. Liu (2018), "A perspective on the performance of the CFOSAT rotating fan-beam scatterometer." *IEEE Transactions on Geoscience and Remote Sensing*, 57, 627–639.
- Lindborg, E (1999a), "Can the atmospheric kinetic energy spectrum be explained by two-dimensional turbulence?" *Journal of Fluid Mechanics*, 388, 259–288.
- Lindborg, E (1999b), "Correlation to the four-fifths law due to variations of the dissipation." *Physics of Fluids*, 11, 510–512.
- Lindborg, E (2002), "Strongly stratified turbulence: A special type of motion." In *Advanced in Turbulence IX, Proceedings of the Ninth European Turbulence Conference, CIMNE, 2002*.
- Lindborg, E (2006), "The energy cascade in a strongly stratified fluid." *Journal of Fluid Mechanics*, 550, 207–242.
- Lindborg, E. and J. YN. Cho (2000), "Determining the cascade of passive scalar variance in the lower stratosphere." *Physical Review Letters*, 85, 5663.
- Liu, J. Q., W. M. Lin, X. L. Dong, S. Y. Lang, R. S. Yun, D. Zhu, K. Zhang, C. R. Sun, B. Mu, J. Y. Ma, et al. (2020), "First results from the rotating fan beam scatterometer onboard CFOSAT." *IEEE Transactions on Geoscience and Remote Sensing*, 58, 8793–8806.
- Liu, Q.H. and N. Nguyen (1998), "An accurate algorithm for nonuniform fast Fourier transforms (NUFFT's)." *IEEE Microwave and Guided Wave Letters*, 8, 18–20.
- Liu, Y. C., S. W. Li, Q. Yi, and D. Y. Chen (2017), "Wind profiles and wave spectra for potential wind farms in South China Sea. part II: Wave spectrum model." *Energies*, 10, 127.
- Lomb, N. R. (1976), "Least-squares frequency analysis of unequally spaced data." *Astrophysics and Space Science*, 39, 447–462.
- Lovejoy, S and D Schertzer (2011), "Space-time cascades and the scaling of ECMWF reanalyses: Fluxes and fields." *Journal of Geophysical Research: Atmospheres*, 116, D14117.
- Lovejoy, S. and D. Schertzer (2013), *The weather and climate: emergent laws and multifractal cascades*. Cambridge University Press.
- Lovejoy, S., A. Tuck, D. Schertzer, and S. Hovde (2009), "Reinterpreting aircraft measurements in anisotropic scaling turbulence." *Atmospheric Chemistry & Physics*, 9, 5007–5025.
- Lovejoy, S, AF Tuck, SJ Hovde, and D Schertzer (2007), "Is isotropic turbulence relevant in the atmosphere?" *Geophysical Research Letters*, 34.
- Lucarini, V., R. Blender, C. Herbert, F. Ragone, S. Pascale, and J. Wouters (2014), "Mathematical and physical ideas for climate science." *Reviews of Geophysics*, 52, 809–859.
- Lumley, J. L. (1992), "Some comments on turbulence." *Physics of Fluids*, 4, 203–211.

- Mandelbrot, B.B. and J.W. Van Ness (1968), "Fractional brownian motions, fractional noises and applications." *SIAM Review*, 10, 422.
- Métais, O., P. Bartello, E. Garnier, J.J. Riley, and M. Lesieur (1996), "Inverse cascade in stably stratified rotating turbulence." *Dynamics of Atmospheres and Oceans*, 23, 193–203.
- Miles, J. W. (1957), "On the generation of surface waves by shear flows." *Journal of Fluid Mechanics*, 3, 185–204.
- Moisy, F., P. Tabeling, and H. Willaime (1999), "Kolmogorov equation in a fully developed turbulence experiment." *Physical Review Letters*, 82, 3994–3997.
- Monaldo, F. (1988), "Expected differences between buoy and radar altimeter estimates of wind speed and significant wave height and their implications on buoy-altimeter comparisons." *Journal of Geophysical Research: Oceans*, 93, 2285–2302.
- Monaldo, F. (1990), "Corrected spectra of wind speed and significant wave height." *Journal of Geophysical Research: Oceans*, 95, 3399–3402.
- Monin, A.S. and A. M. Yaglom (1971), *Statistical fluid mechanics, vols. 1 and 2*. MIT Press, Cambridge, MA.
- Nastrom, G. D., K. S. Gage, and W. H. Jasperson (1984), "Kinetic energy spectrum of large-and mesoscale atmospheric processes." *Nature*, 310, 36–38.
- Nastrom, G.D. and K. S. Gage (1985), "A climatology of atmospheric wavenumber spectra of wind and temperature observed by commercial aircraft." *Journal of the Atmospheric Sciences*, 42, 950–960.
- Ni, R., G.A. Voth, and N.T. Ouellette (2014), "Extracting turbulent spectral transfer from under-resolved velocity field." *Physics of Fluids*, 26, 105107.
- Nie, Q. and S. Tanveer (1999), "A note on third-order structure functions in turbulence." *Proceedings of the Royal Society of London. Series A: Mathematical, Physical and Engineering Sciences*, 455, 1615–1635.
- Oboukhov, A. M. (1962), "Some specific features of atmospheric turbulence." *Journal of Fluid Mechanics*, 13, 77–81.
- Obukhov, A (1941), "Spectral energy distribution in a turbulent flow." *Izvestiya Akademii Nauk SSSR, Seriya Geografii i Geofiziki*, 5, 453–466.
- Obukhov, A.M. (1959), "On influence of buoyancy forces on the structure of temperature field in a turbulent flow." *Doklady Akademii Nauk SSSR*, 125, 1246.
- O’Gorman, P. A. and T. Schneider (2007), "Recovery of atmospheric flow statistics in a general circulation model without nonlinear eddy-eddy interactions." *Geophysical Research Letters*, 34.
- Olauson, J. (2018), "ERA5: the new champion of wind power modelling?" *Renewable Energy*, 126, 322–331.
- Pandey, P.C., R.M. Gairola, and B.S. Gohil (1986), "Wind-wave relationship from SEASAT radar altimeter data." *Boundary-Layer Meteorology*, 37, 263–269.

- Patoux, J. and R. A. Brown (2001), "Spectral analysis of QuikSCAT surface winds and two-dimensional turbulence." *Journal of Geophysical Research: Atmospheres*, 106, 23995–24005.
- Pearson, R. K. (2002), "Outliers in process modeling and identification." *IEEE Transactions on Control Systems Technology*, 10, 55–63.
- Pearson, R. K., Y. Neuvo, J. Astola, and M. Gabbouj (2015), "The class of generalized Hampel filters." In *2015 23rd European Signal Processing Conference (EUSIPCO)*, 2501–2505, IEEE.
- Pearson, R. K., Y. Neuvo, J. Astola, and M. Gabbouj (2016), "Generalized Hampel filters." *EURASIP Journal on Advances in Signal Processing*, 2016, 1–18.
- Percival, D.B. and A.T. Walden (1993), *Spectral analysis for physical applications: multitaper and conventional univariate techniques*. Cambridge University Press.
- Phillips, O. M. (1957), "On the generation of waves by turbulent wind." *Journal of Fluid Mechanics*, 2, 417–445.
- Phillips, O.M. (1985a), "The equilibrium range in the spectrum of wind-generated waves." *Journal of Fluid Mechanics*, 4, 426–434.
- Phillips, O.M. (1985b), "Spectral and statistical properties of the equilibrium range in wind-generated gravity waves." *Journal of Fluid Mechanics*, 156, 505–531.
- Pierson Jr, Willard J (1991), "Comment on "Effects of sea maturity on satellite altimeter measurements" by Roman E. Glazman and Stuart H. Pilorz." *Journal of Geophysical Research: Oceans*, 96, 4973–4977.
- Pierson Jr., Willard J. and L. Moskowitz (1964), "A proposed spectral form for fully developed wind seas based on the similarity theory of S.A. Kitaigorodskii." *Journal of Geophysical Research*, 69, 5181–5190.
- Pinardi, N. and R. F. Milliff (2004), "Comparing the kinetic energy vs. wavenumber in surface wind fields from ECMWF analyses and the NASA QuikSCAT scatterometer." Technical report, Istituto Nazionale di Geofisica e Vulcanologia.
- Pinel, J and S Lovejoy (2014), "Atmospheric waves as scaling, turbulent phenomena." *Atmospheric Chemistry and Physics*, 14, 3195–3210.
- Pinel, J., S. Lovejoy, and D. Schertzer (2014), "The horizontal space–time scaling and cascade structure of the atmosphere and satellite radiances." *Atmospheric Research*, 140, 95–114.
- Pizzo, N., L. Deike, and A. Ayet (2021), "How does the wind generate waves?" *Physics Today*, 74, 38–43.
- Pope, S. B. (2000), *Turbulent flows*. Cambridge university press.
- Portilla, J., F. J. Ocampo-Torres, and J. Monbaliu (2009), "Spectral partitioning and identification of wind sea and swell." *Journal of Atmospheric and Oceanic Technology*, 26, 107–122.
- Portilla, Y. J. (2018), "The global signature of ocean wave spectra." *Geophysical Research Letters*, 45, 267–276.

- Quentin, C. G. (2002), *Study of the ocean surface, its radar signature and its interactions with turbulent momentum fluxes within the framework of the FETCH experiment*. Ph.D. thesis, Université Pierre and Marie Curie-Paris VI.
- Resio, D. T., Val R Swail, Robert E Jensen, and Vincent J Cardone (1999), “Wind speed scaling in fully developed seas.” *Journal of Physical Oceanography*, 29, 1801–1811.
- Ribal, A. and I. R. Young (2019), “33 years of globally calibrated wave height and wind speed data based on altimeter observations.” *Scientific Data*, 6, 1–15.
- Richardson, L. R. (1922), *Weather prediction by numerical process*. Cambridge University Press.
- Riley, J. J. and S. M. DeBruynkops (2003), “Dynamics of turbulence strongly influenced by buoyancy.” *Physics of Fluids*, 15, 2047–2059.
- Rogers, L. (1997), “Arbitrage with fractional Brownian motion.” *Mathematical Finance*, 7, 95–105.
- Romeiser, R. (1993), “Global validation of the wave model WAM over a one-year period using Geosat wave height data.” *Journal of Geophysical Research: Oceans*, 98, 4713–4726.
- Salort, J., B. Chabaud, E. Lévêque, and P.-E. Roche (2012), “Energy cascade and the four-fifths law in superfluid turbulence.” *Europhysics Letters*, 97, 34006.
- Scannell, B. D., T. P. Rippeth, J. H. Simpson, J. A. Polton, and J. E. Hopkins (2017), “Correcting surface wave bias in structure function estimates of turbulent kinetic energy dissipation rate.” *Journal of Atmospheric and Oceanic Technology*, 34, 2257–2273.
- Scargle, J. D. (1982), “Studies in astronomical time series analysis. II-Statistical aspects of spectral analysis of unevenly spaced data.” *The Astrophysical Journal*, 263, 835–853.
- Schertzer, D. and S. Lovejoy (1985), “Generalised scale invariance in turbulent phenomena.” *Physico Chemical Hydrodynamics*, 6, 623–635.
- Schertzer, D. and S. Lovejoy (1987), “Physical modeling and analysis of rain and clouds by anisotropic scaling multiplicative processes.” *Journal of Geophysical Research: Atmospheres*, 92, 9693–9714.
- Schmitt, F, D Schertzer, S Lovejoy, and Y Brunet (1993), “Estimation of universal for atmospheric turbulent multifractal indices velocity fields.” *Fractals*, 1, 568–575.
- Schmitt, F. G. and Y.X. Huang (2016), *Stochastic analysis of scaling time series: from turbulence theory to applications*. Cambridge University Press.
- Scott, R. B. and B. K. Arbic (2007), “Spectral energy fluxes in geostrophic turbulence: Implications for ocean energetics.” *Journal of Physical Oceanography*, 37, 673–688.
- Scott, R. B. and F. M. Wang (2005), “Direct evidence of an oceanic inverse kinetic energy cascade from satellite altimetry.” *Journal of Physical Oceanography*, 35, 1650–1666.
- Semedo, A., K. Sušelj, A. Rutgersson, and A. Sterl (2011), “A global view on the wind sea and swell climate and variability from ERA-40.” *Journal of Climate*, 24, 1461–1479.
- Semedo, A., R. Vettor, Ø. Breivik, A. Sterl, M. Reistad, C. G. Soares, and D. Lima (2015), “The wind sea and swell waves climate in the Nordic seas.” *Ocean Dynamics*, 65, 223–240.

- Spencer, M. W., C. Wu, and D. G. Long (1997), "Tradeoffs in the design of a spaceborne scanning pencil beam scatterometer: Application to seawinds." *IEEE Transactions on Geoscience and Remote Sensing*, 35, 115–126.
- Sreenivasan, K. R. and R.A. Antonia (1997), "The phenomenology of small-scale turbulence." *Annual Review of Fluid Mechanics*, 29, 435–472.
- Steunou, N., J.D. Desjonquères, N. Picot, P. Sengenès, J. Noubel, and J.C. Poisson (2015), "Altika altimeter: Instrument description and in flight performance." *Marine Geodesy*, 38, 22–42.
- Sugianto, D. N., M. Zainuri, A. Darari, S. Suripin, S. Darsono, and N. Yuwono (2017), "Wave height forecasting using measurement wind speed distribution equation in Java Sea, Indonesia." *International Journal of Civil Engineering and Technology*, 8, 604–619.
- Sujbert, L. and G. Orosz (2016), "FFT-based spectrum analysis in the case of data loss." *IEEE Transactions on Instrumentation and Measurement*, 65, 968–976.
- Sukoriansky, S., N. Dikovskaya, and B. Galperin (2007), "On the arrest of inverse energy cascade and the Rhines scale." *Journal of the Atmospheric Sciences*, 64, 3312–3327.
- Suquet, R. R., L. Hermozo, C. Tourain, C. Tison, D. Hauser, P. Schippers, L. Delaye, L. Aouf, A. Dalphinnet, A. Mouche, et al. (2019), "CAL/VAL phase for the SWIM instrument onboard CFOSAT." In *IGARSS 2019-2019 IEEE International Geoscience and Remote Sensing Symposium*, 8015–8018, IEEE.
- Takbash, A., I. R. Young, and Ø. Breivik (2019), "Global wind speed and wave height extremes derived from long-duration satellite records." *Journal of Climate*, 32, 109–126.
- Tarek, M., F. P. Brissette, and R. Arsenault (2020), "Evaluation of the ERA5 reanalysis as a potential reference dataset for hydrological modelling over North America." *Hydrology and Earth System Sciences*, 24, 2527–2544.
- Toba, Y. (1972), "Local balance in the air-sea boundary processes." *Journal of Oceanography*, 28, 109–120.
- Toffoli, A. and E. M. Bitner-Gregersen (2017), "Types of ocean surface waves, wave classification." *Encyclopedia of Maritime and Offshore Engineering*, 1–8.
- Tourain, C., F. Piras, A. Ollivier, D. Hauser, J. C. Poisson, F. Boy, P. Thibaut, L. Hermozo, and C. Tison (2021), "Benefits of the Adaptive algorithm for retracking altimeter nadir echoes: results from simulations and CFOSAT/SWIM observations." *IEEE Transactions on Geoscience and Remote Sensing*, 59, 1–14.
- Tournadre, J. (1993), "Time and space scales of significant wave heights." *Journal of Geophysical Research: Oceans*, 98, 4727–4738.
- Urraca, R., T. Huld, A. Gracia-Amillo, F. J. Martinez-de Pison, F. Kaspar, and A. Sanz-Garcia (2018), "Evaluation of global horizontal irradiance estimates from ERA5 and COSMO-REA6 reanalyses using ground and satellite-based data." *Solar Energy*, 164, 339–354.
- Vallgren, A., E. Deusebio, and E. Lindborg (2011), "Possible explanation of the atmospheric kinetic and potential energy spectra." *Physical Review Letters*, 107, 268501.

- Vallis, G. K. (2017), *Atmospheric and oceanic fluid dynamics*. Cambridge University Press.
- Van Atta, C. W. and W. Y. Chen (1970), "Structure functions of turbulence in the atmospheric boundary layer over the ocean." *Journal of Fluid Mechanics*, 44, 145–159.
- Verron, J., P. Sengenès, J. Lambin, J. Noubel, N. Steunou, A. Guillot, N. Picot, S. Coutin-Faye, R. Sharma, R. M. Gairola, et al. (2015), "The SARAL/AltiKa altimetry satellite mission." *Marine Geodesy*, 38, 2–21.
- Villas B., Ana B., F. Ardhuin, A. Ayet, M. A. Bourassa, P. Brandt, B. Chapron, B. D. Cornuelle, J. T. Farrar, M. R. Fewings, B. Fox-Kemper, et al. (2019), "Integrated observations of global surface winds, currents, and waves: requirements and challenges for the next decade." *Frontiers in Marine Science*, 6, 425.
- Vinnichenko, N. K. (1970), "The kinetic energy spectrum in the free atmosphere—1 second to 5 years." *Tellus*, 22, 158–166.
- Vogelzang, J., G. P. King, and Ad. Stoffelen (2015), "Spatial variances of wind fields and their relation to second-order structure functions and spectra." *Journal of Geophysical Research: Oceans*, 120, 1048–1064.
- Waite, M. L. and P. Bartello (2004), "Stratified turbulence dominated by vortical motion." *Journal of Fluid Mechanics*, 517, 281–308.
- WAMDI Group (1988), "The WAM model—a third generation ocean wave prediction model." *Journal of Physical Oceanography*, 18, 1775–1810.
- Wang, D. and D. Gilhousen (1998), "Separation of seas and swells from NDBC buoy wave data." In *Fifth Int. Workshop on Wave Hindcasting and Forecasting*, 155–162, Environment Canada Melbourne, Florida, FL, ASCE.
- Wang, D. W. and P. A. Hwang (2001), "An operational method for separating wind sea and swell from ocean wave spectra." *Journal of Atmospheric and Oceanic Technology*, 18, 2052–2062.
- Wang, L. P. and Y. X. Huang (2017), "Intrinsic flow structure and multifractality in two-dimensional bacterial turbulence." *Physical Review E*, 95, 052215.
- Wikle, C. K., R. F. Milliff, and W. G. Large (1999), "Surface wind variability on spatial scales from 1 to 1000 km observed during TOGA COARE." *Journal of the Atmospheric Sciences*, 56, 2222–2231.
- Wood, A.T.A. and G. Chan (1994), "Simulation of stationary Gaussian processes in $[0, 1]$ d." *Journal of Computational and Graphical Statistics*, 3, 409–432.
- Wyngaard, J. C. (2010), *Turbulence in the Atmosphere*. Cambridge University Press.
- Xia, H., D. Byrne, G. Falkovich, and M. Shats (2011), "Upscale energy transfer in thick turbulent fluid layers." *Nature Physics*, 7, 321–324.
- Xia, H., H. Punzmann, G. Falkovich, and M. G. Shats (2008), "Turbulence-condensate interaction in two dimensions." *Physical Review Letters*, 101, 194504.
- Xu, Y. S., L. L. Fu, and R. Tulloch (2011), "The global characteristics of the wavenumber spectrum of ocean surface wind." *Journal of Physical Oceanography*, 41, 1576–1582.

- Young, I. R. (1998), “Observations of the spectra of hurricane generated waves.” *Ocean Engineering*, 25, 261–276.
- Young, I. R. and M. A. Donelan (2018), “On the determination of global ocean wind and wave climate from satellite observations.” *Remote Sensing of Environment*, 215, 228–241.
- Young, I. R. and A. Ribal (2019), “Multiplatform evaluation of global trends in wind speed and wave height.” *Science*, 364, 548–552.
- Young, I. R. and L. A. Verhagen (1996), “The growth of fetch limited waves in water of finite depth. Part 2. Spectral evolution.” *Coastal Engineering*, 29, 79–99.
- Young, Roland M. B. and Peter L. R. (2017), “Forward and inverse kinetic energy cascades in Jupiter’s turbulent weather layer.” *Nature Physics*, 13, 1135–1140.
- Zhang, K., X. L. Dong, D. Zhu, and R. S. Yun (2021a), “Estimation and correction of geolocation errors of the CFOSAT scatterometer using coastline backscatter coefficients.” *IEEE Journal of Selected Topics in Applied Earth Observations and Remote Sensing*, 14, 53–61.
- Zhang, Y. B., E. Bodenschatz, H. T. Xu, and H. D. Xi (2021b), “Experimental observation of the elastic range scaling in turbulent flow with polymer additives.” *Science Advances*, 7.
- Zhang, Y. J., L. Comerford, I. A. Kougoumtzoglou, and M. Beer (2018), “ l_p -norm minimization for stochastic process power spectrum estimation subject to incomplete data.” *Mechanical Systems and Signal Processing*, 101, 361–376.
- Zheng, K. W., J. Sun, C. L. Guan, and W. Z. Shao (2016), “Analysis of the global swell and wind sea energy distribution using WAVEWATCH III.” *Advances in Meteorology*, 2016.
- Zhou, Q., Y. X. Huang, Z. M. Lu, Y. L. Liu, and R. Ni (2016), “Scale-to-scale energy and enstrophy transport in two-dimensional Rayleigh–Taylor turbulence.” *Journal of Fluid Mechanics*, 786, 294–308.
- Zhou, Y. (2021), “Turbulence theories and statistical closure approaches.” *Physics Reports*, 935, 1–117.
- Zieger, S., A. V. Babanin, W. E. Rogers, and I. R. Young (2015), “Observation-based source terms in the third-generation wave model WAVEWATCH.” *Ocean Modelling*, 96, 2–25.

List of Publications

Publication from the Master thesis

Yang Gao, Yongxiang Huang, Hongyang Lin, Jia Zhu, Zhenyu Sun, Jianyu Hu (2020). “Surface currents measured by GPS drifters in Daya Bay and along the eastern Guangdong coast”. *Frontiers of Earth Science*, 14(10): 376-383

Publications from the PhD thesis

Yang Gao, Ruixin Huang, Jia Zhu, Yongxiang Huang, Jianyu Hu (2020). “Using the sigma-pi diagram to analyze water masses in the northern South China Sea in spring”. *Journal of Geophysical Research Oceans*, 125(7):e2019JC015676

Guiwen Tan, **Yang Gao**, Yongxiang Huang, Lipo Wang (2021). “Multi-level dissipation element analysis of the surface temperature of the South China Sea”. *Dynamics of Atmospheres and Oceans*, 94(1):101218

Yang Gao, Francois G Schmitt, Jianyu Hu, Yongxiang Huang (2021). “Scaling analysis of the China France Oceanography Satellite along-track wind and wave data”. *Journal of Geophysical Research Oceans*, 126(8):e2020JC017119

Yang Gao, Francois G Schmitt, Jianyu Hu, Yongxiang Huang (2023). “Probability-based wind-wave relation”. *Frontiers in Marine Science*, 9: 1085340

Yang Gao, Francois G Schmitt, Jianyu Hu, Yongxiang Huang (2023). “Scale-to-Scale Energy and Enstrophy Fluxes of Atmospheric Motions via CFOSAT”. *Journal of Geophysical Research Atmospheres* (In preparation)

Yang Gao, Francois G Schmitt, Jianyu Hu, Yongxiang Huang (2023). “Scaling Analysis of the Global Surface Air Temperature”. *Atmospheric Chemistry and Physics* (In preparation)

Curriculum Vitae

Basic Information

Name: YANG GAO

Gender: Male Nationality: Chinese Date of birth: Nov 28.1993

Contact Details:

28 Avenue du Maréchal Foch, Laboratoire d'Océanologie et de Géosciences, 62930 Wimereux, France

Rm. C3-305, Xiping Bld. No. 4221 South Xiang'an Road, Xiamen Univ., 360011, Xiamen, China

Tel: +86-18860026189

Fax: NA, Email:yanggao@stu.xmu.edu.cn

EDUCATION

- 2012.9-2016.6 B.Sc. Zhejiang Ocean University, China, Dept. Marine Science
- 2016.9-2018.6 Ma.Sc Xiamen University, China, Dept. Physical Oceanography
- 2018.9-now Cotutorial PhD program between Xiamen University and Université du Littoral Côte d'Opale, Dept. Physical Oceanography

PUBLICATION LIST

1. **Yang Gao**, Yongxiang Huang, Hongyang Lin, Jia Zhu, Zhenyu Sun, Jianyu Hu (2020). "Surface currents measured by GPS drifters in Daya Bay and along the eastern Guangdong coast". *Frontiers of Earth Science*, 14 (10) 376-383
2. **Yang Gao**, Ruixin Huang, Jia Zhu, Yongxiang Huang, Jianyu Hu (2020). "Using the sigma-pi diagram to analyze water masses in the northern South China Sea in spring". *Journal of Geophysical Research Oceans*, 125 (7) e2019JC015676
3. Guiwen Tan, **Yang Gao**, Yongxiang Huang, Lipo Wang (2021). "Multi-level dissipation element analysis of the surface temperature of the South China Sea". *Dynamics of Atmospheres and Oceans*, 94 (1) 101218
4. **Yang Gao**, Francois G Schmitt, Jianyu Hu, Yongxiang Huang (2021). "Scaling analysis of the China France Oceanography Satellite along-track wind and wave data". *Journal of Geophysical Research Oceans*, 126 (8) e2020JC017119
5. **Yang Gao**, Francois G Schmitt, Jianyu Hu, Yongxiang Huang (2023). "Probability-based wind-wave relation". *Frontiers in Marine Science* , 2022(9)

6. **Yang Gao**, Francois G Schmitt, Jianyu Hu, Yongxiang Huang (2023). "Scale-to-Scale Energy and Enstrophy Fluxes of Atmospheric Motions via CFOSAT". Journal of Geophysical Research Atmospheres (In preparation)
7. **Yang Gao**, Francois G Schmitt, Jianyu Hu, Yongxiang Huang (2023). "Scaling Analysis of the Global Surface Air Temperature". Atmospheric Chemistry and Physics (In preparation)

PhD dissertation

Scaling and Coupling Analysis of Wind Speed and Wave Height, Using CFOSAT and Other Satellites

Cotutorial PhD program between Xiamen University and Université du Littoral Côte d'Opale
Supervisors: Francois G. Schmitt (France) and Yongxiang Huang (China)

Conferences

Participation to Summer School

1. Ecoles d'été France Excellence organisé conjointement par l'Ambassade de France/Institut français de Chine (IFC), "Climate Change in the Arctic - scientific and societal perspectives", Versailles, France, 2018. 07.1-27. (visiting student)

International Conferences

1. **Yang Gao**, Jianyu Hu, Yongxiang Huang. Fourier power spectrum of scaling process with missing data or irregular sampling steps. Fourth Xiamen Symposium on Marine Environmental Sciences, Xiamen, P.R. China, 2019. 01. 6-9, (poster).
2. **Yang Gao**, Jianyu Hu, Yongxiang Huang. Fourier power spectrum of ocean data with missing or irregular sampling. General Assembly 2019 of the European Geosciences Union, Vienna, Austria, 2019. 04. 7-12, (poster).
3. **Yang Gao**, Francois G Schmitt, Jianyu Hu, Yongxiang Huang. Scaling analysis of the China France Oceanography satellite along track wind and wave data. General Assembly 2020 of the European Geosciences Union, Vienna, Austria, 2020. 05. 06. (online "chat" presentation due to the Covid-19).
4. Yongxiang Huang, **Yang Gao**, Qianguo Xing, Francois G Schmitt. Scaling analysis of the algal blooms. General Assembly 2020 of the European Geosciences Union, Vienna, Austria, 2020. 05. 06. (poster).

5. **Yang Gao**, Francois G Schmitt, Jianyu Hu, Yongxiang Huang. Scaling feature of the ocean surface wind field. General Assembly 2021 of the European Geosciences Union, Vienna, Austria, 2021. 04. 20. (online “chat” presentation due to the Covid-19).
6. **Yang Gao**, Francois G Schmitt, Jianyu Hu, Yongxiang Huang. Estimation of the Scale-to-Scale Energy Flux of Ocean Surface Winds using CFOSAT satellite data. American Geophysical Union General Assembly 2021, New Orleans, America, 2021. 12. 15. (online “chat” presentation due to the Covid-19).
7. **Yang Gao**, Francois G Schmitt, Jianyu Hu, Yongxiang Huang. Wave Partitioning and Global View of Wind-Wave Coupling. Ocean Science Meeting 2022, Honolulu, America, 2022.03.01. (online “chat” presentation due to the Covid-19).
8. **Yang Gao**, Francois G Schmitt, Jianyu Hu, Yongxiang Huang. Scale-to-scale Energy and Enstrophy Fluxes of Atmospheric Motions via CFOSAT. General Assembly 2022 of the European Geosciences Union, Vienna, Austria, 2022. 05. 25. (online “chat” presentation due to the Covid-19).
9. **Yang Gao**, Francois G Schmitt, Jianyu Hu, Yongxiang Huang. CFOSAT wave field from wind-wave model. The 3rd CFOSAT science team meeting. Saint Malo, France, 2022. 09. 14. (online “chat” presentation due to the Covid-19).
10. **Yang Gao**, Francois G Schmitt, Jianyu Hu, Yongxiang Huang. Scaling Analysis of the Global Surface Air Temperature. American Geophysical Union General Assembly 2022, Chicago, America, 2022. 12. 15. (online “chat” presentation due to the Covid-19).

National Conference

1. **Yang Gao**, Yongxiang Huang, Hongyang Lin, Jia Zhu, Zhenyu Sun, Jianyu Hu. Surface current measured by GPS drifters in the Daya Bay and along the eastern Guangdong coast, South China Sea Annual Meeting 2018, Nanjing, P.R. China, 2018. 10. 26-28. (oral).

Group Meeting

1. **Yang Gao**, Francois G Schmitt, Jianyu Hu, Yongxiang Huang. Spatial and temporal multiscale analysis of the interactions between turbulence wind forcing and wave height dynamics using CFOSAT data. Remote Sensing and Geovisualization Day, Wimereux, France, 2019. 12. 04. (oral)

Rewards

Second Scholarship of Zhejiang Ocean University, 2013

Second Scholarship of Zhejiang Ocean University, 2014

Second Scholarship of Zhejiang Ocean University, 2015

Full grant from the French Embassy in the Program France Excellence 2018

Scholarship from Cotutella doctoral research project by Région Hauts-de-France 2019

Scholarship from Zhongtian Ocean System 2020

National scholarship for doctoral students 2021

Abstract

The China-France Oceanography Satellite (CFOSAT) was launched in October 2018 as a collaboration between Chinese and French space agencies. It provides simultaneous observations of wind and waves for the study of air-sea interactions. Based on these data, this study develops three new methods: 1) For the discontinuity data induced by factors such as lands or bad measurements, an improved Fourier power spectrum algorithm is proposed based on the Wiener-Khinchine theorem. Then the spectra for satellite along-track wind and waves are estimated to study the scaling features at the scale of 100-3,000 km. 2) We seek to improve the filter-space-technique to process the wind data which contain gaps, and obtain the features for energy and enstrophy fluxes of the atmospheric movements at the scale of 12.5-500 km. 3) We propose a probability-based swell identification method without the wave spectrum data, and establish a unified wind-wave power-law relationship model. The results obtained in this thesis contribute to enrich the fundamental knowledge of ocean surface processes.

Keywords: CFOSAT; scaling analysis; energy flux; wind-wave relation; air-sea interaction

Résumé

Le satellite océanographique Chine-France (CFOSAT) a été lancé en octobre 2018 dans le cadre d'une collaboration entre les agences spatiales chinoise et française. Il fournit des observations simultanées du vent et des vagues pour l'étude des interactions air-mer. Sur la base de ces données, cette étude développe trois nouvelles méthodes : 1) Pour les données de discontinuité induites par des facteurs tels que les terrains ou de mauvaises mesures, un algorithme amélioré de spectre de puissance de Fourier est proposé basé sur le théorème de Wiener-Khinchine. Ensuite, les spectres du vent et des vagues le long de la trajectoire du satellite sont estimés pour étudier les caractéristiques d'échelle à l'échelle de 100 à 3 000 km. 2) Nous cherchons à améliorer la technique de l'espace-filtre pour traiter les données de vent qui contiennent des lacunes et obtenir les caractéristiques des flux d'énergie et d'énstrophie des mouvements atmosphériques à l'échelle de 12,5 à 500 km. 3) Nous proposons une méthode d'identification de la houle basée sur la probabilité sans les données du spectre des vagues, et établissons un modèle unifié de loi de puissance vent-vague. Les résultats obtenus dans cette thèse contribuent à enrichir les connaissances fondamentales sur les processus de surface des océans.

Mots-clés: CFOSAT; analyse de mise à l'échelle; flux d'énergie; vent-vague relation; air-mer interaction

摘 要

对海气相互作用动力学过程认知的缺乏是气候模型不确定性主要来源之一，这其中海表风、浪间的相互作用决定了能量、热量、物质等交换过程，是理解海气相互作用的关键。然而，风和浪的运动涉及米至数千公里的空间尺度，包含着复杂的多尺度动力学过程，对应着空间上的标度特征。同时由于非线性相互作用的存在，在不同尺度间还存在能量、涡度拟能等物理量的传递与交换，形成复杂的湍流串级过程。然而由于风、浪观测数据和研究方法的不足，限制了风、浪标度、能量通量及风—浪耦合关系的研究，而这些研究对于我们理解海气相互作用中的海表动力学特征极其重要。中法海洋卫星为海气相互作用研究提供了同时观测的风、浪数据集，围绕这些数据，本文发展了三个新的方法并开展以下工作：1) 针对由于陆地等因素导致数据不连续的问题，基于 Wiener-Khinchine 定理提出改进的傅里叶能谱算法，计算卫星沿轨非完整风、浪数据的能谱以研究风、浪在 100-3,000 km 尺度的标度特征。2) 改进不依赖于湍流模型的空间滤波算法，处理存在数据丢失的卫星风场，获得风场在 12.5-500 km 尺度的能量通量和涡度拟能通量特征。3) 结合浮标和卫星观测风、浪数据提出一个无需海浪谱信息的基于概率的涌浪分离法，建立一个适用于全球海域的风—浪幂律关系模型。

我们的研究发现风、浪多尺度标度的时空变化特征，风场在不同尺度间的能量通量和涡度拟能串级的特点，以及提出一个基于概率的涌浪分离法和建立一个适用性更广的风—浪耦合模型。本论文中的研究结果不仅丰富我们关于海表动力过程的基础知识，而且还为海洋或大气模型的输出结果提供参考。

关键词： 中法海洋卫星；标度分析；能量通量；风-浪关系；海气相互作用